DOCTOR OF PHILOSOPHY

Synthesis, characterisation and applications of diamond materials

Shi Su

2013

Aston University

SYNTHESIS, CHARACTERISATION AND APPLICATIONS OF DIAMOND MATERIALS

SHI SU

Doctor of Philosophy

23th JUNE, 2013

Declaration

The work in this thesis is the results of research carried out in Nanoscience Group at School of Engineering and Applied Physics, Aston University, Birmingham, United Kingdom. I declare it to be my own work unless referenced to the contrary in the text.

To my parents

Acknowledgement

I would like to first express the most sincere appreciation to my supervisors, Dr. Haitao Ye (Supervisor, Reader of SEAS, Aston University) and Prof. Lin Zhang (Professor of SEAS, Aston University). Without their generosity of knowledge sharing, endless support and encouragement, it would be impossible to carry out this research programme and complete the thesis. Moreover, I am grateful for other group members, Jiangling Li, Vojtěch Kundrát, and D. Coathup in the Nanoscience Research Group for the academic discussions, their selfless help and expertise whenever I needed throughout the project.

Also, many thanks should be delivered to Mr. A. M. Abbot for his assistance in some of the technical issues during my experiments. I also acknowledge the contribution made by Prof. J. Sullivan, Dr S. Saied and Dr B. Shi, for their suggestions to my thesis and XPS analysis throughout the whole project. I would like to express my thanks to G. CB. Lee for his contribution to the femtosecond-laser patterning work at the early stages of this project. Last but not least, I would like to thank the Science Research Investment Fund (SRIF) via Aston University, Aston University Ph.D. studentship and British Engineering and Physical Sciences Research Council (EPSRC) for the financial sponsorships offered to this doctoral programme.

A PhD thesis is a work of art: it demonstrates the creative expression of the author. Behind the whole process of a PhD thesis, it contained both painful and ecstatic moments belonging to my own. I would like to dedicate this thesis to my dear parent, as well as every friend I met during the past four years, impossible to every name them all. Their endless support and help accompanies me overcome the difficulties in my PhD period.

Abstract

This thesis presented a detailed research work on diamond materials. Chapter 1 is an overall introduction of the thesis. In the Chapter 2, the literature review on the physical, chemical, optical, mechanical, as well as other properties of diamond materials are summarised. Followed by this chapter, several advanced diamond growth and characterisation techniques used in experimental work are also introduced. Then, the successful installation and applications of chemical vapour deposition system was demonstrated in Chapter 4. Diamond growth on a variety of different substrates has been investigated such as on silicon, diamond-like carbon or silica fibres. In Chapter 5, the single crystalline diamond substrate was used as the substrate to perform femtosecond laser inscription. The results proved the potentially feasibility of this technique, which could be utilised in fabricating future biochemistry microfluidic channels on diamond substrates. In Chapter 6, the hydrogen-terminated nanodiamond powder was studied using impedance spectroscopy. Its intrinsic electrical properties and its thermal stability were presented and analysed in details.

As the first PhD student within Nanoscience Research Group at Aston, my initial research work was focused on the installation and testing of the microwave plasma enhanced chemical vapour deposition system (MPECVD), which will be beneficial to all the future researchers in the group. The fundamental of the on MPECVD system will be introduced in details. After optimisation of the growth parameters, the uniform diamond deposition has been achieved with a good surface coverage and uniformity. Furthermore, one of the most significant contributions of this work is the successful pattern inscription on diamond substrates by femtosecond laser system. Previous research of femtosecond laser inscription on diamond was simple lines or dots, with little characterisation techniques were used. In my research work, the femtosecond laser has been successfully used to inscribe patterns on diamond substrate and fully characterisation techniques, *e.g*. by SEM, Raman, XPS, as well as AFM, have been carried out. After the femtosecond laser inscription, the depth of microfluidic channels on diamond film has been found to be 300~400 nm, with a graphitic layer thickness of 165~190 nm. Another important outcome of this work is the first time to characterise the electrical properties of hydrogen-terminated nanodiamond with impedance spectroscopy. Based on the experimental evaluation and mathematic fitting, the resistance of hydrogen-terminated nanodiamond reduced to 0.25 MΩ, which were four orders of magnitude lower than untreated nanodiamond. Meanwhile, a theoretical equivalent circuit has been proposed to fit the results. Furthermore, the hydrogen-terminated nanodiamond samples were annealed at different temperature to study its thermal stability. The XPS and FTIR results indicate that hydrogen-terminated nanodiamond will start to oxidize over 100°C and the C-H bonds can survive up to 400°C. This research work reports the fundamental electrical properties of hydrogen-terminated nanodiamond, which can be used in future applications in physical or chemical area.

Key Words: Diamond, Nanodiamond, Nanotechnology, Microwave Plasma-Enhanced CVD, Raman Spectroscopy, Femtosecond Laser, Impedance Spectroscopy.

Relevant Publications

S. Su, J. Li, G. C. B. Lee, K. Sugden, H. Ye, Femtosecond laser-induced microstructure on diamond for microfluidic sensing devices applications, *Appl. Phys. Lett.*, **102**, 231913, 2013.

S. Su, J. Li, A. M. Abbot, H. Ye, Hydrogen-terminated Detonation Nanodiamond: Impedance Spectroscopy and Thermal Stability Studies, *J. Appl.Phys.*, **113**, 023707, 2013.

S. Su, J. Li, V. Kundrát, A. M. Abbot, H. Ye, Hydrogen-passivated detonation nanodiamond: An impedance spectroscopy study, *Diam. Relat. Mater.*, **24**, 49-53, 2012.

J. Li, S. Su, L. Zhou, V. Kundrát, F. Mushtaq, D. Ouyang, D. Robertsd, A. M. Abbot, H. Ye, Carbon nanowalls growth by microwave plasma enhanced chemical vapor deposition during carbonization of polyacrylonitrile fibers, *J. Appl.Phys.*, **113**, 024313, 2013.

G. CB. Lee, S. Su, J. Li, K. Sugden, N. Roohpour, H. Yan, H. Ye, Analysis of femtosecond laser surface patterning on bulk single-crystalline diamond, *J. Exp. NanoSci.*, **7**, 662-672, 2012.

H. Ye, S. Su, Biological and Biomedical Coatings Handbook, Applications, Chap.4: Impedance Spectroscopy on Carbon-based Materials for Biological Applications", *CRC Press*, Taylor Francis Group, ISBN: 978-1-4398-4996-5.

Contents

Abbreviations

HTHP	high-temperature high-pressure
MPECVD	microwave plasma enhanced chemical vapour deposition
fcc	face-centred cubic
NEA	negative electron affinity
DOS	density-of-state
GVD	group velocity dispersion
GC	glassy carbon
CNTs	carbon nanotubes
SHE	standard hydrogen electron
CV	cyclic voltammetry
HOPG	highly-oriented pyrolytic graphite
FET	field effect transistor
CPE	constant phase element
BDD	boron-doped diamond
EIS	electrochemistry impedance spectroscopy
HFCVD	hot-filament chemical vapour deposition
DND	detonation nanodiamond
TEM	transmission electron microscopy
FTIR	Fourier transform infrared
NV	nitrogen-vacancy
PL	photoluminescent
FTIC	fluorescein isothiocyanate
TAMRA	tetramethylrhodamine
SEM	scanning electron microscopy
PE	primary electrons
SE	secondary electrons
BSE	back scattered electrons
XPS	X-ray photoelectron spectroscopy
FWHM	full width at half maximum
UHV	ultra-high vacuum
AFM	atomic force microscopy
RMS	root mean square
VDOS	vibrational density of state

FFT	fast Fourier transform
IS	impedance spectroscopy
AC	alternative current
GI	grain interior
GB	grain boundary
HOD	highly-oriented films
BEN	bias-enhanced nucleation
DI	de-ionised
FIB	focused ion beam
DLC	diamond-like carbon
RIE	reactive ion beam
fs	femtosecond
PA	polyacetylene
NMR	nuclear magnetic resonance
H-DND	hydrogen-terminated nanodiamond
UHV	ultra-high vacuum
sccm	standard cubic centre metre
Q-DLTS	charge-based deep-level transient spectroscopy
TGA	thermogravimetric analysis
BE	binding energy
TNT	trinitrotoluene

Symbols

E_g	semiconductor bandgap
χ	negative electron affinity barrier height
$F(E)$	Fermi-Dirac distribution
$n(E)$	electron density
$N(E)$	energy state per unit volume
E_F	Fermi level
k (electrical)	Boltzmann constant
N_c	effective density-of-state in conduction band
N_v	effective density-of-state in valence band
T	Kelvin temperature
n_i	intrinsic carrier concentration
h	Planck’s constant
$n_{(vac)}$	refractive index (in vacuum)
n_d	refractive index of diamond
λ	wavelength
n_0	linear refractive index
E	applied optical electrical field
n_2	non-linear refractive index
v_d	propagation speed of light in media
$\chi^{(3)}$	non-linear optical coefficient
τ	electron relaxation time of a carrier in semiconductor
m^*	average effective mas
m_l	longitudinal electron mass
m_t	transversal electron mass
E_{pc}	reduction peak in cyclic voltammetry
E_{pa}	oxidization peak in cyclic voltammetry
i_{pc}	reduction current
i_{pa}	oxidization current
k (electrochemistry)	reversible electrochemistry parameter
n (electrochemistry)	amount of electrons in chemical exchange process
j_0	exchange current
F	Faraday constant
α	cathodic reaction

β	anodic reaction
γ	CV scanning rate
E (electrochmistry)	voltammetry potential
E (mechanical)	Young's modulus
σ (mechanical)	uniaxial stress
ε (mechanical)	uniaxial strain
M	Mohs number
H	hardness
K (mechanical)	piezoresistivity
γ (electrical)	emission barrier height coefficient
ω	angular frequency
α	diamond crystal parameter
E_k	kinetic energy
E_B	binding energy of electrons
ΔE	XPS energy resolution
v_m	vibrating characteristic frequency
v_o	Rayleigh scattering
δ	grain boundary size
σ	frequency-dependent correction factor
ε_0	permittivity of free space
$\varepsilon_\mathrm{gb/gi}$	grain boundary/grain interior relative dielectric constant

List of Figures

List of Tables

Chapter 1: Introduction

Introduction

Diamond-based materials have been developed in 1970s and its applications had a tremendous progress in the last two decades. The diamond materials have several particular properties, such as extreme hardness (~100 GPa), chemical stability in acid/alkali solution, very low coefficient of friction, highest thermal conduction (2,000 $W.m^{-1}.K^{-1}$), high carriers mobility (2,400 $cm^2.V^{-1}.s^{-1}$ for electrons, 2,100 $cm^2.V^{-1}.s^{-1}$ for holes), wide bandgap (5.47 eV) and biocompatibility.

However, the extremely scarce storage and supply of diamond in nature and the difficulties of the high-temperature high-pressure (HTHP) method has encouraged scientists to find a new method to produce diamond. Hence, the chemical vapour deposition (CVD) method has been developed to enable the feasibility of fast-growth of diamond on heteroepitaxial/homoepitaxial substrates.

The development of nanodiamond created a new subject in diamond research. Early research proved that the nanodiamond can be used in *in-vivo* drug delivery carriers, electrochemical catalyst, biomedical markers, and bacterial binding sensors, *etc*. In the nano/sub-nano scale, the small size effect of diamond modifies its property and distinguishes it as in macro-scale. However, little research was done on its electrical properties for its extremely small grain size. Thus, the characterisation of the electrical properties of nanodiamond forms an important part of this thesis.

In Chapter 2, the intrinsic properties of both diamond and nanodiamond will be introduced and compared as a literature review for the thesis. The specific area covers its electrical, optical, chemical, as well as mechanical properties. Some of the state-of-the-art applications have also been presented at the end in this chapter.

Chapter 3 demonstrates the advanced techniques utilised in the research of diamond materials. The microwave plasma enhanced CVD (MPECVD) and hot-filament CVD (HFCVD) hosted in Aston University will be introduced. Then, the other characterisation method, such as SEM, XPS, AFM, Raman spectroscopy, FTIR and impedance spectroscopy, will be illustrated for both diamond films and nanodiamond.

Chapter 4 reports the diamond growth on different substrates using the MPECVD system. The optimised growth conditions have been obtained, which laid a solid foundation for future research work.

In Chapter 5, the femtosecond laser technique was used to fabricate microfluidic channels on a single-crystalline diamond substrate. The fs-laser inscribed channels were then characterised by SEM, Raman, XPS as well as AFM. Based on these techniques, the composition of the graphitic layer formed on the micro-channels was determined. By comparing the AFM profiles before and after the removal of the graphitic layer, the average thickness can be deduced from the cross-sectional images. This work developed an ultra-fast laser inscription technique to fabricate microfluidic channels on diamond substrates.

The electrical properties of hydrogen-terminated nanodiamond were investigated in Chapter 6. The impedance of nanodiamond decreases by four orders of magnitude after hydrogen-plasma treatment. An equivalent circuit has been proposed to correlate with the conduction mechanism. Arrhenius relationship explains the different in activation energy levels existing between room temperature and 400˚C. The hydrogen-terminated nanodiamond has been further annealed at different temperature and characterised by FTIR and XPS. The results proved that the nanodiamond started to oxidise over 100˚C and survived up to 400˚C in air.

Finally, the previous research has been summarised and future research directions are proposed. This PhD project has built a fundamental research work for future potential applications of femtosecond laser inscription on diamond and the biological applications of nanodiamond.

Chapter 2: Characteristics and Properties of Diamond Materials

Characteristics and Properties of Diamond Materials

2.1 Introduction

2.1.1 Diamond and Crystal Structure

Diamond is an allotrope of carbon (C), and is one of the hardest materials in the world which is widely used as a gemstone and in jewellery.[1] Carbon is located in Group IV of the periodic table, which contains 6 protons in the atom core and 6 electrons outside the core. It has 16 isotopes, while two states of them are stable (^{12}C and ^{13}C). The electrons configuration of carbon is $1s^22s^22p^2$. Classified by the different bonds types, the carbon atoms can form $sp + 2\pi$, $sp^2 + \pi$, and sp^3 hybridization, as shown in **Figure 2.1**.[2]

Figure 2.1 The carbon family classification scheme outline and the structures.[1]

The sp^2 hybridization is shown in **Figure 2.2**, where the angle existing between the two atoms is 120° degrees, and all the covalent bonds (π bonds) are in the same plane. Comparing with the sp^2 hybridization and π bonds, the sp^3 hybridization was formed by a 2s electron moving to 2p orbital because of an excitation. The covalent bonds are named σ (sigma) bonds, which is even stronger than the π bonds. The angle between two σ bonds is 109.5° degrees.

Figure 2.2 Carbon *sp*^{2} (left) and *sp*^{3} (right) orbitals and structure.[1]

In diamond, there is only periodic C *sp*^{3} hybridization. It is arranged in the format of face-centred cubic (fcc) crystal structure (**Figure 2.3**), which is widely known as the diamond lattice. In the diamond cubic structure the lattice constant (a) of diamond is 3.567 Å, and the space group is $Fd3m\text{-}O_h^7$. Each C atom has four *sp*^{3} bonds connecting with four neighbouring C atoms and the bond length is 1.54 Å. Every lattice has eight atoms per unit cell and no infrared absorption in the one-phonon region. The diamond atomic density is $1.77\times10^{23}/\text{cm}^3$ and its specific gravity is 3.52±0.01 (density: 3.5-3.53 g/cm^3).[3]

Figure 2.3 The diamond cubic crystal structure of carbon *sp*^{3} hybridization.[4]

2.1.2 Classification of Diamond

Diamond can be classified into four categories according to its different impurity types, as seen in **Figure 2.4** and **Table 2.1**.[5] Pure diamond is only constructed by carbon *sp*^{3} structure in lattice. However, some impurities can be cooperated into the diamond and the basic classification is based on the existence of the nitrogen, as well as other impurities. Type I diamond contains a high nitrogen content of 500~3,000 ppm and type II has a lower nitrogen content of less than 5 ppm. The type I diamond could be separated to type Ia and type Ib. Both types have nitrogen impurities in the bulk, but in a different format. The type Ia has aggregated nitrogen atoms whilst the nitrogen impurities in type Ib diamond are isolated apart from each other. In type Ia diamond, the different link between the nitrogen could be divided into two types, IaA and IaB, as shown in **Figure 2.4**.

In IaA type diamond, the nitrogen atoms are aggregated in pairs. On the other hand, the nitrogen atoms in IaB type diamond have a vacancy in the centre, the so-called ‘4N+V’ structure. In contrast, the Ib type also has nitrogen impurities, but the nitrogen atoms are distributed separately.

Table 2.1 Classification of diamond.[5]

For type II diamond, there is a rare content of nitrogen impurities, usually N < 5ppm. The difference between type IIa and IIb diamond can be distinguished by the non-nitrogen impurities than nitrogen. Type IIa type contains no other impurities, while the IIb type also contains boron. The IIa type diamond has the highest thermal conductivity and the extreme hardness when comparing with the other types of diamond. The boron impurities make IIb diamond a *p*-type semiconductor with a blue or grey colour.

Figure 2.4 The classification chart of diamond.[5]

2.2 Diamond Properties

2.2.1 Electrical Properties

Diamond has a tetrahedral *sp*^{3} covalent bonded carbon atomic structure. It has been widely known as a wide-bandgap semiconductor with a bandgap (E_g) of 5.47 eV at room temperature (300 K). The resistivity of type Ia, Ib and IIa diamond have been reported ranging from 10^{16}~10^{18} Ω.m.[6],[7] While in contrast, type IIb diamond has a much lower resistivity of 1~10^5 Ω.m and its boron dopants have an activation level of 0.35~0.38 eV above the valence band, as shown on **Figure 2.5**. To create an *n*-type semiconductor, phosphorous (P) and nitrogen (N) can be used as dopants. The phosphorous-dopant will generate a donor energy level of 0.6 eV and the nitrogen dopant will create 1.7 eV below the conduction band minimum.[3] In addition, the C-H bonds on the single crystalline diamond will create a negative electron affinity (NEA) barrier height χ, which varies from -1.27 eV (diamond: 1×1) surface to +0.38 eV (diamond 2×1) surface on (111) diamond.[8] For a (100) diamond surface, the NEA will be -2.2 eV.[9]

For an intrinsic semiconductor, the carriers generated from the thermal activation are much more than that produced from the doping impurities. The electron density $n(E)$ can be deduced from the Fermi-Dirac distribution $F(E)$ as well as the energy state per unit volume $N(E)$, which is expressed by

$$F(E) = \frac{1}{1+e^{\frac{E-E_F}{kT}}} = \begin{cases} 0, & e^{-(E-E_F)/kT} \gg 1 \\ 1, & e^{-(E-E_F)/kT} \ll 1 \end{cases} \qquad \textbf{Equation 2.1}$$

The probability of electron states with an energy, $F(E)$ is calculated by **Equation 2.1**. The Fermi level E_F is the energy of the probability at one-half and k is the Boltzmann constant.[10] Thus, the electron density in the conduction band can be expressed by **Equation 2.2**, whilst N_c is the effective density-of-states (DOS) in the conduction bands. E_c and E_v represent the level of conduction band and valence band, respectively.

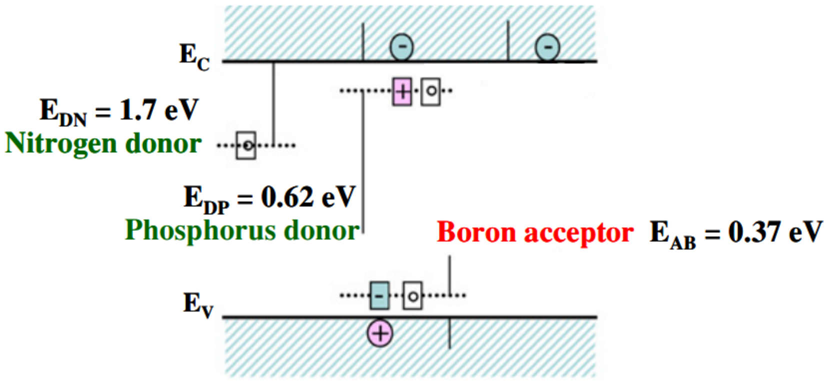

Figure 2.5 Bandgap structure of diamond and impurities doping in diamond.[11],[12]

$$\boldsymbol{n(E) = N_c e^{-(E_c - E_F)/kT}}$$ **Equation 2.2**

For diamond material, N_c is given by **Equation.2.3**:

$$\boldsymbol{N_C = 2(\frac{2\pi m_e^* kT}{h^2})^{3/2}}$$ **Equation 2.3**

m_e^* is the density-of-states effective electron mass and h is Planck's constant. Similarly, the holes in the valence band can be calculated by **Equation 2.4**.

$$\boldsymbol{N_V = 2(\frac{2\pi m_h^* kT}{h^2})^{3/2}}$$ **Equation 2.4**

Combined **Equation 2.3** and **2.4**, the intrinsic carrier concentration for diamond is expressed by

$$\boldsymbol{n_i^2 = np = N_C N_V e^{-E_g/kT}}$$ **Equation 2.5**

while E_g is the bandgap width, n is the electron concentration and p is the holes concentration.[16]

Table 2.2 Electronic properties of semiconductor materials comparing with diamond.[17]-[19]

Properties		Ge	Si	GaAs	SiC (3C)	SiC (4H)	SiC (6H)	GaN	Diamond
Band Gap (eV)		0.66	1.1	1.4	2.23	3.2	2.86	3.39	5.47
Band Gap Type		Indirect	Indirect	Direct	Indirect	Indirect	Indirect	Direct	Indirect
Lattice Constant (Å)		5.660	5.431	5.653	4.359	3.073	*a*: 3.08 *c*: 15.1	*a*: 3.19 *c*: 5.19	3.567
Density (g/cm^3)		5.60	2.42	5.32	3.16	3.16	3.16	6.1	3.52
Dielectric Constant		16.0	11.8	12.8	9.72	9.6	*a*: 9.66 *c*: 10.0	*a*: 9.5 *c*: 10.4	5.68
Mobility (cm^2/V.s)	Electron	3,900	1,350	8,600	1,000	900	450	900	1,800
	Holes	1,900	480	400	50	100	50	400	1,600
Thermal Conductivity (W/cm.K)		0.58	1.51	0.54	4.9	4.9	4.9	1.3	20.9
Saturation Velocity (10^7 cm/s)		0.6	1.0	2.0	2.7	2.7	2.7	2.0	V_e: 2.5 V_h: 1

According to **Equation 2.5**, the intrinsic thermal activation exceeds ~1,000˚C. These properties of diamond make it a suitable substrate material for electric power devices. Compared with the other semiconductor materials, the diamond-based devices can reduce the possibility of malfunction caused by overheating due to the heat sink of the substrate because of its highest thermal conductivity.[10],[13] In addition, the hole and electron mobility of diamond is also extraordinary among various types of common semiconductors, as shown on **Table 2.2**. In summary, the conducting mechanism of *p*-type semiconductor is the mobility of holes, which is created from the acceptor. On the other hand, the donor in semiconductor induces electrons and creates an *n*-type energy level. The *p*-type doping of diamond has been realised by boron acceptor (E_{AB}=0.37 eV) and is utilised as a substrate for many devices. The B-doped diamond will lower the activation energy and enable Ohmic contacts. However, the *n*-type dopants phosphorous donor (E_{DP}=0.62 eV) and nitrogen donor (E_{DN}=1.7 eV) are shallow donor in diamond. The shallow donor will introduce new energy levels in a semiconductor, which will alter its fundamental electronics properties. Thus, the *n*-type doping of diamond is not promising.[14] The *p*-channel diamond MESFETs and MISFETs, transistors, as well as bipolar structures have been developed and reviewed in relevant articles.[15]

2.2.2 Optical Properties

Diamond can transmit ultraviolet from the visible to the infrared regions and it is one of the rare materials that has a wide far-infrared transmission range (light wavelength: 30-450 μm), as well as excellent resistance to thermal shock. Because of these optical properties, diamond can be fabricated as a microwave shield window for visible and ultraviolet radiation.[20] In this section, the optical properties of diamond will be reviewed.[1]

In optics, the refractive index, *n*, of a certain materials (optical medium) is used to describe the propagation of light in that material. Take the value *n* in vacuum at 0˚C as 1, the refractive value of diamond n_{d} can be calculated by:

$$\boldsymbol{n_{vac} \cdot sin\theta_{vac} = n_d . sin\theta_d} \qquad \textbf{Equation 2.6}$$

or

$$\boldsymbol{n_d = \frac{v_{Vacuum}}{v_{Diamond}}} \qquad \textbf{Equation 2.7}$$

where θ represent the angle of incidence formed by the interface and the transmission path of light in each medium. The velocity of light in vacuum (v_{Vacuum}) is 299,792 km/s, and 123,083 km/s in diamond (v_{Diamond}). Thus, the refractive index of diamond is n_{d}=2.39225, corresponding

---

[1] This work is also a cooperative research program with Dr. M. Vladimir, Aston Institute of Photonic Technology.

to the light wavelength of 1.026 μm, as shown on **Figure 2.6**.[20],[22] On the other hand, the Cauchy relationship indicates that the relationship between refractive index n_d and wavelength λ, which can be calculated as:

$$\boldsymbol{n = a_0 + a_1\lambda^{-2} + a_2\lambda^{-4} + a_3\lambda^{-6} \ldots = \sum_{i=0}^{n} a_i\lambda^{-2(i+1)}} \qquad \textbf{Equation 2.8}$$

$$\boldsymbol{n = A + \frac{B}{\lambda^2} + \frac{C}{\lambda^4}} \qquad \textbf{Equation 2.9}$$

or throughout Sellmeier dispersion equation:

$$\boldsymbol{n^2 = 1 + \frac{A_1\lambda^2}{\lambda^2 - \lambda_1^2} + \frac{A_2\lambda^2}{\lambda^2 - \lambda_2^2} + \cdots} \qquad \textbf{Equation 2.10}$$

The parameters A_1, A_2, are 0.3306, 4.3356, and λ_1, λ_2 are 0.175 μm, 0.106 μm, which were calculated from **Equation 2.10**, respectively.[23] The refractive index of diamond versus light wavelength is plotted by **Figure 2.6**.

Aston University

Illustration removed for copyright restrictions

Figure 2.6 Diamond refractive index relationship with light wavelength.[22]

The refractive index of diamond can be deduced by **Equation 2.10** and n_d = 2.39225 corresponding with the light wavelength of 1.026 μm.[24] The transmission ratio versus the wavelength of light is shown on **Figure 2.7**. The significant absorption at mid-wavelength infrared absorption is derived from the impurities and crystal defects of diamond. The absorption ratio is calculated by A= -$\log_{10}(T)$, where A is the absorption and T represents the transmission rate. The infrared absorption in diamond can be derived from the nitrogen impurities incorporated in diamond film. The nonlinear refractive index is defined as:

$$\boldsymbol{n = n_0 + n_2 < E^2 >} \qquad \textbf{Equation 2.11}$$

$$\boldsymbol{n_2 = 12\pi^2\chi^{(3)}/n_0^2} \qquad \textbf{Equation 2.12}$$

while n_0 is the linear refractive index and E is applied optical electrical field.[25] The nonlinear refractive index is critical for the high-power devices. The n_2 is determined by several different physical parameters. The empirical expression for n_2 is

$$\boldsymbol{n_2 = \frac{K(n_d-1)(n_d^2+2)^2}{v_d\left[1.517+\frac{(n_d^2+1)(n_d+1)}{6n_d}v_d\right]^{1/2}} \times 10^{-13}} \qquad \textbf{Equation 2.13}$$

while $\chi^{(3)} = 1.8\times10^{-13}$ and n^2 for diamond is 1.3×10^{-15} $cm^2.W^{-1}$.[26]

Figure 2.7 Diamond optical transmission versus light wavelength.[22]

In diamond optics, the dispersion is related to the velocity of the light, which is related to its frequency. The group velocity dispersion (GVD) can be recognised as the group delay dispersion parameter D, which is calculated as:

$$\boldsymbol{D = n - \lambda\frac{dn}{d\lambda}} \qquad \textbf{Equation 2.14}$$

For the light wavelength of 1026 nm, the GVD coefficient is 1.4741.[23] The electron relaxation time τ is defined as the average free time of a carrier in semiconductor and inversely proportional to the scattering probability, which is expressed as:

$$\boldsymbol{\tau = \frac{m^*}{n_e e^2} = \frac{m^* e n_e \mu_e}{n_e e^2} = \frac{m^* \mu_e}{e}} \qquad \textbf{Equation 2.15}$$

while the electron mobility in diamond is 1,800~2,500 cm^2/V.s, and an average effective mass of $m^* = (m_l.m_t^2)^{1/3}$. m_l is longitudinal electron mass and m_t is transversal electron mass.[27]

2.2.3 Chemical Properties

The traditional carbon electrode, *e.g.*, glassy carbon (GC), carbon fibre or carbon nanotubes (CNTs) are indispensable materials, for their low cost, large surface-to-area ratio and wide potential window. The conductive boron-doped diamond film can be used as an alternative material to the traditional carbon electrodes. The electrochemistry properties have been reviewed by Pleskov, Fujishima, and Nebel *et al.*[28]-[30] The boron doped diamond electrode can drive the photoelectrochemistry reactions with different solutions, as shown in **Figure 2.8**. The electrochemical reaction was measured by Standard Hydrogen Electron (SHE), which represented the reaction: $2H^+ + e^- \rightarrow H_2$.

Figure 2.8 Energy band diagram for diamond with various redox couples at pH 4.5.[28]

One of the most important diamond electrode properties is the wide potential window. **Figure 2.9** shows the cyclic voltammetry (CV) response of different types of diamond electrodes. Cyclic voltammetry measurement is an electrochemical measurement based on the potential-dynamic principles. In the CV measurement, **Figure 2.9 (a)** is the CV plot of a high quality polycrystalline diamond electrode and **Figure 2.9 (b)** belongs to the low quality polycrystalline diamond electrode. **Figure 2.9 (c)** and **(d)** are the platinum electrode and highly-oriented pyrolytic graphite (HOPG), respectively. The solution is 0.5 M H_2SO_4, with a scan rate of 200 mV.s^{-1}.[28]

Figure 2.9 Cyclic Voltammetry of different types of electrodes: (a) high quality polycrystalline diamond electrode; (b) low quality polycrystalline diamond electrode; (c) platinum; (d) highly-oriented pyrolytic graphite (HOPG). The solution is 0.5 M H_2SO_4 with a scan rate of 200 mV.s^{-1}.[28]

From **Figure 2.9**, it is obvious that the high-quality diamond electrode has a relative wide potential window of approx. 3.55V, comparing with the low-quality diamond (2.2V), platinum (1.5V), and HOPG (2V). The high-quality diamond demonstrated a wide electrochemistry window, which enable the possibility of detecting reactions in this range. As shown on **Figure 2.10**, the peak on the CV plot was assigned as the E_{pc} (reduction peak, Quadrant I) and E_{pa} (oxidization peak, Quadrant IV), and their heights on Y-axis were i_{pc} and i_{pa}, respectively.[29] The relationship can be expressed as

$$|\boldsymbol{E_{pc}} - \boldsymbol{E_{pa}}| = \frac{\mathbf{57}\ \boldsymbol{m}\mathbf{V}}{\boldsymbol{n}} \qquad \textbf{Equation 2.16}$$

$$\boldsymbol{k} = |\frac{\boldsymbol{i_{pc}}}{\boldsymbol{i_{pa}}}| \qquad \textbf{Equation 2.17}$$

while n is the amount of electron take part in the process. If the reaction is a reversible electrochemistry process, k =1. When the process is irreversible, k is higher or lower than 1. On the other hand, as the charge-transfer resistance R_{ct} was determined by the electrochemical impedance method. The exchange current j_0 is given by

$$\boldsymbol{R_{ct} = RT/(nFj_0)} \qquad \textbf{Equation 2.18}$$

while R is the gas constant (8.314 J.K^{-1}.mol^{-1}), T is the Kelvin Temperature and F is the Faraday constant. According to this equation, the transfer coefficient α (cathodic reaction) or β (anodic reaction) can be calculated as

$$\boldsymbol{\alpha\ (\beta) = -\gamma.\left(\frac{RT}{nF}\right)\left(\frac{\partial ln|i_p|}{\partial E}\right)} \qquad \textbf{Equation 2.19}$$

while E is the voltammetry potential and γ is the CV scanning rate.[30]

Figure 2.10 Cyclic Voltammetry results.[31]

2.2.4 Mechanical Properties

Diamonds highest strength is derived from the carbon sp^3 bonds. It is quite difficult to dislocate the bonds between any two carbon atoms. The Young's modulus E of a material is defined as the ratio of uniaxial stress σ versus uniaxial strain ε measured by stress.

$$\boldsymbol{E = \frac{\sigma}{\varepsilon}} \qquad \textbf{Equation 2.20}$$

The Young's modulus of polycrystalline diamond varies from 400 to 800 MPa and 2,000 to 3,000 for single crystal diamond. The summary of diamond mechanical properties is shown in Table 2.3.

On another hand, diamond was also measured in the Mohs hardness, which is a type of scratch hardness method for solid-state materials relating to its indentation hardness. The relationship between the Mohs number M and the indentation hardness H (kg/mm^2) has been determined by

$$\log H = 0.2\,M + 1.5 \qquad \textbf{Equation 2.21}$$

The diamond material has a Mohs number of 10, comparing with other materials, *e.g.* tungsten (7.5), chromium (8.5), and boron (9.5).

Table 2.3 Summary of Mechanical Properties for CVD Diamond[20],[32]-[34]

Properties	Polycrystalline CVD Diamond	Singlecrystalline CVD Diamond	Nanodiamond
Hardness (GPa)	85~100	70~100	70~145
Fracture Toughness (MPa)	5.5	3.4	6.9~9.8
Tensile Strength (MPa)	400~800	2,000~3,000	63~67
Compressive Strength (GPa)	>90	>90	>47
Young’s Modulus (GPa)	1,220	1,140	776~925

2.3 Diamond Extraordinary Properties

In this section, the properties of diamond are summarised. Diamond material has the following key features: (1) super-wide band gap semiconductor (~5.47 eV) with an extraordinary breakdown voltage of over 100 V; (2) the highest thermal conductivity among the natural materials and (3) chemical inertness with a very wide potential response window. Meanwhile, the refractive index of diamond is as high as 2.4 in the visible light. Other properties related to diamond are listed in **Table 2.4**.

Table 2.4 Other specific properties of diamond material.[35]-[37]

Properties	Values	Units
Hardness*	10,000	kg/mm^2
Strength (tensile)	>1.2	GPa
Strength (compressive)	>110	GPa
Lowest Compressibility	8.3×10^{-13}	$m^2.N^{-1}$
Young’s Modulus*	1,050-1,220	GPa
Thermal Conductivity*	20.9	W/cm.K
Poisson’s Ratio	0.2-0.1	N/A
Debye Temperature*	2,200-1,860	K
Melting Temperature	3,820	K
Dielectric Constant	5.7	N/A
Thermo Expansion Coefficient	1×10^{-6}	/K (@300K)
Friction coefficient	0.1	N/A

* denotes the highest value in solid materials.

2.4 Diamond Films

2.4.1 Growth of Diamond Film

Chemical vapour deposition (CVD) method has been widely used in the synthesis of thin-film coating on other substrates. The diamond CVD deposition technique has been studied since early 1980s. The substrates used in CVD diamond growth can be either on the diamond film, which is referred to as homoepitaxial growth, or on other non-diamond substrate which is defined as heteroepitaxial growth.[38] The first high-temperature high-pressure (HTHP) method for diamond CVD deposition was reported by Wentorf, *et al*.[39] The growth condition diagram is shown in **Figure 2.11**. The experimental growth condition was as high as 1,300 K at a pressure of 3.1×10^{7} Pa. As an alternative method, *i.e*. plasma-assisted CVD method was developed, the diamond films could be deposited under a carbon-contained species atmosphere. The heteroepitaxial growth of diamond films can be accomplished by thermal or plasma-assisted CVD techniques, in which a hydrocarbon carbon source gas is mixed in hydrogen gas.

Figure 2.11 Diagram of diamond growth with different carbon source and condition phase (at 1,300 K/3.1×10^{7} Pa).[40]

In the plasma-assisted CVD system, the plasma is stimulated by electrical discharge from a microwave generator. The plasma generates the atomic hydrogen as well as carbon precursors in the chamber.

Figure 2.12 (a): schematic diagram of MPECVD system, and (b): the source gas flow distribution in the reaction chamber.[38]

The growth rate of diamond from gaseous reactants is fundamentally based on the flux of the species on the substrates surface and the products generated from it, as well as the temperature inside the chamber. For the gas dissociation, electric discharge, microwave/RF and hot-filament are usually applied. The crystalline orientation and quality of diamond film is not only determined by different types of carbon precursor, but also includes the oxygen concentration. *e.g.* hydrocarbons, alcohols, ketones, and carbon monoxide. The most abundant gas species, which take part in the deposition, are methyl radicals and acetylene molecules. The hydrogen gas is required to be sufficient in the reaction chamber and served as a reducing agent. Meanwhile, graphite and other non-diamond species are also deposited with diamond simultaneously. The substrates are commonly pre-treatment of adhering micrometre diameter diamond particles to enhance the nucleation or scratching on the surface. Different substrates and CVD diamond deposition are summarised in **Table 2.5**. Compared with the other types of diamond deposition methods, the MPECVD method has a little contamination with a lower temperature and pressure. Besides, the deposition area of MPECVD system is as high as 100 cm^2.

During the reaction process, the hydrogen serves the critical role in reducing the percentage content of carbon source gas. The hydrogen molecules have been detached by the environment, *e.g.* hot-filament, or microwave plasma, and then presented in the state of hydrogen radicals, which are highly reactive hydrogen atom.[20] The reaction can be expressed as

$$\boldsymbol{H_2 + e^- \xrightarrow{external\ energy} H^+ + H^+ + e^-} \qquad \textbf{Equation 2.22}$$

Under the circumstances of CVD synthesis, the carbon *sp*^{2} phase was deposited as the same time as the growth of diamond. However, the presence of hydrogen radicals can etch away the carbon *sp*^{2} species. At the same time, the hydrogen radical can terminate the surface dangling carbon bonds and prevent it from being substituted by a non-diamond element. A suitable condition for diamond growth has been proven to be between 700˚C and 1,200˚C.[3]

For polycrystalline diamond growth, the ‘nuclei’ or so-called ‘nucleation’ process is helpful for the initial deposition process. Before the diamond heteroepitaxial growth on another substrate, the nucleation seeding or scratching micrometre diamond particles on the substrate surface is always applied.

Table 2.5 Different types of CVD diamond deposition.[38]

2.4.2 Applications of Diamond Films

The properties and growth of diamond films have been reviewed in the previous sections. In this section, the applications of diamond films will be introduced.

- *Piezoresistive Devices*

The diamond films can be applied in both sensors and MEMS technology; it has the highest thermal conductivity, a low thermal expansion coefficient and high chemical inertness. The boron-doped diamond film has been proven to have semi-conductive properties, as described in Sec.2.2. Thus, it exhibits the potential ability for piezoresistive devices. For the piezoresistive materials, the resistance has a relationship with the loaded compressive stress.[41] The piezoresistivity is expressed by

$$\boldsymbol{K} = \frac{(\Delta \boldsymbol{R}/\boldsymbol{R})}{\boldsymbol{\varepsilon}} \qquad \textbf{Equation 2.23}$$

where K is the Gauge factor, and ε is the strain of diamond film. R and ΔR are the resistance without strain force and the resistance changed with loaded strain force. Adamschik, *et al*. investigated high oriented diamond (HOD) films deposited on a p-type silicon wafer.[42] The HOD film was deposited on a 3-inch silicon substrate on the (100) plane by using the bias-enhanced nucleation (BEN) method, as shown in **Figure 2.13**. The free-standing diamond cantilever was fabricated by boron-doped method to create piezoresistive at the end of the beam.

Aston University

Illustration removed for copyright restrictions

Figure 2.13 Diamond cantilever structure by dry etching on an HOD film.[41]

- *MEMS Acceleration Sensor*

The diamond based acceleration MEMS device was proposed by Kohn, *et al*. and shown on **Figure 2.14**.[43] The substrate was a HOD film and a silicon seismic mass was hold by four diamond piezoresistive beams. The seismic silicon was fabricated by the reactive ion etching (RIE) method. The Young’s modulus is 825 GPa and the fracture strength is 4.7 GPa, with the corresponding resonance frequency at 4.5 kHz. The ultimate measuring limit was ranging as high as 7,000 G and response time is around 10 ms. The diamond acceleration MEMS devices can survive up to 700˚C and maintain a consistent performance up to 500˚C.

Figure 2.14 Left: diamond-based MEMS acceleration sensor with Si seismic mass; Right: piezoresistive beam and attached the suspension element.[43]

- *Field Emission Devices*

For a single crystalline diamond film, it will exhibit a charge-up phenomenon during SEM observation. A reasonable explanation for this is the hydrogen termination on the surface, which can enhance the surface conductivity. In the previous chapters, the hydrogen terminated boron-doped diamond and its properties on negative electron affinity (NEA) have been introduced. It described how electrons were excited to the conduction band of H-terminated diamond; they would be spontaneously emitted to the vacuum band presumably across a small barrier on the C-H surface.[3] Based on this property, the field emission device was fabricated on a heteroepitaxial undoped (100) diamond film, which was deposited on Ir (100) substrate by Yamada, *et al*.[44] According to the *I-V* characteristics of the hydrogenated and oxidised diamond surface shown in **Figure 2.15**, and the emission was uniform in the 3 mm × 3 mm area. The threshold voltage was measured to be 40 V/μm and the corresponding current was 10^{-11} A. The emission barrier height coefficient (γ) can be calculated through Equation 2.24. Δo / ΔH expresses the slope of the F-N plot extracted from the hydrogenated and oxidised surface.

$$\boldsymbol{\gamma = (\frac{\Delta_o}{\Delta_H})^{\frac{3}{2}}} \qquad \textbf{Equation 2.24}$$

Figure 2.15 The I-V relationship between the oxidized and hydrogenated surface heteroepitaxial diamond film.[44]

- *HOD film pH Sensors*

Denisenko, *et al*. investigated a pH sensor based on a diamond substrate. The H-terminated thin layer occupies a 3-10 nm thick on boron doped diamond surface, which exhibit a *p*-type characteristic with a hole density of $10^{13}/cm^2$.[45] The principle was based on field effect transistor (FET). There is an open channel on the sensor, where the solution can be directly contacted with. The open channel protects the substrate from strong acid/alkali solution. With the different H^+/OH^- density in the solution, the corresponding electric field has an influence on the resistance between the source and drain. The forming channels were gradually depleted with the increasing OH^- ion radicals, while the surface C-H dipoles were also influenced. Because of the extreme wide bandgap of the diamond substrate, there was no charge transfer effects occurred between the diamond and two solution interface.

Figure 2.16 Left: image of pH sensor based on HOD diamond film and its structure; Right: the relationship between grain current and gate bias potential of diamond substrate pH sensor.[45]

- *Ultraviolet Sensor*

The single crystalline diamond has a wide bandgap of 5.47 eV, which corresponds to a light wavelength of λ =227 nm. While the absorption occurs on the diamond film, it will generate electron-hole pairs. Thus, the diamond material is photon-sensitive to the ultraviolet light (λ <227 nm). Hayashi, *et al*. developed a highly-oriented diamond UV detector on Si substrate with a Pt electrode, as shown on **Figure 2.17**.[46] The output voltage was measured between 20~80 V with an ArF laser source irradiation at λ =193 nm. The transient output signal pulse was between 1.1~3.8 ns. The results demonstrated that the UV sensor has a transient response to the ultraviolet laser pulse. The grain size of the crystal boundaries in HOD films is smaller than that of polycrystalline diamond films, and their crystal quality is much more superior.

Figure 2.17 Left: schematic diagram of the diamond UV sensor structure, and Right: the relationship of the output voltage and the bias voltage under the 193 nm laser irradiation.[46]

- *Biosensor*

Recently, diamond has been considered a promising candidate for bioelectronics applications for its electronic and chemical properties. Successful applications of impedance spectroscopy have been reported for immunosensors, enzyme sensors, and DNA sensors. In this section, the electrochemical equivalent circuit models and impedance spectroscopy experiments of different kinds of diamonds will be reviewed.[2]

DNA molecule detection is a basic application in molecular diagnostics. Faradic and non-Faradic impedance spectroscopy has been utilised to study the DNA hybridization by recording

---

[2] This section was partially included in the previous publication by the author.

the impedance modifications in DNA attached layers before and after hybridization. If a semiconductor is used as a signal sensor, its field effect can be induced by the binding of the negatively charged DNA, resulting in the interfacial impedance at the measuring frequencies. Takahashi *et al*. investigated a chlorination/-amination/-carboxylation process on H-terminated diamond for persevering and analysing DNA clips.[47] In 2002, Yang *et al*. modified the nanocrystalline diamond with alkenes and concluded that DNA bonding on diamond material would be much better than that on other substrates.[46] Then, several other methods including chemical reduction and direct amination on diamond with DNA, enzyme, and proteins were investigated by using cyclic voltammetry and other electrochemistry methods.[47] To study the electrical response and the hybridization-induced effects, the impedance data were analysed using equivalent circuit with constant phase elements (CPE). The electrochemical equivalent circuit of DNA-modified diamond film is shown in **Figure 2.18**.[48]

In the equivalent circuit, R_s represents the ohmic resistance of the electrolyte solution. The paralleled resistor R_1 and capacitor C_1 reflects the properties of the molecular layer and the double layer. R_2 and CPE $=(A^{-1}(j\omega)^{-\alpha})$, where A and α are non-integral, adjustable parameters, which describe the impedance of the space charge region of the BDD electrode.

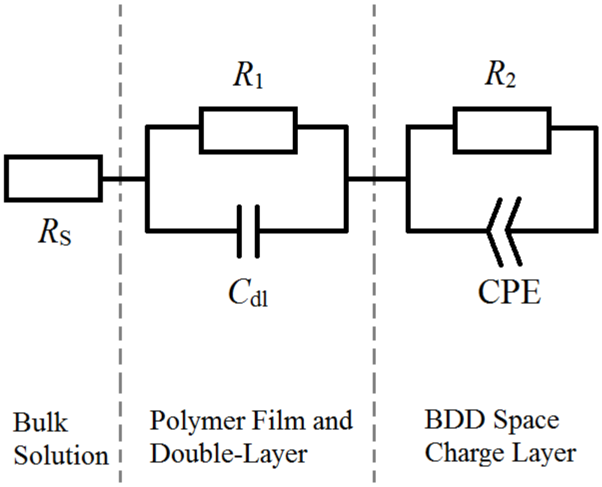

Figure 2.18 EIS equivalent circuit of DNA-modified diamond film.

Between 2006 and 2007, Nebel *et al*. applied the photochemistry technology to attach alkene modules on undoped diamond and electrochemical reduction of diazonium salts to attach nitrophenyl-linker molecules on boron-doped CVD diamond.[51] Thiolmodified single-stranded probe DNA (ss-DNA) was bonded to diamond by hetero-bifunctional cross-linker. Then, the substrate surfaces were exposed to fluorescence-labelled target ss-DNA to investigate hybridization on the DNA-FET structure. CVD diamond growth process and photochemistry methods were introduced and x-ray photoelectron spectroscopy, atomic force microscopy, and fluorescence microscopy were utilized to characterise the surface with DNA.

Figure 2.19 shows the EIS properties of DNA-modified nanodiamond films. The impedance was shown by Nyquist plot, which were detected from ss-DNA exposure to 4-base mismatched DNA and after exposure to complementary DNA in pH 7.4 phosphate buffer with 1 mM $Fe(CN_6)^{3-/4-}$. The Nyquist plot indicated discriminating hybridization of matched and mismatched DNA. The author gave interpretation of these results, which depends on several factors, including variations of ss-DNA and double-strand DNA layers, external electric fields, as well as the effect of redox molecules such as $Fe(CN_6)^{3-/4-}$ on the dielectric and conductivity properties of DNA films on diamond.[51]

Figure 2.19 Nyquist plot of nanodiamond film biosensor with 1mM $Fe(CN6)^{3-/4-}$ solution.[51]

Yang *et al*. in 2007 investigated the properties of the antibody–antigen–modified BDD surfaces.[52] The diamond samples were all *p*-type BDD (deposition concentration: 10^{18} cm^{-3}), on *p*-type Si (100) substrate using the MPECVD method. EIS experiments were performed using human immunoglobulin *G* (human IgG, Sigma I4506) and human immunoglobulin *M* (human IgM, Sigma I8260) linked to surfaces, whereas binding experiments were performed using the complementary antibodies antihuman IgG (Fc specific, Sigma F9512) and antihuman IgM (m-chain specific, Sigma F5384). **Figure 2.19** shows Nyquist plots of *Z*' and *Z*" from 100Hz to 1.1 MHz, with 10-mV root-mean-square (rms) modulation for different kinds of antibody-antigen-modified diamond surfaces. After anti-IgG and anti-IgM modified, the Cole-Cole plot had only slightly changed in real component response (*Z*' changes from 110 to 112 Ω at 200 kHz). Then the impedance *Z*' (before and after exposure to anti-IgG) increased from 110 to 190 Ω at 200 kHz. The author also gave the electrochemistry equivalent circuit, as shown in **Figure 2.20**.

Figure 2.20 Equivalent circuit model representation of the IgG-modified semiconductor interfaces and used to fit the data on *n*-type and *p*-type silicon.[53]

- *Diamond Electrochemical Electrode*

The BDD applications for surface electrochemistry pre-treatment are reported in this chapter. For the chemical stability and surface reproducibility, BDD is an excellent candidate for contaminated water treatment. Suffredini *et al*. utilised EIS measurement to illustrate differences after cathodic/anodic pre-treatment on the diamond films. A 0.06 cm × 1.0 cm BBD electrode that was deposited by HFCVD technique on a silicon wafer was used as a working electrode in EIS experiments. The gases in the vapour deposition process were methane, H_2 and trimethyl boron, and the boron content was 4500-5000 ppm. The EIS measurement was performed with 0.5 mol L^{-1} H_2SO_4 and 1×10^{-3} mol L^{-1} $K_4Fe(CN)_6$ or 0.5×10^{-3} mol L^{-1} ferrocene. **Figure 2.21** shows the Nyquist plot obtained at 0.06 V after anodic and cathodic pre-treatments. The resistance calculated from the Nyquist plot at high-frequency range for the anodically treated BDD is similar to the previous reports for the same solution at an oxidised BDD. When the BDD surface was performed cathodic treatment, the resistance reduced as shown in **Figure 2.21**. However, the factor was relative smaller than the previous reports. The author explained that the inner or the surface structure of the BDD material could be modified by this treatment and lead to fast electron transfers consequence. **Figure 2.21** presents Nyquist plots obtained at 0.37 V in a 0.5×10^{-3} mol L^{-1} ferrocene + 0.5 mol L^{-1} H_2SO_4 solution for the BDD electrode after anodic and cathodic pre-treatment. The value of the high-frequency resistance element after the cathodic surface pre-treatment is also obvious as in $Fe(CN)_6^{4-/3-}$

couple. The EIS experiments demonstrated that a discontinuous passive layer or an internal carriers transportation of the BDD would decrease the surface blocking, which is caused by the cathodic pre-treatment.[53]

Figure 2.21 The Nyquist plots for the boron-doped diamond electrode in $K_4Fe(CN)_6$ + H_2SO_4 after (a) anodic pre-treatment at 3.0V or (b) cathodic pre-treatment at -3.0 V.[54]

2.5 Nanodiamond

2.5.1 Synthesis, Characterisation, and Properties of Nanodiamond

- *Introduction*

The first nanoscale diamond particles were developed by the USSR during the 1960s' by the detonation method.[54] At the beginning of 1990s, nanodiamond particles with a diameter ranging of 4~5 nm were investigated. It was widely known that the carbon *sp*^{3} clusters should be either stabilized with terminal functional groups or linked with *sp*^{2} carbon structures. The non-functionalised nanodiamond exhibits similar properties as the bulk films. The surface of nanodiamond has a transformation from *sp*^{3} carbon to *sp*^{2} clusters with octahedral, cuboctahedral and spherical structures. The surface of nanodiamond can be composed by 76% graphitization shell, including onion-like, small/large carbon clusters.[55] The characteristics and applications of nanodiamond has been summarised and listed on.[56]

- *Synthesis*

Nanodiamond can be synthesized by different methods, *e.g.* detonation, laser ablation, HPHT milling, autoclave synthesis, ion irradiation on graphite, electron irradiation on carbon onions, ultrasonic cavitation and PECVD. The detonation method is one of the most common commercial methods of nanodiamond production.[55],[56]

Figure 2.22 (a) detonation species and common diameter of nanodiamond; (b) phase diagram of nanodiamond synthesis condition, including pressure and temperature; (c) the schematic of detonation process and products.[55]

Figure 2.22 (a) shows the raw materials of detonation nanodiamond. The raw materials contains a negative oxygen balance, which is composed by a mix of 60 wt.% TNT $(C_6H_2(NO_2)_3)CH_3$ and 40 wt% hexogen $(C_3H_6N_6O_6)$. Then, they were detonated in a huge, closed and heavy metallic chamber within an atmosphere of N_2, CO_2 and H_2O. After the detonation process, the residues will be collected and transferred to purification process.

Table 2.6 Characteristics and applications of nanodiamond materials.[56]

In **Fig.2.24 (b)**, the phase diagram demonstrates that the appropriate temperature and pressure for nanodiamond (point A, named as Jouguet point). As the pressure and temperature deviates from the diamond-graphite equilibrium line, the explosive residues will be replaced by graphite products.[57] **Figure 2.22 (c)** explains the different zones in the detonation chamber by temperature gradient distribution. In zone (I), the detonation was caused by the first detonation shock wave and chemical reactions decomposed the explosive molecules. Zone (III) indicates the Chapman-Jouguet plane (red line in **Figure 2.22 (b)**), which is the equilibrium condition for nanodiamond production. The zone IV~VII represents the expanding detonation products, carbon nanoclusters, coagulation of liquid nanodroplet, and crystallization/agglomeration of nanodiamond, respectively. The nanodiamond synthesised by this method was named as detonation nanodiamond (DND).

- *Post-synthesis processing*

The biological applications of nanodiamond required extremely high purity of diamond phase in DND. However, the detonation residues contain both the graphite-like materials (25-45 wt.%) and incombustible impurities, *e.g.* metal and metal oxidize (1-8 wt.%).[58] The impurities of DND are much higher than the HTHP diamond films. After the post-synthesis process of DND, the composition of DND can be including carbon (~80-89 wt.%), nitrogen (~2-3 wt.%), hydrogen (~0.5 wt.%), oxygen (~5-10 wt.%) and incombustible residues (~0.5-8 wt.%).[59]

The tentative structure scheme of DND particles is shown on **Figure 2.23**. The non-diamond carbon includes graphite nanocrystals, graphite ribbons, carbon onions, and other amorphous carbon.[56] Most of them are located tightly outside the DND particles.[60] In order to remove the internal impurities, the tight DND agglomerates should be isolated. It is relatively easier to remove the metal from the DND complex surface by using liquid oxidization, *e.g.* H_2SO_4/CrO_3, H_2SO_4/HNO_3, HCl, $KClO_3/H_2SO_4$.[61] Other purification scheme includes KOH/KNO_3, Na_2O_2, HNO_3/H_2O_2, within a certain atmosphere of pressure and sulphuric or perchloric acids. [56]

Figure 2.23 Tentative scheme of DND particles and their soot-like structure outside the cores (Left) and commercial DND particles after post-synthesis process (Right).[59]

There is alternative method for DND by treating DND in an environment with elevated temperature, which can reduce the requirement of oxidization chemicals. This method was named as ozone method and it is more efficient for carbon *sp*^{2} removal in industrial scale. An optimisation temperature for DND heat treatment was verified at 400~430°C.[62] The surface hydrogen atmosphere method is a novel approach for DND purification, but the carbon *sp*^{2} could not be effectively removed from the nanodiamond core.

- *Characterisation*

After the well-purification process, the nanodiamond particles contain relatively negligible non-diamond phases. **Figure 2.24** demonstrated the DND particles through transmission electron microscopy (TEM). The TEM image illustrated that the nanodiamond particle was built up by *sp*^{3} carbon phase, with an outer graphitic shell, or amorphous carbon structures. The outside dangling bonds can be terminated with C-H bonds or other functional groups.

Figure 2.24 An individual nanodiamond particle, which is constituted by a high oriented diamond core, has a clean facet shape around the inner carbon *sp*^{3} core.[59]

Figure 2.25 shows the Raman spectroscopy (325 nm ultraviolet laser excitation) of different types of nanodiamonds. The diamond characteristic peak is shown in inset ***a***, while the combination of peaks can be deconvoluted into (I): larger scattering domain, and (II) smaller scattering domain, respectively. The broad shoulder at 1500-1800 cm^{-1} in the fitting spectrum (inset ***b***) was derived from the oxidized nanodiamond surface and carbon *sp*^{2} atoms, as well as the absorbed molecules. The nanodiamond core was surrounded by a graphitic layer, which could be proven by the Raman analysis. The *G*-band of graphitic layer can be observed at 1590 cm^{-1} and diamond peak was not significant. After the purification process, the diamond peak at

1328 cm^{-1} is clearly observed on the Raman spectra as well as the oxidized sample. It could be concluded that the outer thin layer was removed from the inner core by the oxidization air.

Fourier transform infrared (FTIR) can also provide an effective insight on the nanodiamond surface functional groups.[63] The characteristic peaks for nanodiamond after post-synthesis process can be O-H stretch (3200-3600 cm^{-1}) and bend (~1635 cm^{-1}), C=O stretch (1700-1800 cm^{-1}), and C-H stretch (2850-3000 cm^{-1}). The O-H groups are derived from the surface absorbed water and C=O bonds can be derived from ketone, aldehyde, carboxylic acid, ester, anhydride, cyclic ketone, lactone, and lactam, *etc.*[64] A detailed discussion on Raman and FTIR applications on characterisation will be introduced in Chap. 3.

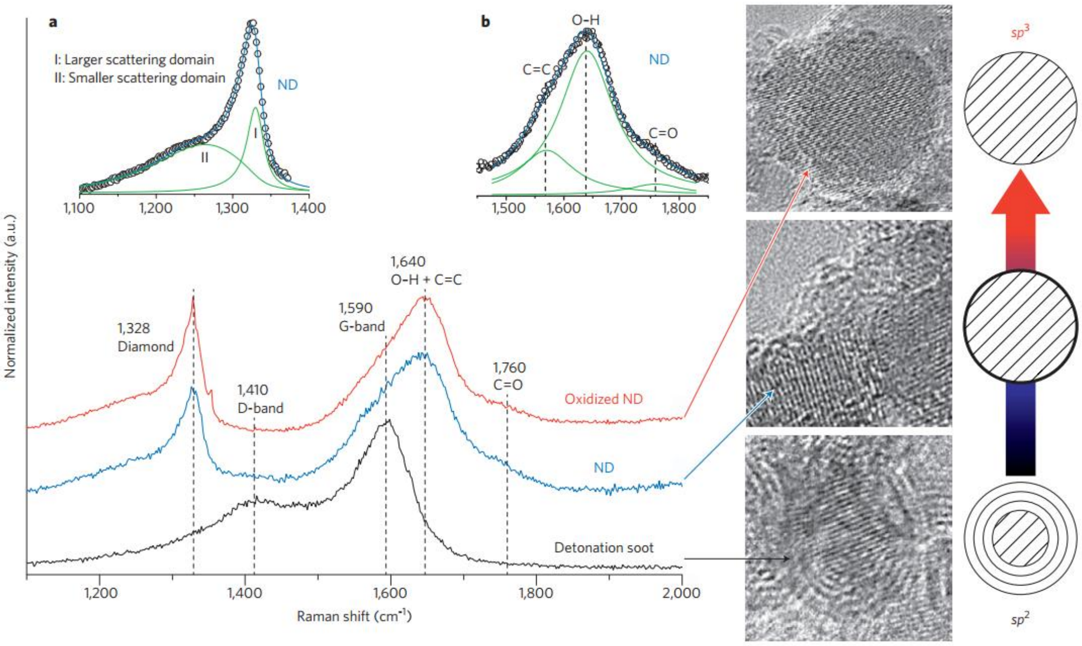

Figure 2.25 Left: Raman spectroscopy and deconvolution of different types of nanodiamond (oxidized, purified and detonation soot). Right: TEM images of these three types of nanodiamonds.

- *Modification*

Different types of functional groups can be found on the DND surface and also can be applied to covalent functionalization. It is more likely to perform surface modification with nanodiamond after deep purification and ozone oxidization, for the rich –COOH groups on its top. The MPECVD method with a H_2 atmosphere at 700˚C can effectively reduce the surface –COOH groups as well as the other oxygen species.[65] The surface modification diagram is shown on **Figure 2.26**. The precise control on the diamond surface required simple and unitary surface termination. Nanodiamond particles with carboxylic groups (-COOH, shown on **Figure 2.26** green area) were utilised as the preliminary raw materials. The surface can be functionalised by high temperature treatment (red zone), or wet chemical method (blue zone). Heating DND powder in NH_3, Cl_2, and F_2 can form stable C=N, acylchlorides, and C-F group, respectively.[66],[67] Annealing DND in a H_2 rich atmosphere can reduce the C=O or C-O-H bonds and transform them to C-H. Other biofunctional groups, including hydrophilic and hydrophobic polymer brush, have been synthesised as well.[68] A hydroxylated DND with alkyl chains with carboxylic acid chlorides on surface hydroxyl groups had been synthesised by Krueger, *et al.*[69]

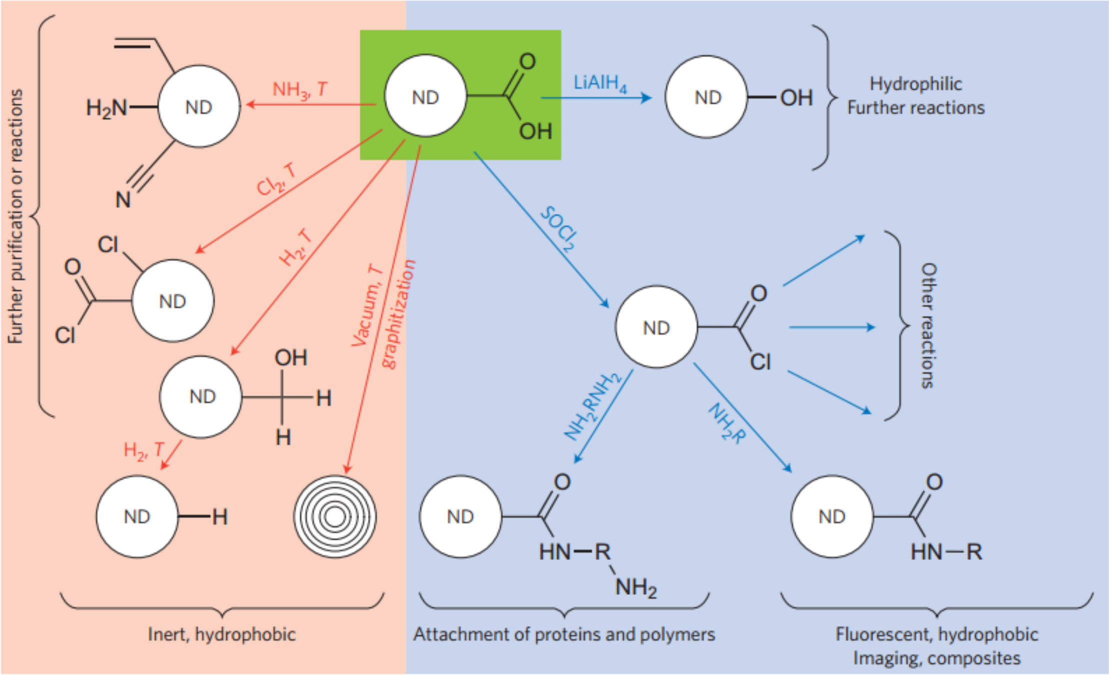

Figure 2.26 The surface modification process of nanodiamond.

2.5.2 Nanodiamond Applications

As the techniques to fabricate nanodiamond where developed, the applications of nanodiamond were also widely explored. The nanodiamond inherits t most of the diamond film properties, *e.g.* extreme hardness and Young’s modulus, biocompatibility, fluorescence, as well as chemical stability. In this section, the applications utilised these properties of nanodiamond will be introduced.

- *Fluorescence and biological fluorescent label*

In nanodiamond, the nitrogen-vacancy (NV) centre can generate a photoluminescent (PL) property. The NV centre can be fabricated in a nanodiamond core with high energy irradiation after annealing in vacuum atmosphere at 600-800°C.[70] PL nanodiamond can also be produced by chemical linking or absorption.[71],[72] The synthesised PL nanodiamond has the advantage of biocompatibility, non-toxic, which is suitable for future potential *in-vivo* biological image application.

The nanodiamond has an intrinsic absorption wavelength of 236.4 nm, which is quite closed to that of natural diamond films.[56] The NV defect-related has an absorption wavelength at 576 and 638 nm, corresponding to the NV^0 and NV^- centres, respectively. Both HPHT nanodiamond and DND can generate an intrinsic PL without high energy treatment, which can be detected by microscopy or flow cytometer conveniently.[73] **Figure 2.27** shows the DND powder with different surface modification, *e.g.* –NH2, fluorescein isothiocyanate (FTIC), as well as dye tetramethylrhodamine (TAMRA). The TAMRA-DND can be applied in tracing in cytotoxicity environment.[74]

Figure 2.27 Images of DND powder modified with NH_2, FITC and TAMRA on the surface of the particles.[56]

- *Non-insoluble medicine drug delivery*

The DND powder is insoluble in water, which can inhibit the mutation of cells and reduce the chances of a secondary tumour.[75] The preliminary experiments suggested that nanodiamond, *e.g.*, detonation, HPHT, and natural, can be selected as the drug delivery carriers. The most important factors to drug delivery nanodiamonds are their surface functionalization, the drug release-duration and shielding capability.[76]

M. Chen, *et al*. reported a 4-6 nm nanodiamond powder for water-insoluble drug delivery.[77] The TEM images are shown in **Figure 2.28**. After an ultrasonic bath, centrifugation and milling treatment, the nanodiamond was surface modified with strong acid to form carboxyl groups. The surface carboxylic groups can promote nanodiamond to be a stable suspension in water.

Then, 4-Hydroxytamoxifen (4-OHT) was selected as a water-insoluble cancer therapeutic for this delivery system. The results proven that the nanodiamond served as a biocompatible platform for enhanced water dispersion of this drug. K. Liu, *et al*. investigated nanodiamond-conjugated paclitaxel with covalent bonds, which could be applied in lung carcinoma cell delivery.[78] Other applications have been summarised and reviewed by E. Osawa, *et al*.[79]

Aston University

Illustration removed for copyright restrictions

Figure 2.28 Left: TEM image of pristine nanodiamond; Right: 4-OHT residue on the nanodiamond surface to drug interface.[79]

- *Lubrication for Engines*

DND powder can be an addictive in lubrication and decrease ~5% of fuel consumption and enhance engine lifetime.[58] The lubrication mechanism can be derived from the nanodiamond reduced friction by polishing sliding surfaces and provided tribology performance when dispersed in fuel. Preliminary study revealed that nanodiamond for lubrication might be embedded into carbon steel surface, which will reduce friction and enhance wear resistance. It is reasonable to predict that nanodiamond in the metal surface can separate the sliding surface and protect the metal-to-metal adhesion interface.

- *Biomarkers*

C. Fu, *et al*. had developed surface modified nanodiamond as cellular biomarker applications.[80] A 100nm DND was surface modified with carboxyl groups by H_2SO_4:HNO_3 (9:1 in volume) bath at 75˚C for 3 days, and following then by 0.1 M NaOH solution at 90˚C for 2 hours, and finally by 0.1 M HCl at 90˚C for 2 hours. The oxidized DND was then linked with amino groups with *N*-(3-dimethylaminopropyl)-*N*'-ethyl-carbodiimide hydrochloride. The observation of single digit DND using functionalized DND for live Hela cell is shown on **Figure 2.29**. It is obvious to find out that most of the loaded DND particles are located along the cytoplasm. The separation between two particles is approximate 1 μm. The DND and fluorescence labelled DNA molecule was excited by 514 nm Ar-ion laser. The biomarkers photophysical properties did not deteriorate after surface functionalization and interact with DNA molecules by forming covalent bonding.

Figure 2.29 (a) bright-field and epifluorescence images of HeLa cell after loaded DND biomarkers. (b) single epifluorescence image of a single HeLa cell with enlarged zoom.[80]

- *Cold Water Cleaning*

In 2012, X. Cui and H. Ye, *et al*. developed surfactant-mediated nanodiamond to remove triglyceride away from hydrophobic surface in cold water.[81] The nanodiamond was prepared with oxidized, reduced, ω-alkylcarboxylic acid and ω-alkylamidoamine modification.

Figure 2.30 The principles of nanodiamond lipid removal. (a) nanodiamond absorption can promote insertion of surfactant in lipid layer, as well as tristearin lift-off. (b) surfactant lipid budding process. (c) and (d) solubilisation process with/without nanodiamond.[81]

The results proven that the nanodiamond could improve the lipid removal and roughen the surface in order to enhance surfactant absorption by providing negative curvature on the surface sites. On the other hand, the strong electrostatic interaction existing between the nanodiamond and surfactant improves the absorption ability. The principle of nanodiamond lipid removal was shown as **Figure 2.30** and it provided a novel tool for cold-water cleaning.

2.6 Summary

In this chapter, the fundamental properties of diamond materials, including single/poly-crystalline diamond films and nanodiamond, were introduced. Diamond can be considered as a superior material to alternatives with extraordinary properties, such as extreme mechanical hardness, high electronic saturation velocity and carrier mobility, the best thermal conductivity, very high optical refractive index and biocompatibility. Besides, the synthesis methods and applications of diamond-related materials have been reviewed as well. In the next chapter, the different characterisation methods on diamond materials will be introduced.

Chapter 3: Growth and Characterisation of Diamond Materials

Growth and Characterisation of Diamond Materials

3.1 Introduction

The previous chapter focuses on the literature review on diamond properties and the principles of chemical vapour deposition. This chapter will discuss the various techniques used to growth and characterise diamond materials. The chemical vapour deposition (CVD) reactors are mostly utilised to deposit the diamond films and other microscopy or spectroscopy equipment are used to characterise the specific properties of the materials. There are different types of CVD reactors for diamond film synthesis. More specifically, microwave plasma enhanced chemical vapour deposition system (MPECVD), and hot-filament chemical vapour deposition system (HFCVD) will be built up and discussed in details. Then, the different techniques usually used to characterise the diamond materials, are introduced in this chapters.

3.2 Chemical Vapour Deposition Reactor for Diamond Growth

In the past, the deposition of diamond depended on the high-temperature high-pressure technique (HTHP), which was limited because of its extreme growth condition (>2,000˚C, >10 GPa). Thus, it cannot be used to deposit large-area or large-scale growth of diamond films. Today, we have a wide range of chemical vapour deposition (CVD) techniques which are used for the fabrication of diamonds. Chemical vapour deposition is defined as a group of process which involves deposition a solid material based on a gaseous phase environment. It is one of the most common processes to produce high-purity thin films. The CVD process has the advanced characteristics, such as fine crystalline grains, high-purity, *etc*. The CVD systems are classified by the different energy sources used to promote the reaction, *e.g.* microwave plasma assisted (MPECVD), hot filament (HFCVD) and arc discharge CVD (DC Arc-jet CVD), *etc*. In this section, the MPECVD and HFCVD deposition systems hosted in Aston University will be introduced.

3.2.1 Microwave Plasma Enhanced Chemical Vapour Deposition System

Microwave plasma enhanced CVD allows the synthesis of diamond films on substrates at a low temperature and pressure, which is generally more suited for commercial manufacturing requirements. The traditional HPHT method to deposit the diamond films has been proven as too difficult to be economical for commercial purposes. In the MPECVD method, the glow-discharge (non-isothermal) plasma is generated by a microwave generator in a chamber, which is filled with deposition gas in a high-frequency electric field at a relative low pressure. The electrons are quickly accelerated to high energy levels above ~5,000˚C, whilst the heavier ions remain very low temperature. Under the assistance of the high-frequency electric field, the precursor gas molecules, *e.g.* CH_4, C_2H_2, are ionised by the electric field and become ions and electrons.[84] Typical CVD diamond growth required optimised conditions, such as low pressure (about 1-25 kPa) and various kinds of source gases in the reaction chamber. The source gas always includes the carbon sources gas (*e.g.* CH_4, C_2H_2) and the hydrogen gas, which plays a critical role during the deposition process. The phase diagram of carbon is shown on **Figure 3.1**.[83] The formation of diamond *sp*^{3} is determined by the thermodynamic condition inside the reaction chamber.

Figure 3.1 Carbon phase diagram.[83]

The MPECVD technique enables the deposition of diamond on a wafer larger than 15 cm (6 inch) with relatively lower pressure and lower temperature, which can be applied in the future microelectronics devices. Another important attribute of the MPECVD technique is the ability to control the properties of the diamond films by regulating the gas flow rate and the concentration of the carbon-sources gases (C_xH_y) and the hydrogen. The possible deposition types include the single crystalline diamond with and/without various dopants (*e.g.* phosphorous, nitrogen, or boron) and polycrystalline diamond film with grain size from several nanometres to micrometres. The basic reaction in general CVD systems involves the decomposition of hydrocarbons which can be expressed as:

$$C_xH_{2y}(g) \rightarrow xC(sp^3) + yH_2(g) \qquad \textbf{Equation 3.1}$$

The hydrogen ions selectively etch non-diamond species during the diamond deposition process with a common microwave power at a frequency of 2.45 GHz. The MPECVD film deposition system has three unique properties: firstly a relatively high substrate temperature which is typically around 700~1,200˚C; secondly a gas pressure of around 20~150 Torr (1 Torr =133.3 Pa); and thirdly a low methane concentration of 1~5% with diluted hydrogen gas.[85] The typical structure of ASTeX^{TM}-type MPECVD is shown in **Figure 3.2**.[86]

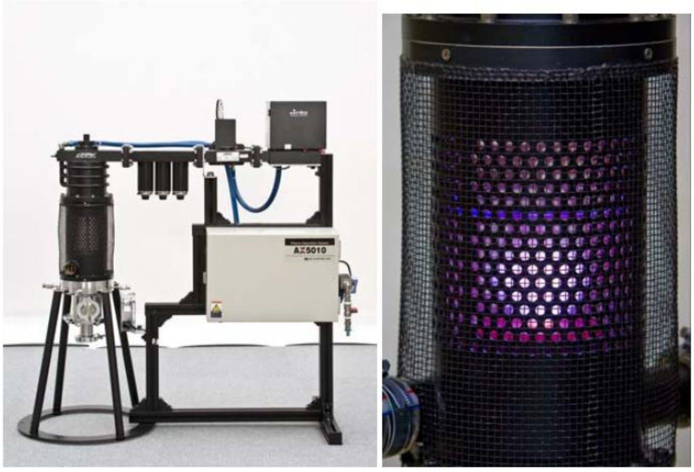

AX5010 Reactor Kit

Reactor Chamber

Figure 3.2 Left: 1.5 kW ASTeX^{TM} MPECVD system in Aston University (Seki Technotron Corp.); Right: the reactor chamber with plasma inside.

The schematic drawing of the ASTeX^{TM} MPECVD system in Aston University and each component is illustrated by **Figure 3.3**. The standard configuration and parameters are shown as below.

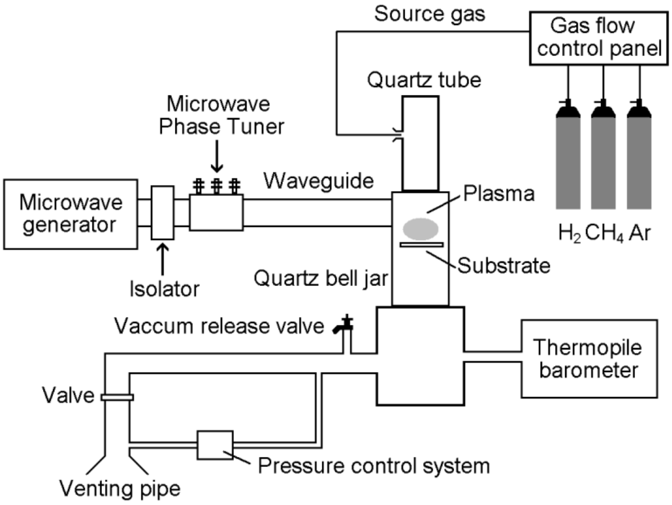

Figure 3.3 Schematic drawing of ASTeX^{TM} 5010 MPECVD and its accessories.

The input gas source includes: 0~1,000 sccm (standard cubic centimetre) hydrogen, 0~10 sccm methane, and 0~100 sccm Argon gas (or Helium). In the reactor chamber, the CH_4 and H_2 molecules were dissociated thermally by the plasma and then fragmented into hydrocarbons as well as atomic hydrogen. **Figure 3.4** shows the structure of the MPECVD system in Nanoscience Group of Aston University. The operation procedure will be attached in Appendix 1 and the diamond films deposited on silicon wafer will be discussed in Chap.4.

- Operation pressure: 1.3~6.7 kPa (approx. 10-50 Torr).
- Pumping speed: 5.6×10^{-3} m^3/sec (20 m^3/hr).
- Leak threshold: < 8.0×10^{-8} Pa.m^3/sec (6.0×10^{-7} Torr/sec).
- Incident Power: 600 W.
- Substrate Temperature: 800-1,000˚C
- Carbon content: C:H ratio: 1:99.
- Gas flow rate: 20~200 sccm.
- Vacuum pump type: oil rotary pump.
- Vacuum seal: Elastomer O-rings.
- Reactor chamber: Quartz bell jar.
- Cooling system: Force air blower.

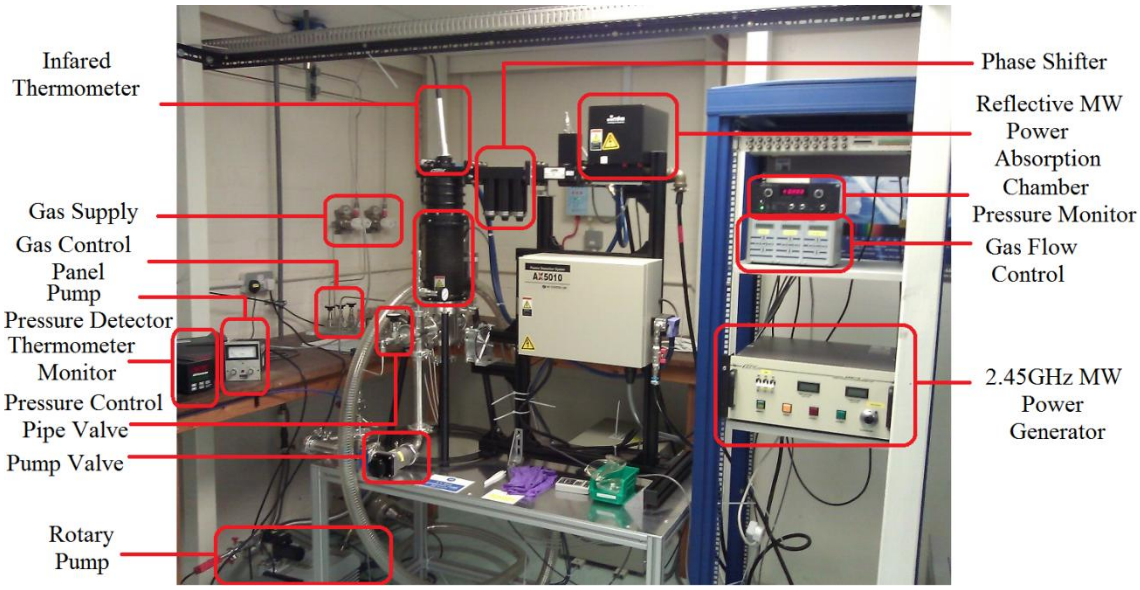

Figure 3.4 Structure of MPECVD system in Nanoscience group of Aston University.

3.2.2 Hot-Filament Chemical Vapour Deposition Reactors

Other types of reactors are also used for diamond deposition, *e.g*. hot-filament (HF) CVD, DC-plasma CVD, thermal RF plasma CVD, plasma jet, and combustion CVD, *etc*. In this section, the HFCVD built in Aston University will be introduced. The condition for HFCVD is different with the MPECVD, because the mechanism of carbon *sp*^{3} formation. The MPECVD utilises the microwave to ignite plasma and breaks the C-H in methane, while the HFCVD uses the thermal dynamic method.

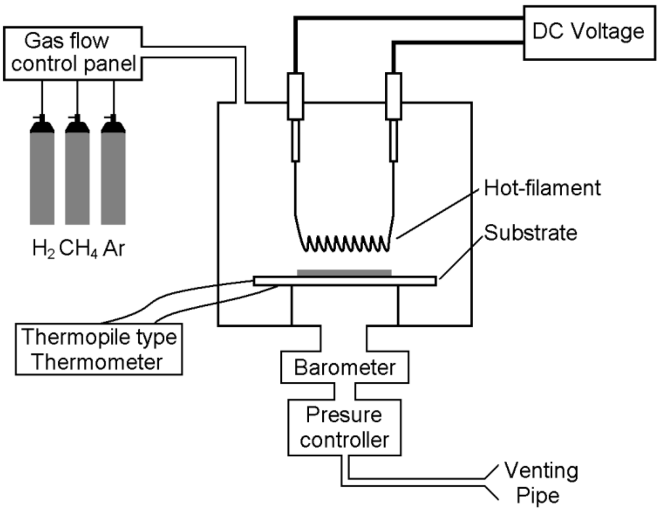

Figure 3.5 Schematic diagram of HFCVD in Aston University.

In the HFCVD reactor structure, the hot-filament can be made of tungsten (melting point 3,422˚C) or tantalum (melting point 2,996˚C). The hot-filament will be heated up to 2,000~2,200˚C and placed 5~10 mm above the substrate (as seen on **Figure 3.5**). A thermocouple was embedded in the substrate and the thermocouple measured the real-time temperature on the stage.

The home-built HFCVD system in the Aston Nanoscience group is shown in **Figure 3.6**.

The typical parameters of HFCVD system are listed as follow.[87] The condition can be further optimised in the future work.

- Filament temperature: 2,200˚C ~2,300˚C
- Substrate temperature: 800˚C~850˚C
- Gas flow rate: CH_4 : H_2 =1~2%, 100~200 sccm
- Carbon content: 0.5%~2%
- Chamber pressure: 20~100 Torr (26.6~133.322 mbar)

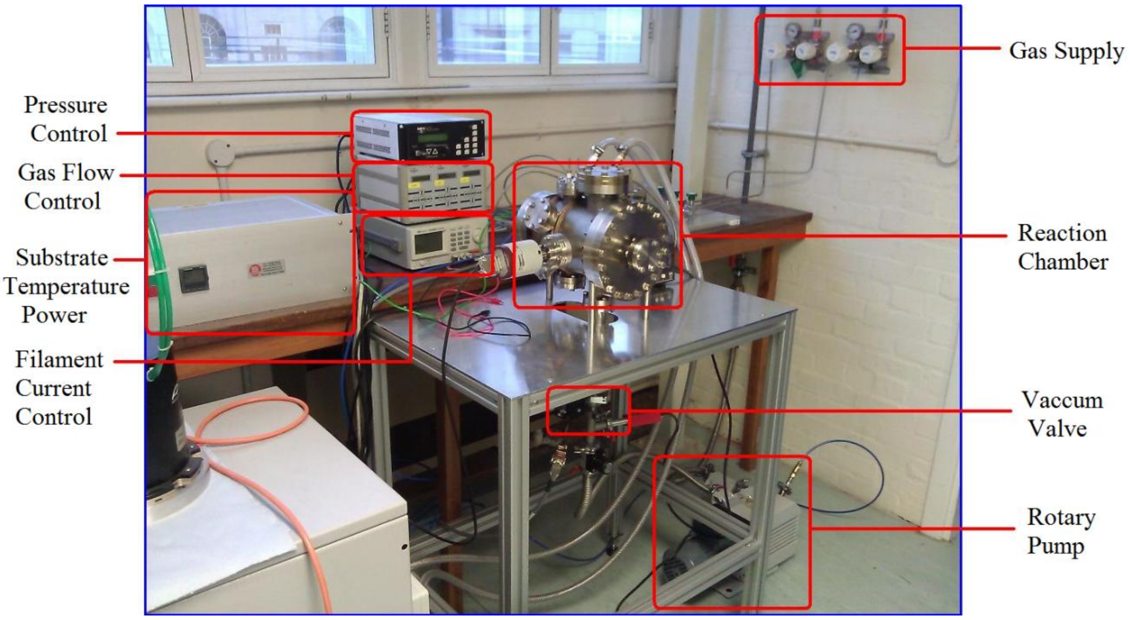

Figure 3.6 Home-built HFCVD system in Aston University.

3.3 Diamond Characterisation

In this section, the equipment and techniques used to characterise the diamond materials will be discussed.

3.3.1 Scanning Electron Microscopy

The scanning electron microscope (SEM) technology was first developed in the 1930's and the first commercial application was in 1965. The SEM utilises a beam of high-energy electrons to characterise a sample by scanning its surface topological structures from where the signal reflected from the sample contains the information of material texture, external morphology and orientation of crystals. The magnification range varies from 20X to 30,000X or even higher, corresponding to a minimum spatial resolution of 50 to 100 nm.[88] The sample under measurement should be solid-state and the vacuum level should be stable between 10^{-5}~10^{-6} mbar. Chemical elements below atom number 11 cannot be detected due to their minimum size. If it is an insulated sample should be coated by conductive metal layer.

For the signal generated from the electron beam, the primary electrons (PE), including secondary electrons (SE) and backscattered electrons (BSE), can be detected by the device. The others products include the Auger electrons, cathodoluminescence (*e.g.* photon UV, IR, vis).[89] As the energy exchange process occurs at the surface of the sample, the PE will be generated by both elastic and inelastic scattering. The specimen will be collected by a specialised detector and utilised to create 2-D images.

The SEM techniques can be used to characterise the diamond growth morphology, crystal orientation, coverage, and other properties. **Figure 3.7** shows the SEM images of cubo-octahedral diamond nuclei grown on (100) silicon.[90]

Figure 3.7 SEM images of cubo-octahedral diamond nuclei growing on (100) Si wafer. Left: top-view, Right: side-view.[90]

To characterise the diamond crystal growth morphology, the parameter α has been defined as a growth parameter by:

$$\boldsymbol{\alpha = \sqrt{3}\,\frac{v_{100}}{v_{111}}} \qquad \textbf{Equation 3.2}$$

where v_{100} and v_{111} are the diamond growth rate of (100) and (111), respectively.[91] The different parameters α and corresponding growth morphology are shown on **Figure 3.8**.

Figure 3.8 Growth rate parameter and corresponding morphology in SEM, Left: α=3; Middle: 1.5<α<2; Right: 2<α<2.5.[92]

The diamond films grown <100> silicon substrate by ASTeX^{TM} MPECVD are shown in Figure 3.8.[93] The bias nucleation was applied with bias voltage of 170-200 V and current of 300-400 mA. The microwave power for nucleation was set to 1,000W with a pressure of 20 Torr. The total gas flow was set to 306 sccm (H_2:CH_4=300:6). The duration for nucleation was 15 mins and temperature was measured at ~800˚C. Then, the parameters were modified for subsequent produce growth. The microwave power was set to 1,300W and pressure was fixed at 35 Torr. The carbon gas source and hydrogen ratio was changed to 15: 180 with additional CO gas of 5 sccm. The whole deposition duration took 40 hours with a substrate temperature of 650˚C. It was shown that most of the diamond nuclei were aligned with the (100) faces parallel to the substrate whilst the <110> plane direction parallel to each other.

Figure 3.9 Diamond crystals growth aligned with the orientation <100>.[93]

The SEM images of diamond film grown on Si (111) wafer are presented in **Figure 3.10**.[94] The deposition system was 5 kW at 2.45 GHz using a CH_4-H_2-O_2 gas mixture. The chamber pressure was maintained at 100-120 Torr with a total gas flow of 400 sccm (CH_4: 0.25~8.0%, O_2: 0.0~3.0%). The microwave power was set at 4 kW during the whole process. In **Figure 3.10**, various samples are shown with different levels of oxygen. It is obvious from **Figure 3.10** that the oxygen gas flow has a significant influence on the final diamond grain size after deposition.

Figure 3.10 SEM micrograph of diamond films deposited by MPECVD, with oxygen concentration varies from 0%~3.0%, with a power of 4 kW and 100 Torr, respectively.[94]

The SEM can also be used to characterise the nanodiamond powder, as shown in **Figure 3.11**. Due to the extremely high surface energy, the ultradispersed nanodiamond is made up of the conglomerates in the order of one micron in size, rather than the isolated particles with characteristic diameters. The dried powder tended to form particles with a few hundred nanometres to several microns.[95] It was found difficult to break the aggregates into several nanometres independent nanoparticles by ultrasonic bath.

Figure 3.11 SEM images of nanodiamond powder with heat treatment in hydrogen atmosphere (500˚C for 3 hours).[95]

3.3.2 X-ray Photoelectron Spectroscopy

X-ray Photoelectron Spectroscopy (XPS) can be used to analyse the composition and chemical state as well as the bonding state in a quantitative method. In XPS, photoelectrons are ejected from core atomic levels due to transfer on energy from an incident X-ray photon. After the photoelectrons are emitted, the kinetic energy (E_k) of the electron is quantitatively analysed by the spectrometer. The binding energy of the electrons (E_B) is the parameter that varies with different elements. The relationship between the parameters can be expressed as:

$$\boldsymbol{E_B = h\nu - E_K - W} \qquad \textbf{Equation 3.3}$$

where $h\nu$ is the photon energy, E_K is the kinetic energy of the energy collected by the photoelectron spectrometer and W is the work function.[96] The principle and process of photoemission shown in **Figure 3.12**. An electron from the K shell is ejected because of the incident X-ray. After a photoelectron is emitted, the corresponding ionized atom will relax, leading to X-ray fluorescence emitted electrons. Then energy will be analysed and hence a spectrum of electron intensity versus energy is generated and displayed. The XPS spectra can be quantitatively analysed with each corresponding orbitals. The energy resolution ΔE is defined by the peak width, which is often measured by full width at half maximum (FWHM). The XPS testing should be taken under an ultra-high vacuum environment, with an atmosphere of 10^{-8} to 10^{-10} mbar.[97]

Figure 3.12 Schematic diagram of the photoionization principle of XPS, a 1*s* electron ejection from an atom.[96]

When a pure element has a change in its chemical bonding, there will be also a change in binding energy of a core electron, which is named as ‘chemical shift’. The core binding energies changed by electrostatic interaction between electrons and nucleus. The electrostatic shielding will be influenced by nuclear charges from other electrons in the atom, or removal/addition of electronic charge in bonding.[98]

A typical XPS analysis of a diamond film has been plotted on **Figure 3.13**.[99] The diamond sample has been loaded in an ultra-high vacuum (UHV) chamber equipped with an X-ray photoelectron spectrometer. The C1*s* spectra were recorded with a pass energy of 10 eV by using mono-chromatized Al Kα X-ray (1486.6 eV). The carbon sp^2, sp^3, C-O, and C=O were located at 284.6 eV, 285.3~285.5 eV (+ 0.7~0.9 eV), 286.1~286.4 eV (+1.5~1.8 eV) and 287.6 eV (+3.0 eV), respectively.[97]

Figure 3.13 C1s XPS spectra of a diamond sample.[99]

In **Figure 3.13**, the narrow view of peak C1*s* has been synthesized into three peaks, named as peak A, B, C. respectively. The binding energy has a shift of 0.3 eV for this sample because of the surface dielectric properties. The scale of binding energy was calibrated with Ag $3d_{5/2}$ core level. The peak A (sp^2), B(sp^3) and C(C-O) were found located at 284.5 eV, 285.7 eV and 287.0 eV, respectively. The FWHMs of peak A, B, and C were 1.00 eV, 1.37 eV, and 1.70 eV, respectively.

3.3.3 Atomic Force Microscopy

Atomic Force Microscopy (AFM) was developed in the early 1980s and commercially applied in the 1990s. AFM technology is based on the scanning probe method and the minimum resolution can be as small as nanometre-level. It consists of a piezoelectric cantilever beam, which works as a precious scanning probe. A focused laser beam was utilised to measure the movement on the vertical direction. While the beam scans the sample surface, the laser spot intensity will be different and the photodiode sensor will generate various corresponding current. The change in current is detected and analysed by the computer. **Figure 3.14** shows an AFM image of a DNA-functionalised and hybridised surface of single-crystalline diamond film.[100] The AFM (Molecular Imaging Pico Plus) cantilevers were used in oscillating-mode with a spring constant of 3.5 N/m. The RMS (root mean square) roughness overs this large area detected by AFM was less than 1Å, which indicated a relatively smooth surface.

Figure 3.14 AFM image of surface morphology of highly boron-doped single crystalline diamond film.[100]

The AFM profile after being DNA-functionalised and hybridised is shown in **Figure 3.15**. The thickness of the DNA layer can be calculated by measuring the scratch area with AFM (**Figure 3.15 a**). The height between the tilted arrangement and the diamond substrate was 90Å. The topographic surface image (**Figure 3.15 b**) revealed that the collective DNA oligomers had a periodicity of ~30-50 nm with an amplitude current of ±5Å.

Figure 3.15 (a). Left: AFM measurement and profile at the boundary of DNA-modified diamond film. (b). Right: detailed topographic AFM image of DNA-modified diamond surface.[100]

3.3.4 Raman Spectroscopy

Raman spectroscopy is a type of vibrational spectroscopy, while other important techniques use mid-/near-IR spectroscopy, *etc*. Raman spectroscopy is suitable for symmetric vibrations and non-polar groups, whilst the IR spectroscopy is better at asymmetric vibrations of polar groups.[101] Raman spectroscopy was based on the theory of inelastic scattering of light as well as the Raman scattering effect, which was named by its discoverer, *Sir. C.V. Raman*.

The Raman effect is derived from a molecule's deformation, which is produced by an oscillating electromagnetic wave, *e.g.*, laser. At the induction of the energy from laser, the molecules will have a periodical deformation while vibrating at a characteristic frequency ν_{m}. Such oscillating dipoles generate three different types of frequencies: Rayleigh scattering (frequency: ν_{o}, the same frequency as the excitation source), Stokes (frequency: ν_o-ν_{m}), and Anti-Stokes (frequency: ν_o+ν_{m}). The emitted photons from Rayleigh scattering then can be detected by the sensor and transferred to Raman spectroscopy.[101]

Raman spectroscopy is an effective method to characterise the carbon or carbon-related materials with non-destructive approaches. The most common Raman spectra feature peaks in graphitic carbon are the *G* and *D* peaks, which exist at 1560-1620 cm^{-1} and ~1360 cm^{-1}, respectively. The *G* peak can be derived from the C sp^2 bond stretching and the *D* peak is due to the sp^2 atom rings breathing mode.[102] The *G* peak can be assigned as the zone centre photons of $E_{2\mathrm{g}}$ symmetry, whilst the *D* peak is associated with the *K*-point photons of $A_{1\mathrm{g}}$ symmetry. The Raman spectra at 1332 cm^{-1} can be attributed as the diamond $T_{2\mathrm{g}}$ zone centre mode.[103]

Figure 3.16 Raman spectra of natural diamond.[104]

The Raman characteristic spectra of diamond is a single sharp peak at 1332 cm^{-1}, as shown in **Figure 3.16**.[104] For the non-optimum CVD growth, some other Raman peaks can be spotted, *e.g.*, 1150 cm^{-1} and 1260 cm^{-1}. These two peaks are related to the nanocrystalline phase diamond particles and vibrational density of state (VDOS) of diamond.[105] In some CVD diamond films, a broad shoulder can be found at 1550 cm^{-1}, which is derived by amorphous sp^2-bonded carbon or silicon carbide.[106]

Figure 3.17 Raman spectrum of (A) tetrahedral amorphous carbon film, (B) low quality CVD diamond film, and (C) the VDOS of diamond.[105]

Figure 3.17 shows three Raman spectra of a tetrahedral amorphous carbon (ta-C) film, a low quality CVD diamond film grown by MPECVD device and the vibrational density of states (VDOS) of diamond. For the (B) and (C), the peaks located at 1150 cm^{-1} and 1450 cm^{-1} were referred to as v_1 and v_3. Nemanich *et al*. has argued that the 1150 cm^{-1} and 1450 cm^{-1} peak were related to nanocrystalline or amorphous carbon.[108] However, Ferrari *et al*. suggested that the peak was the characteristics of transpolyacetylene. In addition, the sharp peaks, which are located at 1175 cm^{-1} and 1260 cm^{-1}, can be attributed to the VDOS from ~*X* and ~*L* point near the grain boundaries.[105]

For the diamond film with defects, the most notable Raman peaks could be spotted at 1490 and 1630 cm^{-1}, as seen in **Figure 3.18**.[106] The peaks are collected from confocal Raman on different analysis depths. The Raman spectroscopy of detonation nanodiamond samples are shown in **Figure 3.19**. There are only two wide shoulders at ~1350 and ~1640 cm^{-1} and no obvious diamond sp^3 peak at 1333 cm^{-1} can be observed.[107]

Figure 3.18 First order diamond Raman spectra and damaged characterisation peak at ~1450 1490, 1630 and 1680 cm^{-1}.[106]

Figure 3.19 Raman spectra of detonation nanodiamond sample: line 1-untreated ND powder, line 2-ND under 900°C ammonia-treatment, line 3-ND under 1000°C carbon tetrachloride treatment.[107]

The assignment of diamond and other carbon-related materials in Raman spectra is summarised in **Table 3.1**.

Table 3.1 Raman Spectra and assigned functional groups

Raman Position	Assignment
1150	(a) nanocrystalline diamond or amorphous carbon[105] (b) transpolyacetylene[108]
1230~1240	defective nanocrystal diamond[108],[109]
1332	typical diamond characterisation peak
1350	*D* peak of sp^2 A_{1g} symmetric[102],[103]
1400	disordered graphitic component[109]
1450	transpolyacetylene[108]
1470~1490	(c) defective nanocrystal diamond[109] (d) vacancies in diamond above 1100°C[106]
1500	disordered sp^3-bonded carbon[109]
1530~1580	disordered graphitic carbon[107][109]
1560-1620	*G* peak of sp^2 E_{2g} asymmetric[102],[103]
1630	<100> split-interstitial, so-called “dumbell” defect[106]
1640	defective nanocrystal diamond[109]

3.3.5 Fourier-Transform Infrared Spectroscopy

Infrared (IR) light is a type electromagnetic radiation outside the visible light, which is always emitted by the thermal radiation of objects. For infrared spectroscopy, the IR radiation is transmitted through a sample, in which a certain percentage will be absorbed and the other will pass through. The resulting IR spectrum represented the molecular absorption and transmission properties. Therefore, no two compounds can produce the exactly same IR spectrum. The energy level will be determined by the potential energy surface, the mass of the atoms as well as the associated functional groups. In addition, the IR spectrum can be quantitative and the absorption/transmission is a direct indication of the corresponding functional groups.[110] The final analyst required for a frequency spectrum, which gave the intensity at each different frequency. The Fourier-Transformation algorithm will be used as decoding to accomplish the plot from the IR spectrum results.

If the molecule is symmetric, the vibration band cannot be detected by FTIR but only by Raman spectroscopy. The asymmetric structure molecule, *e.g.* CO, can be active in IR spectrum. The organic functional group can exhibit six types of vibration modes: symmetric/asymmetric stretching, scissoring, rocking, wagging and twisting. However, the symmetric stretching, scissoring and twisting vibration mode cannot be detected by FTIR (IR inactive). All the vibration modes are shown in **Figure 3.20**. The main IR absorption peak and corresponding characteristic compounds that commonly found in diamond-related materials are listed in **Table 3.2**.[111]

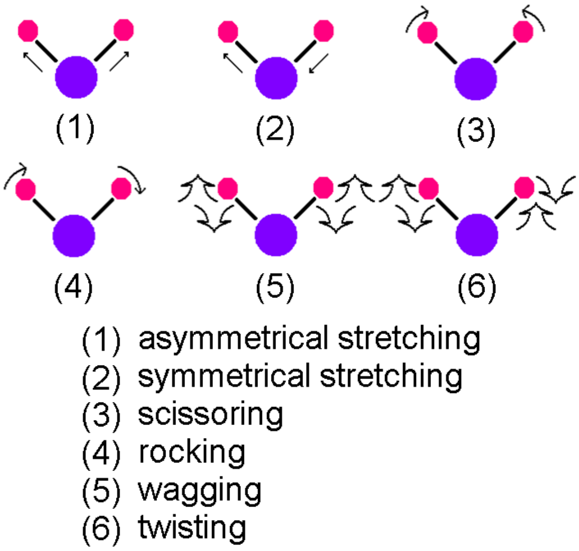

Figure 3.20 The six types of molecule vibration modes. The symmetric stretching, scissoring, and twisting vibration mode can not be IR active.

The FTIR results of singlecrystalline diamond films were investigated by Linares, *et al*.[112] A free-standing natural IIa and a singlecrystalline diamond were used as standard samples. The optical properties were measured by *BioRad* FTIR spectroscopy, as shown in **Figure 3.21 (a) and (b)**. The common features of these two spectra are the strong peaks at ~1975 cm^{-1}, 2020 cm^{-1} and 2159 cm^{-1}, which are considered as the inherent two-phonon lines associated with the C-C bonds.

Figure 3.21 FTIR spectra of (a) natural IIa diamond film, (b) CVD single crystalline diamond film.[112]

Table 3.2 Characteristic infrared absorption wavenumber and compounds

Bonding	Compounds	Specific Bond	Absorption (cm^{-1})	Intensity
C-H	Alkyl	Methyl	2960-2870	Strong
			2960-2850	Strong
		Methylene	1470-1350	Strong
	Vinyl	C=CH, C=CH$_2$	3080-3020	Medium
		Cis-disubstituted alkenes	700-670	Strong
C=C	*sp*^{2}		1680-1640	Medium
	Terminal alkynes		2260-2100	Sharp
C-O	Alcohols	Primary	1060-1040	Strong
		Secondary	1100	Strong
		Tertiary	1200-1150	Medium
	Phenols		1200	
	Ether	Aliphatic	1120	
	Carboxylic acids		1300-1250	
	Esters		1300-1100	
C=O	Ketones		1775-1685	
	Carboxylic acids	Saturated	1710	
O-H		Monomeric: Alcohols, Phenols	3640-3160	Broad
		Hydrogen: Alcohols, Phenols	3600-3200	Broad
		Carboxylic acid	3000-2500	Broad
N-H	Amines	Primary	3500-3300	Medium
			1650-1580	Medium
C-N	Aliphatic amines		1220-1020	Medium
	C=N		1700-1615	

Figure 3.21 (a) has two broad shoulders at 1280 and 1370 cm^{-1}, which are related with the nitrogen atoms in diamond (A and B centre incitation). The A centre is derived from three nitrogen atoms in a cluster together with a vacancy, and lead to an absorption at 415 nm wavelength. The B centre has four nitrogen atoms on the lattice site corresponding to the peak at

1370 cm^{-1}, while the substituted nitrogen has an absorption peak at 1130 cm^{-1}. Deduction from the FTIR results, the nitrogen content can be less than 10 ppm, the purest form of the diamond.

On the other hand, Jiang, *et al*. studied the detonation nanodiamond powder with FTIR (**Figure 3.22**).[113] The significant shoulder at ~3430 cm^{-1} is derived from the surface water absorption. The tiny peaks at ~2980-2950 cm^{-1} can be attributed to the methyl bonds, while the ~619 cm^{-1} peak is from the vinyl bonds. The ketones characteristic peak locates at ~1750 cm^{-1}. The ~1630 cm^{-1} peak represents C=C bonds and C-O alcohol characteristic peak exists at ~1050 cm^{-1} to ~1130 cm^{-1}. Other peaks and the corresponding functional groups can be found in **Table 3.2**. It is difficult to define the surface functional groups with Raman spectroscopy because of the incorporation of the sp^2 graphitic layer. In addition, the Raman spectroscopy cannot represent the C-H bonds that are formed by the hydrogen plasma treatment. However, the FTIR can detect varieties of functional groups, including the C-H bonds and overcome the other limitations. The FTIR can be complimentary technique to Raman spectroscopy.

Two different methods were adopted to remove the non-diamond content on the DND particle surface, One of them is to immersed into perchloric-nitric-hydrochloric acids (6:1). The other one is to mix sample with 98% H_2SO_4, fuming H_2SO_4 and 65% HNO_3 (2:1:1). Each sample was purified and then dried at 140˚C for 5 hours. The FTIR spectra were collected using a Digilab FTS 15/90 FTIR spectrometer. The DND sample was mixed with potassium bromide and pressed into a KBr pellet.

Previous research revealed that the characteristic peak at 1332 cm^{-1} could not be detected on diamond powder with a diameter less than 5 nm.[114] Two broad bands were observed between the region of 2500-1100 cm^{-1}, but the phonon confinement effect forbade the appearance of such phonon process with infrared excitation.[115] The absorbance at ~1260 cm^{-1} was derived from the nitrogen induced one phonon or the defect structure mode. Other absorbance peak located at ~3350, ~1650 and ~600 cm^{-1} could be linked to the amide groups in different formats. On the other hand, the peak at 1733-1740 cm^{-1} was assigned as the absorbance of surface carbonyl bonds, i.e. C=O and –COOH.[115] The peak located at 1760 cm^{-1} is related to the ketonic groups, which indicated a rigid cyclic structure. In addition, the 1130 cm-1 was either $v_{C\text{-}O\text{-}C}$ or the –OH groups.

Figure 3.22 FTIR spectra of DND powder: (a) DND powder purified by $HClO_4$ and HNO_3; (b) DND powder purified by H_2SO_4 mixed with fuming H_2SO_4 and HNO_3; (c) DND powder treated by hydrogen plasma for 4 hours.[113]

Hydroxyl stretching vibration (between 3550-3200 cm^{-1}) was observed after heating DND above 800˚C. The author determined them to be the characteristic peak of v_{OH} and v_{NH} on the DND particles' surface. These peaks were detected after thermal treatment, this represents that these peaks on the surface are stable at temperatures up to 800˚C. The C-H bonds after hydrogen treatment are found at 2955 to 2852 cm^{-1} after fitting the shoulder, which correspond to the v_{asCH3}, v_{asCH2}, v_{sCH3}, and v_{sCH2}.[114] In addition, the sharp peak at 1697 cm^{-1} was considered as the presence of the cyclic carbon in cyclic lactams together with nitrogen element. The FTIR absorbance and peak assignments have been shown in **Table 3.3**.[113],[114]

Table 3.3 FTIR absorbance and assignments.

IR Range[3]	Absorbance (cm^{-1})	Assignment	Remarks
3590s-3430**s**	3558-3590	v_{OH}	Bonded –OH
	3434-3425	v_{OH}	water, tertiary alcohol
		v_{NH}	amide
2980-2850**s**	2965-2955	v_{asCH3}	CH_3 asymmetrical stretching
	2928-2927	v_{asCH2}	CH_2 asymmetrical stretching
	2873-2871	$v_{\mathrm{sCH3,}}$ v_{CH}	CH_3 symmetrical stretching,
	2852	v_{CH2}	CH_2 bending
1776**m**	1783-1780	$v_{\mathrm{C=O}}$	cyclic ketonic, cyclic lactam ester, carboxylic groups
	1759-1755		
	1736		
1676**m**	1679-1676	$v_{\mathrm{C=O}}$	amide I
1630**m**	1632-1630	δ_{OH}, v_{CO}	water, amide II (C-O)
1590**m**	1597-1587	δ_{NH}	amide II
1460**w**	1460	$\delta_{\mathrm{as\ CHx}}$	asymmetrical stretching
1261**m**	1261-1254	v_{CO}	epoxy, ester, or δ_{CNH} (amide III), v_{CCO} (=C-OH), N-induced/defect in DND, v_{CN}, v_{CC}
1217**m**			
1190**sh**	1194-1187	$v_{as\ \mathrm{COC}}$, δ_{OH}	ether, or water
1130**s**	1130-1225		
1047**sh**	1049-1043	δ_{OH}	water
618**w**	619-618	δ_{CCC}, δ_{NCO}	amide IV
550**b**	~550		

---

[3] Peak shape abbreviations: **s**: small; **m**:medium; **w**: wide; **sh**: sharp; **b**: broad.

3.3.6 Impedance Spectroscopy

Impedance spectroscopy (IS) is a relatively novel and useful method in characterising the electrical properties of materials, both on the surface and in the bulk. It can be utilised to investigate the boundary mobile electrons dynamics in the bulks or interfacial regions of solid/liquid materials, *e.g.*, semiconductors, dielectrics, ionics, as well as mixed electronic-ionic, *etc*.[115] The working background of IS will be introduced in this section as an analysis method of simple solid-state material and the principle of function will be discussed. The most common and standard approach to measure the impedance can be achieved by applying a single-frequency current/potential to the interface and examining the parameters, which include amplitude and phase shift, real and imaginary parts. Then response signal is then analysed by either analogue circuitry or the fast Fourier transform (FFT) method.[116],[117]

Figure 3.23 Dielectric permittivity over a wide frequency range.[118]

The fundamental of the AC impedance spectroscopy is based on the material dielectric response to a certain applied electric field, as seen in **Figure 3.23**. As the applied AC electric excitation varies, the mechanism of polarization will change. For the impedance measurement, a suitable frequency range will be 10^{-3}-10^{7} Hz, which involves both the dielectric relaxation and ionic relaxation.

In Ohm's law, the frequency domains voltage $V(j\omega)$ and current $I(j\omega)$, relationship and the impedance, $Z(j\omega)$, is defined as $Z(j\omega)=V(j\omega)/I(j\omega)$. The complex $Z(j\omega)$ is composted by the real $Re(Z)$ and imaginary $Im(Z)$ parts, which is expressed as:

$$\boldsymbol{Z = Re(Z) + j.Im(Z)}$$ **Equation 3.4**

while $j \equiv \sqrt{-1}$, and

$$\boldsymbol{Re(Z) = Z' = |Z|\cos\theta = R}$$ **Equation 3.5**

$$\boldsymbol{Im(Z) = Z'' = |Z|\sin\theta = \frac{1}{j\omega C} + j\omega L}$$ **Equation 3.6**

$$\boldsymbol{|Z| = \sqrt{(Z')^2 + (Z'')^2}}$$ **Equation 3.7**

$$\boldsymbol{\theta = tan^{-1}(Z''/Z')}$$ **Equation 3.8**

Consider a simple *RC* parallel circuit with an AC signal: $V = Vt\sin(\omega t + \theta)$, the impedance and the modulus of the circuit will be calculated as:

$$\boldsymbol{Z(\omega) = R// \frac{1}{j\omega C} = \frac{\frac{R}{j\omega C}}{R+\frac{1}{j\omega C}} = \frac{R}{1+j\omega RC} = \frac{R}{(1+\omega^2R^2C^2)} + j\frac{(-\omega R^2C)}{(1+\omega^2R^2C^2)}}$$ **Equation 3.9**

$$\boldsymbol{\sqrt{(\frac{R}{(1+\omega^2R^2C^2)} - \frac{R}{2})^2 + (\frac{(-\omega R^2C)}{(1+\omega^2R^2C^2)})^2} = \sqrt{\left[Re(Z) - \frac{R}{2}\right])^2 + [Im(Z)]^2} = \frac{R}{2}}$$ **Equation 3.10**

Figure 3.24 shows the relationship between the real and imaginary part of the impedance. The plot is based on a vector diagram via plotted $|Z|$ on the axis composed by real part versus imaginary part. In the semicircle, *ω* is the frequency in radius and *θ* is the phase shift.

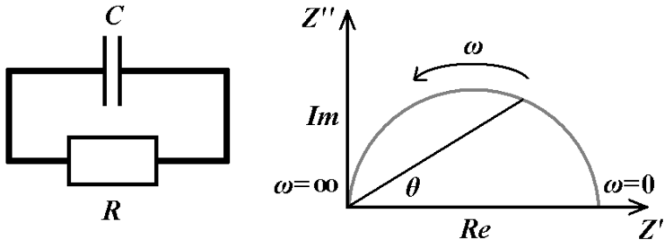

Figure 3.24 A simple *RC* parallel circuit and corresponding impedance plot.

When *ω* is approaching to 0, it is obvious that the intercept distance on the real part axis is *R*, which represents when the AC frequency is closed enough to 0, the resistance can be considered as the DC resistance and derived from the plot. This plot was named as Cole-Cole plot and introduced by Barsoukov, *et al*.[119]

When it is not a perfect semicircle, the centre of the circle will not be on the *Z*' axis and the capacitance will be replaced by a Constant Phase Element (CPE), as shown on **Figure 3.25**.

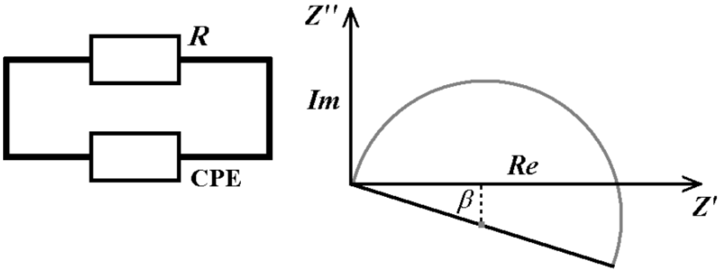

Figure 3.25 Non-perfect semicircle response and corresponding equivalent circuit with a CPE.

Here, the CPE is described as:

$$\boldsymbol{Q} = \left(\frac{\mathbf{1}}{\boldsymbol{j\omega}}\right)^{-\boldsymbol{\beta}} \cdot \frac{\mathbf{1}}{\boldsymbol{C}} \qquad \textbf{Equation 3.11}$$

while 0< β <1. When β =1, the CPE will be an ideal capacitor and the whole model will be the same as *RC* parallel circuit. Similarly, if β =0, the CPE will be an inductance.

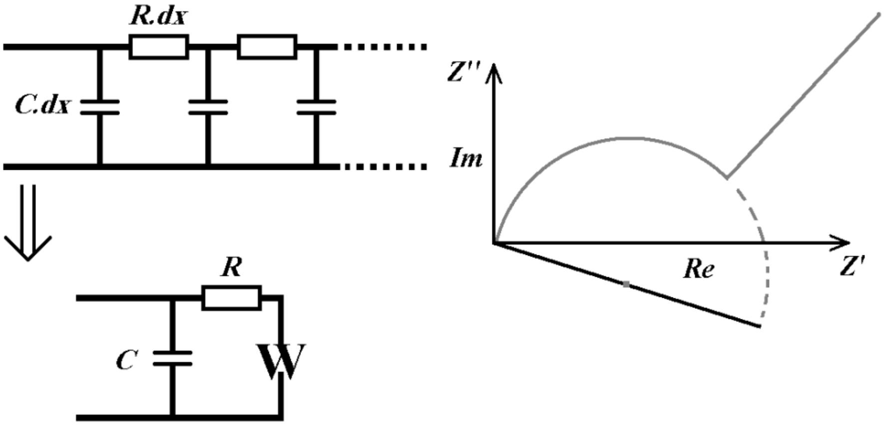

Figure 3.26 Semi-infinite *RC* parallel model, corresponding Warburg equivalent circuit model (Left) and impedance spectroscopy response (Right).

Consider the semi-infinite *RC* parallel circuit composed only by resistors and capacitors, the circuit model will be the same as **Figure 3.26**. It is quite similar to the transmission line in microwave circuit. The impedance spectroscopy response will be composed by a CPE with a constant phase of 45˚. A linear relationship is following the CPE and has a constant angle against both the axis. This model is named as Warburg element and the solution is:

$$\boldsymbol{W} = \boldsymbol{A_w}(\boldsymbol{j\omega})^{-\mathbf{0.5}} \qquad \textbf{Equation 3.12}$$

In a common electrical circuit, the elements in the circuit will be transformed into another state, as shown in **Table 3.4**.[120]

Table 3.4 Electronic element and corresponding impedance element

Electronic Element	Explanation	Impedance (Ohm)	Admittance (Siemens)
R	Resistance	R	$1/R$
C	Capacitance	$1/j\omega C$	$j\omega C$
L	Inductance	$j\omega L$	$1/j\omega L$
W	Semi-infinite Warburg	$1/Y_0\sqrt{j\omega}$	$Y_0\sqrt{j\omega}$
Q	CPE	$Y_0(j\omega)^\alpha$	$1/Y_0(j\omega)^\alpha$

Impedance spectroscopy can be used to characterise the electrical properties by using the equivalent circuit in a non-destructive method. Theoretically, a model composed by a succession of *RC* parallel circuits in series could be used to describe the different conduction mechanism. The complex impedance will be expressed as:

$$\boldsymbol{Z' = \sum_{i=1}^{n} \frac{R_i}{1+\omega R_i^2 C_i^2}}$$ **Equation 3.13**

$$\boldsymbol{Z'' = \sum_{i=1}^{n} \frac{\omega R_i^2 C_i}{1+\omega R_i^2 C_i^2}}$$ **Equation 3.14**

In these two equations, *n* represents the different conduction paths, which can be attributed as the contribution from grain interior (GI), grain boundary (GB) and electrode.

The impedance spectroscopy can be applied in characterising the electrical properties of diamond and diamond-like materials. Curat, *et al*. applied the impedance spectroscopy to study the *n*-type phosphorus-doped diamond film.[121] The sample was phosphorous-doped homoepitaxial diamond film grown by MPECVD. Four heavily phosphorous doping areas were formed at the square corners with P^+ contact with Au electrodes. The impedance spectroscopy was carried out with a Solartron 1260A with a frequency from 0.1 Hz up to 10 MHz and an amplitude potential of 0.05V. The impedance spectroscopy (Cole-Cole plot) is seen in **Figure 3.27**.

The equivalent circuit was extracted from the Cole-Cole plots with an *RC* parallel circuit (plots at 25˚C and 50˚C) and two *RC* parallel circuit in series from 75˚C ~300˚C (*RC*)(*RC*). At low temperature range, the impedance response was only one semi-circle, which indicated that there is only one conduction mechanism in the material. As the temperature rose above 75˚C, an additional semicircle extended to low frequency range. The resistance and capacitance were extracted from the equivalent circuit. The capacitance derived by fitting the semicircles indicated that two different capacitance values exsisted at 10^{-9} and 10^{-12} farad level.

Aston University

Illustration removed for copyright restrictions

Figure 3.27Cole-Cole plots of the P-doped homoepitaxial diamond film at different temperature varied from 25˚C to 300˚C.[122]

The capacitance can be linked with the microstructure by a physical model composed of grain interior, grain boundaries and electrode behaviour. The simple model (Brick model) structure could be described as a two-phase mixture in a series layer, as seen in Figure 3.28.[122],[123]

In **Figure 3.28**, the model has a cross section area of A and length of L, δ represented the grain boundary width, whilst d represented the grain size of the crystalline.[123] The electronic current can be considered as one-dimension and the effect at corners is negligible. The only two paths for electron transportation are through the grain interior or grain boundaries. According to the relative different magnitude of grain interior and grain boundary, one or two paths may be involved during the conduction progress. This model has been widely applied in many materials and characterised the bulk resistance.[124]

Figure 3.28 Brick model of idealised polycrystalline material.[122]

In terms of grain interior electrical response, the capacitance can be expressed by:

$$C_{gi} = \sum_{i=1}^{n} \varepsilon_{gi} \cdot \frac{S}{D} = \sum_{i=1}^{n} \varepsilon_{gi} \cdot \frac{d^2}{d} = \sum_{i=1}^{n} \varepsilon_{gi} \cdot d \qquad \textbf{Equation 3.15}$$

where ε_0 is the permittivity of free space (8.85×10^{-12} F/m) and ε_{gi} is the grain interior relative dielectric constant. Meanwhile, the grain boundary capacitance can be calculated as:

$$C_{gb} = \sum_{i=1}^{n} \varepsilon_{gb} \cdot \frac{S}{D} = \sum_{j=1}^{3} \sum_{i=1}^{n} \varepsilon_{gb} \cdot \frac{d^2}{\delta} \qquad \textbf{Equation 3.16}$$

where ε_{gb} is the grain boundary relative dielectric constant. The total number of the blocks is n, which can be calculated as:

$$n = \frac{AL}{(d+\delta)^3} \qquad \textbf{Equation 3.17}$$

Hence, when the size of grain boundary size δ is infinitesimal, it is an approximation $n \approx A.L/d^{\,3}$. In this case, C_{gi}/C_{gb} can be expressed as:

$$\frac{C_{gi}}{C_{gb}} = \frac{3\delta}{d} \frac{\varepsilon_{gi}}{\varepsilon_{gb}} \qquad \textbf{Equation 3.18}$$

This Equation indicates that the grain capacitance and grain boundary is proportional to the grain boundary width δ and the reciprocal of grain size d. Meanwhile, the ε_{gb} and ε_{gi} were in the same magnitude for the same material. Thus, empirical capacitance value for diamond materials indicated that the grain boundary capacitance is located in 10^{-9} F level, and the grain interior capacitance can be 10^{-12} F. The capacitance response derived from the electrode is around 10^{-6} F level.[125],[126]

In 2008, Bevilacqua, *et al*. investigated the electrical properties of aggregated DND powder (SuperSyndia SSX 0-3.5) with Solartron 1260 impedance system and 1296 dielectric interface.

The experiment was carried out in a stainless steel chamber, which can be filled with ambient gas or air. The impedance spectra have been shown in **Figure 3.29**.[127]

Figure 3.29 Cole-Cole plot for DND powder measured in air at (a) 350-450˚C, (b) 450-550˚C, (c) 450-550˚C after several circles.[127]

The impedance exhibited a resistance greater than $10^{13}\Omega$/sq, which is similar to the typical high quality polycrystalline diamond film. The DND powder was considered as the mixture of sp^3, sp^2 and impurity species. The author assumed that the DND sample in electrical measurement could be considered as the three dimensional network, which was different with the continuous diamond film. Numerical fitting on the semi-circle response exhibited a capacitance at nanofarad level, which was thought to be grain-boundary conduction, rather than grain interior conduction. As the heating temperature at 550˚C, the agglomeration at the grain boundaries occurred at the same time as the uniformation of the sp^2 species.[127]

3.4 Summary

In this chapter, the equipment for diamond growth and properties characterisation has been introduced. The structures of MPECVD and HFCVD system were demonstrated. The SEM has been used to observe the surface morphology of diamond materials. The XPS can distinguish the impurities in diamond materials. The Raman and FTIR spectrum can be applied to find out the functional group on diamond. For Raman spectrum, it is more obvious to distinguish the difference between carbon sp^2 and sp^3 bonds, while in FTIR, all the surface functional groups can be determined. In addition, the IS can be utilised to detect the electrical properties and find out the conduction mechanism.

Chapter 4: Diamond Film Growth with MPECVD System

Diamond Film Growth with MPECVD System

4.1 Introduction

In this chapter, the diamond growth on different substrate using MPECVD method has been studied. The synthesis of diamond film growth was performed using an ASTeX™ 5010 system (Seki. Corp.), as introduced in Chap.3. The detailed synthesis process of diamond (100) substrates is covered in Sec.4.2, including the analysis and optimisation. Based on the optimised conditions, the diamond film growth on silicon (111) substrate, diamond-like carbon (DLC) film and silica fibres are reported, respectively.

4.2 Diamond Growth on (100) Silicon Wafer

In the 1990's, Stoner *et al*. firstly investigated bias enhanced nucleation for diamond growth on Si (100) oriented substrate.[128] Y. Hayashi, *et al*. then developed highly-oriented (100) diamond (HOD) films.[129] In 1996, the heteroepitaxial HOD growth on β-phase silicon carbide films with extremely low angular spread was successfully synthesised by Kawarada, *et al*.[130] All these diamond deposition process were performed with bias-enhanced nucleation (BEN), which created a better nucleation effect before the diamond growth. Comparing the previous works with hundreds of hours growth duration, we presented diamond synthesis on (100) silicon wafer without BEN device in this section. For the MPECVD system configuration in our group, we can only perform the diamond growth without any voltage bias.[4]

In this section, diamond films were deposited on silicon wafers with the following procedures: pre-heating, nucleation, growth, and surface-termination. The parameters were adjusted in order to optimise the growth condition.

4.2.1 Experimental Process

A boron doped *p*-type (100) silicon wafer, with a diameter of 100 mm and thickness of 500 μm, was cut into ~1.5×1.5 cm^2 pieces and used as the deposition substrates. The silicon wafer was immersed in acetone and isopropanol solution, and then taken ultrasonic bath at 60˚C for 30 mins to remove surface organic contaminations. Different processes for substrate preparation have been applied in order to find out a suitable deposition condition. After this process, the silicon wafer was rinsed by de-ionised (DI) water and dried by flushing compressed N_2 gas. Followed by these steps, the silicon wafer was boiled in 95% sulphuric acid (120˚C), as well as *Aqua Regia* (HCl: HNO_3=3:1, 80˚C) for 1 hour each. The surface graphite content and metal

---

[4] BEN module was not included in ASTeX™ 5010 system in our group.

species were totally removed by this acidic etching. Finally, the silicon wafer was flushed by DI water and dried.

The diamond substrate was carefully transferred to the molybdenum stage and installed into the quartz bell-jar of the MPECVD system. The chamber was vacuumed and flushed with hydrogen gas for 10 mins. After the microwave power was turned off, the methane flow was cut off and the hydrogen gas atmosphere protected the substrate surface from being oxidised. The growth condition is listed in **Table 4.1**, while the optical images were randomly obtained at four positions by Olympus BX41 at 20× lens, as shown on **Figure 4.1~Figure 4.9**. From the optical images, the surface of silicon wafer after deposition is clearly observed. The diamond particles distribution coverage was not ideal and they did not coalesce together, except for sample 0819 and 0824. Most of the diamond particles were grown separately, while some of them got agglomerated in some of the scratched areas. This phenomenon indicated an unsuitable condition for diamond growth. For sample 0819 and 0824, the surface was fully covered by diamond film, which created a uniform coverage.

Table 4.1 MPECVD diamond growth conditions.

Sample	Nucleation				Growth			
	Gas flow rate (CH_4/H_2)	Pressure (Torr)	Power (W)	Duration (hour)	Gas flow rate (CH_4/H_2)	Pressure (Torr)	Power (W)	Duration (hour)
0806	N/A				200/2	50	1000	2
0809	200/4	50	1000	1	200/2	55	900	6
0810	200/4	50	1000	1	200/2	55	950	6
0812	200/4	50	1000	1	200/2	55	850	6
0813	200/4	50	1000	1	200/2	50	900	6
0816	200/4	50	1000	1	200/2	50	850	6
0818	200/4	50	1000	1	200/2	50	950	6
0819	200/4	50	1000	1	200/2	40	950	6
0823	200/4	50	1000	1	200/2	40	850	6
0824	200/4	50	1000	1	200/2	40	900	6

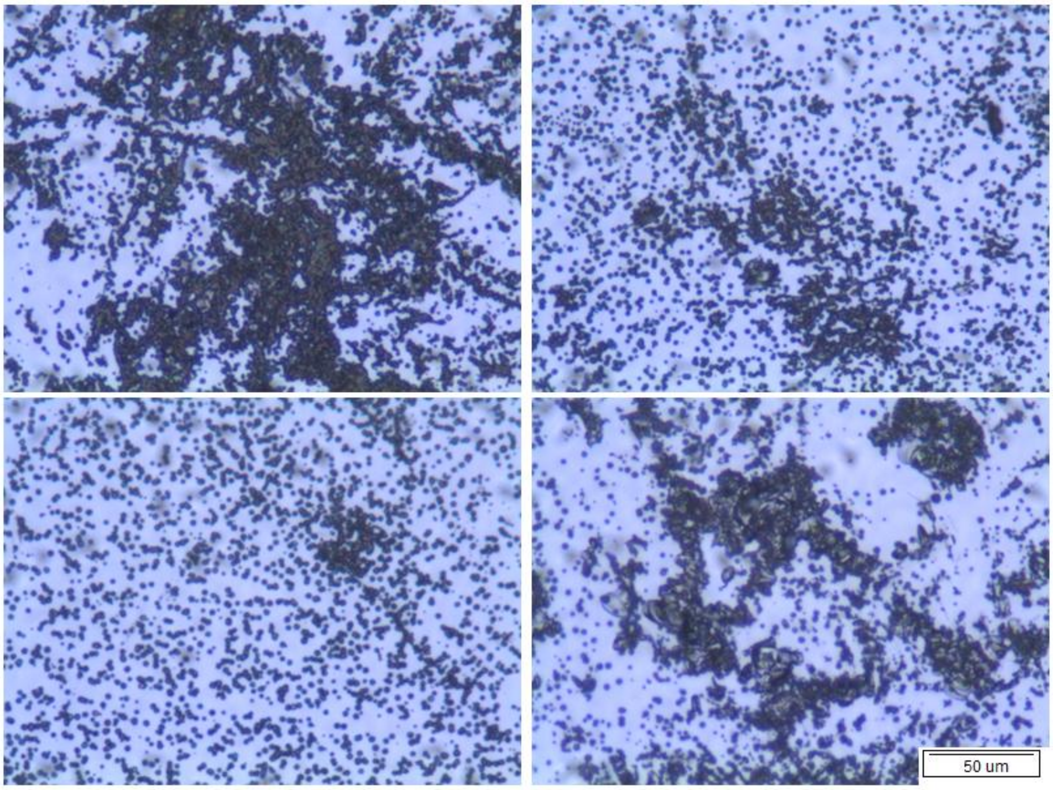

Figure 4.1 Optical image of Sample 0806

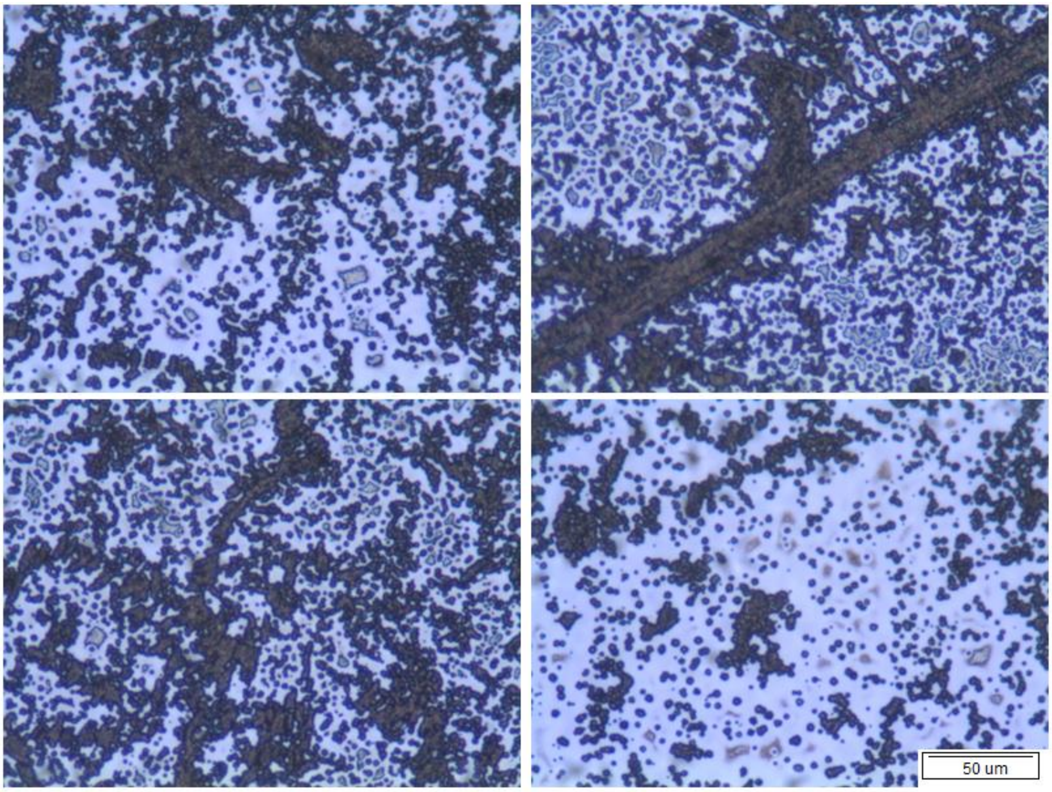

Figure 4.2 Optical image of Sample 0810

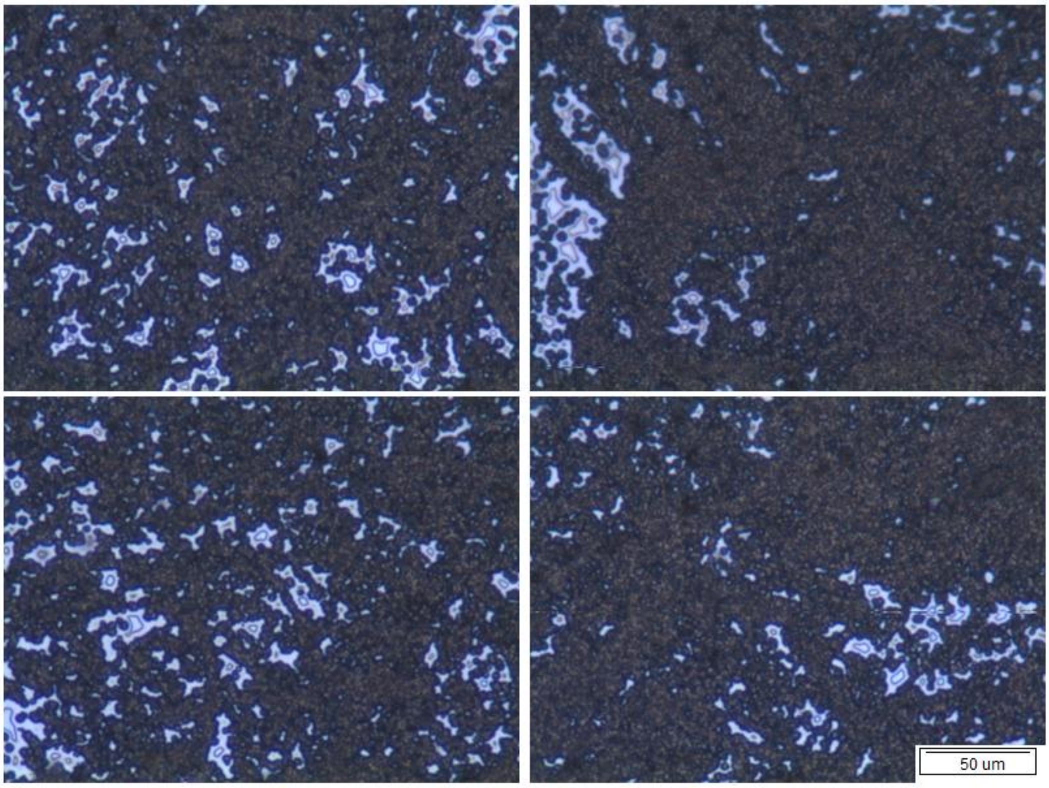

Figure 4.3 Optical image of Sample 0809

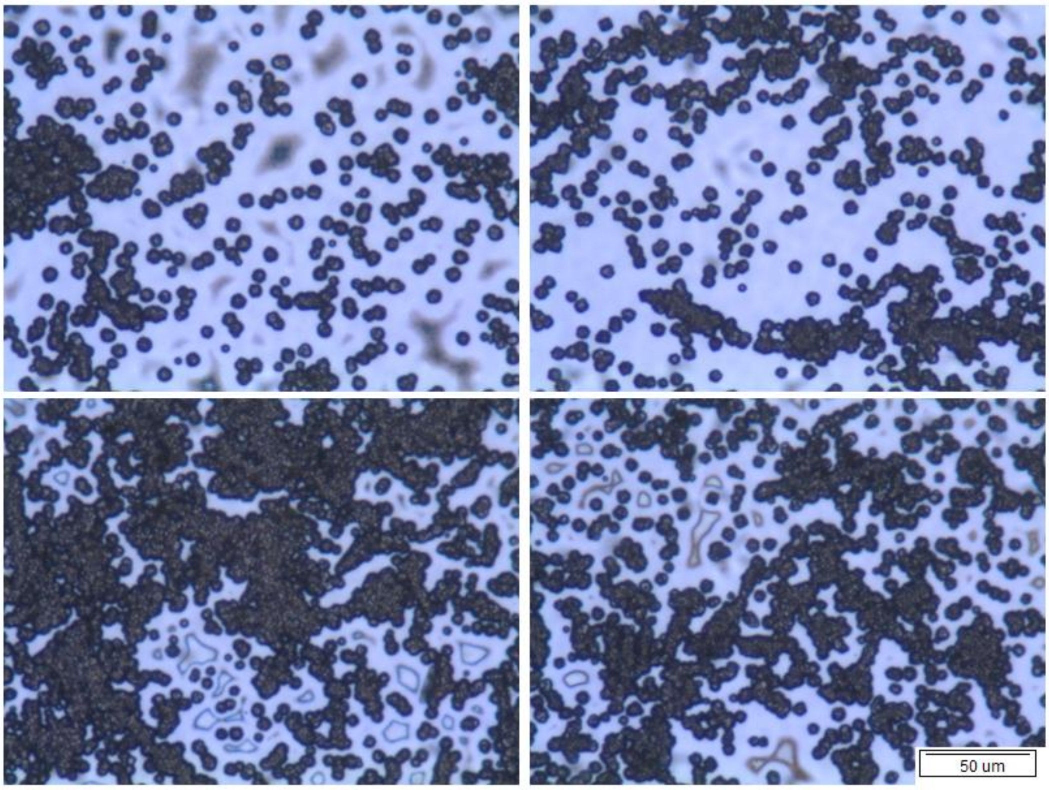

Figure 4.4 Optical image of Sample 0812

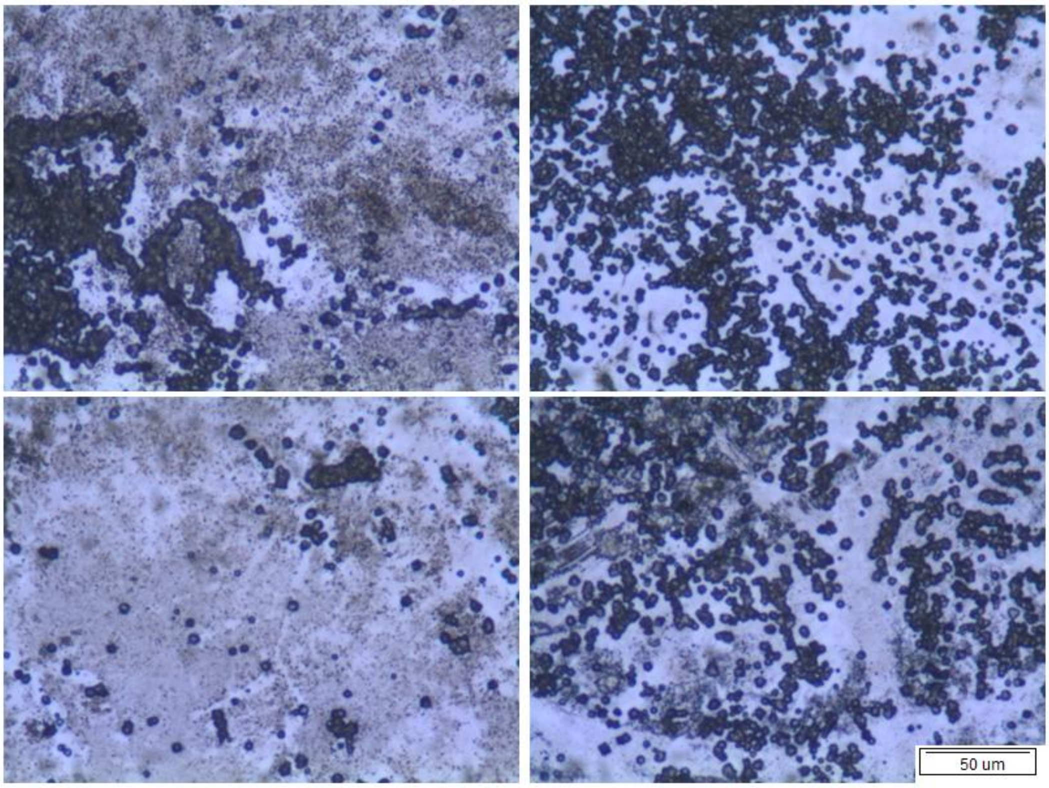

Figure 4.5 Optical image of Sample 0813

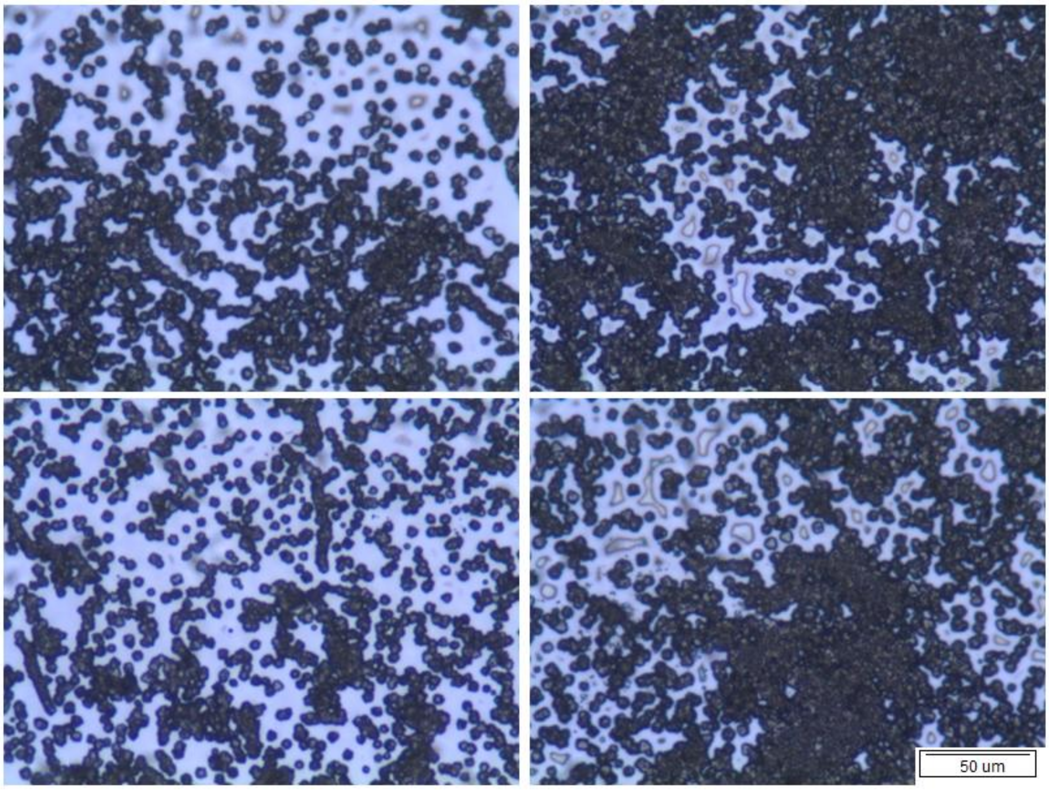

Figure 4.6 Optical image of Sample 0816

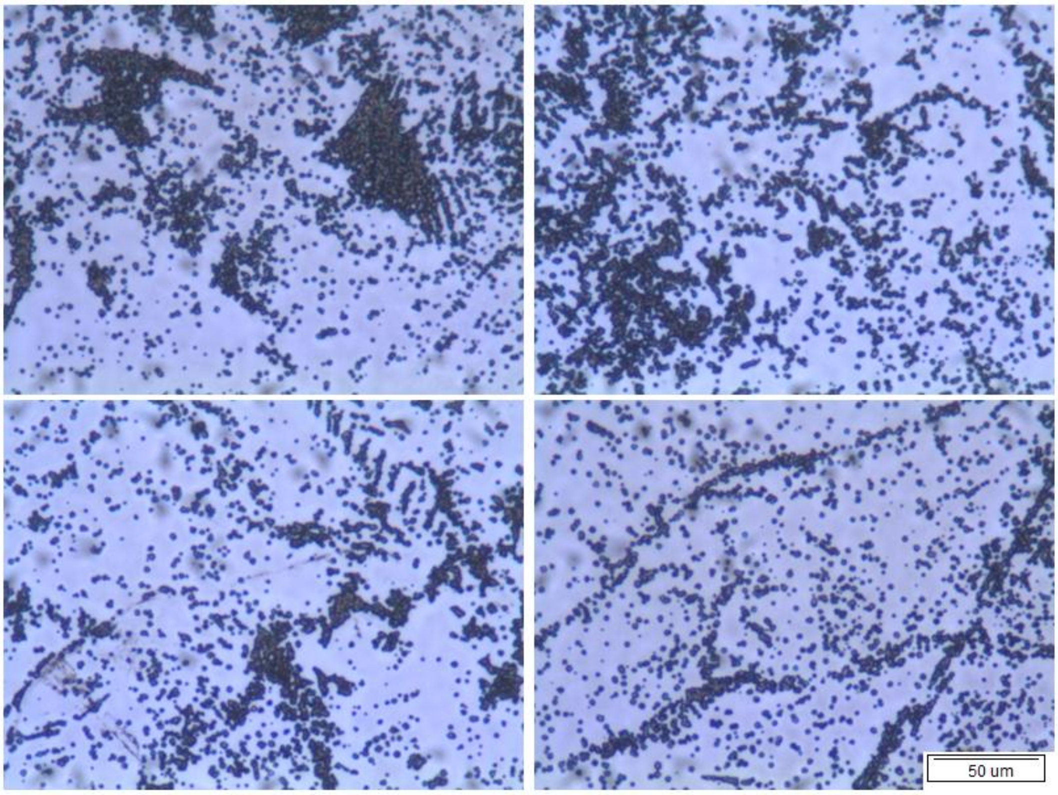

Figure 4.7 Optical image of Sample 0818

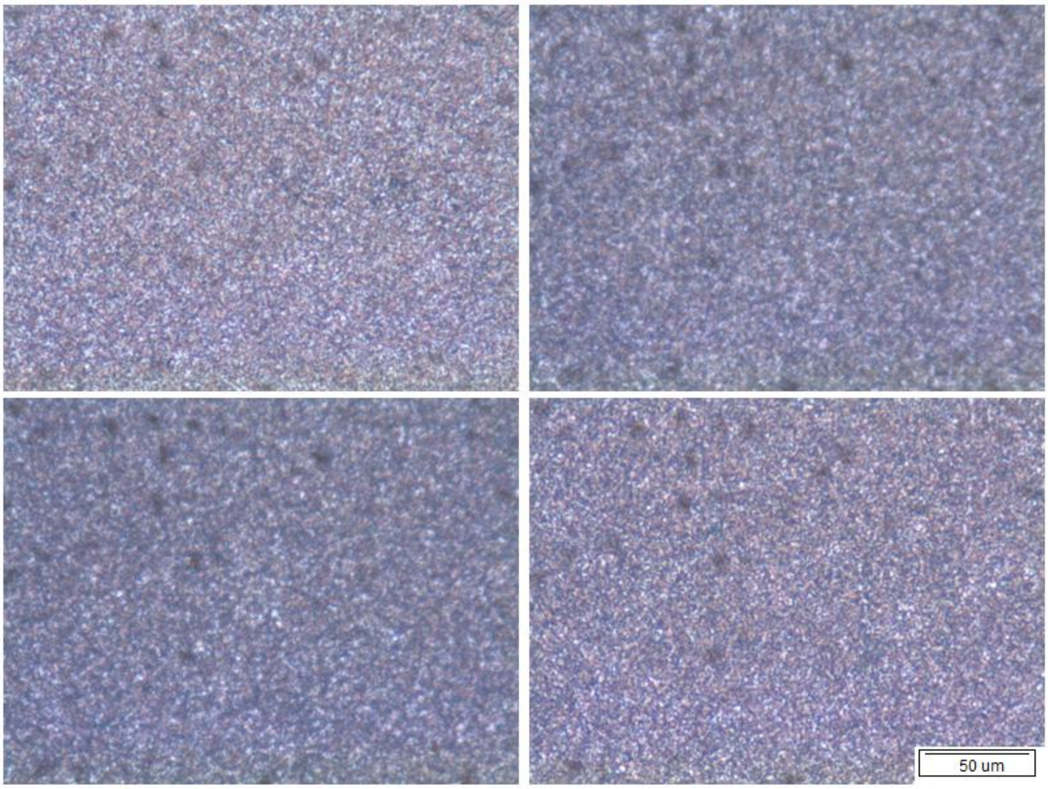

Figure 4.8 Optical image of Sample 0819

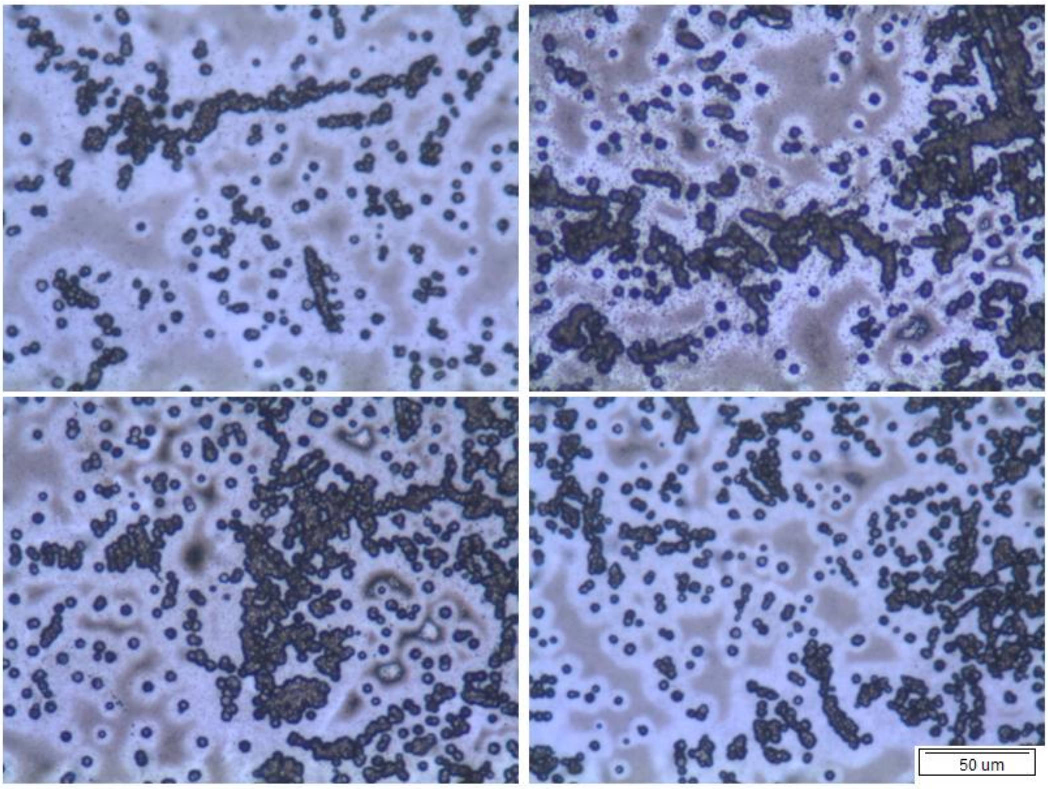

Figure 4.9 Optical image of Sample 0823

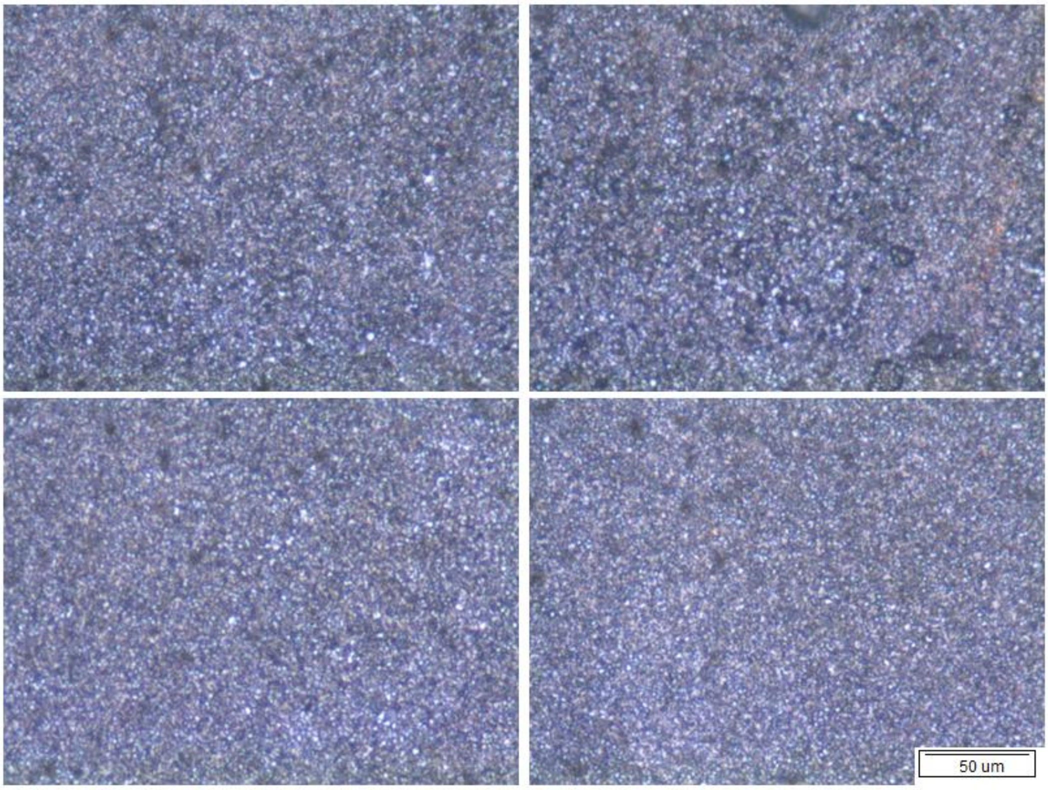

Figure 4.10 Optical image of Sample 0824

4.2.2 Results and Characterisation

Some of the selected samples have SEM images taken of them, as shown in **Figure 4.11~Figure 4.15** with four different magnifications. For the crystal orientation, all samples demonstrated a randomly oriented crystal direction on the (100) silicon wafer. As described in Sec.4.2.1, the uniform deposited diamond layer on sample 0824 was found consistent with previous results. The diamond particles were deposited on the surface with an average agglomerated particle diameter of ~1 μm. In **Figure 4.11~Figure 4.15**, a small percentage of the particles coalesced together, but most of them were apart from each other.

The diamond deposition was based on a layer of silicon carbide, which was formed by the reaction between the silicon wafer and the carbon source gas. Most of the silicon substrate was uniformly covered by SiC layer. However, some part of it was exposed, as labelled in red labels in figures.

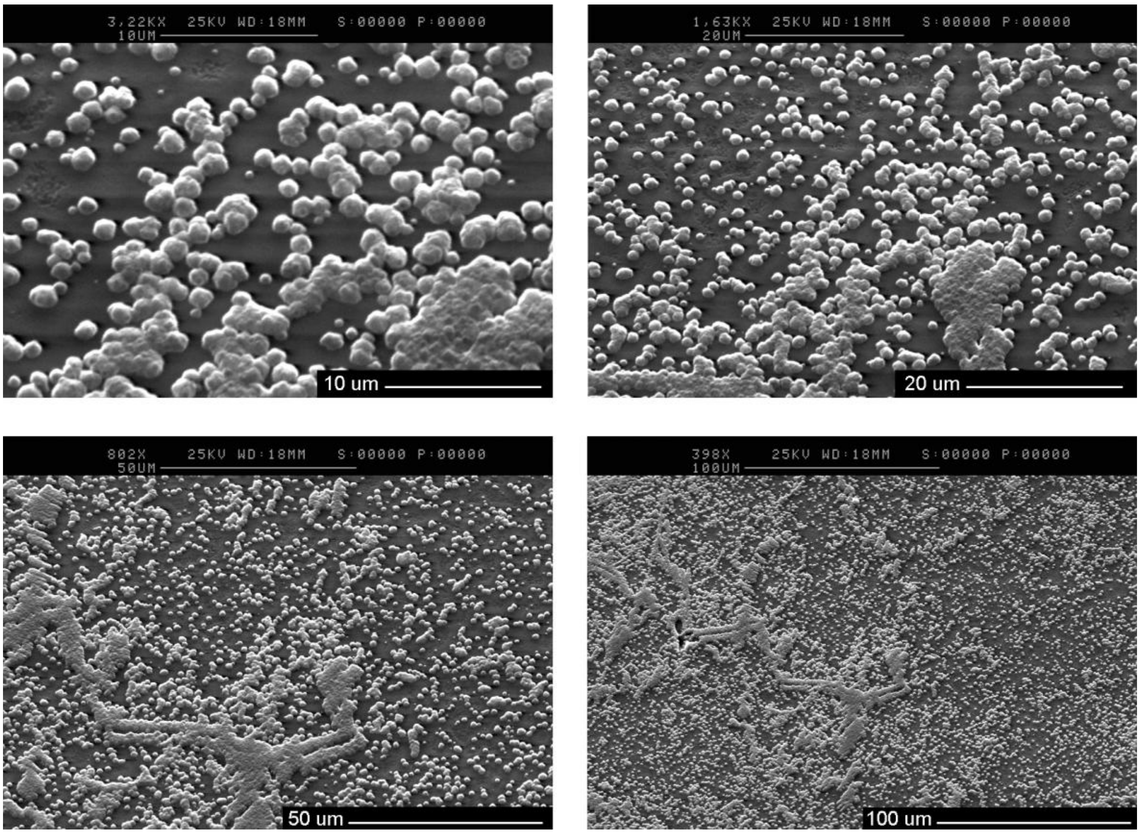

Figure 4.11 SEM images of sample 0809

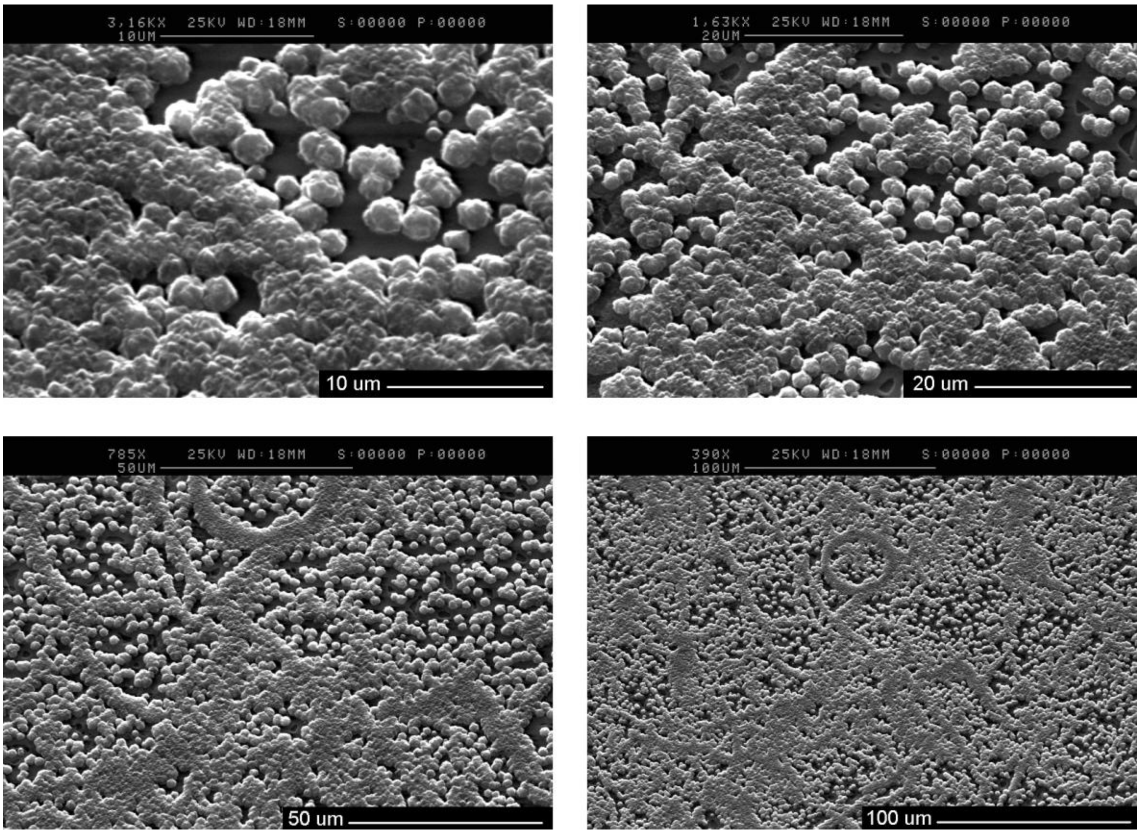

Figure 4.12 SEM images of sample 0810

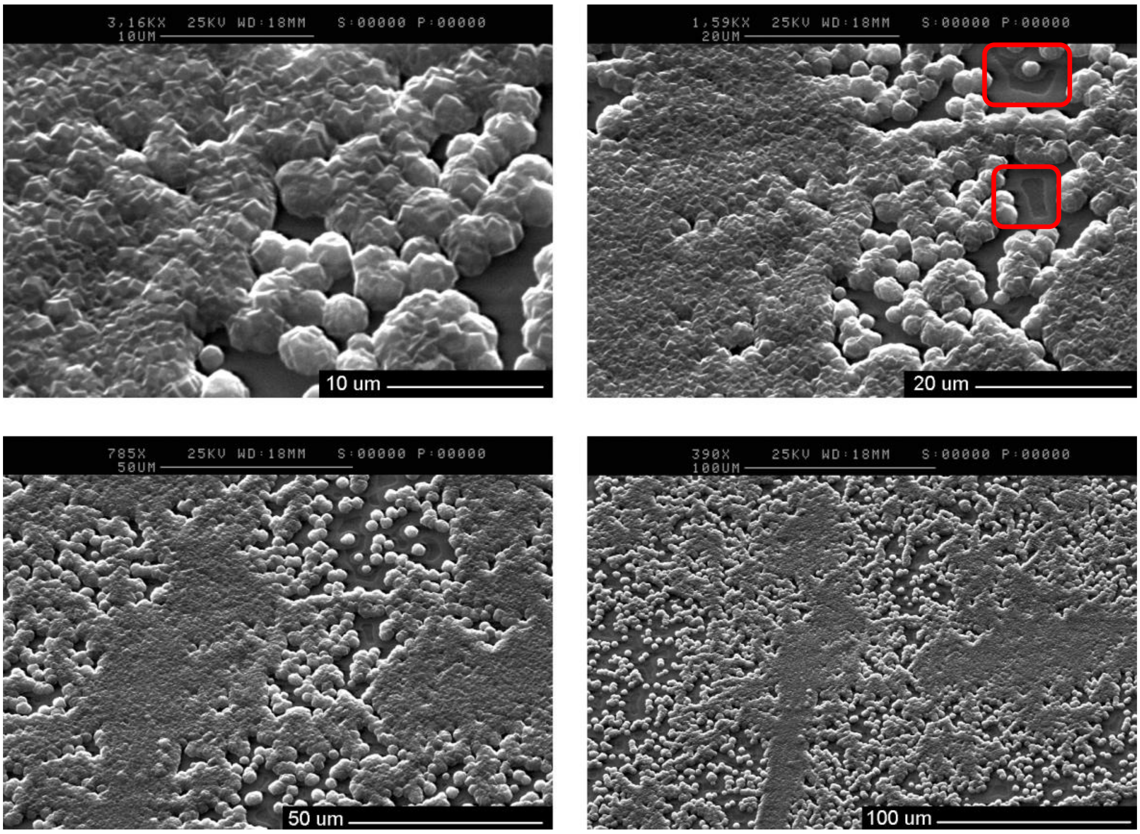

Figure 4.13 SEM images of sample 0812

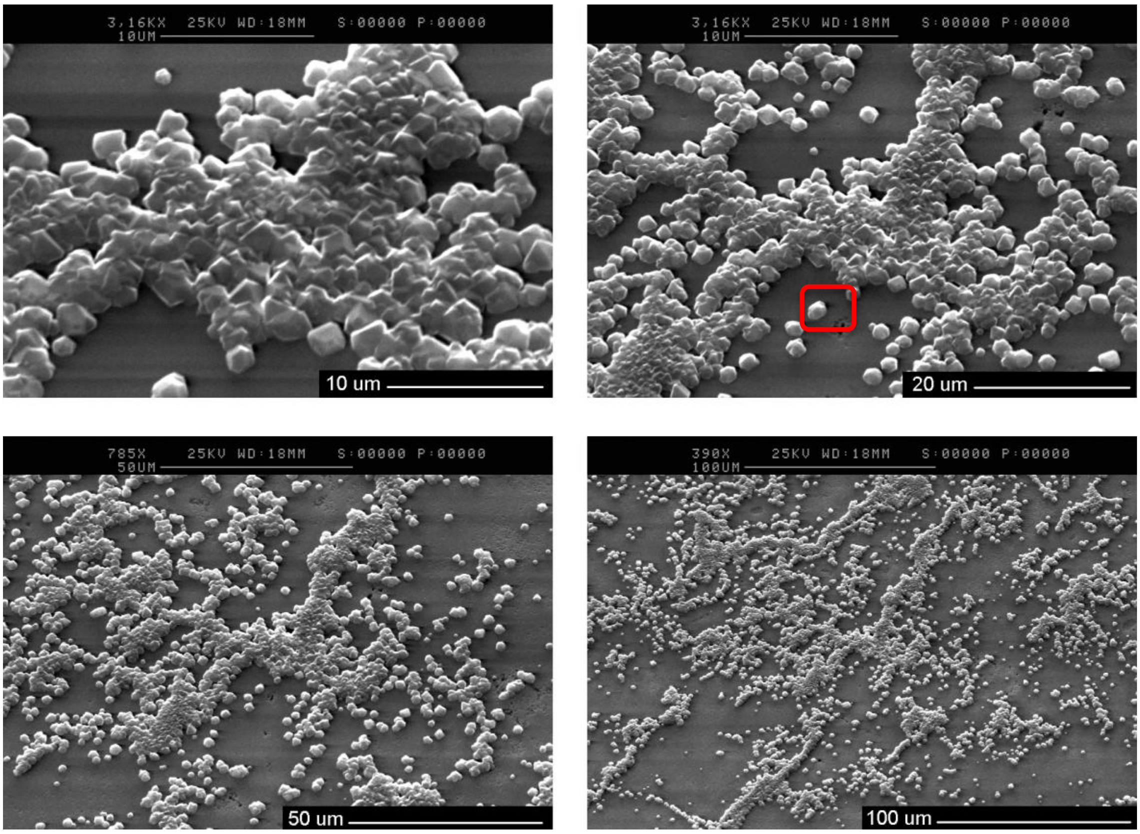

Figure 4.14 SEM images of sample 0813

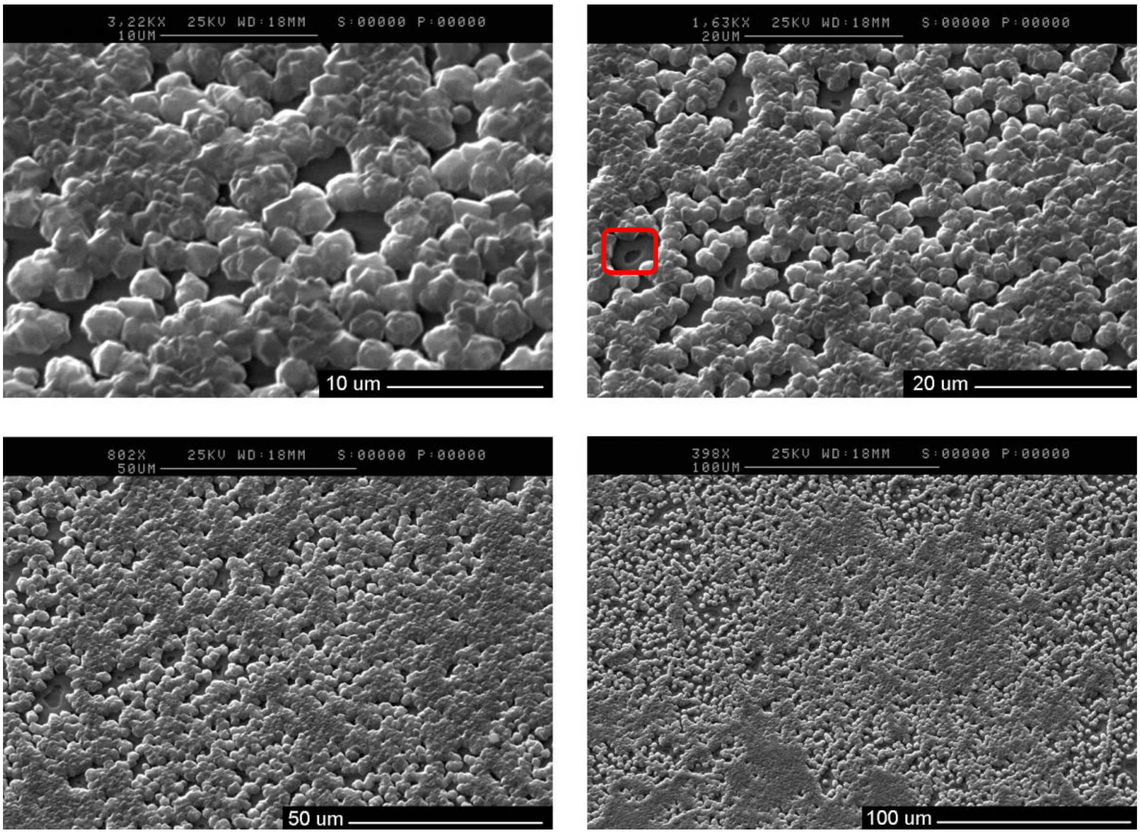

Figure 4.15 SEM images of sample 0816

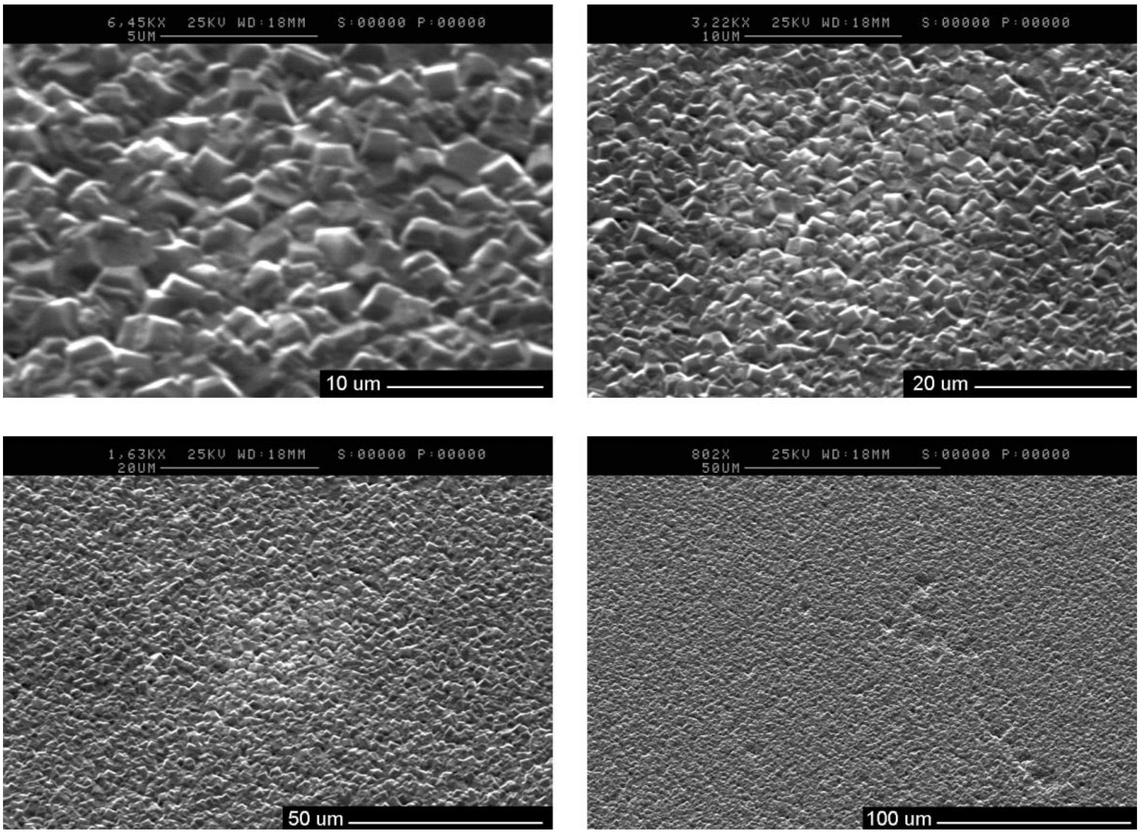

Figure 4.16 SEM images of sample 0824

To verify the surface diamond composition, a Raman spectrometer (Nicolet Almega XR dispersive Raman, Thermo Ltd.) equipped with an optical microscope (Olympus TE-coated Si CCD), was used to characterise the samples. All the results were shown below.

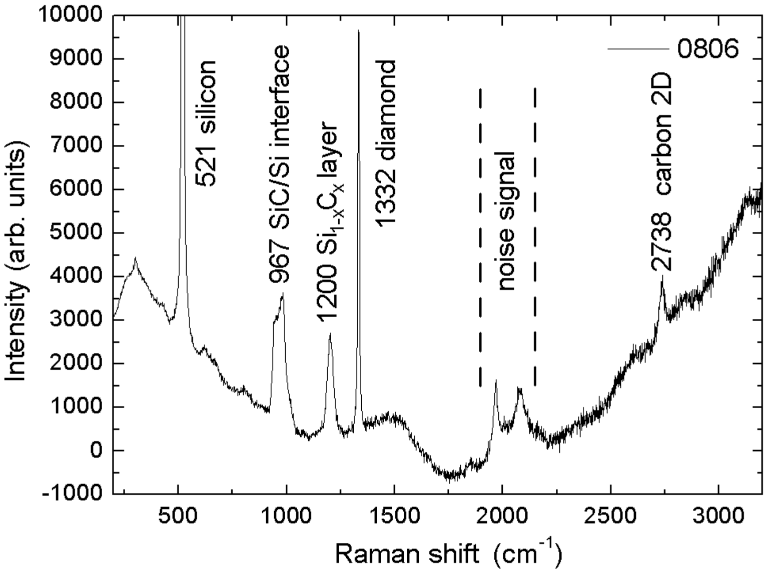

Figure 4.17 Raman spectra of sample 0806

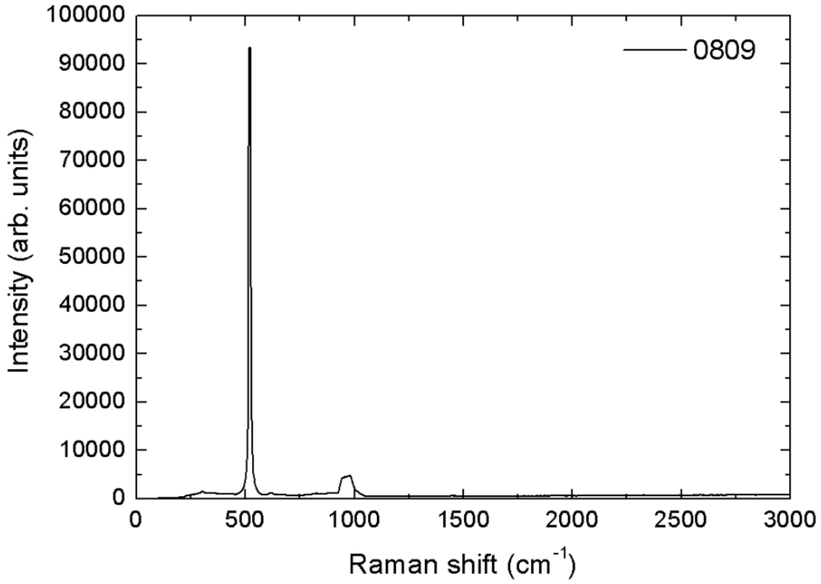

Figure 4.18 Raman spectra of sample 0809.

The significant peak at 521 cm^{-1} in **Figure 4.17** was attributed to the zone centre optical phonon from Si and the peak at 967 cm^{-1} was derived from the interface between SiC/Si.[131][132] Besides, the 1200 cm^{-1} peak has been reported as a lattice vibration of $Si_{1-x}C_x$ epitaxial layer on Si (100) substrate.[133] The sharp peak at 1332 cm^{-1} is a characteristic peak of diamond. The sharp peaks at 1900~2100 cm^{-1} were noise signal, which were most likely to be caused by the outer space emitted ray, as they were not spotted in the rest of other Raman results. The 2738 cm^{-1} is assigned as the 2*D* peak.[134] The Raman results proven that the silicon substrate had a reaction with carbon and some part of the surface had transformed to SiC. It was no uniform diamond films deposited on whole of all the silicon substrates.

In **Figure 4.18**, the diamond Raman characteristic peak was not observed. There were only peaks of silicon at 521 cm^{-1} and SiC at 970 cm^{-1}. The results indicated that on the surface there were no diamond films deposited at all, but a layer of SiC formed.

As seen in **Figure 4.19**, the Raman spectroscopy of sample 0810 has a strong background noise from ~1700 cm^{-1} up to ~3200 cm^{-1} (**Figure 4.19**). A broad shoulder was found at ~1650 cm^{-1}, which could be assigned as the existence of polycrystalline as well as graphite compositions.[135] The evidence of the presence of diamond composition was found at 1335 cm^{-1}. On the other hand, the silicon characteristic peak was also observed at 521 cm^{-1}. It can be proven that the diamond has been successfully deposited on the silicon wafer. However, the diamond layer was not fully covered on the surface. Some part of the silicon substrate was still exposed.

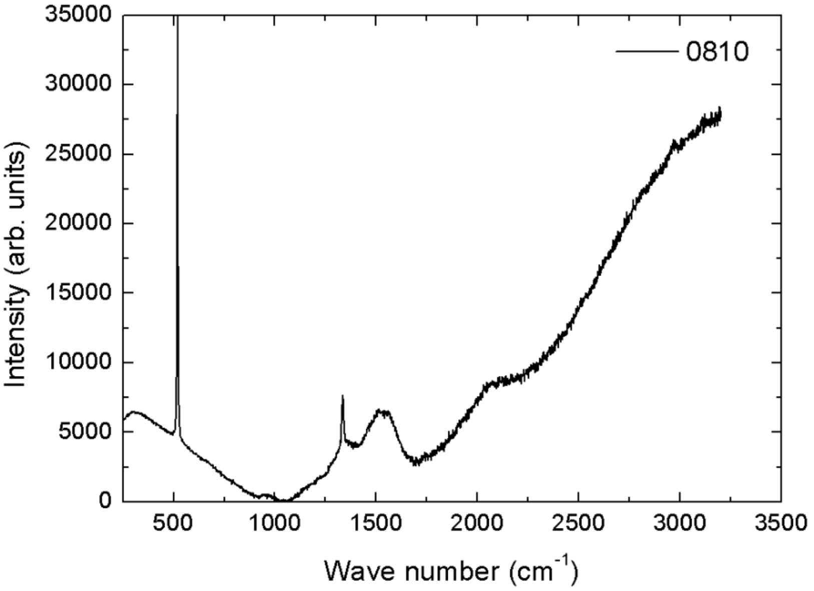

Figure 4.19 Raman spectra of sample 0810

The Raman spectroscopy results of sample 0812 were similar with sample 0810. However, no diamond or carbon characteristic peaks can be observed in the Raman results of sample 0812, 0813 and 0816 which are not shown, but are similar to **Figure 4.18**.

The sample 0818 shows Raman spectra with three peaks of silicon substrates, SiC, and diamond. The broad *G* shoulder was weaker compared to other samples.

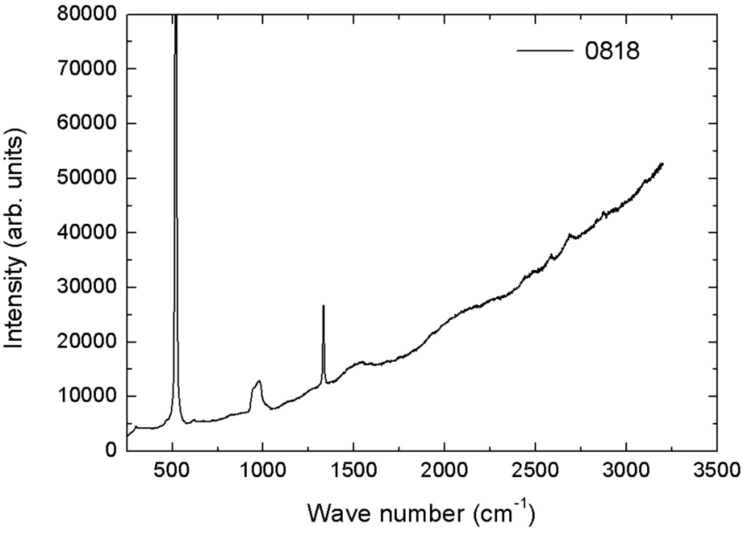

Figure 4.20 Raman spectra of sample 0818

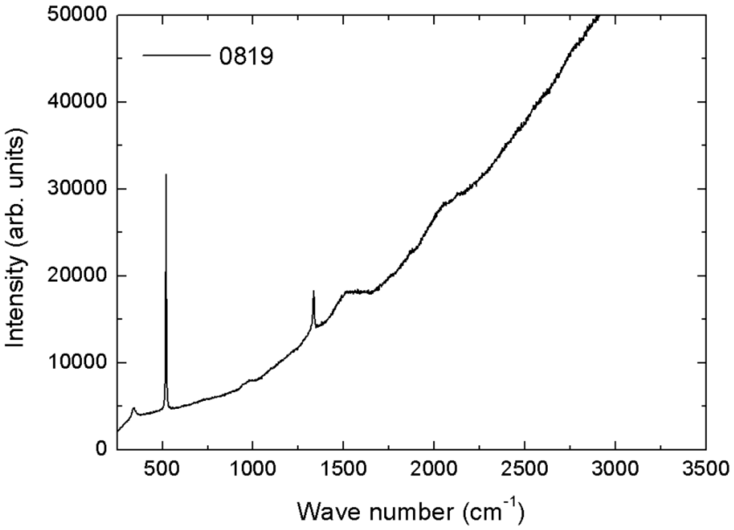

Figure 4.21 Raman spectra of sample 0819

The Raman spectra images of sample 0819 and 0824 were similar, which corresponds to a uniform diamond film. There are only two sharp peaks at 521 cm^{-1} and 1332 cm^{-1}, which indicated that the Raman spectra only contained the information of silicon substrates and diamond layers.

The Raman spectra of sample 0823 have two significant peaks at 521 cm^{-1} and 1333 cm^{-1}. In addition, another three weak shoulders are observed at 1207 cm^{-1}, 2519 cm^{-1} and 2866 cm^{-1}, respectively. The 1207 cm^{-1} was derived from $Si_{1-x}C_x$, as described before. The second-order phonon at 2519 cm^{-1} and 2866 cm^{-1} could be associated with glassy carbon.[136],[137]

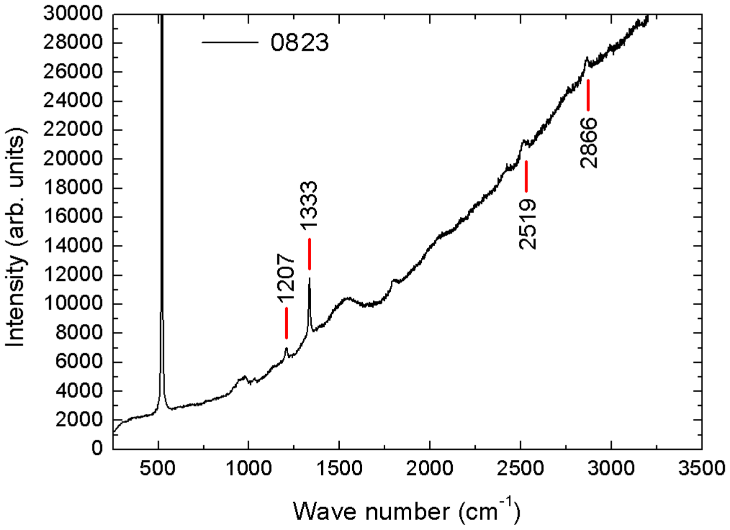

Figure 4.22 Raman spectroscopy of sample 0823.

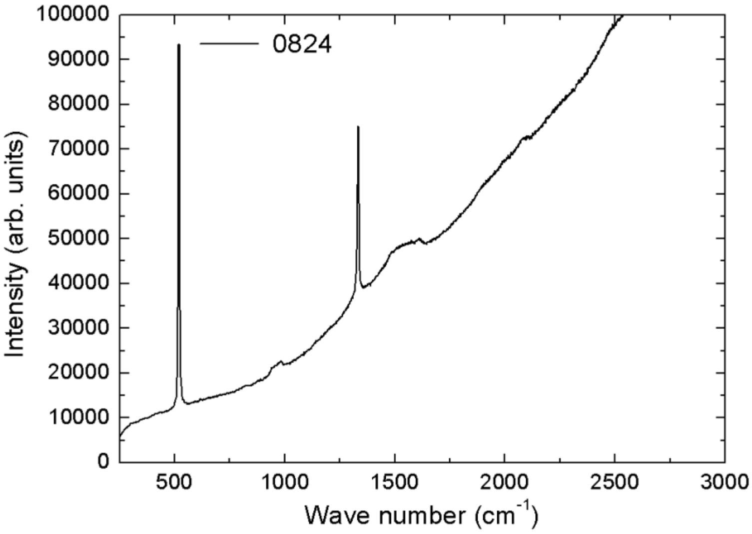

Figure 4.23 Raman spectroscopy of sample 0824.

The SEM and Raman results indicate that a suitable deposition power for Si wafer can be between 950~900 W.

4.2.3 Analysis

To understand the growth mechanism of diamond films on silicon wafers, Stoner, *et al*. utilised XPS to characterise the carbon 1*s* and silicon 2*p* peaks as a function of pre-treatment process.[138] The XPS spectroscopy was used by Riber dual-anode equipped with Mg *Kα* source.

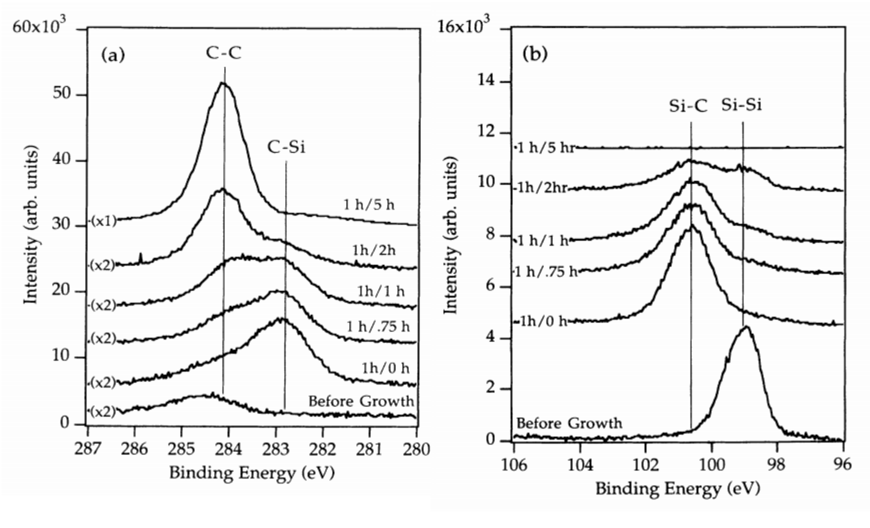

Figure 4.24 XPS analysis of diamond film nucleation on silicon substrate: (a) carbon 1*s* peak progressions; (b) silicon 2*p* peak progressions.[138]

The carbon 1*s* and silicon 2*p* core-level peaks were plotted in **Figure 4.24 (a)** and **(b)**. During the first hour, the percentage of C-Si at 282.8 eV was constant, indicated that carbon was confined at the surface of the silicon surface. After 1.5 hour deposition, the significant C-C peak was found at 284.3 eV. It is suggested that the surface etching started occurring, and formed an interfacial SiC layer. After 2 hours of deposition, the C-C peak took over 90% of all the surface composition. It is the evidence of carbon formation on the silicon surface.

For the silicon species evolution, it was only Si-Si bonding at 99.0 eV before deposition. After 5 mins deposition, the Si-C bonding 100.3 eV became dominant in the spectrum. By 2 hours deposition time, both the Si-Si and Si-C bonding energy decreased, suggesting that the surface had been covered by C-C bonds.

Figure 4.25 XPS analysis of diamond deposition on silicon substrate: (a) carbon 1*s* peak progressions; (b) silicon 2*p* peak progressions.[138]

The XPS spectrum of diamond film deposition versus deposition time after 1 hour nucleation process was demonstrated in **Figure 4.25**. The diamond deposition time was defined as when the nucleation procedure finished. In **Figure 4.25**, the C-Si bonding peak was significant at the beginning. After 2 hours diamond growth, the C-Si was no longer visible and the C-C bonding peak increased. When the deposition time reached 5 hours, there were only C-C peaks in the XPS spectrum. Correspondingly, there was only Si-Si peak before nucleation process, After one hour deposition, the Si-C started to form, which indicated the surface has been covered by Si-C layer. Accompanied with the deposition time, the intensity of Si-C bonding peak decreased, and finally disappeared after 5 hours.

Figure 4.26 The schematic drawing of the diamond evolution process on silicon substrate, contains both the nucleation and growth process.[138]

The schematic drawing of diamond growth and nucleation process is plotted in **Figure 4.26**. The nucleation and growth can be summarised as follows:

(a) Before the deposition process, the surface of silicon substrates contained both amorphous carbon, organic and absorbed oxide species.

(b) Most of the surface organic species were etched away by hydrogen plasma. Meanwhile, some of the oxide species were converted into SiO_2 at the same time.

(c) As the nucleation process continued, the surface SiO_2 was removed and formed a layer of SiC. At this time, some carbon clusters were deposited on the SiC layer.

(d) Clusters start to form sp^3 phase diamond bonds.

(e) As the SiC layer became thicker, more diamond particles are generated at the nucleation site.(so-called “nuclei”)

(f) At the same time of diamond nuclei deposited, the etching process from the hydrogen plasma continues as well. Finally, this evolution reached to a balanced process and the diamond nuclei became to coalesce together. A certain deposition speed of diamond film was confirmed.

In summary, the nucleation process required a relative high carbon flux, which increased the SiC layer deposition speed and created diamond nuclei.

To characterise the diamond growth and crystalline morphology, Wild *et al*.[139] used parameter α to define the different lengths of the [100] and [111] planes, definition the different growth rates of the [100] and [111] planes which could be expressed as:

$$\boldsymbol{\alpha = \sqrt{3}\frac{v_{100}}{v_{111}}} \qquad \textbf{Equation 4.1}$$

Figure 4.27 shows the α-parameter curves and the uniaxial growth by using CH_4 and H_2 source gas.[140] The pressure was 90-140 Torr. In the diagram, the various parameter α was plotted in the CH_4/H_2-T_s plane. Here, the CH_4/H_2 is the effective carbon concentration of the source gas. This diagram illustrated that the parameter α for a specific CVD deposition would determine the shape and the orientation of growth.

Figure 4.27 Diagram of α-parameter, uniaxial growth orientation of MPCVD diamond films.[140]

The cross section profile of diamond deposited film on silicon wafers was characterised by a dual-beam focused ion beam (FIB)/SEM system (FEI dual Beam Strata 235, FEI Company, US). The substrate used to perform FIB milling was sample 0824, which was the best uniform deposition so far. The SEM cross-section image of FIB milled diamond films on silicon wafers is shown on **Figure 4.28**. The surface diamond has been etched by Mg^+ ions beam. It is obvious to observe the boundary between the silicon and diamond layer (red arrows in **Figure 4.28**). A columnar growth of diamond can be clearly visible in the figure. The different colour in SEM image is derived from their difference in material composition and electrical conductivities. This result proves that the columnar growth occurred with diamond facet of fastest growth, and the average size of grains gradually increased with the film thickness.

Previous reports of transmission electron microscopy proven that the thin silicon carbide layer was ~10 nm, while some carbon clusters were formed before the diamond nucleation was deposited.[138] According to the results of diamond deposition on (100) silicon wafer, the orientation of diamond nuclei should be influenced by the substrate crystalline orientation. Besides, ordered chemical bonding is formed across the interface.

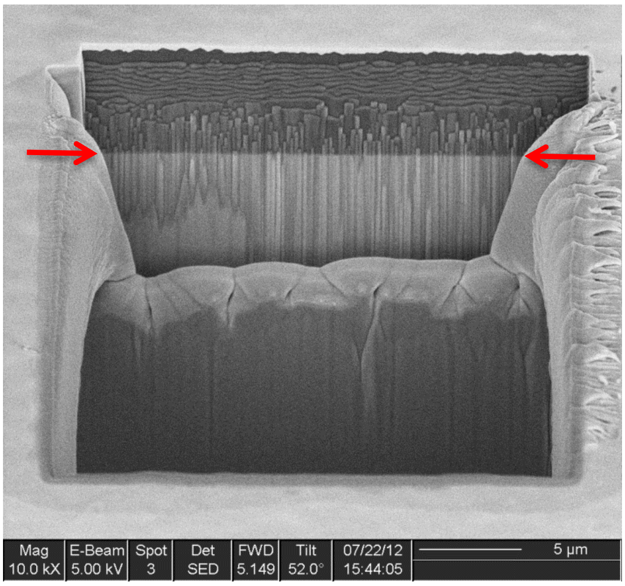

Figure 4.28 Cross-section SEM image of FIB milled diamond film deposited on (100) silicon wafer.

4.2.4 Optimization

The thickness of diamond layer T_{diam} was calculated by the weight increased after deposition (W_{incr}) divided by the density of diamond (ρ_{diam}) and the surface area on silicon wafer (S_{area}), which could be expressed as:

$$\boldsymbol{T_{diam}} = \frac{\boldsymbol{W_{incr}}}{\boldsymbol{\rho_{diamond} . S_{area}}} \qquad \textbf{Equation 4.2}$$

and the relative growth rate is defined as

$$\boldsymbol{P} = \frac{\boldsymbol{W_{incr}}}{\boldsymbol{W_{original}}} . \mathbf{100\%} \qquad \textbf{Equation 4.3}$$

while W_{original} is the weight of Si wafer before diamond deposition. Due to the difference in the shape of the silicon substrate as a result of manual cutting of the substrates, the thickness calculation may not be sufficiently accurate to determine the diamond growth rate. Thus, the relative growth rate seems to become more realistic and reasonable. The relative growth rate was plotted in **Figure 4.29**.

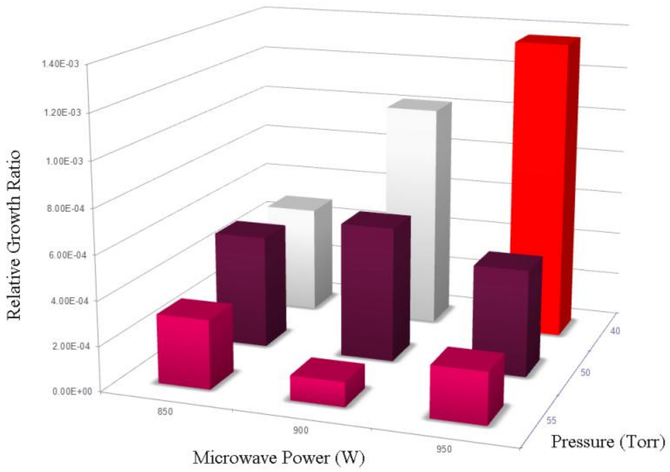

Figure 4.29 Relative growth rate of diamond deposition on silicon (100) wafer with different growth condition.

From **Figure 4.29**, the most suitable deposition condition for our ASTeX^{TM} system was set to 40 Torr with a microwave power of 950 W. Besides, a suitable condition also included the surface film coverage. Based on the previous experimental results, we performed the same deposition process on silicon (100) wafer with the optimised condition. The SEM images were shown in **Figure 4.30**.

In the low magnification (×200) of **Figure 4.30**, a completely uniform diamond random-oriented polycrystalline film was fully covered on the silicon substrate, which proven that the deposition condition was suitable. It is obvious that the diamond nucleations on the surface in ×1,000 magnification image are uniform. In higher magnification images (×40,000, ×65,000), the crystalline grains were clearly presented. Most of them were unperfected crystalline boundaries. However, the stacking crystal planes and uniaxial growth directions were still available, as shown in red labels. The evidence of a uniform random-oriented diamond film indicated an epitaxial SiC film of high quality was formed during the nucleation process.[142]

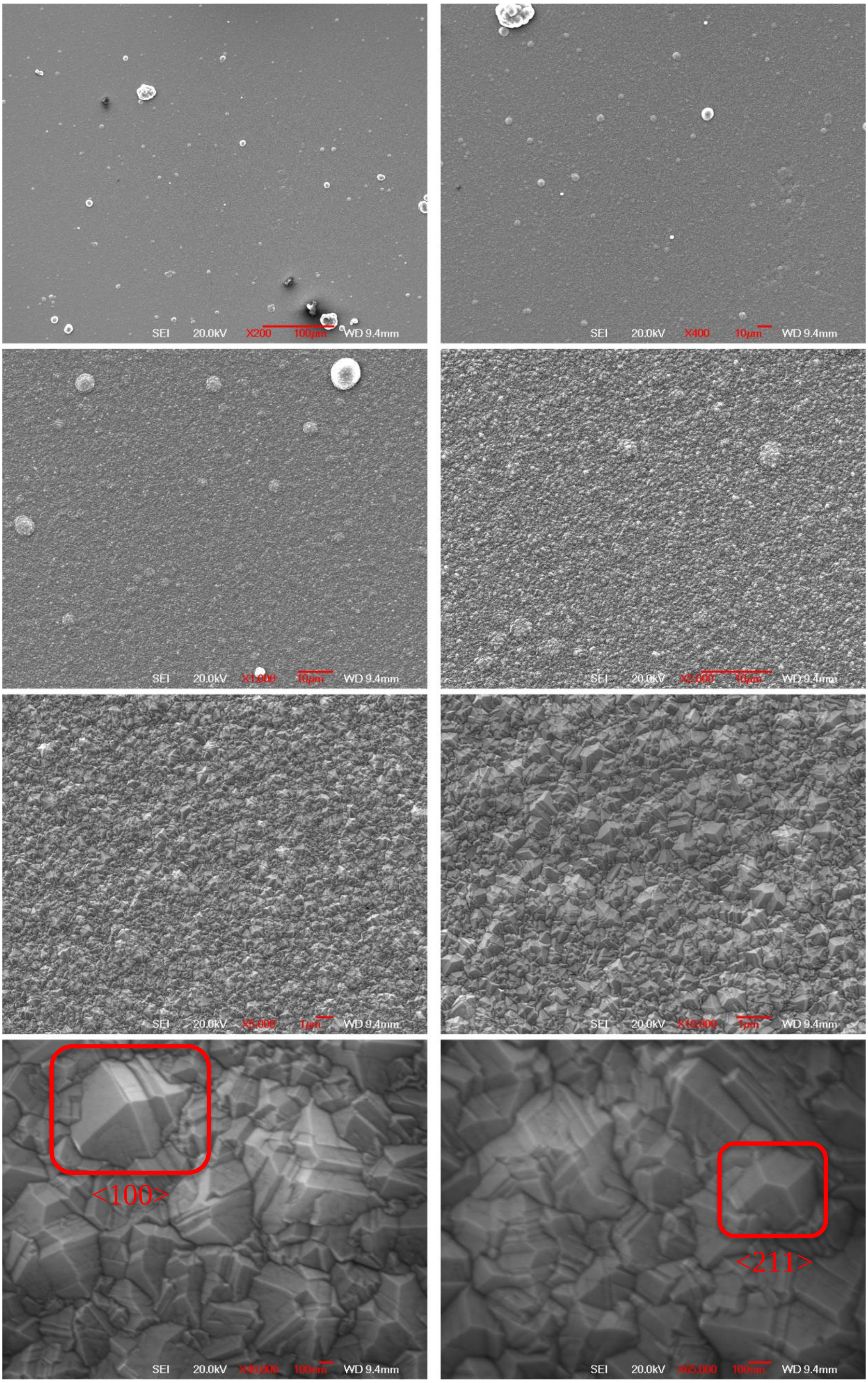

Figure 4.30 SEM images of diamond deposition on silicon wafer after optimization. The <100> direction and <211> direction are labelled in figures, respectively.

4.3 Diamond Deposition on (111) Silicon Wafer

Diamond growth on (111) silicon substrates has been carried out by many researchers.[143] A cubo-octahedral single-crystalline diamond particle with 1.5 μm diameter was observed on silicon wafers. The flow gas consisted of CH_4, H_2 and CO_2. In this research, the diamond deposition on (111) silicon wafer was performed without CO_2 gas source.

The diamond deposition on (111) silicon wafer was similar with the deposition process on the (100) substrate. The pre-treatment surface cleaning and nucleation procedure was as same as the wafer. The deposition condition was set to a 4 sccm/200 sccm methane/hydrogen flow rate. The atmosphere was set to 40 Torr with a microwave power of 950 W. The deposition duration lasted 6 hours and surface deposition was characterised by SEM, as shown in **Figure 4.31~Figure 4.33**.

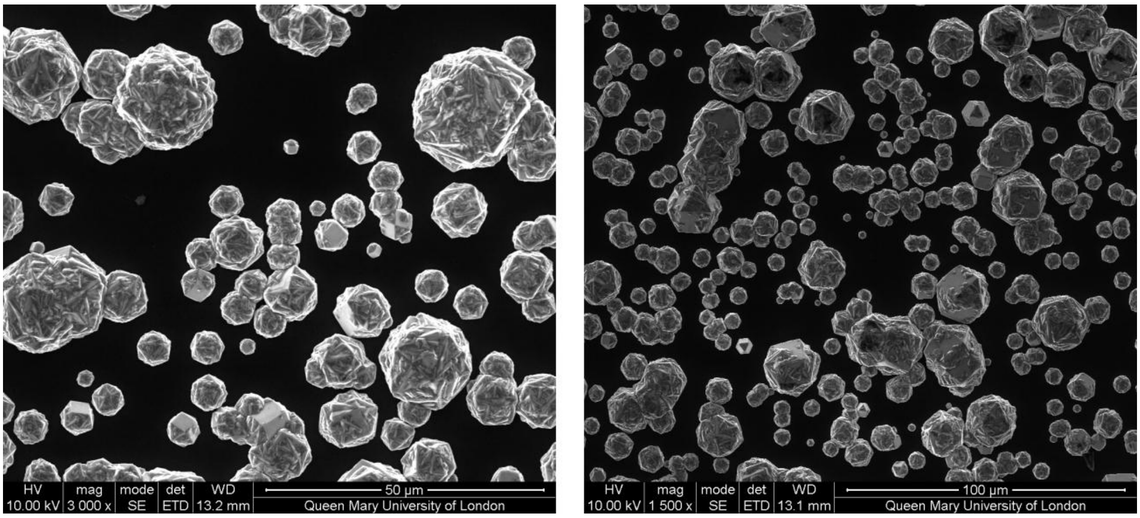

Figure 4.31 Random-oriented diamond particles distributed on (111) silicon wafer.

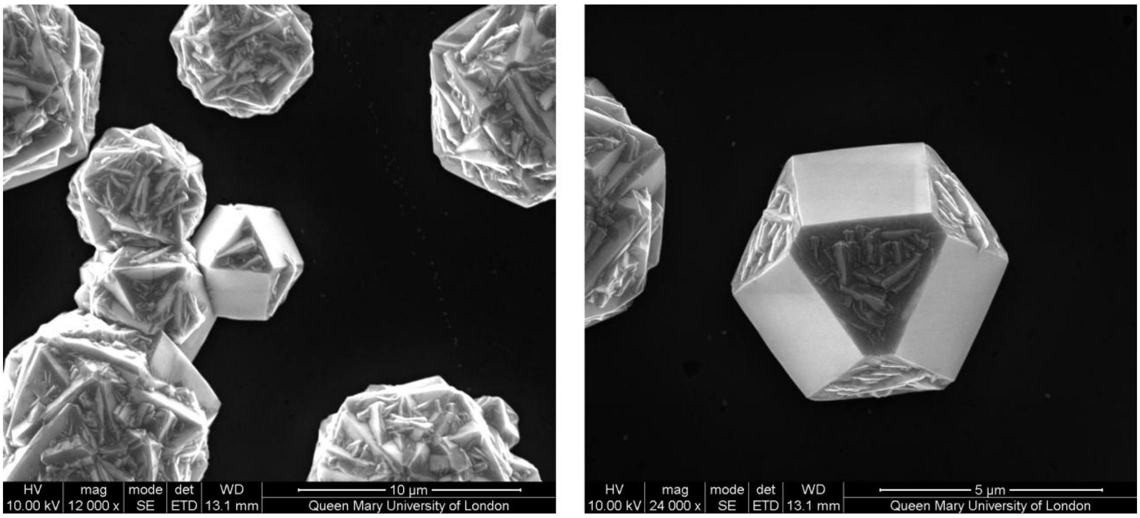

Figure 4.32 (111) plane on individual diamond particles.

Figure 4.31 shows the surface of the (111) silicon wafer, with random-oriented diamond particles. Most of the particles were independent, but some got coalesced. The (111) facets of the crystalline diamond are paralleled to the substrate surface and their [110] edges aligned with the silicon substrates [110] direction.[144] **Figure 4.32** gave a detailed profile of (111) facet of an individual diamond particle. The (100) facets beside the (111) facet were perfect, and the second crystallisation occurred on (111) facet.[141] The growth α-parameter was $3>\alpha>1.5$, approximately.

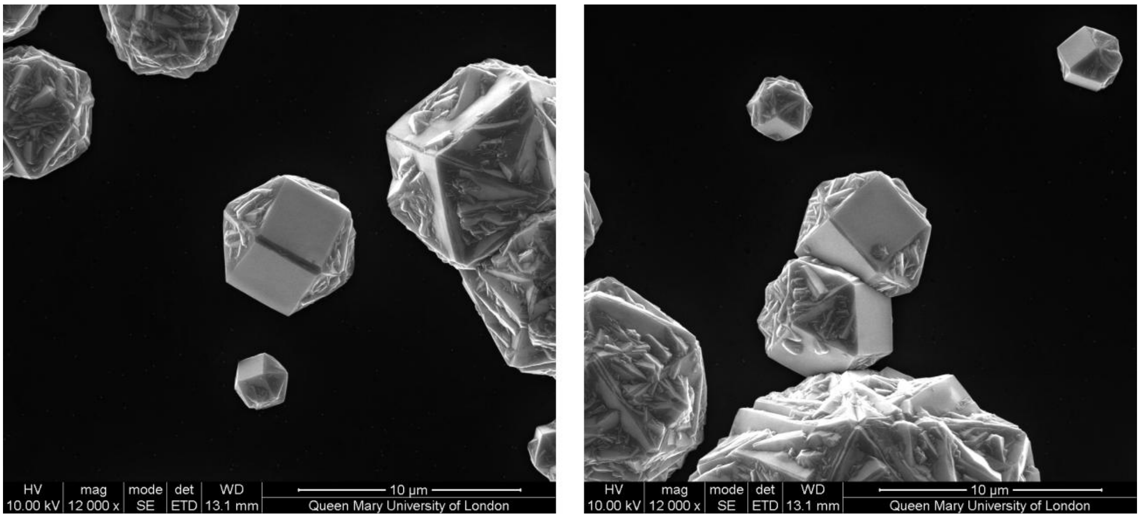

Figure 4.33 (100) planes of individual diamond particles

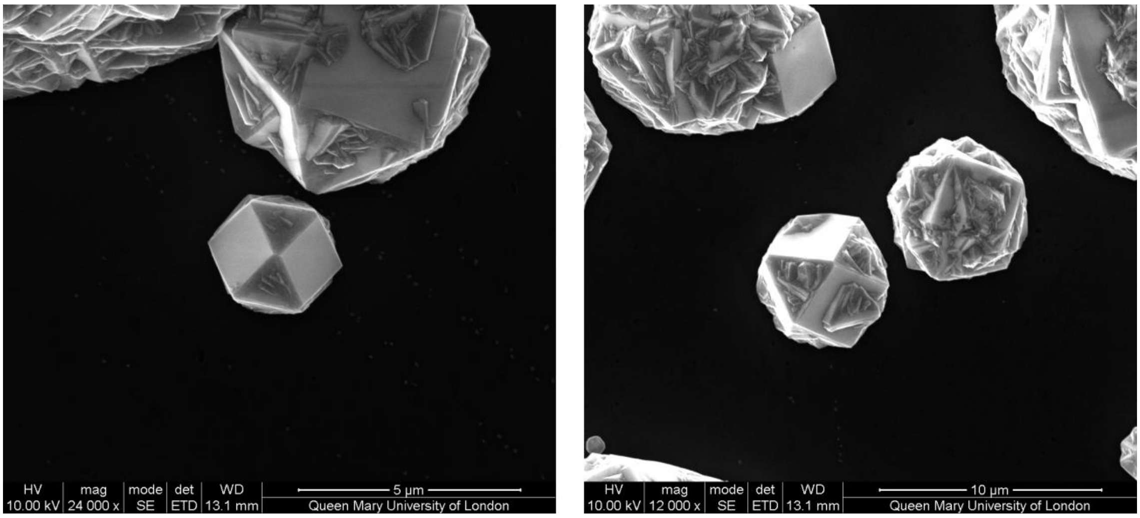

Figure 4.34 (100) planes and secondary crystallisation on this facet.

Two (100) facets on each nanodiamond were presented in **Figure 4.33** and **Figure 4.34**, with $\alpha\approx1.5$. The secondary crystallisation could be clearly observed in the right side of **Figure 4.34**, right hand image. From the previous results, the same deposition condition was also suitable for diamond growth on (111) silicon wafer. To deposit thicker and uniform diamond films, a longer time will be required.

4.4 Diamond Film Growth on DLC Substrates

The diamond also can be deposited on diamond-like carbon (DLC) substrate. The original substrate was M42 tool steel (purchased commercially) with a 1.3 μm interlayer of Chromium/Chromium. The DLC layer was deposited on the top surface with hydrogen terminated treatment. The growth condition for DLC layer was slightly different from the condition on diamond film. The nucleation condition was 20 Torr, 800 W with 100 s.c.c.m total flow rate (10% methane), while the growth condition was 50 Torr, 1,000 W with 100 s.c.c.m total flow rate (2% methane). The duration was 60 mins for nucleation and 240 mins for growth, respectively.

The failed deposition can be attributed to: (1) non-uniform coverage on the top of DLC surface; and (2) warp of Cr_3C_2 layer during the deposition process. To overcome the first one, a longer pre-heating and nucleation time should be required. For the later one, it might be the derived from the temperature difference between the multilayers, which lead to a stress distribution. Thus, a more suitable and controllable temperature during the deposition should be found out and applied.

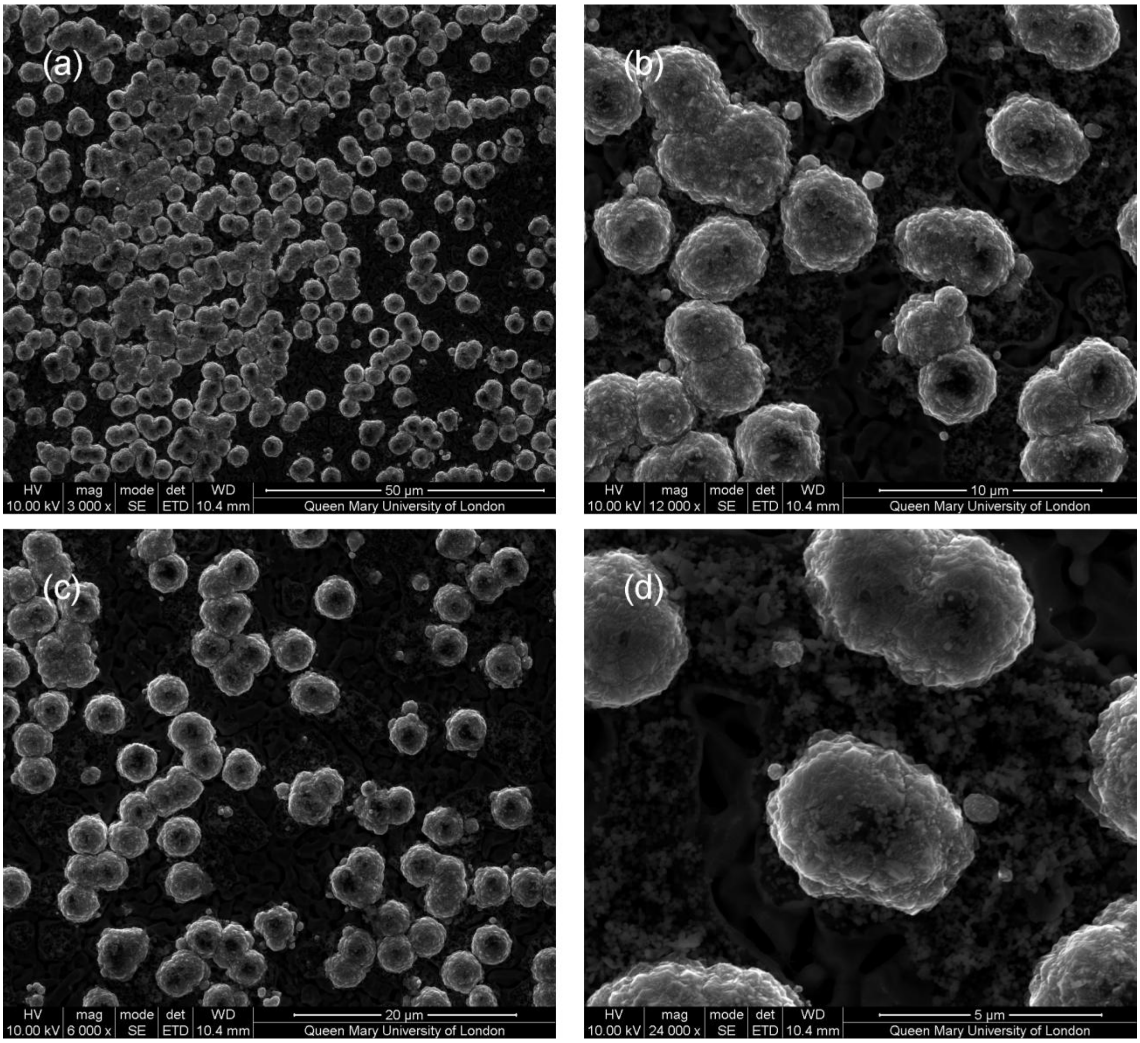

Figure 4.35 Failure diamond deposition on DLC film. The surface coverage was low and diamond particles were separated.

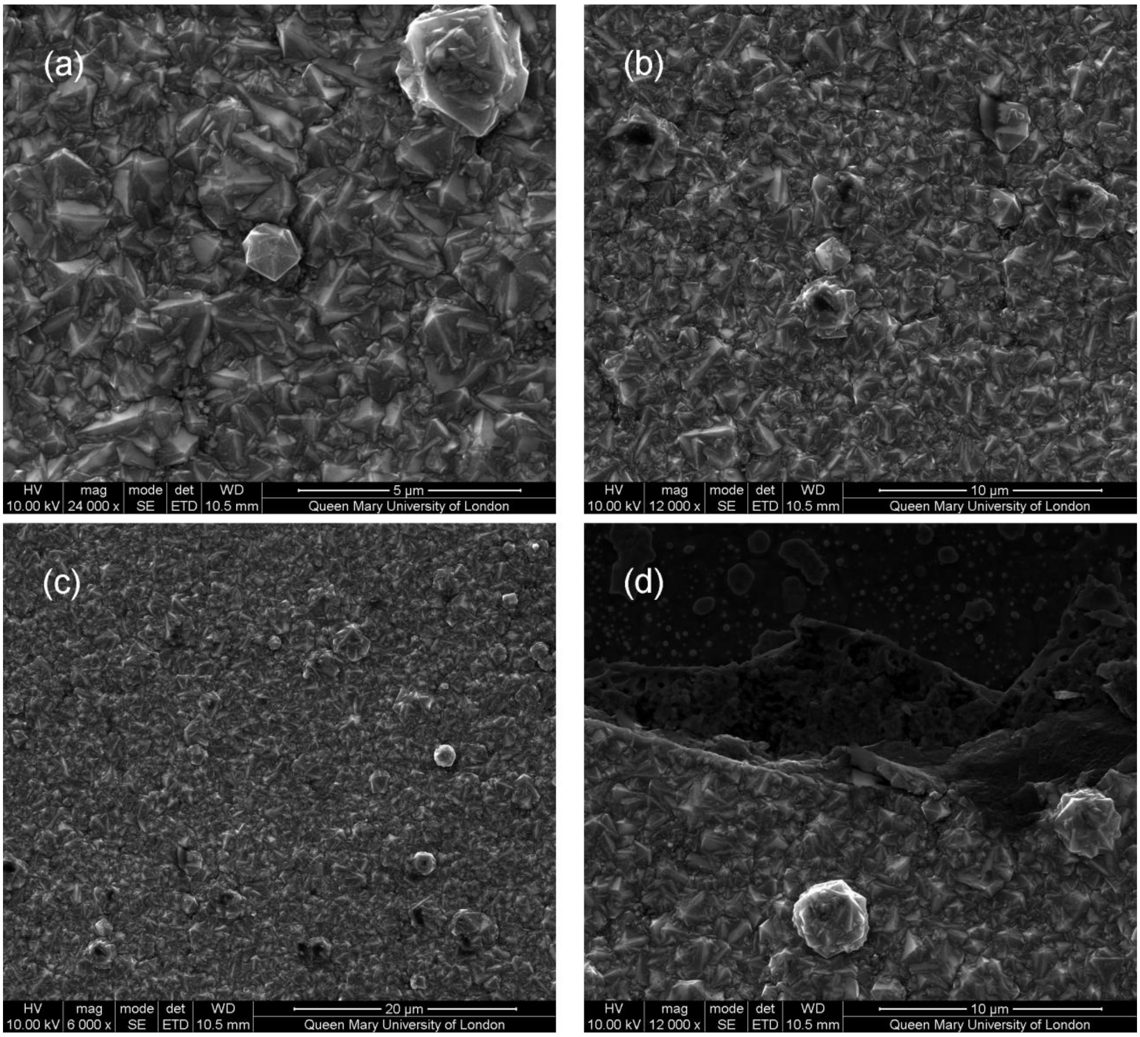

Figure 4.36 Successful diamond film deposition on DLC substrate. Random-oriented and uniform diamond film was observed in SEM images. Figure 4.36 (d) was taken at the edge of sample, where the multiple-layers were obviously detected.

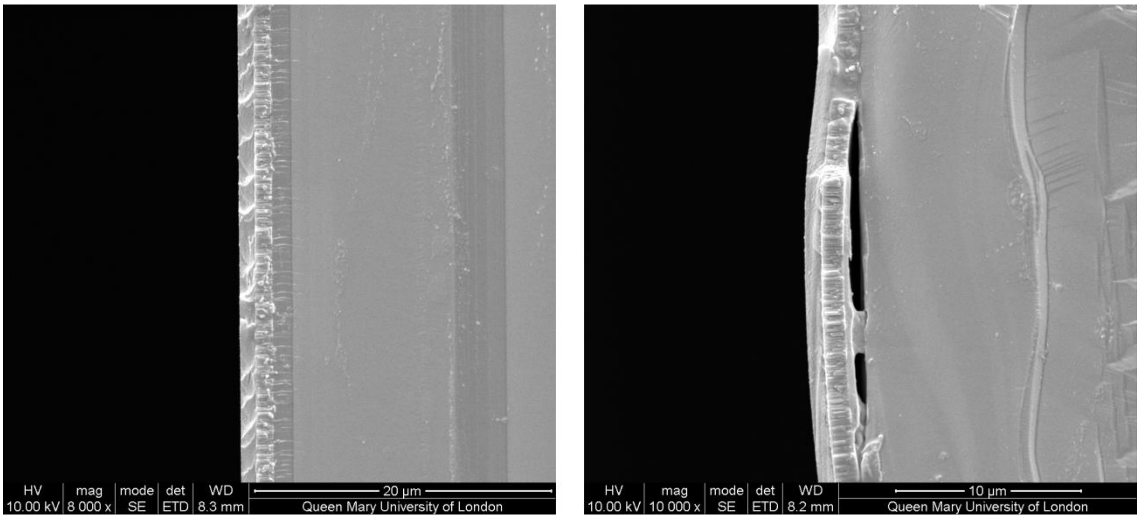

Figure 4.37 Left: cross-section view of successful diamond film deposition on DLC layer. Right: cross-section view of a failed diamond film deposition on DLC layer.

4.5 Diamond Growth on Silica Fibres

The silica fibres were purchased form Photonics group in Aston University.[5] The surface high reflective material coating may provide a research area in laser transmission technology. The diamond growth on silica fibres was performed and the results were shown on **Figure 4.38**. The growth condition was set to 4/200 (methane/hydrogen) s.c.c.m. flow rate, with an atmosphere of 40 Torr and a microwave power of 900W. In **Figure 4.38 (a)**, the cross sectional SEM image view of diamond coated silica fibre was demonstrated. **Figure 4.38 (b)** and **(c)** demonstrated the different interlayers, and a diamond film thickness of ~1 μm could be deduced from the image. **Figure 4.38 (d)** described a broken area on the top of outer diamond film. It is clearly that the boundary between diamond and silica fibre was as its original appearance. **Figure 4.38 (e)** and **(f)** are the top-view images of the diamond coating. It was a uniform deposition with some secondary nucleation.

4.6 Summary

In this chapter, the diamond film deposition was performed using the ASTeX^{TM} 5010 MPECVD system. The growth condition was studied and characterised with SEM and Raman on different substrates. The basic mechanism of diamond deposition was also introduced with silicon wafer. Thus, the optimised condition was found for the future large scale heteroepitaxial deposition. In the following chapters, MPECVD will also be utilised and discussed.

---

[5] This work is a preliminary study for potential collaboration with Aston Institute of Photonics Technologies (AIPT) group.

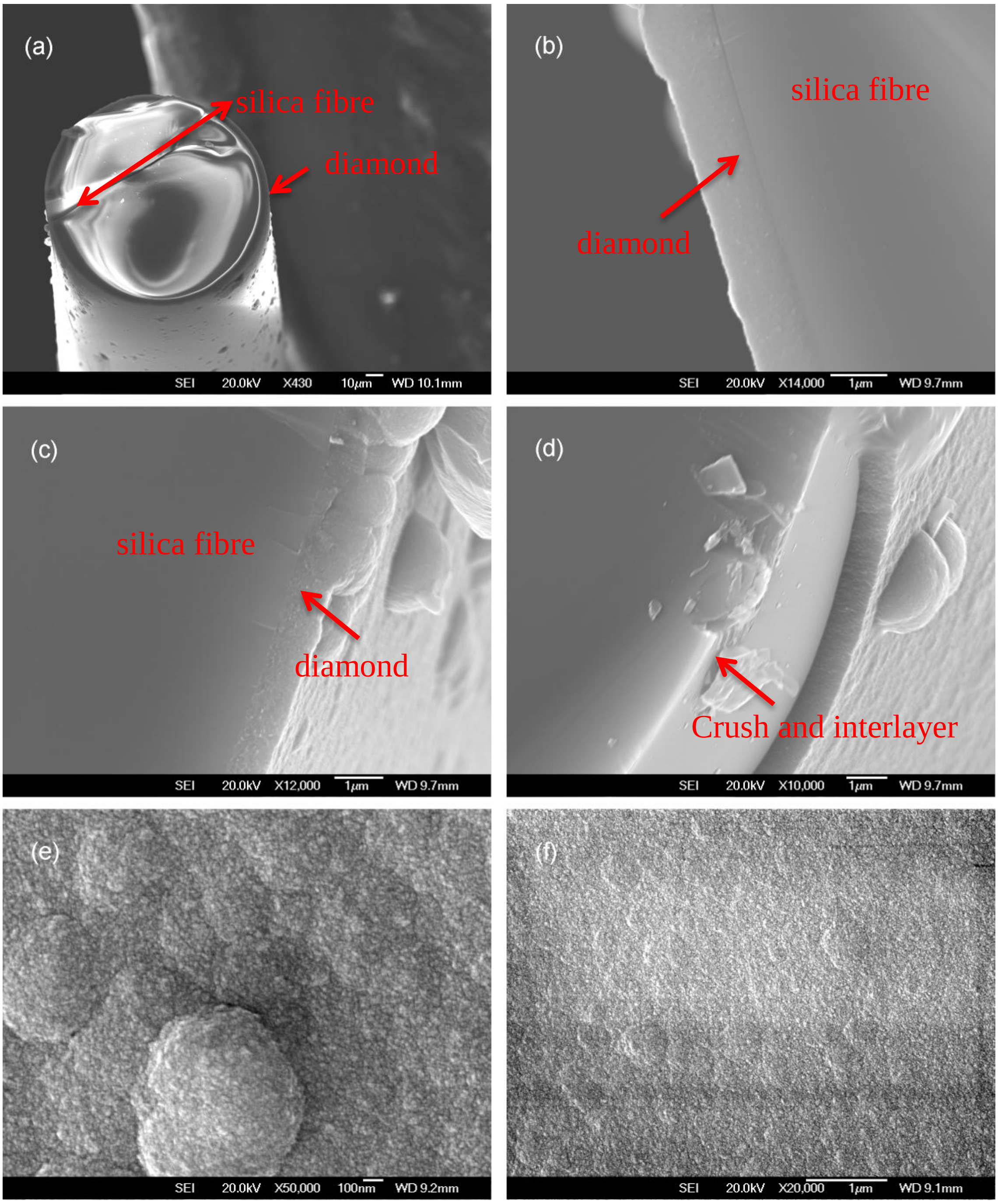

Figure 4.38 Diamond deposition on silica fibre (a)-(d): cross-section SEM images; (e)-(f): top-view SEM images on diamond coated surface.

Chapter 5: Femtosecond Laser Inscription on Single-Crystalline Diamond

Femtosecond Laser Inscription on Single-Crystalline Diamond

5.1 Introduction

Single-crystalline diamond films possess some extremely remarkable properties, such as high mechanical hardness (~100 GPa), highest thermal conductivity (2×10^3 W.m^{-1}.K^{-1}), wide bandgap (5.47 eV), high electric breakdown field (~2×10^7 V.cm^{-1}), high carrier mobility (2,400 cm^2.V^{-1}.s^{-1} for electrons, 2,100 cm^2.V^{-1}.s^{-1} for holes) and chemical inertness, as well as outstanding biocompatibility.[145] The diamond films therefore have been utilized as substrate materials in power devices,[146] cantilever scanning probes,[147] microelectro-mechanical systems (MEMS),[148] and biological/electrochemical electrodes,[149] *etc*. However, little progress on *in-vivo* biocompatible devices has been reported, for the extreme hardness of diamond increases the difficulty of the fabrication of nano/micrometer structures on its surface.[150] Previously, surface modification on diamond substrates was performed by focused ion beam (FIB) technology, which required a relatively longer time (up to hours) to complete the entire fabrication process.[151] Reactive ion etching (RIE) is an alternative method with an inefficient etching rate of ~10 μm.h^{-1} on the diamond surface. For FIB and RIE techniques, both the harsh environmental requirements and diamond crystal lattice has limited their practical applications in addition to their unsatisfactory etching efficiency.[152]

Recently, femtosecond (fs) laser technology has attracted great interest in the scientific and manufacturing communities for its precision and damage-free fabrication capability.[153] The fs-laser technology has enabled the micro-structuring of different materials, including metals, dielectrics as well as semiconductors, for the applications in photonic devices.[154] Furthermore, a number of research groups have carried out the fs-laser inscription on diamond and diamond-like carbon materials. Ozkan *et al.* investigated the periodical ripple patterns after fs-laser irradiation and attributed it as the light reflection from the surface and the laser-generated plasma.[155] M. Shinoda *et al.* applied the fs-laser technology to fabricate ~300 μm long parallelepiped pillar structures on single-crystalline diamond.[156] H. Jeschke *et al*. proposed a non-equilibrium model for transition from diamond to graphitized composition induced by the fs-laser.[157] However, few results related to near-infrared fs-laser inscription on diamond substrates have been reported. In this chapter, we report a three-dimensional microfluidic channel structure, which was fabricated by Yb:YAG 1026 nm femtosecond laser irradiation on a single-crystalline diamond substrate. The femtosecond laser irradiation energy level was optimized at a 100 kHz repetition rate with a sub-500 femtosecond pulse duration. A typical femtosecond laser system and the laser dot focused on diamond sample is shown in **Figure 5.1**.

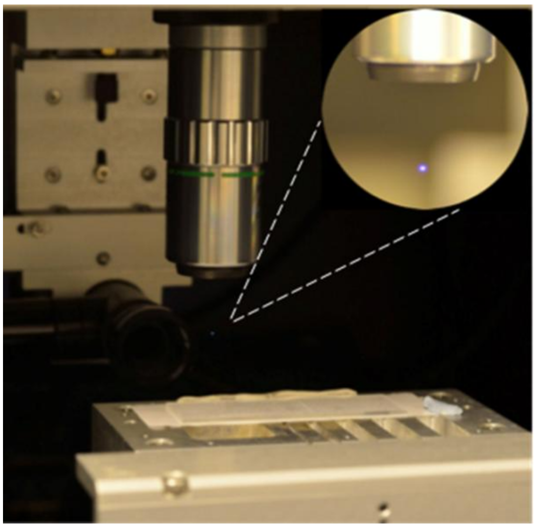

Figure 5.1 Femtosecond laser beam focused through a 20× objective lens. The substrate mounted on a computer controlled air bearing stage.

The morphology and topography of the microfluidic channel were characterized by SEM and AFM. Raman spectroscopy indicated that the irradiated area was covered by a layer of graphitic materials. By comparing the AFM cross-sectional profiles before/after removing the graphitic materials, it could be deduced that the microfluidic channel has an average depth of ~410 nm with periodical ripples which was perpendicular to the irradiation direction. Besides, the graphitic layer thickness was approximately around 200 nm. This work proves the feasibility of using ultra-fast laser inscription technology to fabricate microfluidic channels on biocompatible diamond substrates, which offers a great potential for biomedical sensing applications.

5.2 Experimental

5.2.1 Femtosecond Laser System

The experimental setup of the fs-laser equipment is shown in **Figure 5.2**. Sub-500 fs-laser pulses were generated by a mode-locked Yb:YAG laser system with a center wavelength of 1026 nm (Amplitude System s-Pulse HP) and a repetition rate of 100 kHz. Inscription work was carried out under a 20× objective (Mititoyo MPlan Apo NIR Series) with a numerical aperture of 0.4. The effective laser spot size had an approximate diameter of 2 μm. The fs-laser power was set at 17.5 nJ per pulse. The single-crystalline diamond was secured to a sub-nanometer precision XY air-bearing stage with a mechanical Z-translation (ABL1000, Aerotech) system. The motion of translation stages was controlled through a custom written CNC program. A piece of polished single-crystalline diamond film with a size of 3×3 mm^2 and 0.7 mm thick (Element Six Ltd) was used as the substrate in this experiment. Before the fs-laser irradiation, the diamond was subjected to the process of removing surface contaminations.[150] After finishing surface cleaning process, the diamond substrate was fixed on a flat glass slide for insertion into the fs-inscription system.

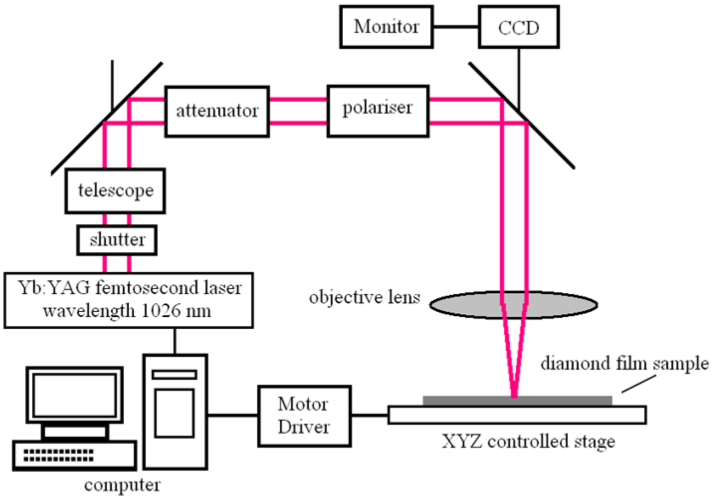

Figure 5.2 Schematic illustration of experimental setup of femtosecond laser inscription system.

5.2.2 Post-procedure

After processing, the diamond substrate was subjected to the following further process: (1) immersion in acetone and isopropanol ultrasonic bath (room temperature, 30 mins for each) to remove organic contamination; (2) boiling in *aqua regia* (70˚C, 2 hours) to remove metallic contamination; (3) boiling in 95% H_2SO_4+ 36% HNO_3 (9:1, 100˚C, 8 hours) to partially remove the graphitic layer generated by the fs-laser.[157][158] Finally, in order to fully remove the residue of the graphitic material, a hydrogen-plasma etching process was performed using a microwave plasma enhanced chemical vapor deposition system (MPECVD, Seki Technotron Corp. ASTeX^{TM} 5010). The hydrogen plasma was ignited by a 2.45 GHz microwave generator at 900 W and maintained for 6 hours, with a diluted hydrogen gas flow rate of 200 s.c.c.m under 50 Torr pressure.

5.2.3 Characterisation Equipment

A Raman spectrometer (Nicolet Almega XR dispersive type, 785 nm, Thermo Ltd) equipped with an optical microscope (Olympus TE-Si CCD), was used to observe and locate the graphitic area.

The topography of the fs-laser induced pattern was characterised by a contact mode AFM (Autoprobe M5, Park Scientific Instrument) with a scanning area of 100×100 μm^2.

The X-ray photoelectron spectra were recorded by a Thermofisher ESCALAB 250 X-ray Photoelectron Spectrometer equipped with a hemispherical sector energy analyser. A monochromated Al Kα X-ray source (1486.5 eV) was used to analyse the resolution. It found the at source excitation energy is 10 kV, the emission current is 15 mA and the analyser pass energy of 80 eV with step size of 0.1 eV were used throughout the experiments.

The SEM images were collected by FEI phenom SEM system and CFEI Quanta 3D FEG FIB-SEM system.

The AFM data was collected by Autoprobe M5 from Park Scientific Instruments. A total area of 100×100 µm of each pattern was analysed subjected to fs-laser inscription.

5.3 Characterisation and Results

5.3.1 Topography

After the fs laser exposure, the patterns on the diamond sample were visually inspected using an optical microscope (Olympus BX41, 20× lens). Zigzag patterns, cross-finger patterns and fully graphitized rectangle blocks are demonstrated in **Figure 5.3**.

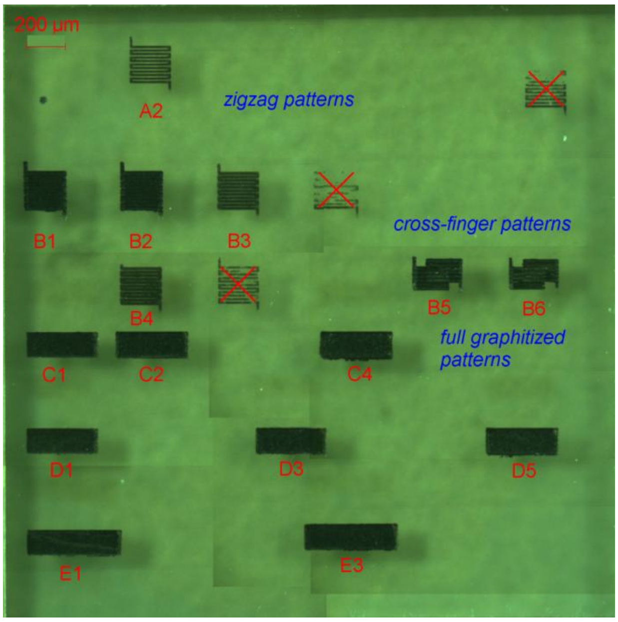

Figure 5.3 Overview optical image of micro-channel structures fabricated on single crystalline diamond substrate. Each pattern was processed using different parameters.

The fs laser patterning parameters are shown in **Table 5.1**. Each pattern took less than 1 min to write. The zigzag pattern was designed to demonstrate the type of intricate 3-D structures that can be fabricated using this approach. The rectangle block pattern was specifically designed so that a large area on the diamond substrate was processed by the fs-laser to enable SEM, Raman spectroscopy and XPS analysis to be carried out with greater efficiency.

Table 5.1 fs-laser processing parameters for each pattern

Pattern information			Laser Parameters
Pattern ID	Pattern Type	Pattern size (μm)	Energy per pulse (μJ)
A2	Zigzag	200×200	17.5
B1	Zigzag	200×200	35.0
B2	Zigzag	200×200	31.5
B3	Zigzag	200×200	28.0
B4	Zigzag	200×200	24.5
B5	Cross-finger	300×200	21.0
B6	Cross-finger	300×200	17.5
C1	Rectangle	360×120	17.5
C2	Rectangle	360×120	21.0
C4	Rectangle	360×120	28.0
D1	Rectangle	360×120	17.5
D3	Rectangle	360×120	21.0
D5	Rectangle	360×120	24.5
E1	Rectangle	480×120	17.5
E3	Rectangle	480×120	21.0

5.3.2 SEM Images

The topological images of the fs-laser inscribed zigzag patterns before post-procedure are demonstrated from **Figure 5.4** to **Figure 5.8**. The fs-laser inscribed cross finger patterns are shown in **Figure 5.9** and **Figure 5.10**. Finally, the fully graphitization fs-laser inscribed rectangle pattern is shown in **Figure 5.11**.

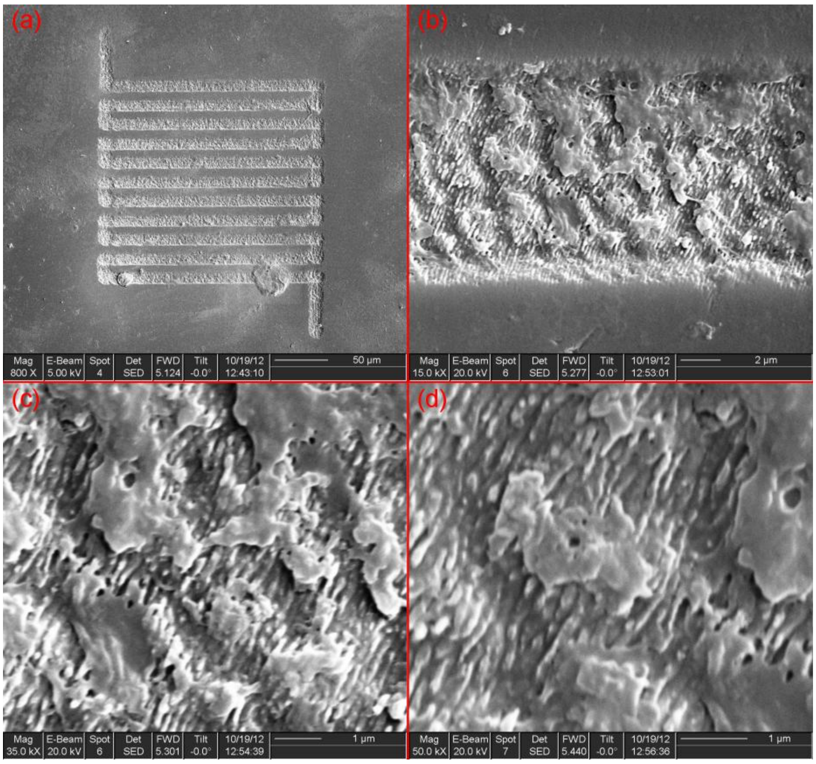

Figure 5.4 SEM images fs-inscribed zigzag pattern on diamond substrate (A2).

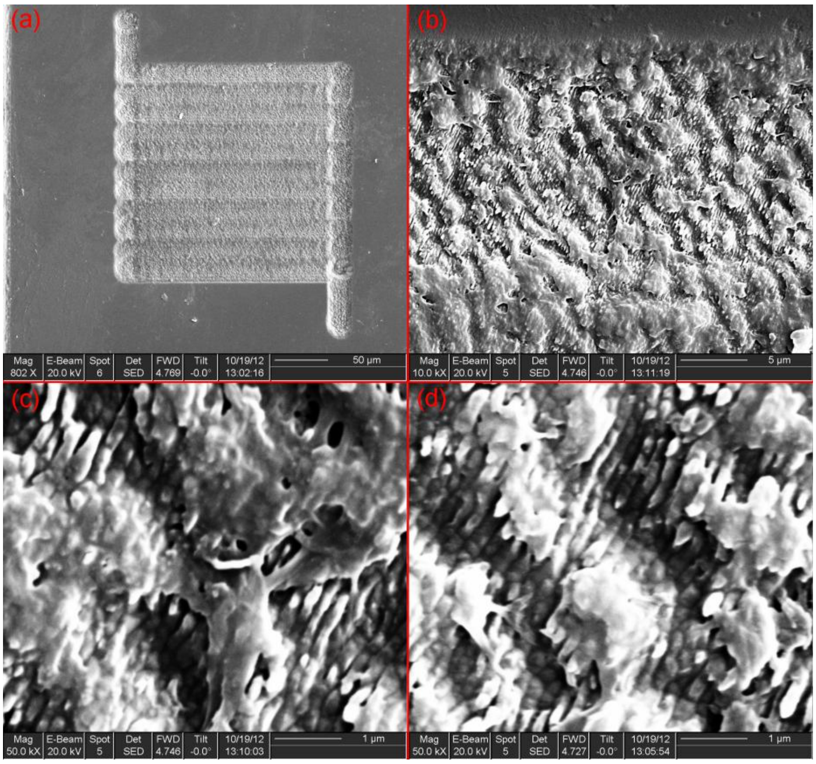

Figure 5.5 SEM images fs-inscribed zigzag pattern on diamond substrate (B1).

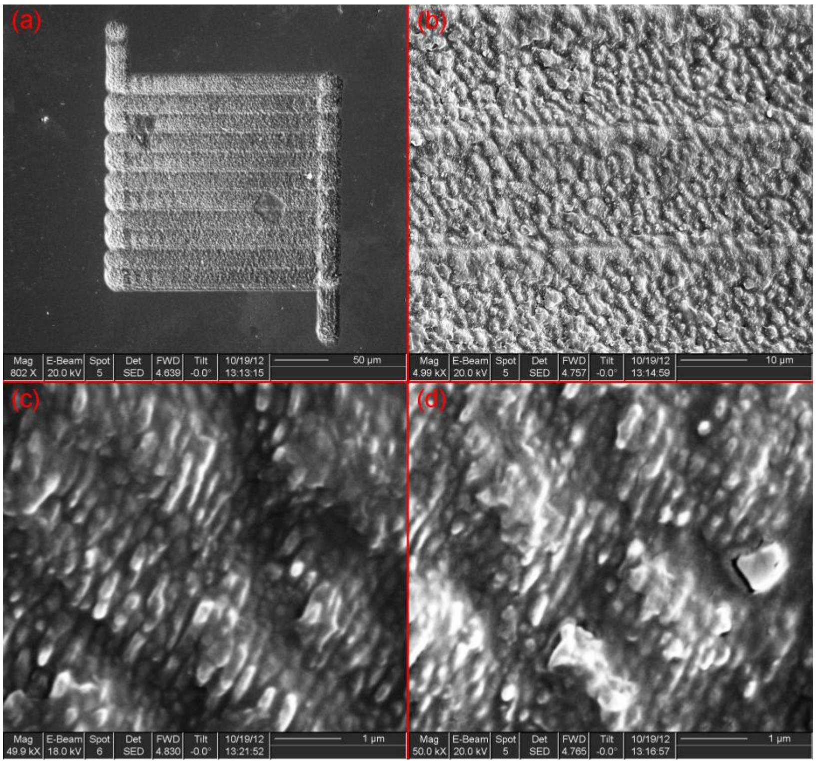

Figure 5.6 SEM images fs-inscribed zigzag pattern on diamond substrate (B2).

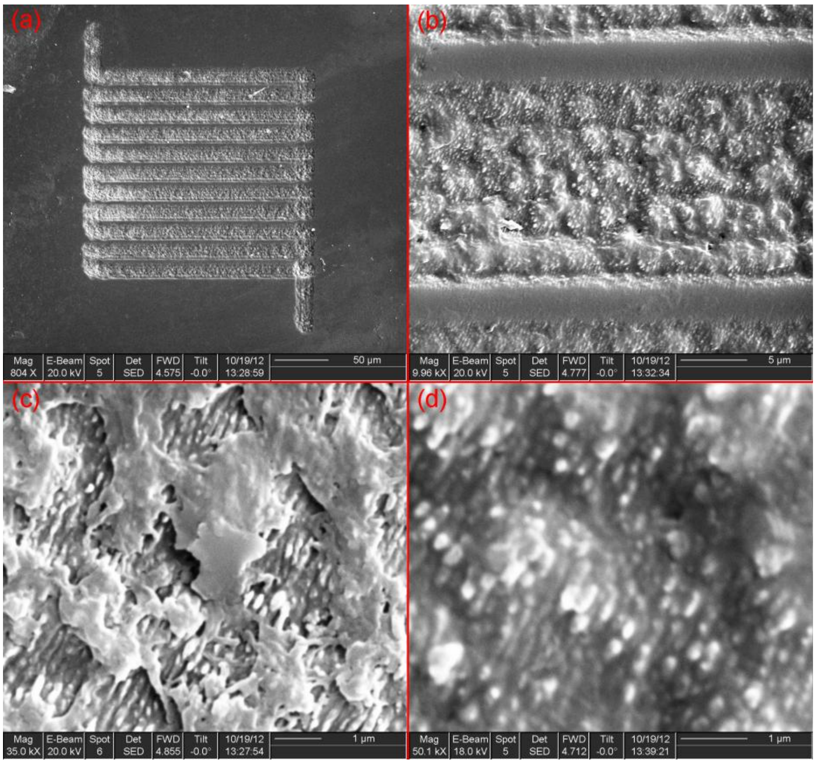

Figure 5.7 SEM images fs-inscribed zigzag pattern on diamond substrate (B3).

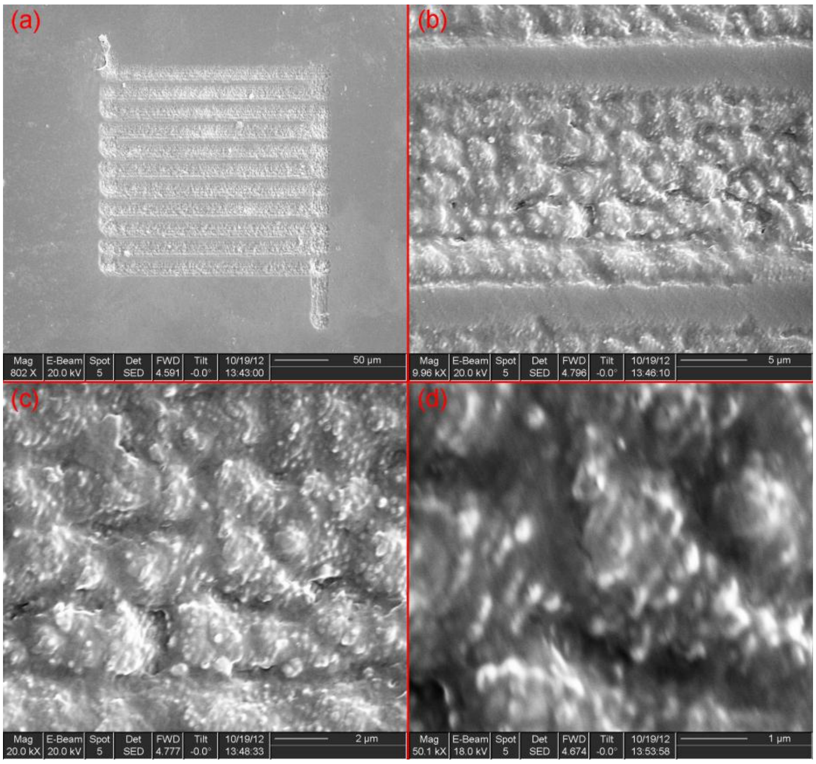

Figure 5.8 SEM images fs-inscribed zigzag pattern on diamond substrate (B4).

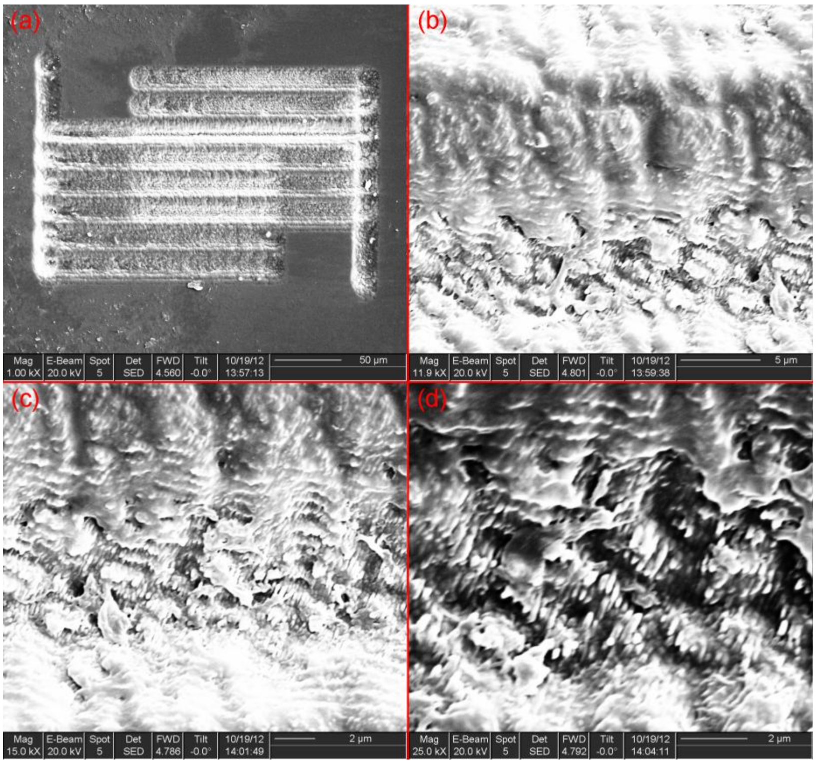

Figure 5.9 SEM images fs-inscribed cross-finger pattern on diamond substrate (B5).

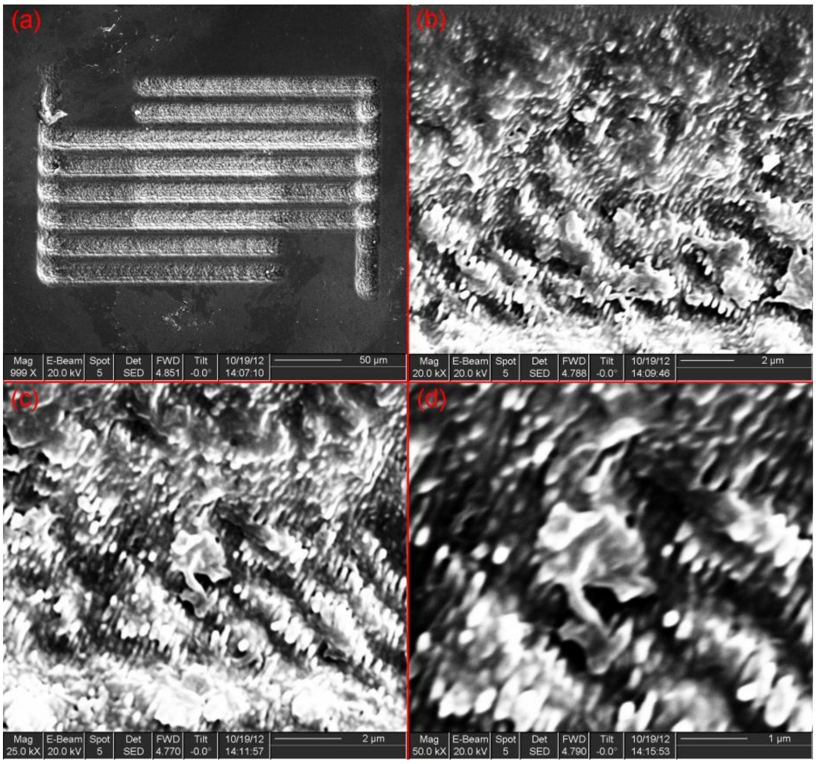

Figure 5.10 SEM images fs-inscribed cross-finger pattern on diamond substrate (B6).

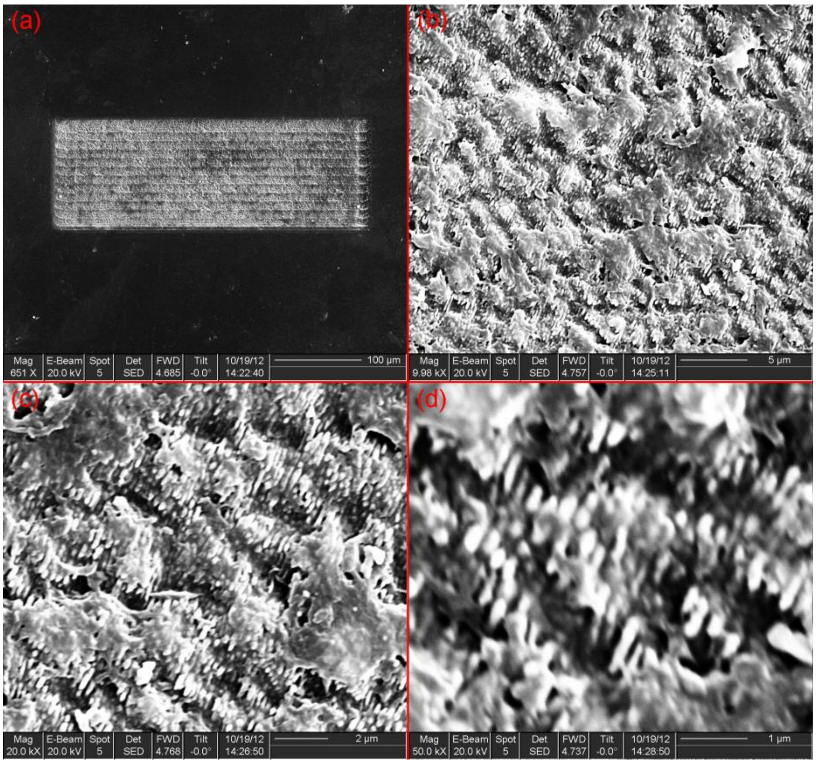

Figure 5.11 SEM images fs-inscribed cross-finger pattern on diamond substrate (C1).

In order to make a comparison before and after the graphitic layer was removed, the SEM images after post-procedure removing the surface graphitic materials are shown on **Figure 5.12** to **Figure 5.19**.

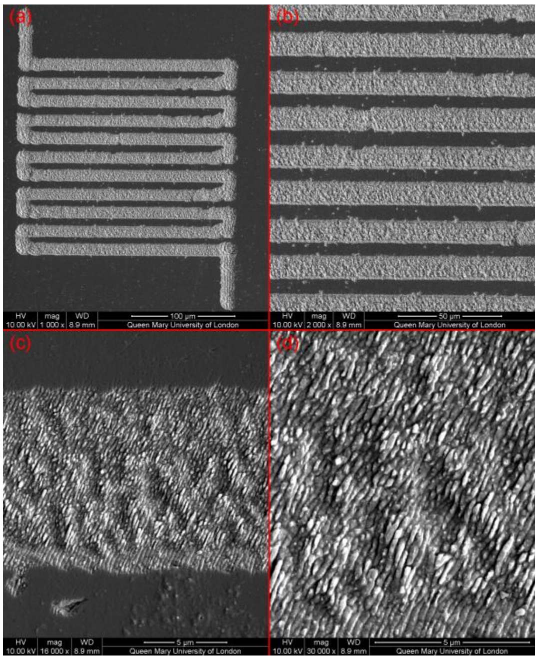

Figure 5.12 SEM image of fs-laser inscribed pattern (A2) after removing graphitic layer.

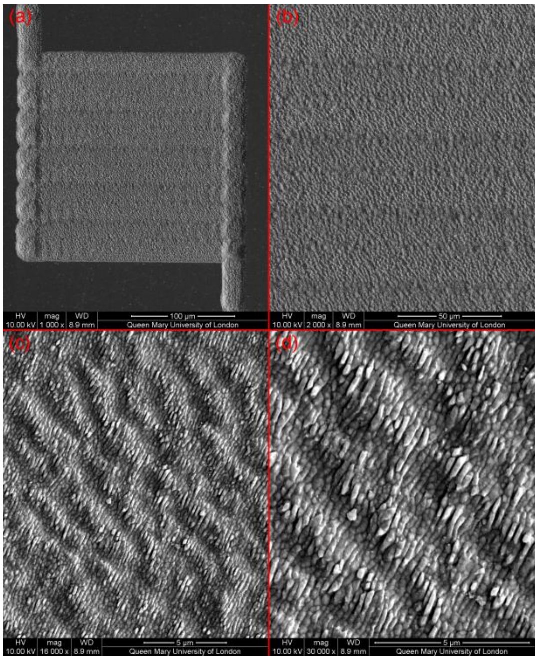

Figure 5.13 SEM image of fs-laser inscribed pattern (B1) after removing graphitic layer.

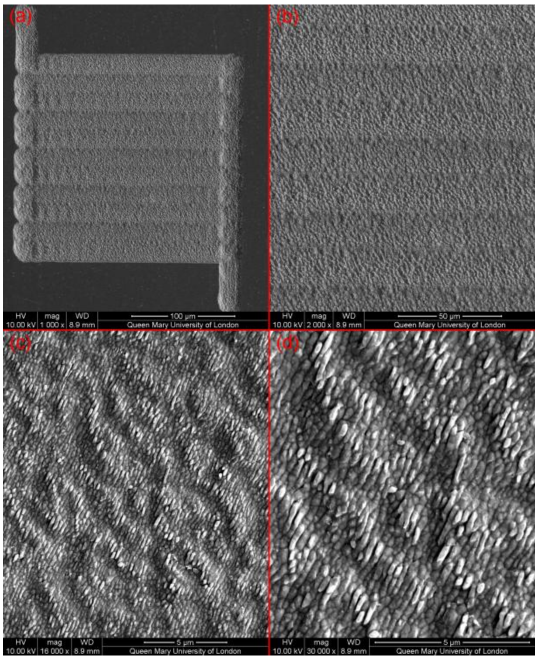

Figure 5.14 SEM image of fs-laser inscribed pattern (B2) after removing graphitic layer.

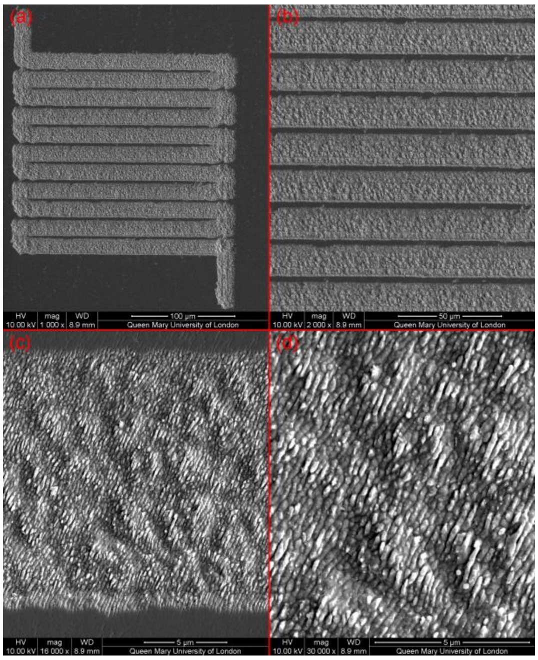

Figure 5.15 SEM image of fs-laser inscribed pattern (B3) after removing graphitic layer.

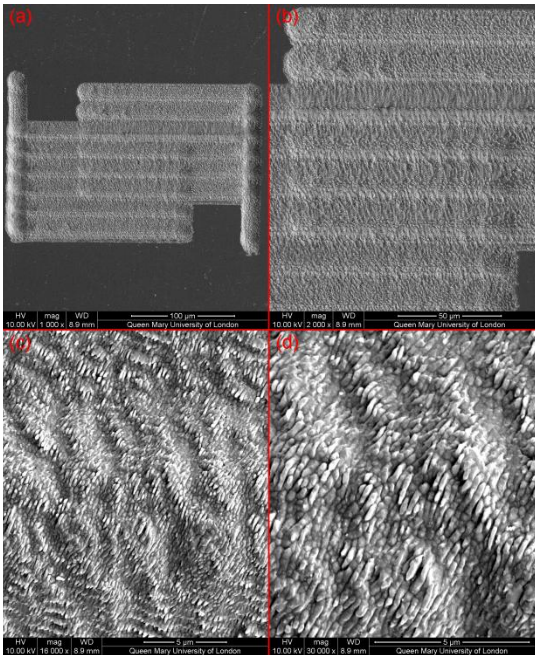

Figure 5.16 SEM image of fs-laser inscribed pattern (B4) after removing graphitic layer.

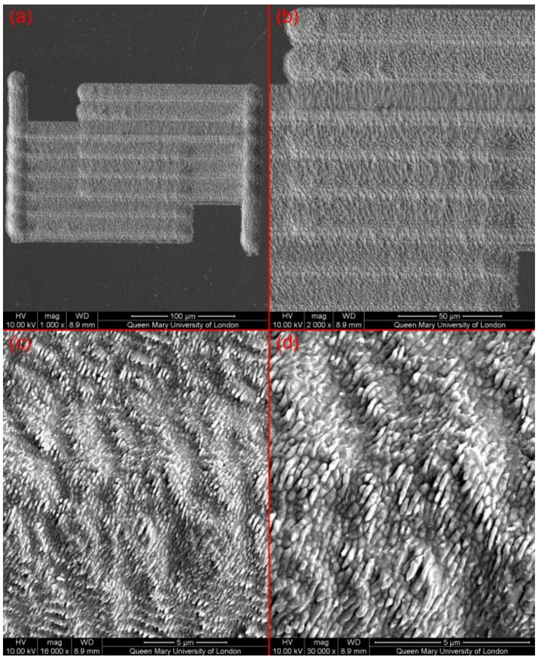

Figure 5.17 SEM image of fs-laser inscribed pattern (B5) after removing graphitic layer.

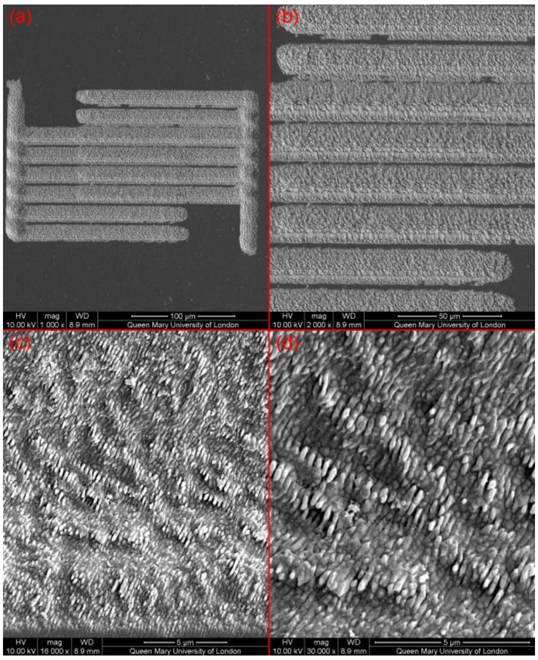

Figure 5.18 SEM image of fs-laser inscribed pattern (B6) after removing graphitic layer.

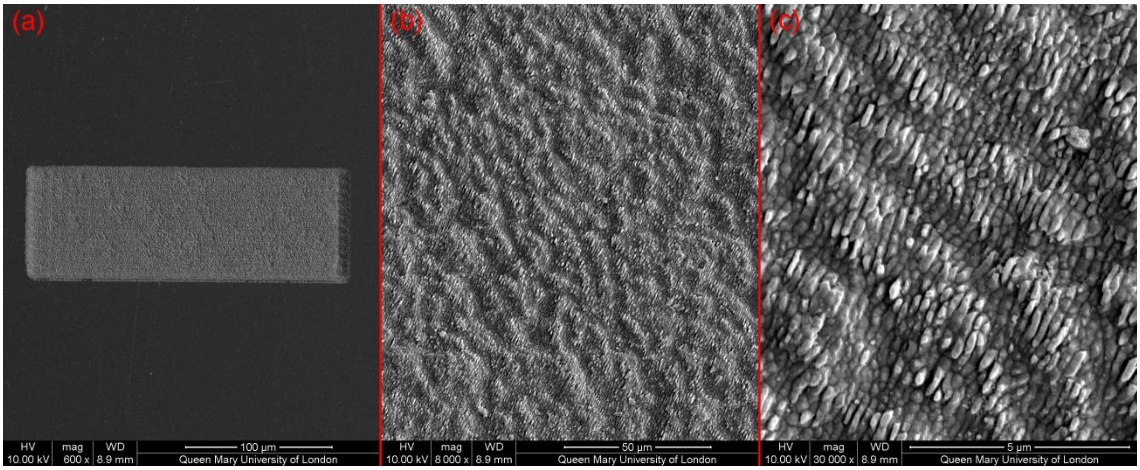

Figure 5.19 SEM image of fs-laser inscribed pattern (C1) after removing graphitic layer.

5.3.3 Raman Spectroscopy

The Raman spectra collected from diamond substrate without irradiation is shown in **Figure 5.20**. The Raman spectra of fs-laser inscribed patterns on diamond substrate before and after removing surface graphitic layer are shown in **Figure 5.21** to **Figure 5.28**.

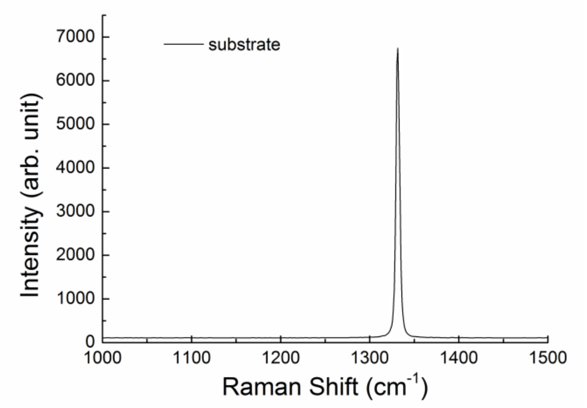

Figure 5.20 Raman spectra of diamond substrate without inscription.

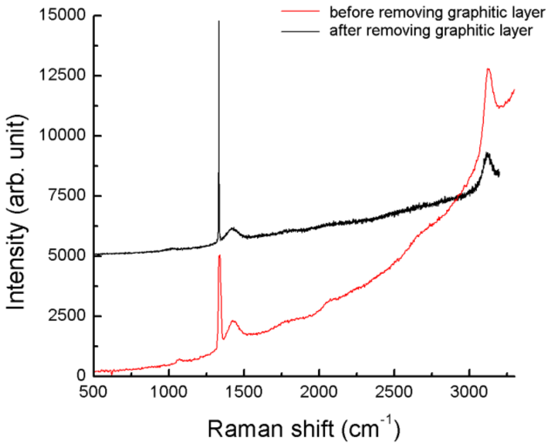

Figure 5.21 Raman spectra of fs-laser inscribed pattern A2.

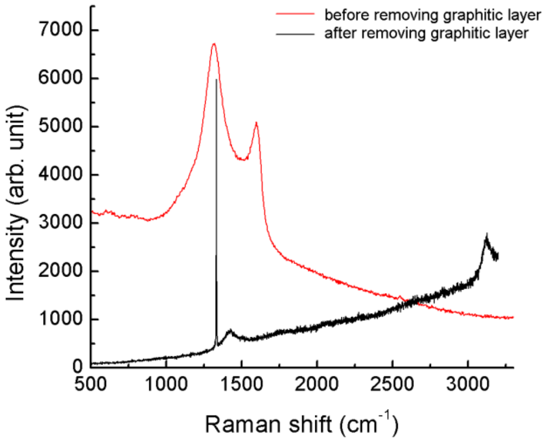

Figure 5.22 Raman spectra of fs-laser inscribed pattern B1.

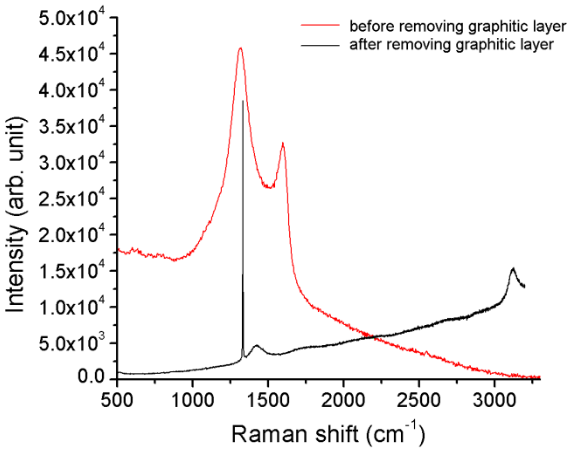

Figure 5.23 Raman spectra of fs-laser inscribed pattern B2.

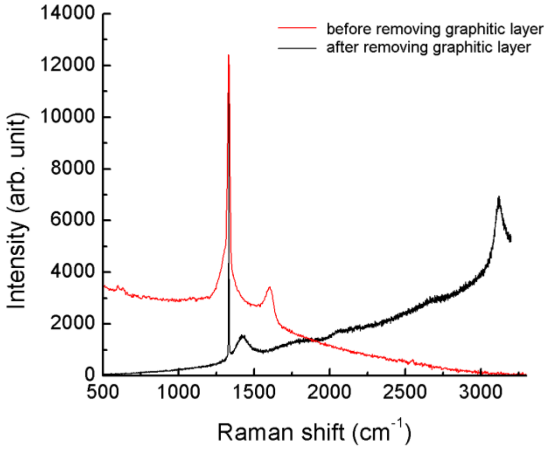

Figure 5.24 Raman spectra of fs-laser inscribed pattern B3.

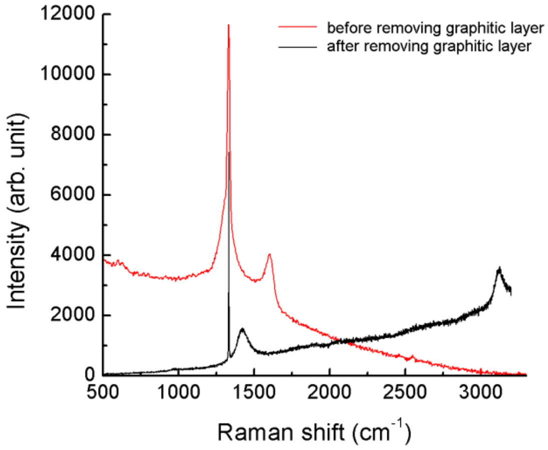

Figure 5.25 Raman spectra of fs-laser inscribed pattern B4.

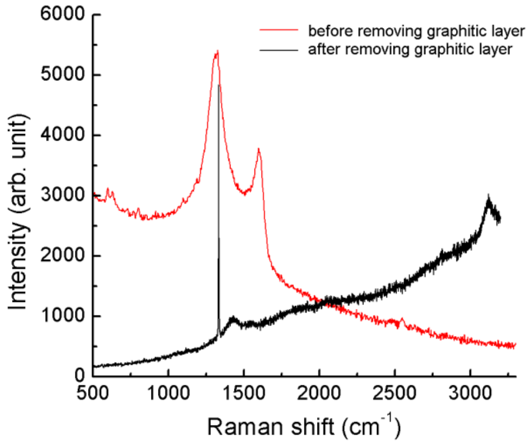

Figure 5.26 Raman spectra of fs-laser inscribed pattern B5.

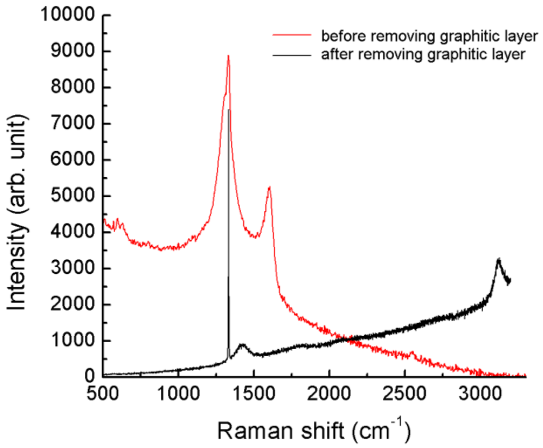

Figure 5.27 Raman spectra of fs-laser inscribed pattern B6.

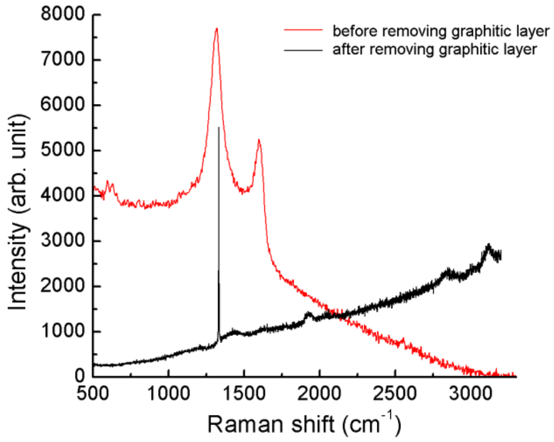

Figure 5.28 Raman spectra of fs-laser inscribed pattern C1.

5.3.4 X-ray Photoelectron Spectroscopy

The XPS measurement was performed on substrates A2, B1, B2, B3, B5, B6, and C1, which was focused on a spot with 120 μm diameter. A total of seven scans were collected from the sample. The binding energy levels are plotted on the X-axis, while Y-axis represents the signal intensity collected by the detector. The quantitative counts do not represent the amount of each element on the surface. It is only a relative signal collected from the photoelectron spectroscopy.

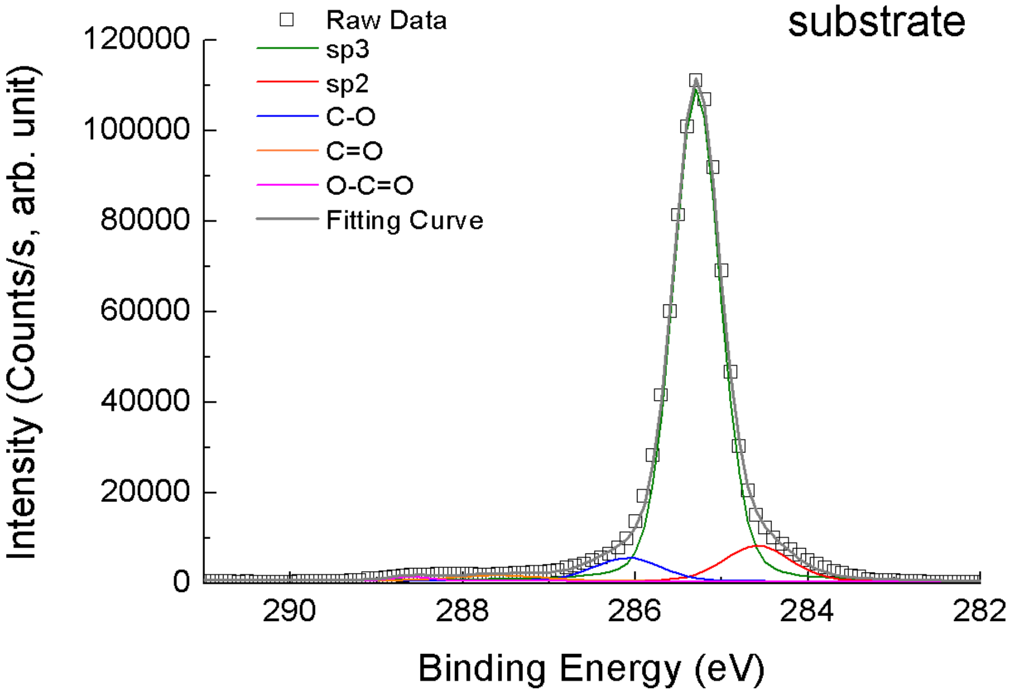

Figure 5.29 XPS spectra of diamond film substrate without fs-laser irradiation.

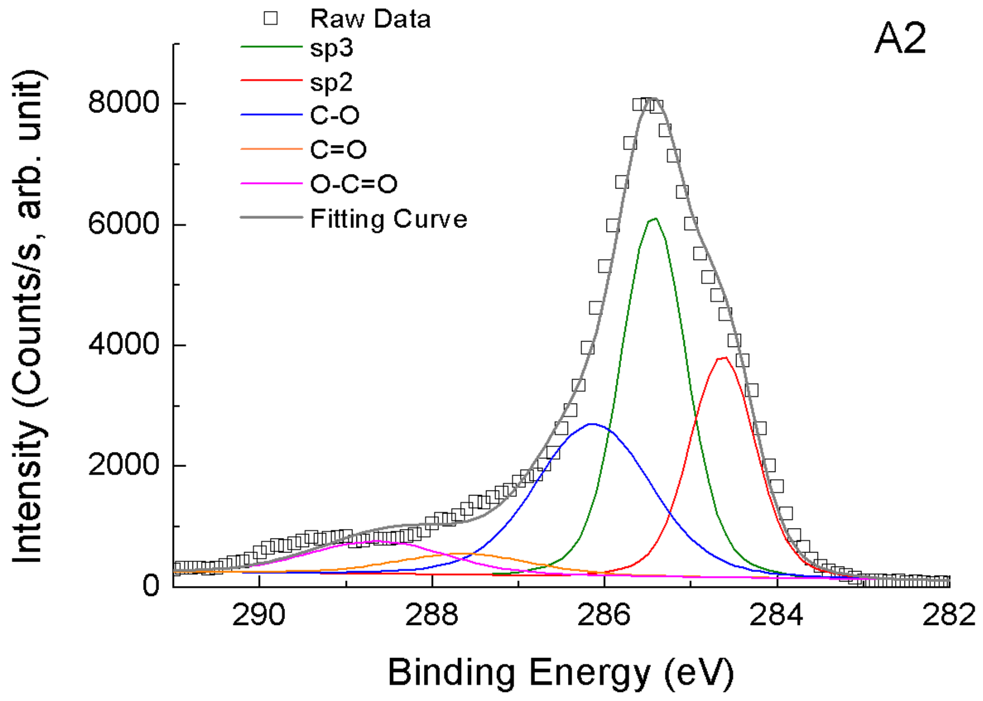

Figure 5.30 XPS spectra of pattern A2.

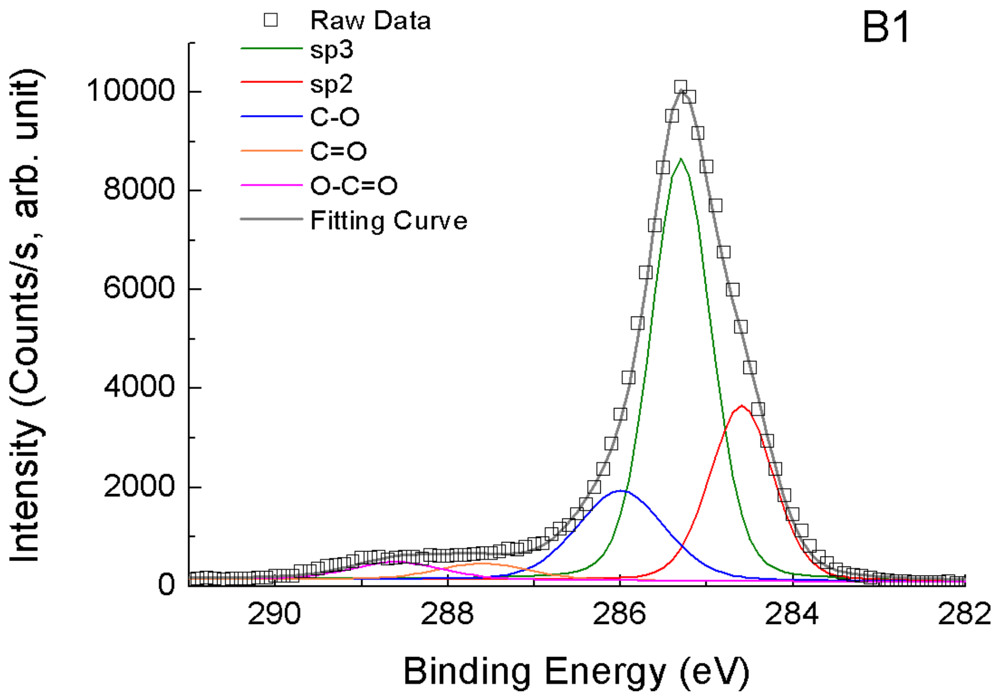

Figure 5.31 XPS spectra of pattern B1.

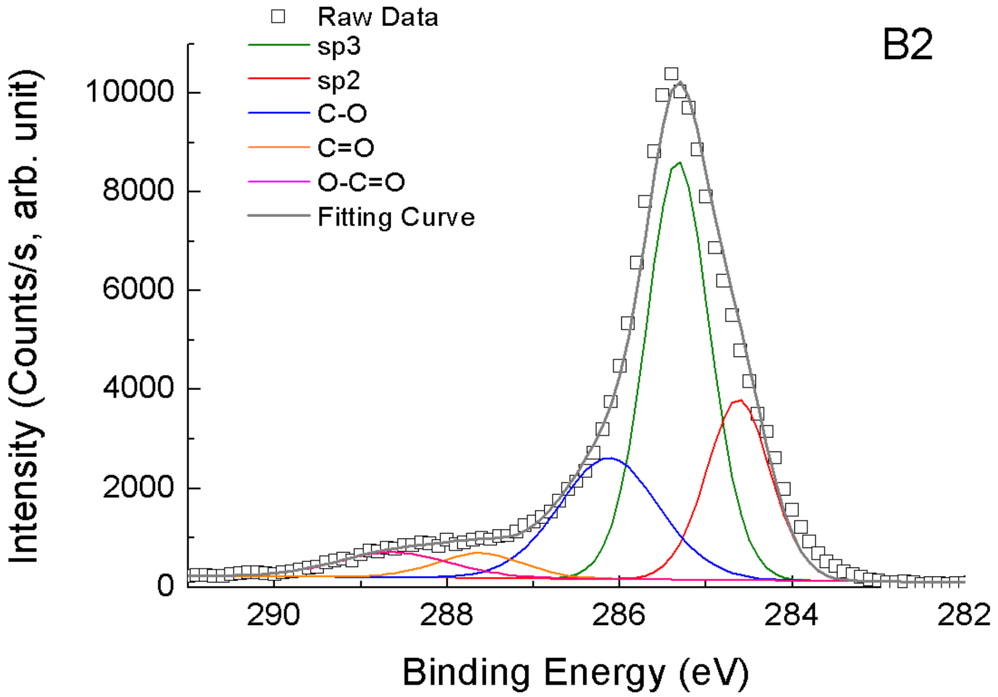

Figure 5.32 XPS spectra of pattern B2.

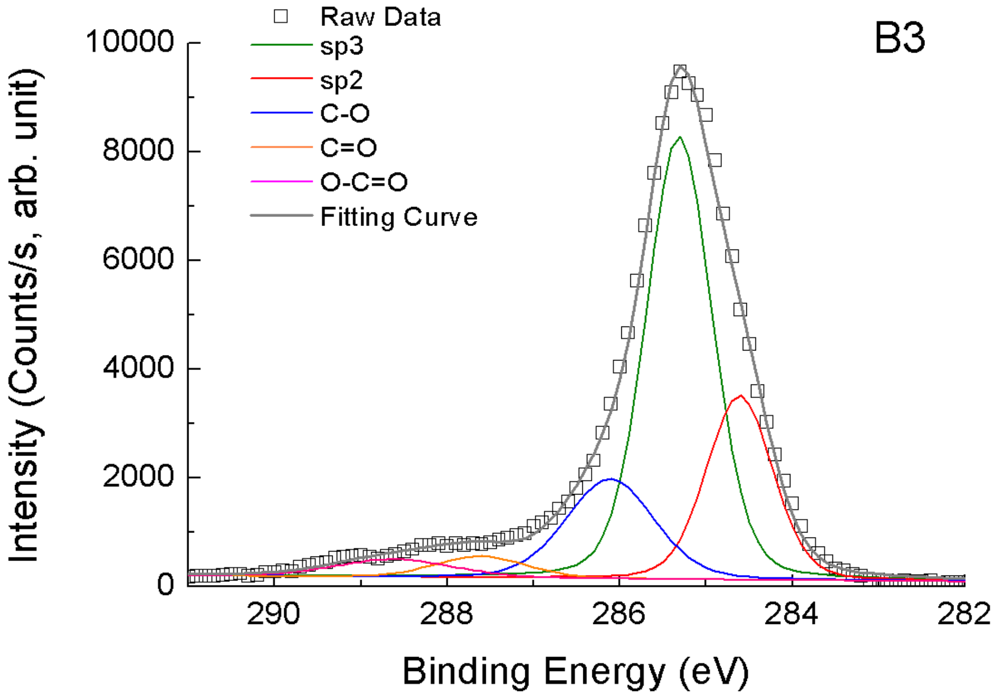

Figure 5.33 XPS spectra of pattern B3.

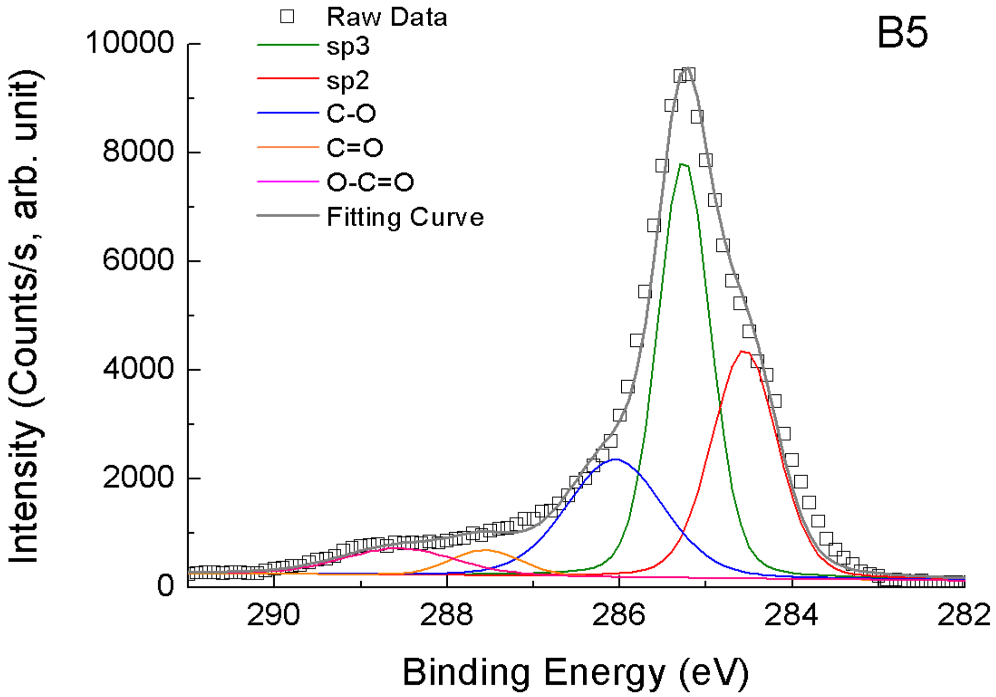

Figure 5.34 XPS spectra of pattern B5.

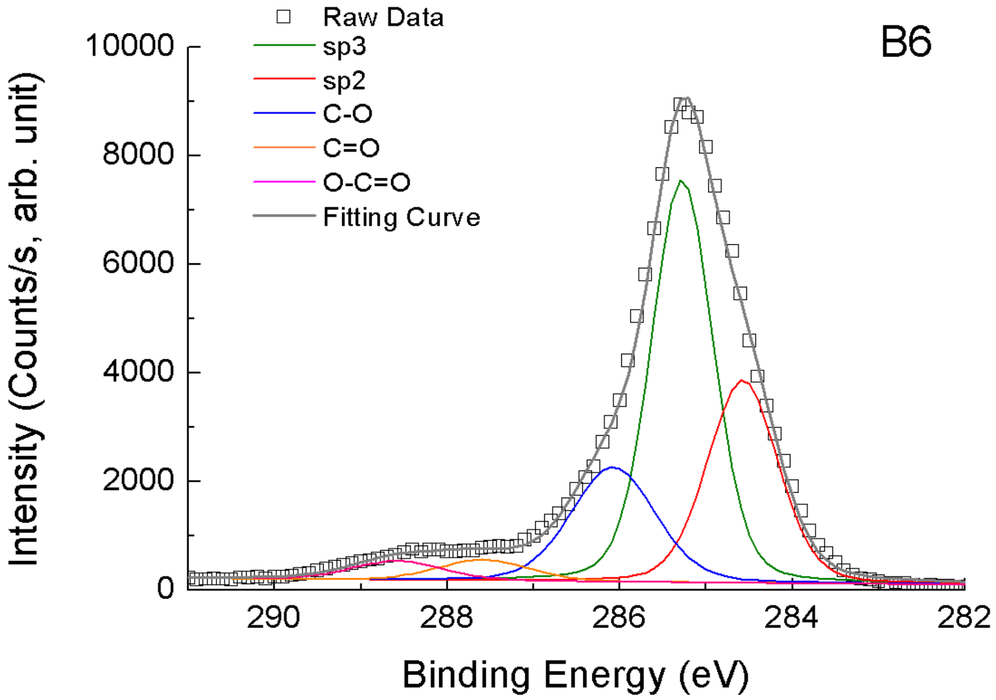

Figure 5.35 XPS spectra of pattern B6.

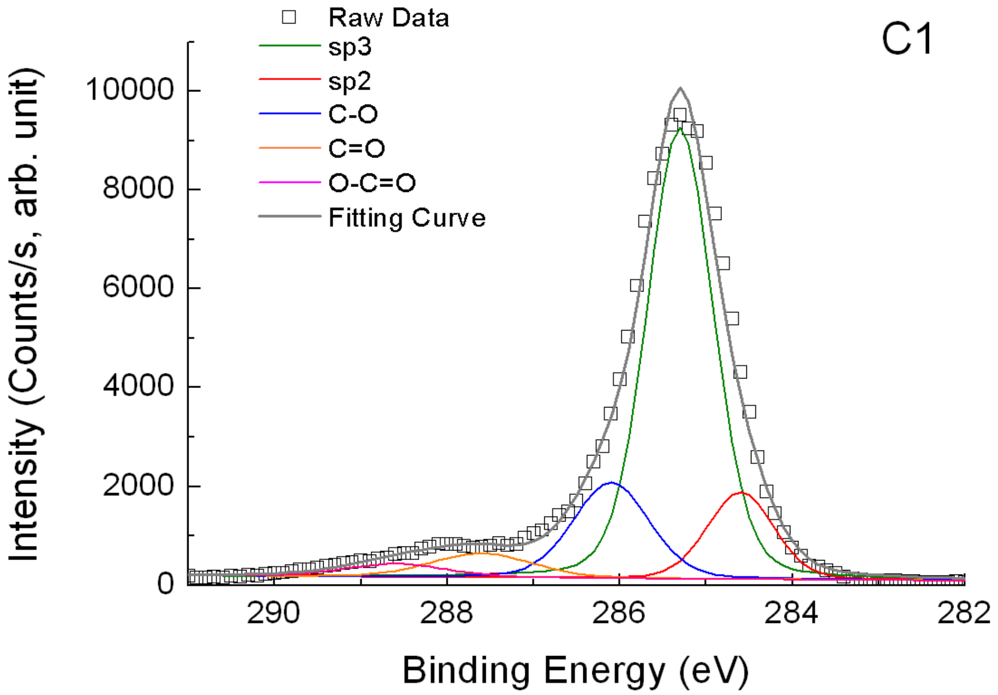

Figure 5.36 XPS spectra of pattern C1.

5.3.5 Atomic Force Microscope

The Atomic Force Microscope (AFM) was used to characterise the morphology of the fs-laser inscribed diamond surface and the periodical structures on it. The AFM results of pattern A2, B1, B2, B3 and C1 are collected and plotted in **Figure 5.37~Figure 5.41**.

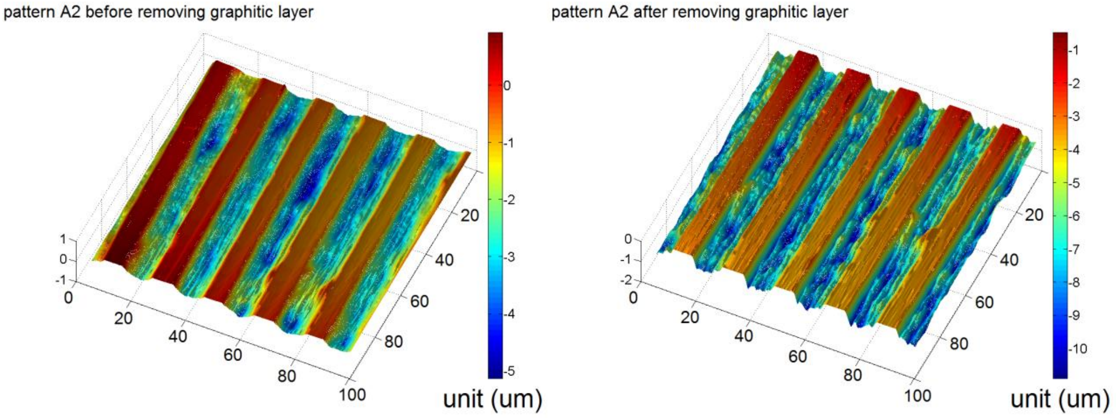

Figure 5.37 AFM morphology of fs-laser inscribed pattern A2, before (left) and after graphitic layer removal (right).

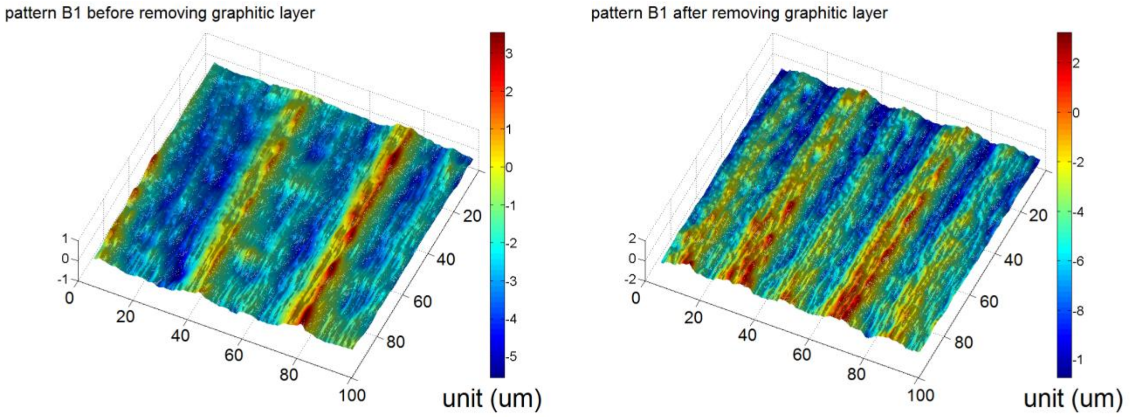

Figure 5.38 AFM morphology of fs-laser inscribed pattern B1, before (left) and after graphitic layer removal (right).

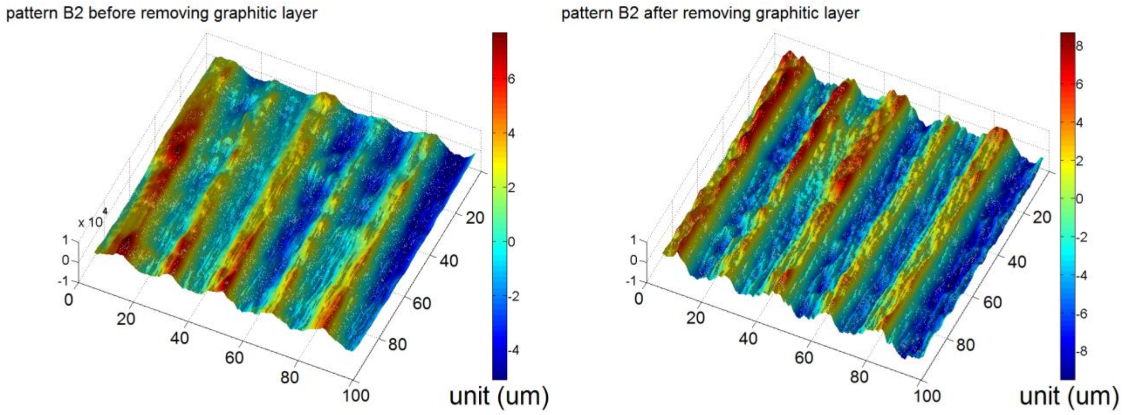

Figure 5.39 AFM morphology of fs-laser inscribed pattern B2, before (left) and after graphitic layer removal (right).

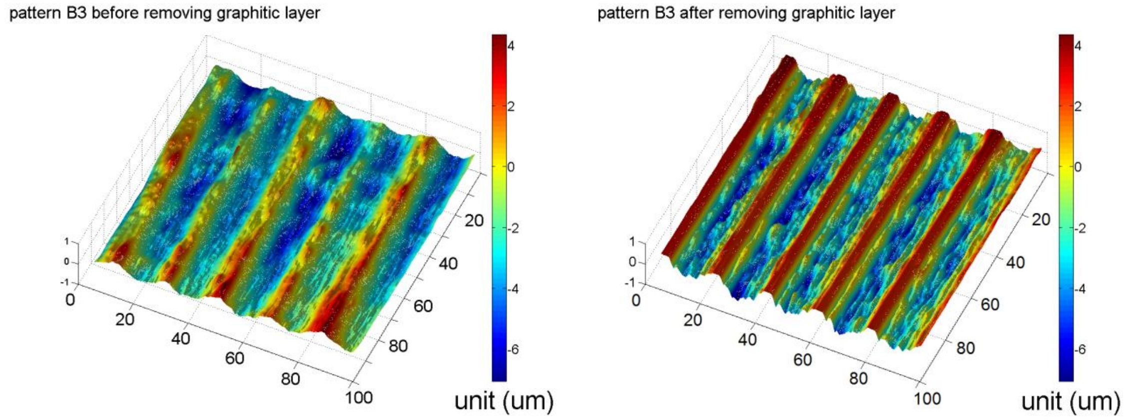

Figure 5.40 AFM morphology of fs-laser inscribed pattern B3, before (left) and after graphitic layer removal (right).

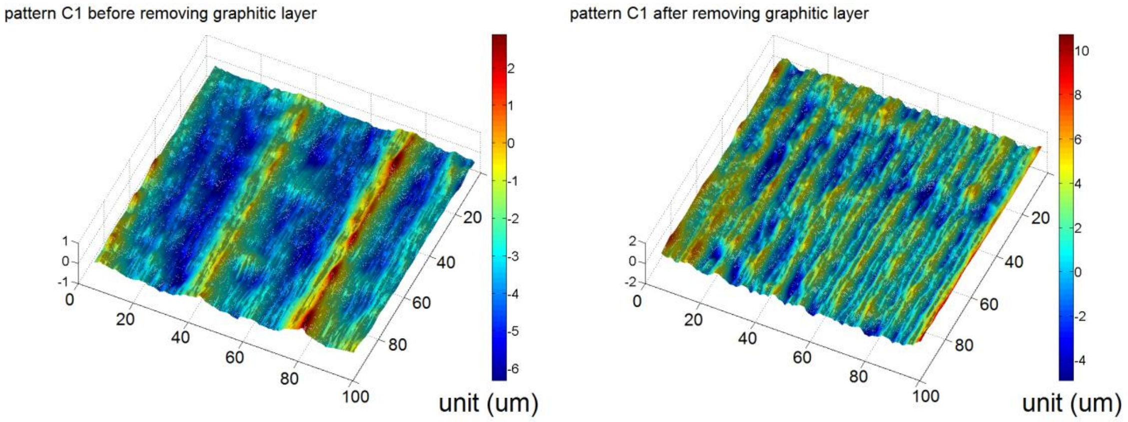
pattern C1 before removing graphitic layer

pattern C1 after removing graphitic layer

Figure 5.41 AFM morphology of fs-laser inscribed pattern C1, before (left) and after graphitic layer removal (right).

5.4 Analysis

5.4.1 Topography

It is seen that the texture of the channel shows a well-defined shape as expected. For the zigzag patterns, the micro-channels can be clearly observed. The whole structure is shown in **Figure 5.4 (a) ~5.8 (a)**, and high magnification images of channels are listed in the rest of the images. It is obvious that the micro-channels have a very rough morphology, which is covered by a layer of graphitic materials. The ripples formed by the fs-laser were perpendicular to the irradiation direction. In **Figure 5.9** and **5.10**, the cross fingers were overlapped and the boundaries were not clearly distinguished. This overlapped area can be attributed to the distance designed between the fingers and the laser energy intensity was excessive. The fully graphitised pattern is shown in **Figure 5.11** and the whole rectangle area has been irradiated.

It is apparent that the part of the channel near a corner shows a rough and porous ‘lava-like’ morphology, which consists of hollowed and crystalline materials. During the inscription process, the fs-laser had been focusing on the irradiated channels for a relatively longer time at the corner of the channel due to the change in direction. Therefore, this area experienced increased exposure to the fs-laser irradiation and more fragmental diamond crystals were exposed and detected in Raman spectra.

The corresponding images after removing graphitic layer are demonstrated in **Figure 5.12** ~ **5.19**. In these figures, it shows a less porous, but more uniform morphology comparing with the images in **Figure 5.4** ~ **5.11**. It can be seen that the channels’ surface morphology becomes smoother and periodical ripples are revealed.

For laser pulses irradiating dielectric materials at the picosecond-level or even longer, the heating mechanism can be explained as an increase in the kinetic energy of the conduction band electrons followed by the transfer of energy to the crystal lattice. This thermal dissipation will influence the surrounding lattices and finally reach a thermal equilibrium with them. In comparison, for femtosecond-level irradiation, the photon energy transfers from free electrons to the lattice within only hundreds of femtoseconds, which is much shorter than the free time of diamond atomic lattice collisions (10^{-11}~10^{-13} seconds).[162] As the fs-laser photon energy (1.21 eV) is higher than the reconstruction energy of diamond surface π-bonds (~0.68 eV), the laser pulse energy will lead to multi-photon absorption and rapid ionization of the surrounding materials to create a dense electron plasma.[163] Thus, there is no thermal equilibrium between the lattice and electrons, while the phase transformation is driven by hot-electron plasma induced by the fs-laser pulses. The surrounding diamond materials were maintained stable due to high thermal dissipation, whilst the fs-laser irradiated area received an incident laser energy sufficient for the phase transformation.[164]

After removing the surface graphitic layer, the ripples in the channels can be clearly observed and the ripple fringes have a periodical repetition. Shinoda and Bhardwaj, *et al.* suggested that the spatial period fringe Λ can be deduced by **Equation 5.1**:[165][166]

$$\boldsymbol{\Lambda = \lambda / 2n} \qquad \textbf{Equation 5.1}$$

where λ is the induced fs-laser free space wavelength, and n is the refractive index. Furthermore, the refractive index n can be calculated by Sellmeier equation, as shown in **Equation 5.2**:

$$\boldsymbol{n^2 = 1 + \frac{A_1\lambda^2}{\lambda^2-\lambda_1^2} + \frac{A_2\lambda^2}{\lambda^2-\lambda_2^2}} \qquad \textbf{Equation 5.2}$$

A_1, A_2, λ_1 and λ_2 are Sellmeier coefficients. In our experiment, λ is 1026 nm and the Sellmeier coefficients of diamond materials are: A_1=0.3306, A_2=4.3356, λ_1=0.175 μm and λ_2=0.106 μm. Thus, the corresponding refractive index can be deduced as n = 2.39. From **Equation 5.1**, one can calculate that the theoretical value of the spatial period fringe Λ is around 215 nm. In the SEM image in **Figure 5.3 (d)**, the spatial period observed for our sample is in a good agreement with the theoretical prediction.

5.4.2 Composition Analysis

In **Figure 5.20**, a diamond characteristic peak at 1332 cm^{-1} derived from T_{2g} mode of significant magnitude was observed.[168] Besides, in **Figure 5.21** and **Figure 5.22**, another minor shoulder at 1450 cm^{-1} could be associated with the nanocrystalline diamond. The bending curve at higher frequency can be derived from the background scattering of the graphitic layer.[169] Thus, the diamond feature peak became sharper after removing graphitic layer and flatter in the full Raman range.

In **Figure 5.22~Figure 5.28**, the Raman spectra before removing the graphitic layer had two relatively broader shoulders. The wide shoulders located at ~1320 cm^{-1} (D peak), which are derived from the K-point photons from the breathing mode of A_{1g} symmetry, and ~1600 cm^{-1} (G peak). After fitting the Raman spectra (b), the D peak was found at 1317 cm^{-1} with a FWHM of 3.8 cm^{-1}. The intensity ratio of $I(D)/I(G)$ was determined as ~1.8, which suggested that the area might be covered by nano-crystalline graphite.[170] After the surface graphitic layer was removed, the Raman spectra shows a sharp peak at 1332 cm^{-1} and a minor shoulder at ~1450 cm^{-1}. The diamond characteristic peak is always located at 1332 cm^{-1}, which can be derived from the T_{2g} zone centre mode. The minor shoulder can be associated with the nano-crystalline phase diamond. The evidence proven that most of the graphitic materials were removed after the chemical/hydrogen plasma etching processes.

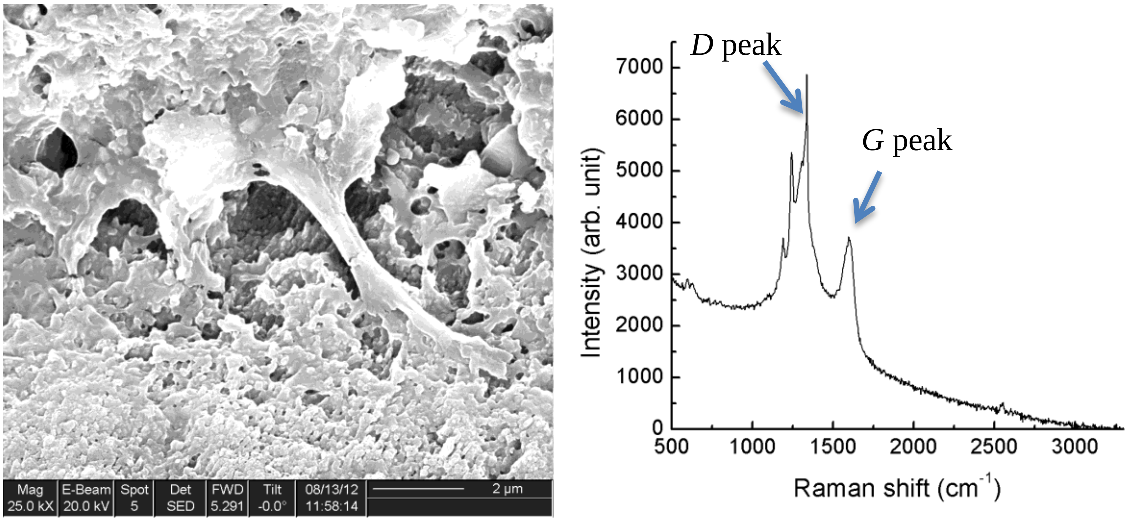

Figure 5.42 Left: SEM image of 'Lava-like' structure at the corner of fs-inscribed area; Right: Raman spectra at this area.

Figure 5.42 Left-hand: SEM images obtained from the corner of the fs-laser irradiated area and 'lava-like' structure; Right-hand: Raman spectrum obtained from this area as shown in **Figure 5.4** upper-left. For the Raman spectra, there are four characteristic Raman peaks, which are located at 1600 cm^{-1}, 1337 cm^{-1}, 1243 cm^{-1}, and 1190cm^{-1}. The peak located at ~1600 cm^{-1} can be attributed to the G peak, which is always assigned to carbon zone centre photons of E_{2g} symmetry.[168] The other three Raman peaks can be considered as split peaks, which is indicative of the presence of inhomogeneous micro stress on the diamond grains.[169] The peak at 1337 cm^{-1} corresponds to the diamond feature peak. The peak at 1190 cm^{-1} might be attributed to either the CC interring stretch vibration or v_1 mode of transpolyacetylene (trans-PA).[170] The latter was derived from the sum and combinations of C=C chain stretching and C-H wagging modes. The sharp peak at 1243 cm^{-1} was also evidence of the existence of trans-PA on the surface, which is not often observed. As the carbon sp^2 sites have a 50-230 times higher absorption sensitivity than the carbon sp^3 bonds, the Raman spectrum still proves this area with diamond sp^3 dominant.[161] From the SEM image shown in **Figure 5.28**, it can be seen that this area is constructed by hollowed and crystalline materials.

Table 5.2 Synthesized XPS peaks of each fs-inscribed patterns.

		sp^2	sp^3	**C-O**	**C=O**	**O-C=O**
Substrate	**Binding Energy (eV)**	284.6	285.3	286.1	287.6	288.6
	FWHM (eV)	0.9	0.6	0.9	1.3	0.6
	At.%	8.5 %	83.3 %	5.8 %	1.8 %	0.6 %
A2	**Binding Energy (eV)**	284.6	285.3	286.1	287.6	288.6
	FWHM (eV)	0.9	0.9	1.6	1.9	1.9
	At. %	23.0 %	37.4 %	27.9 %	4.6 %	7.2 %
B1	**Binding Energy (eV)**	284.6	285.3	286.1	287.6	288.6
	FWHM (eV)	0.9	0.7	1.3	1.0	1.6
	At. %	28.1 %	41.4 %	21.3 %	3.5 %	5.7 %
B2	**Binding Energy (eV)**	284.6	285.3	286.1	287.6	288.6
	FWHM (eV)	0.9	0.9	1.4	1.2	1.6
	At. %	20.9 %	48.1 %	22.0 %	4.0 %	5.2 %
B3	**Binding Energy (eV)**	284.6	285.3	286.1	287.6	288.6
	FWHM (eV)	0.9	0.9	1.2	1.3	1.7
	At. %	22.4 %	53.8 %	16.2 %	3.7 %	4.0 %
B5	**Binding Energy (eV)**	284.6	285.3	286.1	287.6	288.6
	FWHM (eV)	0.8	0.9	1.2	1.3	1.3
	At. %	53.2 %	23.4 %	16.5 %	3.3 %	3.6 %
B6	**Binding Energy (eV)**	284.6	285.3	286.1	287.6	288.6
	FWHM (eV)	0.9	0.9	1.2	1.3	1.3
	At. %	27.1 %	47.3 %	18.4 %	3.8 %	3.4 %
C1	**Binding Energy (eV)**	284.6	285.3	286.1	287.6	288.6
	FWHM (eV)	0.9	0.9	1.1	1.4	1.5
	At. %	12.3 %	63.7 %	15.7 %	5.3 %	3.0 %

In the XPS analysis, all the C 1*s* core peaks were sorted and synthesized with different carbon binding and chemical bonds (**Figure 5.29 ~ Figure 5.36**). Each peak was synthesized to be composed by carbon sp^2, sp^3, C-O, C=O and O-C=O, which are located at 284.6, 285.3, 286.1, 287.6 and 288.6 eV, respectively. Because of the dielectric properties of the diamond substrate, a charging effect of 2.3~2.5 eV was shifted before analysis. All the synthesized results and fitting curves were plotted in **Figure 5.29** ~ **Figure 5.36**. The synthesized peaks were analysed quantitatively by Gaussian-Lorentzian method and listed in **Table 5.2**. The full-width at half-maximum of sp^2 and sp^3 peaks were constrained to 0.7~0.9 eV, whilst the others were

~1.5 eV.[171] The synthesis method was assumed to be 80% Gaussian and 20% Lorentzian by approximating the contribution of the background.[172]

The XPS results have been deconvoluted into several peaks and the synthesized results are listed in **Table 5.2**. For the diamond substrate without fs-laser irradiation, the sp^3 composition is 83.3%. This ratio is much lower than the typical concentration of a single crystalline diamond. A reasonable explanation is the effective examination depth of XPS is approximately around 1-10 nm. The surface carbon structure of diamond cannot be sp^3 or dangling bonds, but composed by sp^2, carbon-oxygen bonds, carbon-nitrogen bonds or other bonds. Thus, the sp^3 content on the surface deduced by XPS is lower than in the bulk.

After the fs-laser inscription the sp^3 content was reduced significantly, which proved the fs-laser inscription process transformed the carbon sp^3 into other carbon bonds, *e.g.* sp^2 graphitic content. For the inscription process was performed in an open air, a certain percentage of carbon-oxygen, carbonyl and carboxyl bonds might be formed on the diamond substrate surface. Both Raman and XPS spectra results indicated that the fs-laser inscription process had significantly modified the carbon sp^2/sp^3 ratio, as well as the other carbon-related groups within the exposed area. On the other hand, the ratio of the C-O, C=O, and O-C=O was not fully determined by the pulse power, but also the fs-laser focused dot position on the diamond surface.

5.4.3 Morphology and Structure

The cross-section profile of the fs-laser inscribed area has been extracted from the AFM results, as shown in **Figure 5.43~Figure 5.47**. A reference surface roughness measurement was obtained by a scanning a 30×30 μm^2 area on an un-inscribed area. The root mean square (RMS) roughness of the substrate was 4.9 nm.[150]

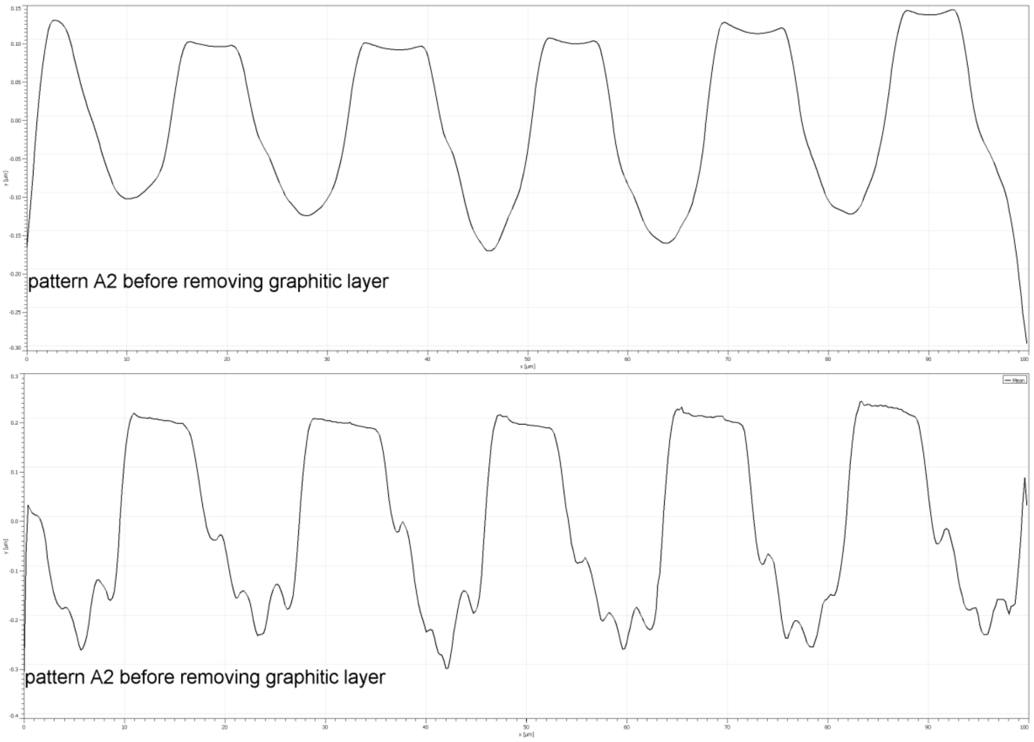

Figure 5.43 The cross-section profile of fs-laser inscribed periodical structure A2 extracted from the AFM results.

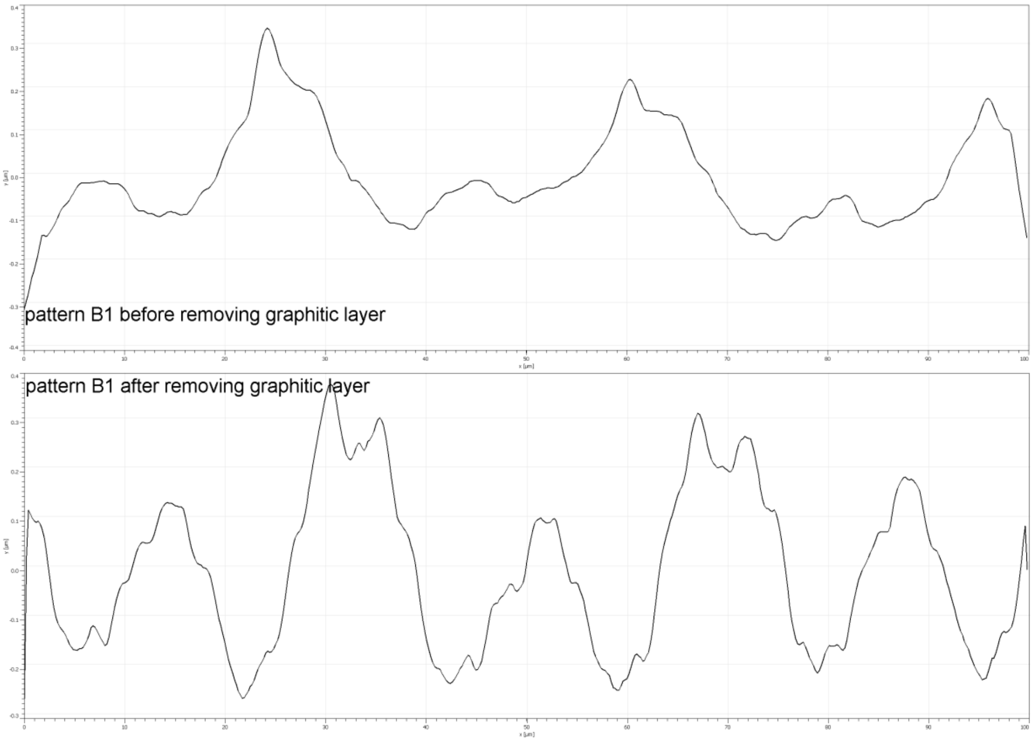

Figure 5.44 The cross-section profile of fs-laser inscribed periodical structure B1 extracted from the AFM results.

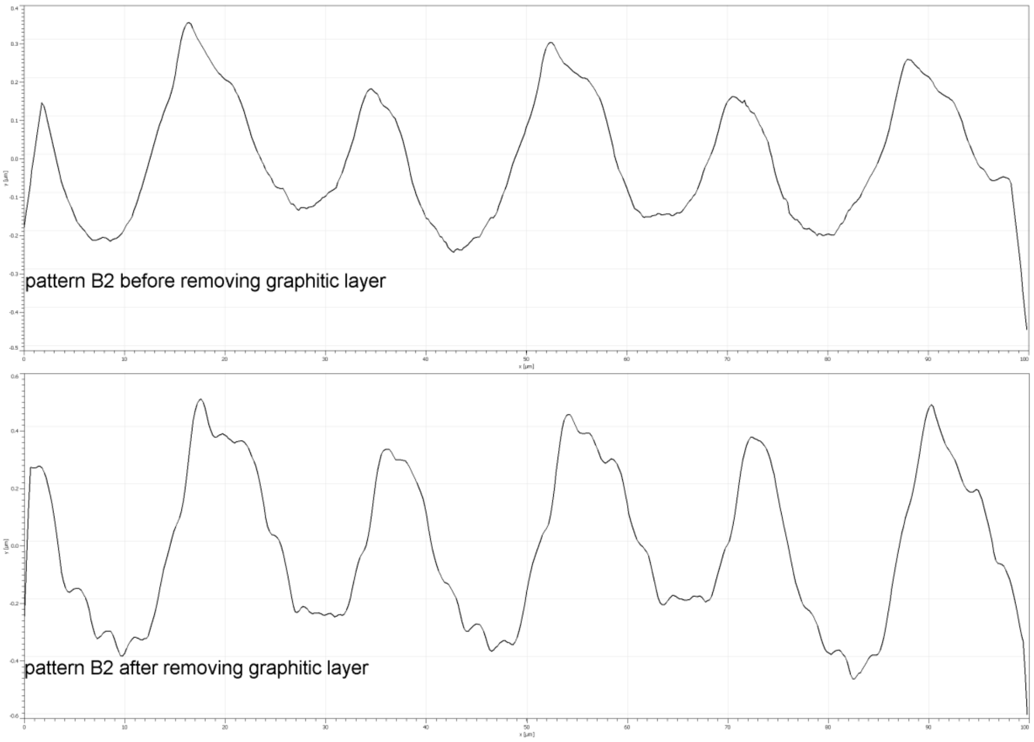

Figure 5.45 The cross-section profile of fs-laser inscribed periodical structure B2 extracted from the AFM results.

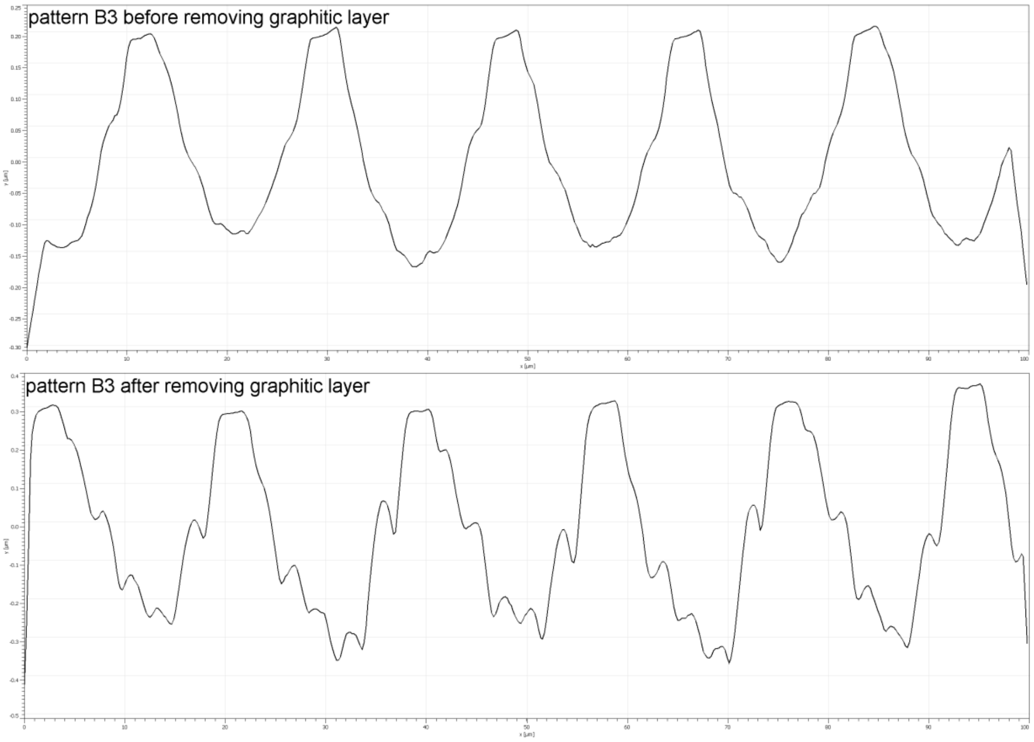

Figure 5.46 The cross-section profile of fs-laser inscribed periodical structure B3 extracted from the AFM results.

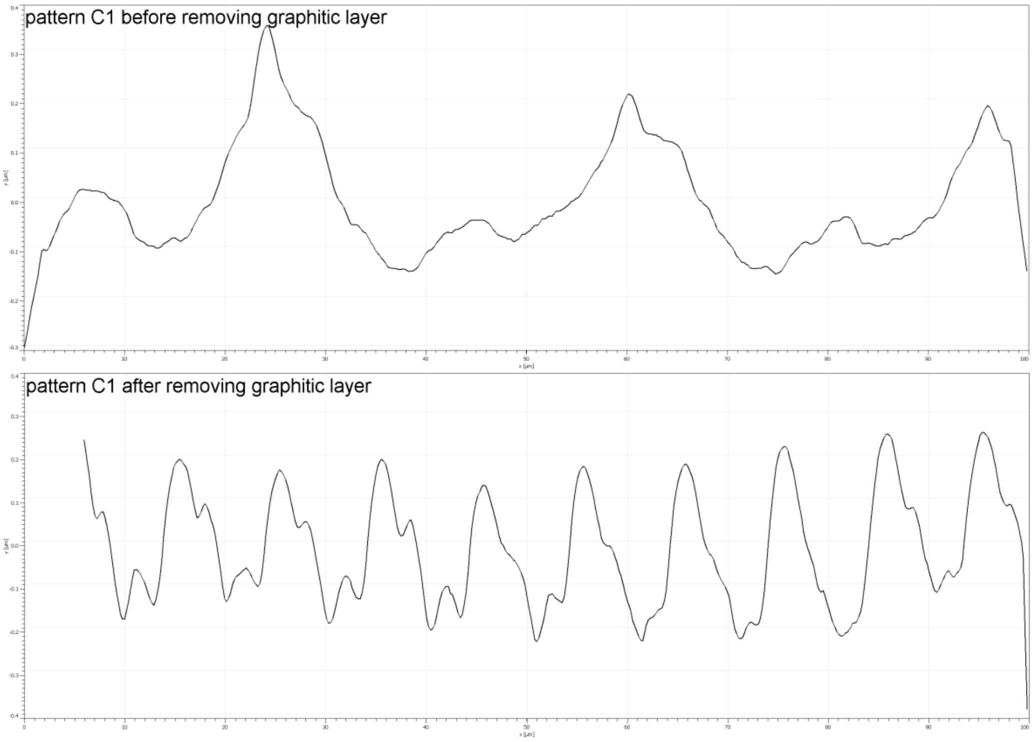

Figure 5.47 The cross-section profile of fs-laser inscribed periodical structure C1 extracted from the AFM results.

The other RMS value has been summarised in **Table 5.3**. It is obvious that the RMS value reduced significantly after the graphitic layer has been removed throughout the post-procedure. It can be deduced that the graphitic layer has a thickness of 165~190 nm. The graphitic layers generated by the fs-laser irradiation not only covered the channels, but also accumulated partially on the edges of the channels where no inscription occurred. This phenomenon was consistent with the results from Okuchi *et al*.[173] The mean value of maximum depth (RTM) was defined as the maximum between the top and bottom of the groove structure. After the graphitic layer was removed from the surface, the RTM value of each pattern was increased as well. In **Figure 5.43 ~ Figure 5.47**, it can be seen that the cross-sectional profile of the microfluidic channel was asymmetric. Other shoulder peaks were observed to be associated with each valley peak. Similar results were reported in the fs-laser inscription on fused silica.[174] This can be explained as the existence of mirrors in the optical path, or the attachments being tilted between diamond substrate and the glass slide. Either of the above factors will result in a tilted plasma dot in the diamond substrates, which leads to an asymmetric inscription. However, these asymmetric structures can be tuned and controlled by the optimization of the process.

5.5 Summary

In conclusion of this section, we have demonstrated that femtosecond laser-induced microfluidic channels can be fabricated on single-crystalline diamonds. The morphology of the fs-laser inscribed area was also demonstrated as well. The fs-laser inscription technique offers a faster and more convenient approach to develop 3D devices and structures on diamond substrates, when compared with conventional techniques such as FIB and RIE, *etc*. Future work will emphasize on the characterization of these devices for biomedical sensing and the theoretical modelling of the inscription process, especially with the laser focused inside the bulk of the diamond substrates. This could offer a potential for the fabrication of self-embedded devices and nanostructures for a number of advanced sensing applications.

Table 5.3 RMS value of diamond substrate and fs-laser inscribed area

Pattern Name	RMS (nm)		Mean RTM(nm)	
	Before removing graphitic layer	After removing graphitic layer	Before removing graphitic layer	After removing graphitic layer
substrate	4.9	N/A	N/A	N/A
A1	64	143	245	410
B1	129	196	N/A	364
B2	214	336	393	445
B3	141	249	304	482
C1	192	322	N/A	219

Chapter 6: Properties and Thermal Stability of Hydrogen-Terminated Nanodiamond

Properties and Thermal Stability of Hydrogen-Terminated Nanodiamond

6.1 Introduction

Detonation-synthesised nanodiamond (DND) has been previously introduced and characterised in Chapter 2 and Chapter 3. DND powder has been utilised as *in-vivo* drug delivery carriers, electrochemistry catalysts, biomarkers, and biosensors, due to its superb chemical stability and biocompatibility.[175]~[179] To achieve these qualities, the manipulation of diamond surface properties is especially critical to its future physical and chemical applications.[180]

The surface of any individual DND particle is surrounded by a 'sootlike' structure, which is composed by several free graphitic layers, metallic residues, as well as other sp^2/sp^3 non-diamond species.[181] The detonation soot also contains 25~45 wt.% graphite-like structures and incombustible impurities (metals and metal oxides 1~8 wt.%). After preliminary purification, the DND powder can be considered as a composite, which is composed of carbon (80~89%), nitrogen (2~3%), hydrogen (0.5%), oxygen (~10%) and incombustible residue (<8%). The final product consists of a mixture of diamond (90~99%) and non-diamond carbon (1~10%).

The oxidised DND powder can be removed from the surface by chemical/physical modification. The oxidisation can be formed by purifying DND powder with liquid oxidizer, *e.g*. H_2SO_4/HNO_3, KOH/HNO_3, Na_2O_2, CrO_3/H_2SO_4, or HNO_3/H_2O_2 solutions.[182],[183] On the other hand, the hydrogen termination is always treated in MPECVD to perform hydrogen surface termination to establish a *p*-type electrical conduction, which is hydrophobic to water. The electrical path and conduction methods of *p*-type films have been thoroughly studied before.[184]~[187] However, the DND powder has an average grain size in the nanometre range, which might present different electrical properties when compared with the two dimensional diamond films. Therefore, the study of DND powder's deaggregation, modification, surface characterisation, as well as thermal stability has attracted great interest. Previous research based on FTIR, NMR, XRD had revealed that the surface of DND powder was composed of various carbon species (*e.g*. C-C, C=C, C-H_x, C-O or C=O).[188] In addition, photoemission spectroscopy (PES) and XPS were also utilised to characterise the thermal annealing effect on DND powder.[189],[190] Also, Xie *et al*. had investigated the graphitisation surface of nanodiamond.[191] However, fewer reports related to the AC electrical properties have been investigated. Recently, Jackman's group has reported the impedance spectroscopy (IS) results on both aggregated DNDs in the as-received state and monodispersed DNDs.[192],[193] The electrical properties of surface-modified DNDs are difficult to characterise for its measurement and instruments.

In this chapter, we have designed a novel testing system, which is suitable for impedance measurement of DND powder. This setup will create a more stable testing environment and collect a more accurate IS data. Also, both untreated DND samples and hydrogen-terminated DNDs (H-DND) were used to perform the IS measurement in order to investigate the contribution from the C-H bonds. Then, the thermal stability of DNDs was studied based on IS measurement at different annealing temperature. Finally, the FTIR and XPS studies provided an insight into the evolution of the physical and chemical modification on H-DND.

6.2 Experimental

'As-received' state DND powder from SIGMA-Aldridge Company with an average grain size of 4-6 nm was used as the original sample. The morphology of the untreated 4-6 nm DND powder was characterised by scanning electron microscope (SEM), as shown in **Figure 6.1**. The extreme small nanometre-scale nanodiamond powder aggregate and form particles with a grain size of 50~150 nm. This state of nanodiamond can be named as 'sootlike' state.

The hydrogen termination process was carried out using an ASTeX^{TM} 5010 (Seki Technotron Corp., 2.45 GHz, 1.5 kW) microwave plasma enhanced chemical vapour deposition (MPECVD) system. A custom-designed molybdenum container was then placed into the chamber in order to constrain the DND powder during the whole hydrogen termination process. The microwave plasma was set at 900 W with an atmosphere pressure of 50 Torr. The hydrogen flow rate was maintained at 200 sccm during the 10 mins hydrogen plasma treatment process. An infrared thermometer (model: Williamson Pro 92-40-C, measurement range: 475-1475˚C) recorded the real-time temperature which was 850˚C. After finishing the hydrogen plasma treatment, the DND sample was kept in the vacuum chamber until the temperature decreased to room temperature. Then, the DND sample was carefully transferred into the testing cell to begin the next step.

Until now, the direct measurement on a single nanodiamond particle is unavailable, hence we have designed a testing system for IS measurement. The whole testing system cell was constructed by two copper plates, as shown in **Figure 6.2**. The substrate plate was electroplated with high-purity nickel. A hollowed ceramic washer was pasted on the substrate after heating up to 150^{o}C. Another stainless steel bolt served as the top electrode and the other copper plate held up the top electrode with two isolated ceramic screws. This setting can ensure the top electrode is isolated from the substrate. Two metal springs were fitted in the ceramic screws to provide a relative constant force on the DND sample. The pressure on the DND sample was critical during the measurement of such porous material or powder, as the springs would make an influence to the porosity/density of the powder sample and consequently impacted on the IS response.[194]

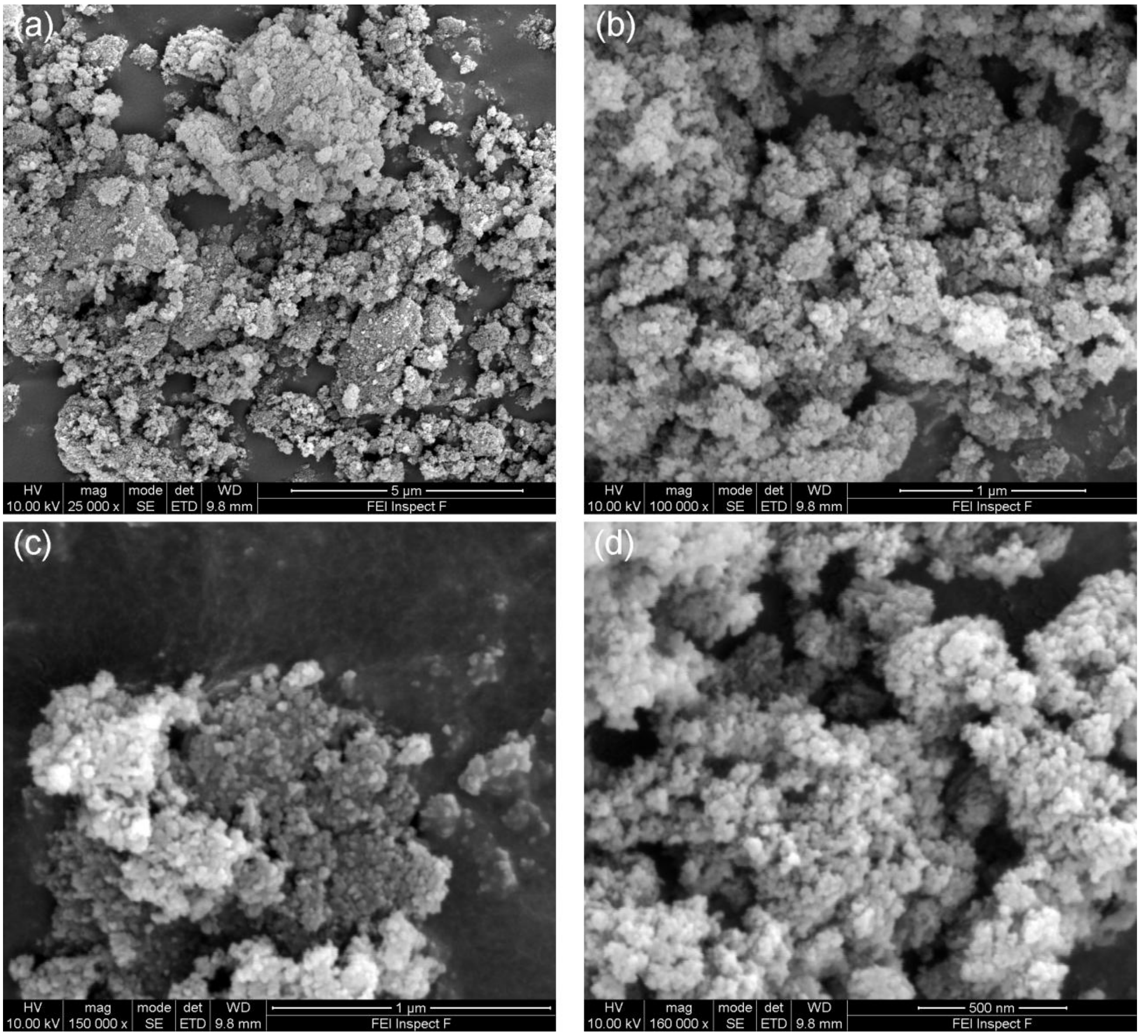

Figure 6.1 SEM images of detonation nanodiamond with average grain size of 4-6 nm; magnification (a)-(d): 5 μm-500 nm.

The IS measurement was performed in standard atmosphere at elevated temperatures varying from 50˚C to 400˚C by Autolab PGSTAT 302N electrochemical system (Windsor Scientific Ltd), which was linked to the testing cell. The maximum heating temperature was limited to 400˚C for the DND sample would experience a catastrophic weight loss and phase change at temperatures higher than 400˚C.[195] The ESCALAB 250 X-ray photoelectron spectrometer (Thermo Corp.), which is equipped with a monochromatised Al $K\alpha$ (1486.5 eV) X-ray source, has been employed to analyse the surface bonding states of the DND powder. The chamber pressure was set to 5×10^{-10} mbar and the analysis pass energy was 20 eV. The DND sample was attached to the testing stage with double-sided conductive carbon tape. The infrared spectra was collected by a Thermo IR 200 FTIR spectrometer with KBr compressed pellets, which was prepared by mixing 25 mg DND powder with 250 mg potassium bromide (SIGMA-Aldrich Corp.). All the pellets were stored into a desiccator with silica gel to get rid of the absorbed water. Each portion of H-DND was annealed at different temperatures from 50˚C to 400˚C.

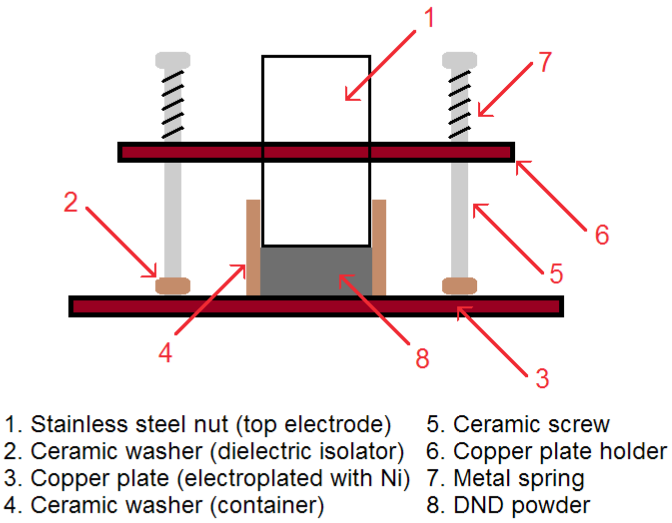

Figure 6.2 Cross-sectional view of schematic structure of testing cell.

6.3 Results

6.3.1 Raman Spectroscopy

The Raman spectroscopy of untreated DND sample is shown in **Figure 6.3**.

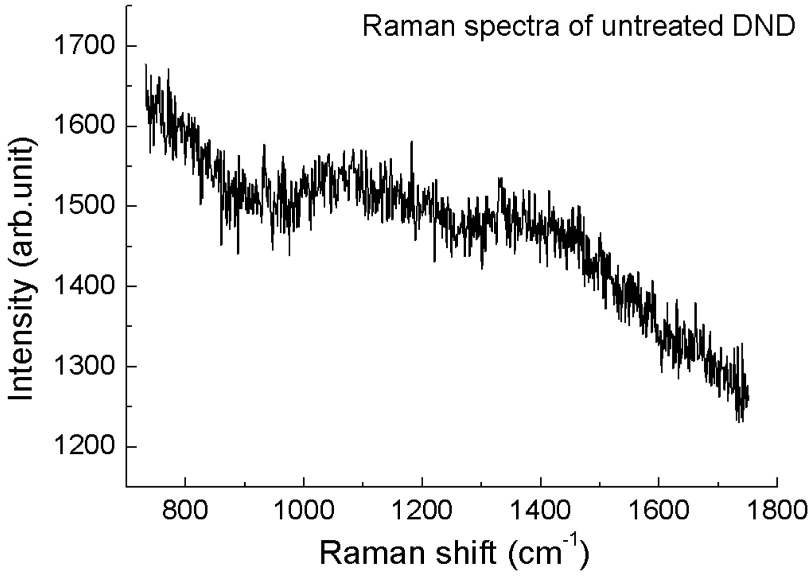

Figure 6.3 Raman spectra of untreated DND sample.

It is known that carbon *sp*^{2} has two broad shoulders located at 1350 cm^{-1} and 1550 cm^{-1}, corresponding to the *D* and *G* peak, respectively.[196] Furthermore, the diamond *sp*^{3} will demonstrate a sharp peak at 1332 cm^{-1}. As seen in the Raman spectra, no characteristic peak of diamond is demonstrated. In addition, the background noise was too strong to observe the intrinsic carbon sp^2 peaks. This can be attributed to the graphite layer having a higher Raman absorption than diamond *sp*^{3} structure.[197] Thus, the Raman spectroscopy may not be considered suitable for characterising DND sample in this experiment.

6.3.2 Impedance Spectroscopy

The impedance spectroscopy is useful for investigating the electric and dielectric properties of different types of ionic, electronic and mixed conductive ceramics.[184] Impedance spectroscopy has already been successfully utilised in characterising electronic properties of polycrystalline, nanocrystalline, δ-doping, and nanodiamond.[184],[187],[192],[193] In essence, the impedance technique involves the measurement of both real and imaginary parts of complex impedance as a function of frequency, which can be expressed as:

$$\boldsymbol{Z(\omega) = Z' + jZ''} \qquad \textbf{Equation 6.1}$$

$$\boldsymbol{Z' = \sum_{i=1}^{n} \frac{R_i}{1+\omega^2 R_i^2 C_i^2}} \qquad \textbf{Equation 6.2}$$

$$\boldsymbol{Z'' = \sum_{i=1}^{n} \frac{\omega R_i^2 C_i}{1+\omega^2 R_i^2 C_i^2}} \qquad \textbf{Equation 6.3}$$

where $Z(\omega)$ is the complex AC impedance as a function of the angular frequency ω. Z' and Z'' are the real and imaginary parts of impedance, respectively. The real part impedance is derived from material resistance while the imaginary one is from its capacitance. The variable *n* can take values between 1 and 3, which corresponds to the different conduction paths. When the real part of impedance versus imaginary part is plotted in one figure as a function of frequency, it is called Cole-Cole plot. The Cole-Cole plot can be fitted with an equivalent circuit and the conduction mechanism can be deduced.[184]~[187]

The impedance spectroscopy results of untreated DND sample and H-DND under different annealing temperature have been plotted as shown in **Figure 6.4**. The Same amount of diamond was taken in each time of measurement and presented in the format of a Cole-Cole plot. The Cole-Cole plot of untreated nanodiamond is shown on **Figure 6.4 (a)**, which can be fitted as a near-perfect semicircle. The diameter of the fitted semicircle that intercepted on the Z' axis indicates the real part of its impedance. The single semicircle demonstrated that only one conduction mechanism existed for the conduction within the untreated DND sample.

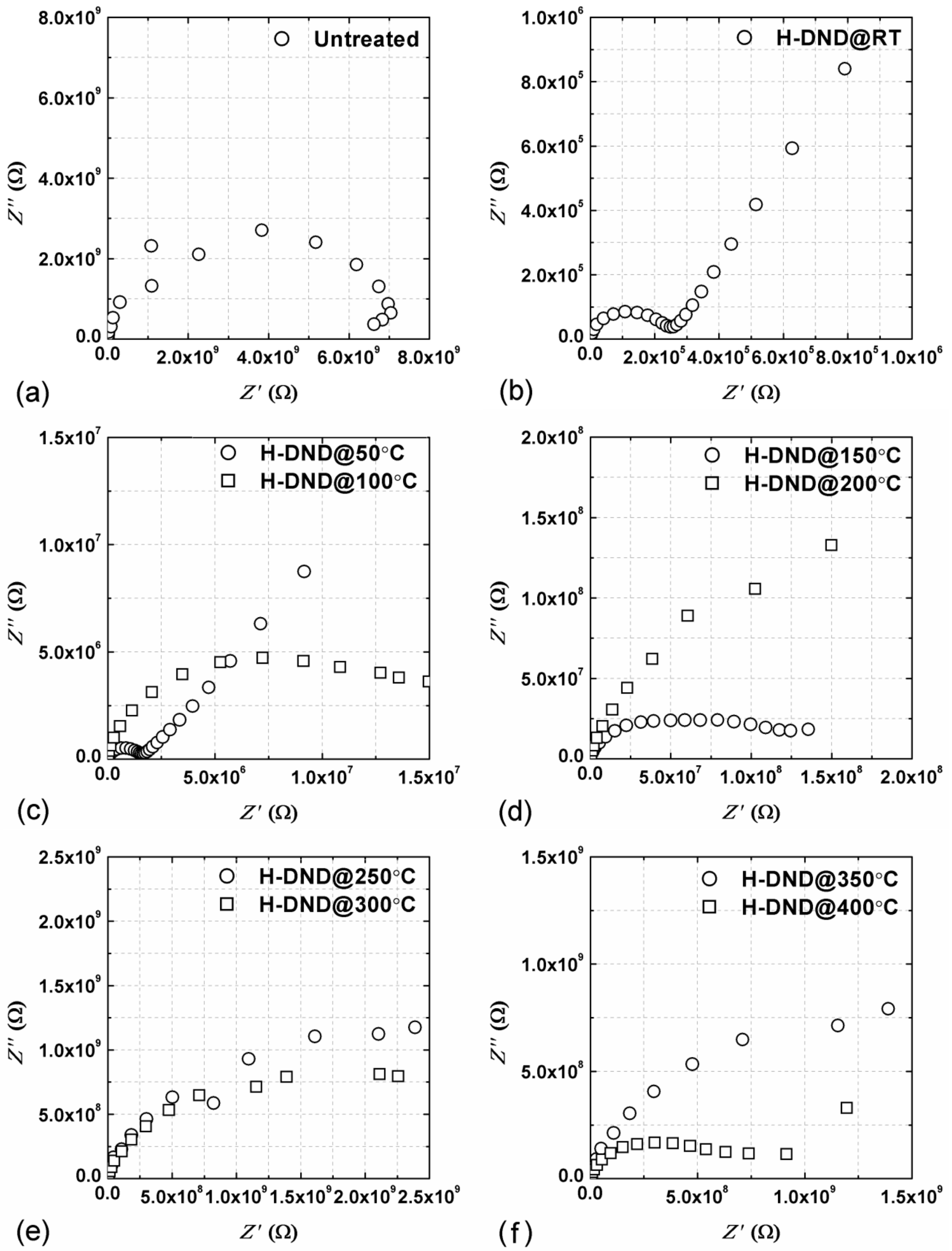

Figure 6.4 Impedance spectroscopy of (a) untreated DND; (b) H-DND measured at room temperature; (c) H-DND annealed at 50˚C and 100˚C; (d) H-DND annealed at 150˚C and 200˚C; (e) H-DND annealed at 250˚C and 300˚C; (f) H-DND annealed at 350˚C and 400˚C.

In order to analyse the impedance data, a single resistor-capacitor (*RC*) parallel equivalent circuit can be used to simulate the electrical properties, as shown in **Figure 6.5 (a)**. The fitting procedure used here is as same as the one described by Kleitz *et al.*[199] Here, the RC parallel circuit can be used to characterise the impedance contributed from the stacked DND powder, which is calculated to be around 7×10^9 Ω by fitting the arc with its equivalent circuit.

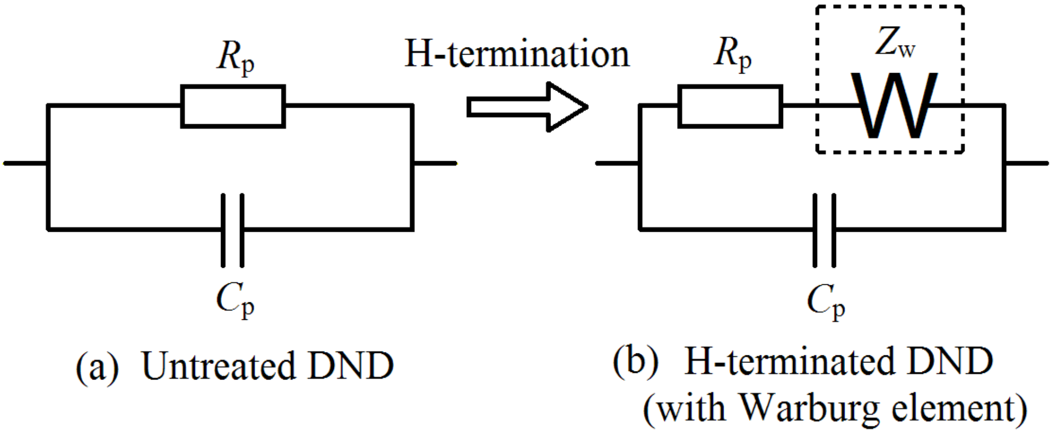

Figure 6.5 Equivalent circuit extracted from Cole-Cole plot before/after hydrogen termination treatment.

The Cole-Cole plot of the H-DND sample at room temperature is shown in **Figure 6.5 (b)**, which consists of a semicircle at high frequency range and a straight line at low frequencies. The diameter of the fitted semicircle intercepts the Z' axis, indicating the resistance of H-DND is around 2.46×10^5 Ω. This value is four orders of magnitude less than untreated DND samples. It is obvious that the low-frequency spectra of H-DND form a straight line at 45° angle to both Z' and Z'' axis. This phenomenon indicates the corresponding equivalent circuit may consist of a Warburg diffusion component (see **Figure 6.5 (b)**).[200] The complex Warburg impedance Z_w is composed by a constant phase element (CPE), which is expressed as

$$\boldsymbol{Z_{CPE} = Z(j\omega)^{-\sigma} = Z(\omega)^{-\sigma}[\cos\left(-\frac{\sigma\pi}{2}\right) + jsin(-\frac{\sigma\pi}{2})]} \qquad \textbf{Equation 6.4}$$

where Z represents the impedance and ω is the angular frequency. The exponent σ is the frequency-dependent correction factor with a value between 0 and 1. If σ is 1, the CPE component is a pure capacitor, whilst for 0 it is for a pure resistor. When the exponent σ equals to 0.5, the equation of CPE can be expressed as

$$\boldsymbol{Z_w = (\frac{A_W}{\sqrt{\omega}})(1-j)} \qquad \textbf{Equation 6.5}$$

which is named as the Warburg diffusion element. The Warburg diffusion element can be used to characterise infinite-length approximation of DND particles stacked together and their mutual interaction after the hydrogen passivation process. Preliminary analysis for the presence of the

Warburg element can be attributed to the water absorption on the surface and the colloidal properties of the DND powder.[201] Besides, the formation of C-H bonds on DND particles' shell enhances the conductivity of them and possibly enables an infinite-length approximation of their electrical properties. A similar result could be found in the electrochemical properties of DND fabricated electrode by Zang *et al*. The author attributed the 45˚ low frequency linear portion to the inhomogeneous porous structure, which lead to a non-ideal capacitive element.[202] As the temperature increased up from 50˚C to 100˚C, the diameter of the semicircle changed while the Warburg effect was significantly weakened (**Figure 6.4 (c)**).[204] The resistance, R_p, increased up to over 5.2 MΩ. This phenomenon can be explained by the absorbed water evaporating from the DND particles surface while heating in air.[191],[199] The absence of water not only limited the Warburg diffusion effect, but also increased the resistance R_p, at the same time. At this temperature, the Warburg effect has become negligible and the overall impedance increased with the increasing temperature. When the temperature reached 150˚C, the Warburg effect almost disappeared, while R_p exceeded more than 150 MΩ, as shown on **Figure 6.4 (d)**. Previous research proven that the water has been totally evaporated from the outer shell at this temperature. The Warburg effect completely disappeared at temperatures of 200˚C and 250˚C as R_p increased up to 1.84 GΩ and 2.22 GΩ, respectively. At 250˚C, the sample demonstrated a maximum resistance value, which was four orders of magnitude higher than the H-DND sample measured at room temperature. The increase in the resistance could be explained as the incorporation of oxygen onto the DND surface,[204] and further evidence will be provided throughout XPS and FTIR measurement. While the temperature increased up from 300˚C to 350˚C, the resistance decreased from 0.834 GΩ to 0.246 GΩ. The drop of the resistance can be derived from the thermal activation of non-diamond phase impurities on the DND particles. Finally, as the temperature increased up to 400˚C, the impedance increased again to 0.8˚C, as shown on **Figure 6.4 (f)**. At this temperature range, the Warburg effect appeared again as it was in room temperature range, which suggested that the phenomenon to be associated with the surface homogeneity on the DND particles.[205] The resistance error results from the following two factors: Autolab equipment system error (±0.2%) and numerical fitting error (±5%).

In **Figure 6.6**, the Arrhenius relationship was plotted by Ln(R_p) versus 1000/T across a range of temperatures between room temperature to 400˚C. It is obvious that the resistance R_p, continuously increases together with the environment temperature up to 150˚C. At this stage, the main conduction mechanism may derive from the surface absorbed water, which provides a conduction path between the aggregated DND particles. Comparing with the as-received DND powder without any hydrogen-plasma treatment, the resistance decreases 10^4 times. A reasonable explanation is that the post-procedure of DND, like thermal oxidization and acid-purification, generates a dielectric layer on the surface outside the particles' shell.[185] In addition, as the temperature increased up from 170˚C to 225˚C, the resistance R_p decreased together with the increasing temperature. The Arrhenius relationship can be expressed as:

$$R = Ae^{-\frac{E_{act}}{kT}} \qquad \textbf{Equation 6.6}$$

$$Ln(R) = -E_{act} \cdot \left(\frac{1000}{T}\right)\left(\frac{1}{1000k}\right) + Ln(A) \qquad \textbf{Equation 6.7}$$

where E_{act} represents the activation energy of a certain kind of semiconductor and k is the Boltzmann's constant. From the Arrhenius relationship, an activation energy of E_{act1}=0.089 eV can be calculated from the data between 170˚C to 225˚C, which could be associated with the thermal activation of the hydrogen-termination on H-DND. Finally, for the temperature at 250˚C and 350˚C, an activation energy of 0.63 eV can be allocated. The relationship of activation energy at different temperature levels and the oxidization evolution process will be concluded in next section.

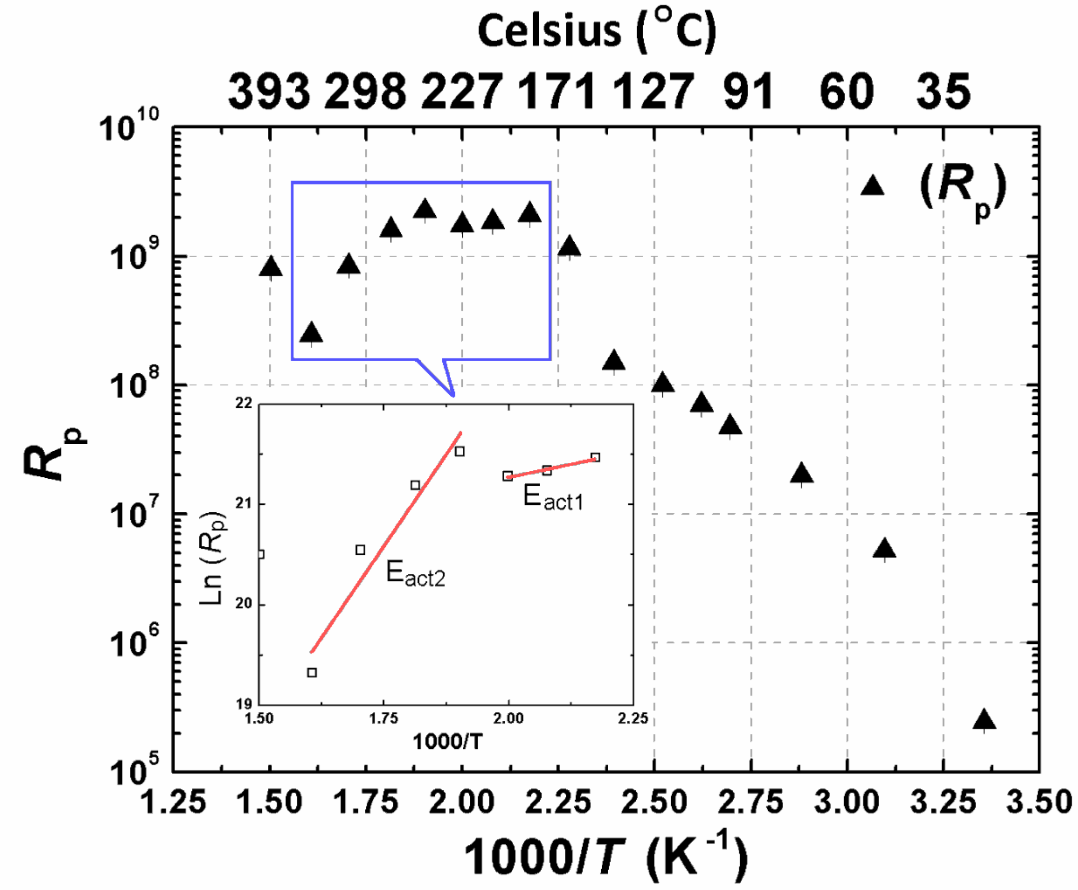

Figure 6.6 Arrhenius relationship of resistance R_p extracted from the Cole-Cole plot.

6.3.3 Fourier-Transform Infrared Spectra

To understand the thermal stability of H-DND, we have performed thermal annealing experiments on H-DND samples, at different temperature varying from 50°C up to 400°C. **Figure 6.7** shows the FTIR results of untreated DND samples, as well as H-DND samples post annealing.

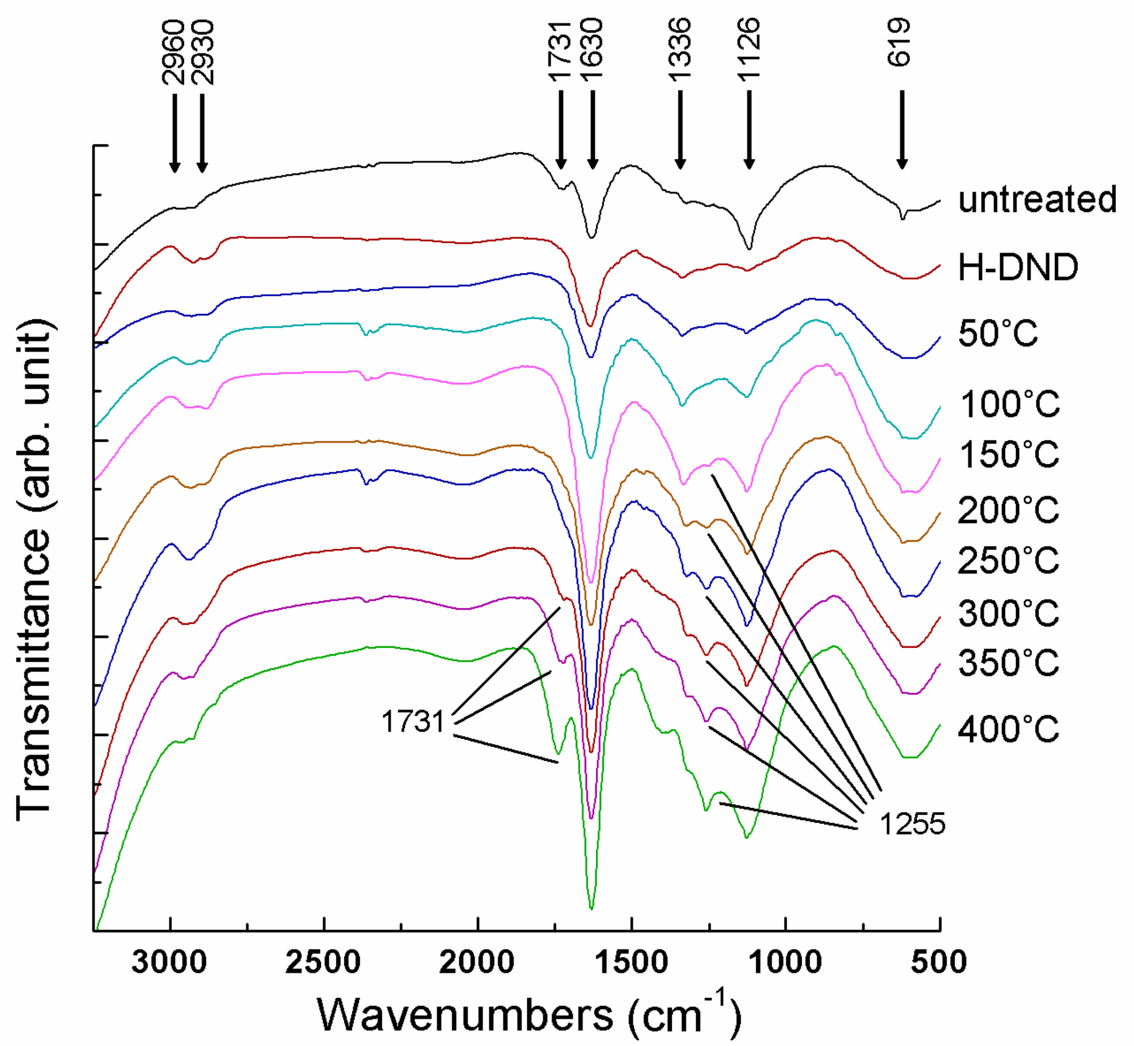

Figure 6.7 FTIR analysis of untreated DND, H-DND and H-DND annealed from 50°C to 400°C. All the DND powder was performed thermal annealing treatment in air and then pressed into KBr pellets.

All the FTIR spectra samples demonstrated a significant peak located at 1630 cm^{-1} (δ_{OH} bend mode), which was derived from the water absorption on the untreated DND surface.[206],[207] For the untreated DND powder spectra, one small peak located at 619 cm^{-1} was observed and disappeared after H-termination. This peak can be associated with the carbon amide bonds on the particles' surface and it is worth noting that it did not appear in air.[188] The peak around

1126 cm^{-1} in the untreated sample might be assigned as either the ether group ($\nu_{C\text{-}O\text{-}C}$) or the δ_{OH} vibration from water. Here, it is more likely to be associated with the water absorbed on the surface of the DND powder rather than the ether group. This peak disappears after h-termination, but starts to remerge at temperatures above 10°C. A possible explanation was the formation of C-H bonds on the surface after H-termination enhanced the hydrophobic properties of the DND particles.[205] The peak at 1126 cm^{-1} became weakened after H-termination, which could be explained by the fact that the H-termination enhanced the hydrophobic properties. The peak at 1255 cm^{-1}, which can be associated with the C-O groups, is not significant in the untreated sample. However, it became dominant as the annealing temperature reached 150˚C or above. This result proven that the H-DND particles started to oxidise at 150˚C. Another weak peak located at 1336 cm^{-1} proven that the existence of the C-N bonds (*e.g.* cyclic carbon in cyclic lactams, -C=N).[188] This peak survived after the H-termination treatment and enlarges with the increasing annealing temperature. Eventually, this peak vanished at 350˚C above. The 1731 cm^{-1} peak could be assigned as ester or organic amide on the DND sample but disappeared after hydrogen plasma treatment. After annealing at 300˚C, the 1731 cm^{-1} peak re-appeared, which implied that the presence of C=O bonds. After the hydrogen plasma termination, the H-DND exhibited surface modification with two broad peaks at 2930 cm^{-1} and 2960 cm^{-1}. These two peaks corresponded to alkyl sp^3 C-H ($-CH_3$/$-CH_2$) bonds stretching vibration mode. In summary, the FTIR results proven that the hydrogen-termination process functionalised by the DND surface with C-H bonds and removed a certain percentage of carbon-oxygen compounds.

6.3.4 X-ray Photoelectron Spectroscopy

The XPS technique has been applied to determine the relative composition of the DND samples. The survey spectra have been recorded for untreated DND, H-DND, and thermal annealed DND powder, as shown in **Figure 6.8**. The significant C1*s* peaks between binding energy (BE) 280.0 eV and 290.0 eV have been normalised in order to highlight the order impurity peaks. The minimal chromium impurities (Cr 2*p*1/2*p*3: 584.7/575.7 eV) can be derived from the post-synthesis process by using a Cr_2O_3/H_2SO_4 mixture to oxidise sp^2 carbon elements.[208] From the survey spectra, there is no evidence that other metallic impurities are present in the DND sample. It is because of this that the as-received DND sample might be purified with acid mixture (*e.g.,* hydrochloric acid/nitric acid mixture).[203],[209] The O1*s* peaks are located at 529.4 eV, which can be associated with the surface ether, hydroxyl, and carbonyl bonds.[189] The N1*s* spectrum included two components with fitted peaks at 400.8 eV and 397.8 eV. The N 1*s* spectrum at 400.8 eV is the evidence of interaction with oxygen and the other one represents nitrogen atoms incorporated into the DND cores.[210]

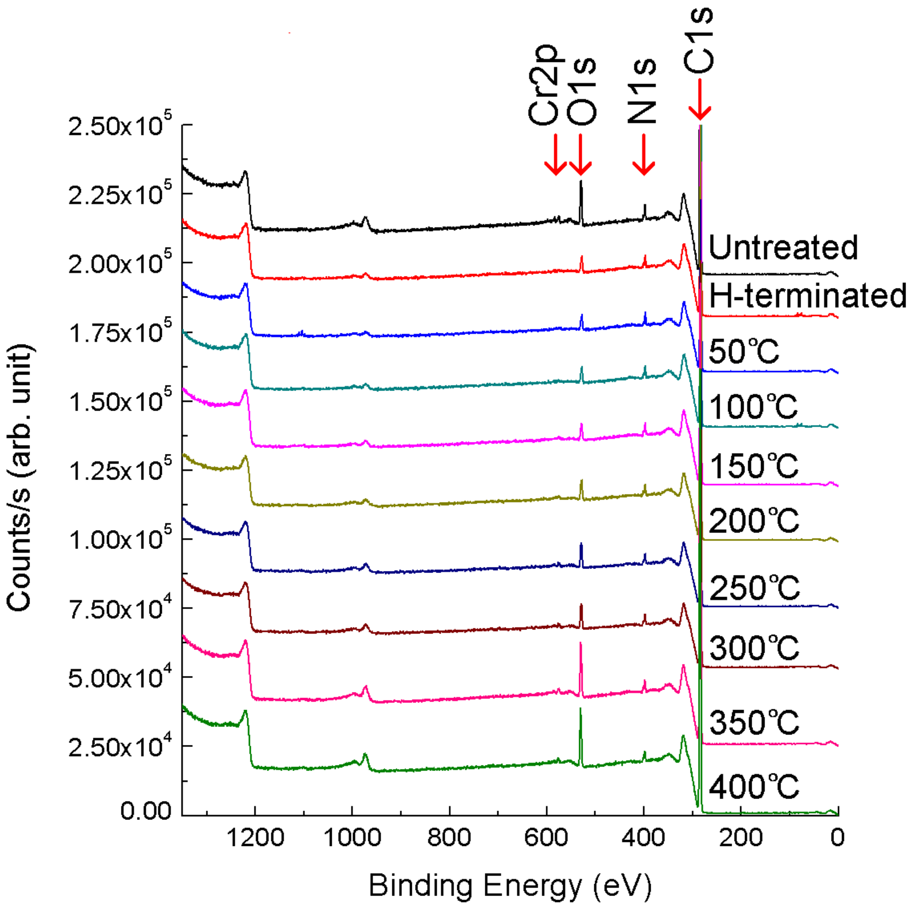

Figure 6.8 XPS survey spectra of DND samples. The top of these C1s peaks have been cut off to highlight the other contents.

For the untreated DND samples, impurities such as oxygen and nitrogen can be attributed to the reaction occurring during the detonation process, which contains oxygen-deficient trinitrotoluene (TNT) and hexogen composition.[211] After the hydrogen termination process, the oxygen composition content has significantly decreased, while nitrogen and chromium peaks remain as before. The percentage of each composition has been listed in **Table 6.1**. From the table, it is clearly observed that the chromium content for each sample is constant before/after hydrogen plasma treatment. As the annealing temperature increased up to 150˚C or above, the oxygen percentage increased as well. Meanwhile, the nitrogen concentration slightly increased together with the increasing annealing temperature from 50˚C to 350˚C.

Table 6.1 XPS survey analysis and content of all the elements in DND sample.

Sample	N1*s* Content (at.%)	O1*s* Content (at.%)	C1*s* Content (at.%)	Cr2*p* Content (at.%)
Untreated	1.5	4.2	94.0	0.3
H-terminated	2.6	1.6	95.5	0.3
50˚C	1.6	1.7	96.3	0.4
100˚C	1.6	2.0	96.1	0.3
150˚C	1.6	1.9	96.2	0.3
200˚C	1.8	2.5	95.4	0.3
250˚C	2.0	3.3	94.4	0.3
300˚C	2.0	5.3	92.3	0.4
350˚C	2.0	4.9	92.8	0.3
400˚C	1.7	5.0	93.0	0.3

6.4 Analysis

6.4.1 Electrical Properties

According to the **Equation 6.3**, when n=3, this equation indicates that there are three conduction mechanisms in the semiconductor material namely: electrode, grain interiors (GI) and grain boundaries (GB).[184]~[187] It was already established in literature that the capacitance associated with grain boundary (C_{GB}) is 2-3 orders of magnitude higher than the capacitance associated with the grain interior (C_{GI}). The parameters R_{p} and C_{p} were extracted from the fitting equivalent circuit and shown in **Table 6.1**. The paralleled resistance R_{p} and capacitance C_{p} represent the intrinsic resistivity and the dielectric properties of the H-DND. The R_{p} was varying together with the evaluating temperature but the parallel capacitance C_{p} was constantly located at pico-farad (pF) level, which suggested C_{p} has little relationship with the surface modification and the thermal annealing process.

Comparing the IS response of the H-DND with the untreated DND sample, a Warburg component was found in the equivalent circuit in the hydrogen-terminated sample. Zang and Portet *et al*. proposed similar Warburg components, which were observed in electrochemical experiments on DND powder.[202],[212] The origin of the Warburg component can be attributed from: (1). the porous structure and the surface roughness; (2). the infinite-element approximation of the material.[201][202] Both of the proposed mechanisms are feasible. At a temperature range lower than 100 °C, the aggregated DND can be considered as a certain kind of porous material with a grain size of micrometers.[181] On the other hand, the aggregated DND powder can be considered as a 3-D dimensional network of individual DND particles in the proposed equivalent circuit model, which is different from continues single/polycrystalline diamond film.[202] The hydrogen plasma treatment might contribute to surface mutual interactions with the presence of the C-H bonds on the surface between each DND particle, which was linked together to form an infinite-element network.

Chaudhary *et al*. reported a DND capacitance of ~10 pF between the temperature ranging from 23 to 150˚C and attributed it to a grain boundary contribution.[193] Bevilacqua *et al*. studied the impedance response of the untreated DND powder and concluded that a ‘grain-interior-like’ electrical conduction below 350˚C, but possibly switched to surface-interface conduction at higher temperature.[192] In our IS measurement of H-DND, there was only single semicircle response observed while the temperature heating up, which indicated only one conduction mechanism occurred during the whole process (**Figure 6.4 (a)-(f)**). The average grain size indicates that the effect of the small-size and the large surface area-to-volume ratio may reduce the capacitance C_p, compared with the capacitance calculated in single/poly-crystalline diamond films. The hydrogen-termination treatment enhanced the grain boundary conduction on the surface of the DND particles and grain interior effect from the core was undermined. Thus, the GB conduction in the IS plot dominated, whilst little evidence for GI conduction was found.[213] Hence, we associated that the capacitance with the grain boundaries conduction contribution for H-DND.

During the temperature elevating process, two Activation energy levels, E_{act1} and E_{act2}, were calculated from the Arrhenius plot, which suggested two different types of conduction principles. It is noteworthy that E_{act1} located between 170 °C and 225 °C, accompany with the significantly increase of resistance R_p. Followed by the slightly decreasing resistance R_p, the Arrhenius curve had a slight drop and an activation energy E_{act1}, of 0.089 eV was deduced. It is known that the hydrogen-termination on single-crystalline diamond film can improve the surface conduction and create a negative-electron-affinity (NEA) surface.[214] Landstrass *et al*. proposed that the conduction might be caused by the movements of hydrogen and defects from nonactive sites during the annealing process.[215] Botev *et al*. presented an activation energy of 0.1 eV from undoped diamond film by charged-based deep-level transient spectroscopy (Q-DLTS) method.[216] Mori *et al*. assumed an existence of surface conductive layer caused by chemical absorption or oxidization.[217] Here, we suggested that the mechanism might be explained as the contribution from surface hydrogen-termination charge carriers on the DND outside shell.

At the temperature from 250°C to 350°C, the activation E_{act2}=0.63 eV could be calculated by fitting the Arrhenius curve. This level of activation is closed to the *n*-type phosphorous doping in diamond film.[218] However, further XPS analysis proven that the DND powder was completely free of phosphorous element. Various explanations to this activation energy level have been proposed by other researchers. Ye *et al.* studied the dielectric properties of nanocrystalline diamond film and found an activation energy of 0.67 eV. The author assumed that the phenomenon might be the change of the crystal field caused by thermal expansion, or by surface bond concentration of nanosized particles.[194] Werner and Huang *et al.* have assigned this effect to the space charge limited current and Poole-Frenkel mechanism for the non-linear electrical response.[221],[222] Here, we associated the activation energy with the crystalline defects, or the surface sp^2 carbon phase (non-diamond materials), which had been reported in undoped diamond film.[221],[224]

6.4.2 Thermal Stability

The FTIR and XPS study focused on the thermal stability of the H-DND. In comparison, the CVD diamond film can be oxidized while heating in an oxygen atmosphere over 500˚C.[223] Previous reports on diamond powder with a micrometer-range grain size indicated the oxidization temperature was 477˚C.[192] Zou *et al.* found that 5-nm DND started to incorporate with the oxygen in air at 228˚C by thermogravimetric analysis (TGA) and completely oxidized over around 600˚C.[225] Based on the FTIR and XPS analysis on DND powder in our research, the state of the DND powder had incorporation with oxygen occurred between the temperature of 100˚C and 150˚C. At this range, the C-O bonds formed in the state of hydroxyl groups. The C=O bonds appears at annealing temperatures higher than 300˚C. The incorporation of the nitrogen could be divided into two states: the first one can be derived from the nitrogen atoms in the core of the DND particles during the detonation process, and the other one is the surface cyclic carbon lactams (C=NH).[185] The later one can be demolished while the temperature is higher than 350˚C. As the annealing temperature increases over 400˚C, the homogeneity of DND powder was enhanced. The FTIR results also revealed that the C-H bonds could survive in the environment temperature as high as 400˚C after hydrogen-termination process.

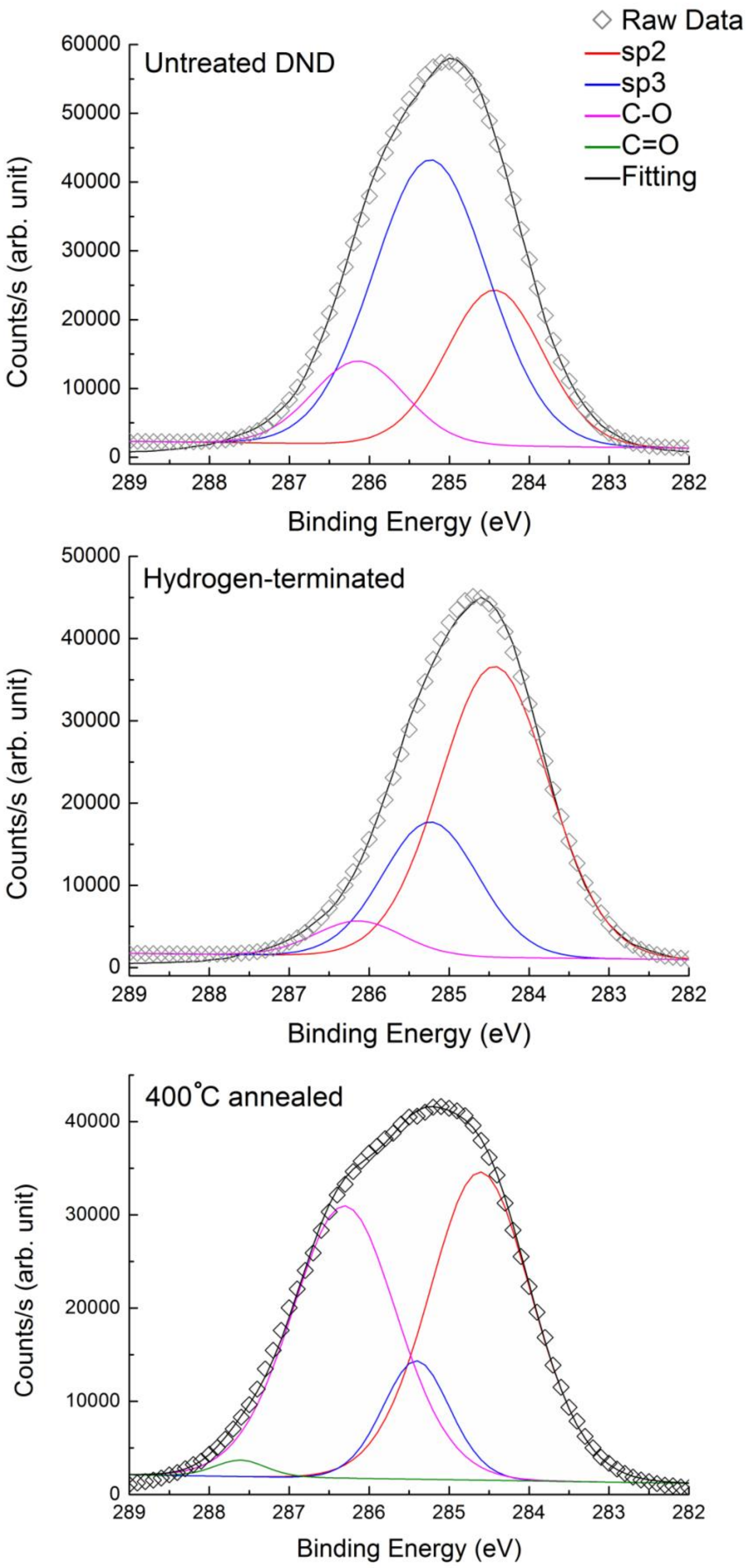

Figure 6.9 C1s XPS spectra data, fitted curves (in square) and synthesized peaks, which has been assigned as C *sp*^{2} (284.6±0.1 eV), C *sp*^{3} (285.4±0.1 eV), C-O (286.3±0.1 eV), and C=O (287.3±0.1 eV).

The C1*s* core peaks on intrinsic, H-terminated and after 400°C annealing samples were extracted from wide survey spectra and synthesized on **Figure 6.9**. The sp^2 hybridized carbon peak can be synthesized and observed at 284.6 eV, which has been reported ~0.8 eV lower than the sp^3 peak. The C-O/C=O peaks locate at +1.7 and +3.0 eV higher than the sp^2 band, respectively.[190],[191]

In **Figure 6.9**, it is obvious to observe that the C1*s* core peak centre shifted from 284.9 eV up to 284.6 eV after H-termination process. This significant change proves that the concentration of the C-O/C=O bonds have been removed during the H-termination process. During the thermal treatment, the oxygen concentration increases as the temperature changes because of the oxidisation on the DND's particles. Therefore, the C 1*s* core peaks shift from the lower BE to higher BE. When the temperature of the stage reaches 400˚C, the C 1*s* peak of H-DND has a higher BE even than the untreated sample. It is reasonable to predict the thermal treatment oxidises the DND surface and the oxygen content increases.

Table 6.2 Synthesis of C1*s* peak

Sample	C1*s* Synthesis Peaks	Binding Energy (eV)	FWHM (eV)	Concentration (At.%)
untreated	sp^2	284.6	1.47	27.3
	sp^3	285.4 (sp^2+0.8)	1.74	58.9
	C-O	286.3 (sp^2+1.7)	1.40	13.8
H-terminated	sp^2	284.6	1.66	66.6
	sp^3	285.4 (sp^2+0.8)	1.45	27.0
	C-O	286.3 (sp^2+1.7)	1.32	6.4
400˚C annealed	sp^2	284.6	1.57	45.75
	sp^3	285.4 (sp^2+0.8)	1.03	11.51
	C-O	286.3 (sp^2+1.7)	1.61	41.53
	C=O	287.3 (sp^2+2.7)	0.78	1.21

To analyse the surface oxidisation reaction quantitatively, the C1*s* peak has been synthesized. The curves fit three critical samples from the spectra (untreated, H-terminated and after thermal treated at 400˚C). All the fitted curves using Lorentzian-Gaussian method with a full-width half-maximum (FWHM) value lower than 1.8 eV as shown on **Figure 6.9**. The synthesized peaks data extracted from the synthesis have been listed on **Table 6.2**. The C *sp*^{2} shoulder is located at ~284.6 eV after calibration, which is 0.8 eV BE lower than the *sp*^{3} component. Moreover, the carbon-oxygen bonds (C-O) are +1.7 eV higher than *sp*^{2} feature peak. The presence of *sp*^{2} component is in agreement with the previous investigation that the graphitic shells are surrounding the DND cores by HRTEM.[191] The synthesized peak located at 287.3±0.1 eV can be assigned as the carbonyl (C=O) bonds. It is worth to note that the C-O and C=O bonds content decreased after H-termination and significantly increased after thermal treatment at 400˚C. Meanwhile, the *sp*^{2} bonds varied as the different treatment that applied on the DND samples, which indicated that the reaction possibly occurred on the surface shell outside the core.

The thermal stability of DND over 400˚C was studied by Thermogravimetric Analysis (TGA), as shown in **Figure 6.10**. At the temperature lower than 100˚C, the weight loss of DND can be explained as the loss of absorbed water on the DND outer surface. As the temperature reached ~450˚C, the irreversible phase transformation occurred and the weight loss dropped dramatically.[225] As high as the annealing temperature reached 600~650˚C, the DND sample was completely oxidised and vanished.

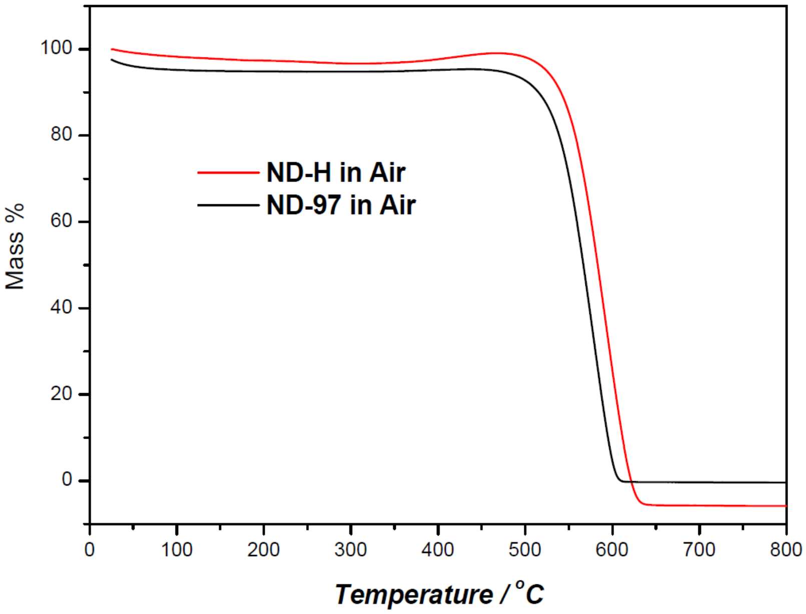

Figure 6.10 TGA measurement of untreated DND, and hydrogen-terminated DND sample in air.

6.5 Summary

Figure 6.10 shows the evolution process of DND powder, which can be summarised as following:

1. The as-received stated DND powder is a mixture of aggregated nanodiamond, surface absorbed water, and metal residues resulting from the detonation process. For the nanodiamond surface, most of the original bonds are C-O, and C=O bonds.(**Figure 6.11 (a)**)
2. After hydrogen plasma treatment, the surface of nanodiamond was transformed to C-H bonds and most of the oxygen content was removed. At this stage, the surface C-H bonds serve as links between DND cores and surface absorbed water. Hence, the conduction path leads to a Warburg diffusion effect, which represents an infinite-length approximation of DND particles stacked together and mutual interaction after hydrogen passivation process.(**Figure 6.11 (b)**)
3. At this temperature, the surface of DND powder was incorporated with nitrogen in air and formed cyclic lactam (=NH/-NH_2). The water absorption still exists on the outer shell. Thus the conduction was mainly driven by the absorbed water and the Warburg effect remained.(**Figure 6.11 (c)**)
4. As the annealing temperature reached 200˚C, the surface of the DND was oxidised and hydroxyl bonds (-OH) were formed. (**Figure 6.11 (d)**)
5. After the DND was annealed at 300˚C, the C=O (carbonyl) was generated. The resistance at this stage was at its maximum. (**Figure 6.11 (e)**)
6. Finally, when the DND powder was heated at 400˚C, the nitrogen content was removed completely from the surface. The Warburg effect appeared again as it was in the room temperature range, which suggested the phenomenon might be associated with the surface homogeneity of the DND particles.(**Figure 6.11 (f)**)

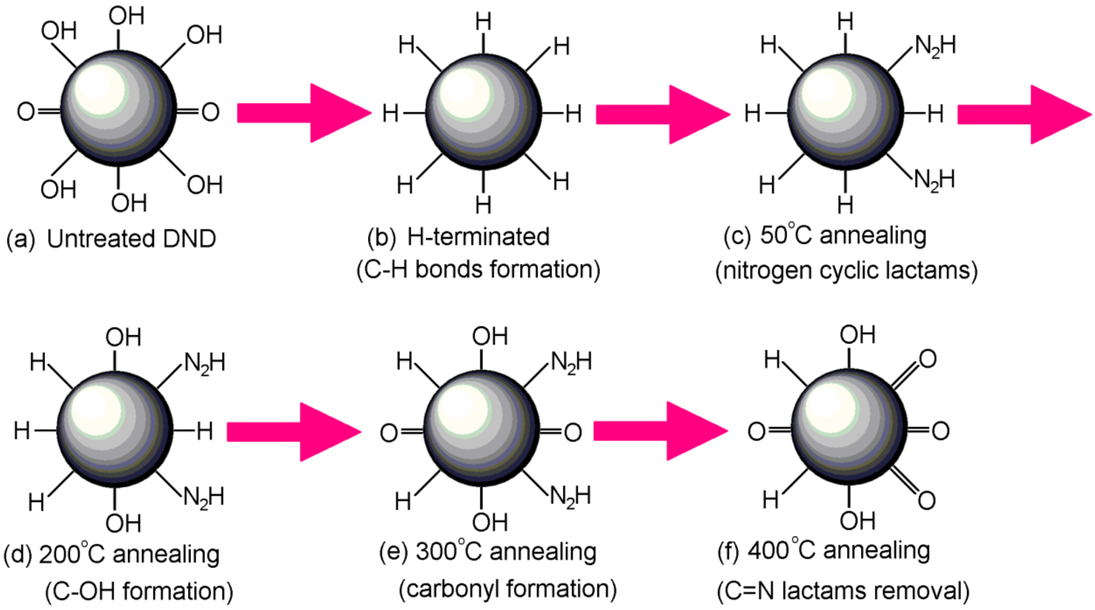

Figure 6.11 Surface chemical bonds evolution of DND (before/after hydrogen plasma treatment, and modification under different annealing temperature).

In this chapter, the thermal stability and conduction mechanism of hydrogen-terminated DND was introduced. This research was the fundamental work for future DND applications, *e.g.* surface modification on DND.[226] The H-DND can be utilised as the raw material for future functionalised ω-alkylcarboxylic acid and ω-alkylamidoamine acid nanodiamond in triglyceride removal application.

Chapter 7: General Discuss of Future Work

General Discuss of Future Work

In the next stage, highly-oriented (100) diamond films will be deposited on (100) silicon wafer and DLC substrates. In addition, the MPECVD method for diamond growth can be extended to deposit other carbon-based materials including carbon nanotubes (CNTs) and graphene. Previous research has been proven that the success of CNTs and grapheme can be synthesised onto metal substrates (*e.g.* copper). This work required a cleaner bell-jar chamber in the CVD system and more accurate flow control. Moreover, confocal Raman and TEM are both necessary for the characterisation of CNTs and graphene.

For the femtosecond laser inscription technique, the ultra-fast patterning on diamond has been achieved. The next step is to utilise physical vapour deposition (PVD) to fabricate metal electrodes, which can be further developed into electronic devices such as UV detectors. Besides, the physical model of femtosecond laser propagation in diamond is an interesting topic. The group has initiated the modelling work in collaboration with Dr. Vladimir Mezentsev. The 2-D plot of transient Gaussian laser energy distribution can be simulated by COMSOL software.[6] The critical problem is that the existing numerical model is based on the inscription inside the bulk, which is not suitable for the surface inscription. Besides, the femtosecond laser inscription can be utilised in some of the other carbon-based materials as well.

After the electrical properties of nanodiamond were investigated and the equivalent circuits were proposed, the detailed conduction mechanism can be further studied. In addition, other surface modification on nanodiamond can be researched and the fundamental conduction mechanism will be linked with the crystal lattice, dopant or surface modification. This work may require Nuclear Magnetic Resonance (NMR) equipment and a better metal-semiconductor contact (C-Au/Pt) to reduce the influence of non-Ohmic contact.

As the development in carbon-based electro-spun fibres in our group, the future study will be extended to a diamond coated fibres with the MPECVD system. Meanwhile, the DND particles could also be added in the DMF solution to improve the mechanical and chemical properties of these fibres.

For the future research, the nanodiamond particles synthesised by Spark Plasma Sintering (SPS) technology can be studied for super high volume-to-surface ratio materials. This material can be utilised as a supercapacitor material or a water-insoluble drug delivery carrier.

---

[6] COMSOL® Multiphysics

Chapter 8: Conclusion

Conclusions

In conclusion, this thesis has presented a systematically investigation of diamond material, including its properties, characterisation and application. The thesis started from a literature review of the diamond basic properties and several other applications in Chapter 2. Then, the most common techniques used for characterising nano-carbon materials were summarised in the Chapter 3. Following by Chapter 3, the main work was introduced in another three chapters.

The successful installation of the MPECVD system enabled the potential carbon-related materials (including diamond) deposition on a variety of substrates, which was presented in Chapter 4. The preliminary work studied the feasibility of diamond deposition on silicon wafers (100) and (111), diamond-like carbon films and silica fibres. The successful deposition of random-oriented and (111) diamond crystals on different substrates has provided a solid foundation work for the future research tasks. Based on the analysis from SEM and Raman, a suitable deposition condition for a uniform and well-coverage diamond film was revealed. This study built up a solid fundamental work for the future research work.

One of the main achievements of this thesis is the femtosecond laser inscription on a diamond substrate. The femtosecond laser technique is an ultra-fast inscription method on the diamond surface. After characterisation by SEM, Raman spectroscopy, XPS and AFM, the graphitic composition that formed on the inscribed area was studied. The results proved that the area under laser irradiated was changed to carbon sp^2 state with periodical ripples. An effective method to completely remove the graphitic layer by strong acid solvent and H^+ plasma etching has also been developed. By comparing the depth from the AFM results, the femtosecond laser inscribed channels have an average graphitic layer of ~ 200nm. Future work will emphasise on the applications of these inscribed structures for biological sensing and theoretical modelling of the inscription process.

The other achievement of this project is the impedance studies of the hydrogen-terminated nanodiamond. A custom-designed testing cell was designed to measure the real-time electrical properties of the nanodiamond at different temperatures. Then, the electrical response was collected and plotted by real part versus imaginary part. The electrical conduction mechanism of hydrogen-terminated nanodiamond was firstly investigated and surface oxidization process on nanodiamond was characterised by FTIR and XPS. The final results indicated the C-H bonds play a critical role during the conduction process, which could successfully sustain under a temperature of 400 $^{\circ}$C. It is the one of the earliest studies on the electrical properties of the DND materials. This research provided an insight into the evolution of the physical and chemical properties of the nanodiamond at elevated temperatures.

In summary, the diamond materials have been proven to have outstanding properties, such as hardness, high thermal conductivity, high carrier mobility, chemical inertness and bio-compatibility, *etc*. This thesis has introduced and investigated several aspects of diamond material's properties, and also demonstrated its potential applications. All these works have built up a solid fundamental study, which can be also extended to a further thorough research.

References

[1]. http://webmineral.com/data/Diamond.shtml#.UJfc0G8xrls (online information)

[2]. *Ultrananocrystalline Diamond: Synthesis, Properties, and Applications*, Edited by A. Shenderova, and D. M. Gruen, William Andrew Publishing, (2006).

[3]. *Diamond Films: Chemical Vapor Deposition for Oriented and Heteroepitaxial Growth*, Edited by K. Kobashi, ELSEVIER, (2005).

[4]. PhD Thesis, S. J. Sque, Bulk and Transfer Doping of Diamond, University of Exeter, (2005).

[5]. C. M. Breeding, and J. E. Shigley, The 'Type' Classification System of Diamonds and its Important in Gemmology, Gem & Gemology, (2009).

[6]. *Fundamental of Physics Extended*, Edited by D. Halliday, R. Resnick, J. Walker, New York: Wiely, (1997).

[7]. *Handbook of Carbon, Graphite, Diamond and Fullerencs-Properties, Processing and Applications*, Edited by H. O. Pierson, William Andrew Publishing, (2004).

[8]. J. B. Cui, J. Ristein, and L. Ley, Electron Affinity of the Bare and Hydrogen Covered Single Crystal Diamond (111) surface, Phys. Rev. Lett., **82**, 429 (1998).

[9]. J. van der Weide, Z. Zhang, P. K. Baumann, M. G. Wnsell, J. Bernhole, and R. J. Nemanich, Negative-electron-affinity effects on the diamond (100) surface, Phys. Rev. B., **50**, 5803 (1994).

[10]. PhD Thesis, M. Gabrysch, Electronic Properties of Diamond, Uppsala University, Department of Engineering Science (2008).

[11]. http://www.ioffe.ru/SVA/NSM/Semicond/Diamond/bandstr.htm (online information)

[12]. E. Kohn, A. Denisenko, M. Kubovic, T. Zimmermann, O. A. Williams, and D. M. Gruen, A New diamond based heterostructure diode, Semicond. Sci. Technol., **21**, L32-L35 (2006).

[13]. J. Isberg, J. Hammersberg, E. Johansson, T. Wikstrom, D. J. Twitchen, A. J. Whitehead, S. E. Coe, and G. A. Scarsbrook, High Carrier Mobility on Single-Crystal Plasma-Deposited Diamond, Science **297**, 5587, 1670-1672 (2002).

[14]. E. Kohn, A. Denisenko, Concept for diamond electronics, Thin Solid Films, **515**, 4333-4339 (2007).

[15]. *Low-Pressure Synthetic Diamond*, Edited by B. Dischler, C. Wild, Chap.17., Springer (1998).

[16]. *Semiconductor Physics and Applications*, Edited by M. Balkanski, R. F. Wallis, Oxford Press (2000).

[17]. *Handbook series on Semiconductor parameters*, Edited by M. E. Levinshtein, S. L. Rumyantsev and M. S. Shur, Vol. 1., World Scientific, Singapore (1996).

[18]. http://www.virginiasemi.com/pdf/generalpropertiessi62002.pdf (online information)

[19]. L. Chen, and M. Lipson, Ultra-low capacitance and high speed germanium photodetectors on silicon, Opt. Exp., **17**, 10, 7901 (2009).

[20]. http://www.e6cvd.com/ (online information)

[21]. http://www.omniadiamonds.com/ (online information)

[22]. www.diamond-materials.com/, "The CVD diamond booklet", Advanced Diamond Technology.(online information)

[23]. *Fundamental Optical Properties of Materials I, Optical Properties of Condensed Matter and Applications*, Edited by W. C. Tan, K. Koughia, J. Singh, and Sp O. Kasap, John Wiley & Sons. Ltd, (2006).

[24]. http://refractiveindex.info/?group=CRYSTALS&material=C (online information)

[25]. R. Adair, L. L. Chase, and S. A. Payne, Nonlinear refractive index of optical crystals, Phys. Rev. B, **39**, 3337 (1989).

[26]. *Nonlinear Optical Materials, Encyclopedia of Materials: Science and Technology*, Edited by R. W. Boyd, and G. L. Fisher, Elsevier Science Ltd., 6237-6244 (2001).

[27]. T. Roth, R. Laenen, Absorption of free carriers in diamond determined from the visible to the mid-infrared by femtosecond two-photon absorption spectroscopy, Opt. Comm., **189**, 289-296 (2001).

[28]. *Diamond Electrochemistry*, Edited by A. Fujishima, Y. Einaga, T. N. Rao, and D. A. Tryk, Elsevier BKC Tokyo (2005).

[29]. Yu. V. Pleskov, Electrochemistry of Diamond: A Review, Russ. J. Electrochem. **38**, 1275-1291 (2002).

[30]. *Thin-Film Diamond I: (Part of the Semiconductors and Semimetals Series)*, Edited by C. E. Nebel, J. Ristein, Elsevier (2003).

[31]. http://www.ceb.cam.ac.uk/pages/linear-sweep-and-cyclic-voltametry-the-principles.html (World Wide Web page information)

[32]. N. Dubrovinskaia, S, Dub, and L. Dubrovinsky, Superior Wear Resistance of Aggregated Diamond Nanorods, Nano. Lett., **6**, 824-826 (2006).

[33]. M. R. Ayatollahi, E. Alishahi, S. Shadlou, Mechanical Behaviour of Nanodiamond /Epoxy Nanocomposite, Int. J. Frat., **170**, 95-100 (2011).

[34]. V. V. Danilenko, Shock-Wave Sintering of Nanodiamonds, Phys. Sol. Stat., **46**, 711-715 (2004).

[35]. P. W. May, Diamond Thin Films: a 21st-century Material, Phil. Trans. R. Soc. Lond A, **358**, 473-495 (2000).

[36]. http://www.chm.bris.ac.uk/motm/diamond/diamprop.htm (online information)

[37]. http://www.diamond-materials.com/downloads/cvd_diamond_booklet.pdf (online information)

[38]. J. J. Gracio, Q. H. Fan, and J. C. Madalemo, Diamond Growth by Chemical Vapour Deposition, J. Phys. D: Appl. Phys. **43**, 374017 (2010).

[39]. F. P. Bundy, H. T. Hall, H. M. Strong, and R. H. Wentorf, Man-made diamonds, Nature, **176**, 51 (1955).

[40]. T. P. Mollart, and K. L. Lewis, Optical-quality diamond growth from CO_2-containing gas chemistries, Diam. Relat. Mater. **8**, 236 (1999).

[41]. O. Dorsch, K. Holzner, M. Werner, E. Obermaier, R. E. Harper, C. Johnston, P. R. Chalker, and I. M. Buckley-Golder, Piezoresistive effect of boron-doped diamond thin films, Diam. Relat. Mater., **2**, 1096 (1993).

[42]. M. Adamschik, R. Müller, P. Gluche, A. Flöter, W. Limmer, R. Sauer, E. Kohn, Analysis of piezoresistive properties of CVD-diamond films on silicon, Diam. Relat. Mater., **10**, 1670 (2001).

[43]. E. Kohn, P. Gluche, M. Adamschik, “Diamond MEMS-a new emerging technology”, Diam. Relat. Mater., **8**, 934-940 (1999).

[44]. T. Yamada, T. Yokoyama, and A. Sawabe, Electron emission from hydrogenated and oxidized heteroepitaxial diamond doped with boron, Diam. Relat. Mater., **11**, 780 (2002).

[45]. E. Kohn, M. Adamschik, P. Schmid, A. Denisenko, A. Aleksov, and W. Ebert, Prospects of diamond devices, J. Phys. D: Appl. Phys., **34**, R77 (2001).

[46]. K. Hayashi, Y. Yokota, T. Tachibana, K. Kobashi, J. Achard, A. Gicquel, C. Olivero, M. Castex, A. Treshchalov, Temporal response of UV sensors made of highly oriented diamond films by 193 and 313 nm laser pulse, Diam. Relat. Mater., **10**, 1794 (2001).

[47]. K. Takahashi, M. Tanga, O. Takai, and H. Okamura, DNA preservation using diamond chips, Diam. Relat. Mater., **12**, 572 (2003).

[48]. W. Yang, O. Auciello, J. E. Bulter, W. Cai, J. A. Carlisle, Surface functionalization of ultra-nanocrystalline diamond thin-films as stable, biologically active substrate, Nat. Mater., **1**, 253 (2002).

[49]. W. Yang, J. E. Bulter, J. N. Russell, Jr, and R. J. Hamers, Interfacial electrical properties of DNA-modified diamond thin films: Intrinsic response and hybridization-induced field effects, Langmuir, **20**, 6778 (2004).

[50]. T. N. Rao, I. Yagi, T. Miwa, D. A. Tryk, and A. Fujishima, Electrochemical oxidization of NADH at highly boron-doped diamond electrode, Anal. Chem., **71**, 2506 (1999).

[51]. C. E. Nebel, D. Shin, B. Rezek, N. Tokuda, H. Uetsuka, and H. Watanabe, Diamond and biology, J. R. Soc. Interface, **4**, 439 (2007).

[52]. W. Yang, J. E. Bulter, J. N. Russell, Jr. and R. J. Hamers, Direct electrical detection of antigen-antibody binding on diamond and silicon substrate using electrical impedance spectroscopy, Analyst, **132**, 296 (2007).

[53]. H. B. Suffredini, V. A. Pedrosa, L. Codognoto, S. A. S. Machado. R. C. Rocha-Filho, and L. A. Avaca, Enhanced electrochemical response of boron-doped diamond electrodes brought on by a cathodic surface pre-treatment, Electro. Acta., **49**, 4021 (2004).

[54]. V. N. Mochalin, O. Shenderova, D. Ho, and Y. Gogotsi, The properties and applications of nanodiamonds, Nat. NanoTech., **7**, 11 (2012).

[55]. O. A. Shenderova, D. M. Greun, Ultrananocrystalline Diamond: Synthesis, Properties, and Applications., Usp Khim., **70**, 687 (2001).

[56]. A. M. Schrand, S. A. Ciftan Hens, and O. A. Shenderova, Nanodiamond Particles: Properties and Perspectives for Bioapplications, Sol. Stat. Mater. Sci., **34**, 18 (2009).

[57]. V. V. Danilenko, Synthesis, Properties, and Applications of Ultrananocrystalline Diamond, Proc. NATO Advance Research Workshop, **181** (2005).

[58]. V. Y. Dolmatov, Detonation synthesis ultradispersed diamonds: Properties and applications, Russ. Chem. Rev., **70**, 607 (2001).

[59]. O. Shenderova, A. Koscheev, N. Zaripov, et al., Surface Chemistry and Properties of Ozone-Purified Detonation Nanodiamonds, J. Phys. Chem. C, **115**, 9827 (2011).

[60]. A. S. Chiganov, Selective inhibition of the oxidization of nanodiamonds for their cleaning, Phys. Sol. Stat., **46**, 620 (2004).

[61]. E. V. Pavlov, and J. A. Skrjabin, Method of removal impurities of non-diamond carbon and device fofr its realization, RU Patent 2168462 (1999).

[62]. I. S. Larionova, I. N. Molostov, L. S. Kulagina, and V. F. Komarov, Method of purification of synthesis ultradispersed diamonds, RU Patent, 2168462 (1999).

[63]. W. W. Zheng, et al., Organic functionalization of ultradispersed nanodiamond: synthesis and applications, J. Mater. Chem., **19**, 8432 (2009).

[64]. S. F. Ji, T. L. Jiang, K. Xu, and S. B. Li, FTIR study of absorption of water on ultradispersed diamond powder surface, Appl. Surf. Sci., **133**, 231 (1998).

[65]. J. C. Arnault, Surface chemical modification and surface reactivity of nanodiamond hydrogenated by CVD plasma, Phys. Chem. Chem. Phys., **13**, 11481 (2011).

[66]. G. V. Lisichkin, I. I. Kulakova, Y. A. Gerasimov, A. V. Karpukhin, and R. Y. Yalkovlev, Halogenation of detonation-synthesis nanodiamond surface, Mendeleev Commun., **19**, 309 (2009).

[67]. Y. Liu, V. N. Khabashesku, and N. J. Halas, Fluorinated nanodiamond as a wet chemistry precursor for diamond coating covalent bonded to glass surface, J. Am. Chem. Soc., **127**, 3712 (2005).

[68]. L. Li, Van Der A. E. Ende, J. L. Davidson, and C. M. Likehart, Nanodiamond/polymer brushes: Synthesis, characterisation and application, Abstr. Paper Am. Chem. Soc., **231** (2006).

[69]. A. Krueger, The structure and reactivity of nanoscale diamond, J. Mater. Chem., **18**, 1485 (2008).

[70]. Y. R. Chang, *et al*., Mass production and dynamic imaging of fluorescent nanodiamond, Nat. Nanotech., **3**, 284 (2008).

[71]. S. C. Hens, *et al*., Nanodiamond bioconjugate probes and their collection by electrophresis, Diam. Relat. Mater., **17**, 1858 (2008).

[72]. L. C. L. Huang, and H. C. Chang, Absorption and immobilization of cytochrome C on nanodiamonds, Langmuir, **20**, 5879 (2004).

[73]. K. K. Liu, C. L. Cheng, C. C. Chang, and J. I. Chao, Biocompatible and detectable carboxylated nanodiamond on human cell, Nanotechnology, **18** (2007).

[74]. A. M. Schrand, Characterization and in vitro biocompatibility of engineered nanomaterials, The school of Engineering, University of Dayton, OH. 276 (2007).

[75]. *Applications of detonation nanodiamond*, Edited by V. Y. Dolmatov, William Andrew Publishing, Norwich, NY, USA, 513 (2006).

[76]. H. J. Huang, E. Pierstorff, E. Osawa, and D. Ho, Protein-mediated assembly of nanodiamond hydrogels into a biocompatible and biofunctional multilayer nanofilm, ACS Nano, **2**, 203 (2008).

[77]. M. Chen, E. D. Pierstorff, R. Lam, S. Li, H. Huang, E. Osawa, and D. Ho, Nanodiamond-Mediated Delivery of Water-Insoluble Therapeutics, ACS Nano., **3**, 2016 (2009).

[78]. K. Liu, W. Zheng, C. Wang, Y. Chiu, C. Cheng, Y. Lo, C. Chen, and J. Chao, Covalent linkage of nanodiamond-paclitaxel for drug delivery and cancer therapy, Nanotech., **21**, 315106 (2010).

[79]. E. Ozawa, and D. Ho, Nanodiamond and its application to drug delivery, J. Med. Alli. Sci., **2**, 31 (2012).

[80]. C. Fu, H. Lee, K. Chen, T. Lim, H. Wu, P. Lin, P. Wei, P, Tsao, H. Chang, W. Fann, Characterization and application of single fluorescent nanodiamond as cellular biomarkers, PNAS, **104**, 727 (2007).

[81]. X. Cui, X. Liu, A. S. Tatton, S. P. Brown, H. Ye, and A. Mash, Nanodiamond Promotes Surfactant-Mediated Triglyceride Removal from a Hydrophobic Surface at or below Room Temperature, ACS Appl. Mater. Inter., **4**, 3225 (2012).

[82]. *Biological and Biomedical Coating Handbook: Applications, Chapter 4 Impedance Spectroscopy on Carbon Based Materials for Biological Application*, Edited by H. Ye, and S. Su, CRC Press, Taylor & Francis Group, (2011).

[83]. R. M. Hazen, R. T. Downs, A. P. Jones, and L. Kah, Carbon Mineralogy and Crystal Chemistry, Rev. Mineral. Geochem., **75**, 7 (2013).

[84]. PhD thesis, R. K. B. Ahmad, *Diamond Nanostructure Devices for Chemical Sensing Applications*, University College London, (2011).

[85]. *Diamond Films: Chemical Vapor Deposition for Oriented and Heteroepitaxial Growth*, K. Kobashi, ELSEVIER, Ltd. (2005).

[86]. http://sekidiamond.com/pdf/AX5010-INT_Brochure_R1.pdf (online information)

[87]. X. L. Peng, T. W. Clyne, Formation and adhesion of hot-filamnet CVD diamond films on titanium substrate, Thin Solid Films, **293**, 261-269 (1997).

[88]. http://serc.carleton.edu/research_education/geochemsheets/techniques/SEM.html (online information)

[89]. http://cime.epfl.ch/files/content/sites/cime2/files/shared/Files/Teaching/MSE_603_2011_spring/Chapter%203%20-%20SEM.pdf (online information)

[90]. H. Maeda, K. Ohtsubo, M. Irie, N. Ohya, K. Kusakabe, and S. Morooka, Determination of diamond [100] and [111] growth rate and formation of highly orientation diamond film by microwave plasma-assisted chemical vapor deposition, J. Mater. Res., **10**, 12 (1995).

[91]. C. Wild, R. Kohl, N. Herres, W. Müller-Sebert, P. Koidl, Oriented CVD diamond film: twin formation, structure and morphology, Diam. Relat. Mater., **3**, 373 (1994).

[92]. M. P. D'Evelyn, J. D. Graham, L. R. Martin, The role for methyl radicals and acetylene in [100] vs. [111] diamond growth, Diam. Relat. Mater., **10**, 1627-1632 (2003).

[93]. B. R. Stoner, and J. T. Glass, Texture diamond growth on (100) βSiC via microwave plasma chemical vapor deposition, **60**, 698 (1992).

[94]. Y. Ando, T. Tachibana, and K. Kobashi, Growth of diamond films by a 5-kW microwave plasma CVD reactor, Diamond Relat. Mater. **10**, 312-315 (2001).

[95]. M. Baidakova, A. Vul', New Prospect and Frontiers of Nanodiamond Clusters, J. Phys. D: Appl. Phys. **40**, 6300-6311 (2007).

[96]. E. Barsoukov, J. R. Macdonald, "Impedance Spectroscopy: Theory, Experiment, and Applications", WIELY-INTERSCIENCE PUBLICATION, Chapter 1, (1992).

[97]. PhD thesis, G. M. Wilson, *An investigation of thin amorphous carbon-based sputtered coating for MEMS and micro-engineering applications*, Aston University 2008.

[98]. http://mmrc.caltech.edu/SS_XPS/XPS_PPT/XPS_Slides.pdf (online information)

[99]. I. Kusunoki, M. Sakai, Y. Igari, S. Ishidzuka, T. Takami, T. Takaoka, M. Nishitani-Gamo, T. Ando, XPS study of nitridation diamond and graphite with a nitrogen ion beam, Surf. Sci., **492**, 315 (2001).

[100]. D. Shin, N. Tokuda, B. Rezek, C. E. Nebel, Periodically arranged benzene-linker molecules on boron-doped single-crystalline diamond films for DNA sensing, EltroChem. Comm., **8**, 844-850 (2006).

[101]. *IR and Raman Spectroscopy: Principles and Spectral Interpretation*, P. J. Larkin, ELSEVIER, Chapter 1, (2011).

[102]. A. C. Ferrari, and J. Robertson, Resonant Raman Spectroscopy of disordered, amorphous, and diamondlike carbon, Phys. Rev. B., **64**, 0754141-1 (2001).

[103]. A. C. Ferrari, J. Robertson, Interpretation of Raman spectra of disordered and amorphous carbon, Phys. Rev. B., **61**,14095 (2000).

[104]. D. S. Knight, W. B. White, Characterization of diamond films by Raman Spectroscopy, J. Mater. Res., **2**, 385 (1999).

[105]. A. C. Ferrari, J. Robertson, Origin of the 1150-cm-1 Raman mode in nanocrystalline diamond, Phys. Rev. B., **63**, 121405 (2001).

[106]. R. Kalish, A. Reznik, W. W. Nugent, and S. Prawer, The nature of damage in ion-implanted and annealed diamond, Nucl. Instr. Met. Phys Res. B., **148**, 626-633 (1999).

[107]. J. Wagner, M. Ramsteiner, Ch. Wild, and P. Koidl, Resonant Raman scattering of amorphous carbon and polycrystalline diamond film, Phys. Rev. B., **40**, 1187 (1989).

[108]. R. J. Nemanich, J. T. Glass, G. Lucovsky, and R. E. Shroder, Raman scattering characterization of carbon bonding in diamond and diamondlike films, J. Val. Sci. Technol. A, **6**, 1783 (1988).

[109]. M. Nishitani-Gamo, T. Tachibana, K. Kobashi, I. Sakaguchi, K. P. Loh, K. Yamamoto, T. Ando, Confocal Raman spectroscopic study of the heteroepitaxial diamond growth on Pt (111), Diam. Relat. Mater., **7**, 783-788 (1998).

[110]. Introduction to Fourier Transform Infrared Spectroscopy, Thermo Nicolet Manual Book, mmrc.caltech.edu/FTIR/FTIRintro.pdf

[111]. http://wwwchem.csustan.edu/Tutorials/INFRARED.HTML (online information)

[112]. R. Linares, P. Doering, Properties of large single crystal diamond, Diamond Relat. Mater., **8**, 909-915 (1999).

[113]. T. Jiang, K. Xu, FTIR STUDYOF ULTRADISPERSED DIAMOND POWDER SYNTHESIZED BY EXPLOSIVE DETONATION, Carbon, **33**, 12, 1663-1671 (1995).

[114]. M. Yoshikawa, Y. Mori, M. Maegawa, G. Katagiri, H. Ishida and A. Ishitani, Raman scattering from diamond particles, Appl. Phys. Lett., **62**, 3114 (1993).

[115]. K. Kuznetsov, M. N. Aleksandro, I. V. Zagoruiko, A. L.Chuvilin, E. M. Moroz, V. N. Kolomiichuk, et al. Study of ultradispersed diamond powders obtained using explosion energy, Carbon, **29**, 665 (1991).

[116]. J. O. Orwa, K. W. Nugent, D. N. Jamieson, S. Prawer, Raman investigation of damage caused by deep ion implantation in diamond, Phys. Rev. B., 62, 5461 (1999).

[117]. D. E. Smith, AC Polarography and Related Techniques: Theory and Practice, J. ElectroAnal. Chem., 1, 155 (1966).

[118]. http://www.usm.edu/polymer (online information)

[119]. Impedance Spectroscopy, E. Barsoukov, J. R. Macdonald, 2nd Edition, WIELY-INTERSCIENCE.

[120]. ApplicationNote, Basic of Electrochemical Impedance, GAMRY INSTRUMENTS.

[121]. S. Curat, H. Ye, O. Gaudin, R. B. Jackman, and S. Koizumi, An impedance spectroscopic study of n-type phosphorous-doped diamond, J. Appl. Phys., **98**, 073701 (2005).

[122]. Ph.D Thesis, and M. Bevilacqua, *Electrical properties of diamond nanostructures*, University College London (2010).

[123]. J. Maier, Ionic conduction in space charge region, Prog. Sol. Stat. Chem., **23**, 171 (1995).

[124]. *Impedance Spectroscopy: Theory, Experiment, and Applications*, Edited by E. Barsoukov, J. R. Macdonald, Wiely-Interscience, (2005).

[125]. H. Ye, R. B. Jackman, and P. Hing, Spectroscopic impedance study of nanocrystalline diamond films, J. Appl. Phys., **94**, 12 (2003).

[126]. H. Ye, O. Gaudin, R. B. Jackman, P. Muret, and E. Gheeraer, DC current and AC impedance measurements on boron-doped single crystalline diamond films, Phys. Stat. Sol., **92**, 96 (2003).

[127]. M. Bevilacqua, S. Patel, A. Chaudhary, H. Ye, and R. B. Jackman, Electrical properties of aggregated detonation nanodiamonds, Appl. Phys. Lett., **93**, 132115 (2008).

[128]. B. R. Stoner, C. Kao, D. M. Malta, and R. C. Glass, Hall effect measurement on boron-doped, highly oriented diamond films grown on silicon via microwave plasma chemical vapour deposition, Appl. Phys. Lett., **62**, 2347 (1993).

[129]. Y. Hayashi, and K. Tachibana, Observation of Coulomb-Crystal Formation from Carbon Particles Grown in a Methane Plasma, Jpn. J. Appl. Phys. **33**, L804 (1994).

[130]. H. Kawarada, C. Wild, N. Herres, R. Locher, P. Koidl, and H. Nagasawa, Heteroepitaxial growth of highly oriented diamond on cubic silicon carbide, J. Appl. Phys. **81**, 3490 (1997).

[131]. M. A. Capono, B. C. Kim, A. R. Smith, E. P. Kvam, S.Tsoi, and A. K. Ramdas, Residual strain in cubic silicon carbide measured by Raman spectroscopy correlated with x-ray diffraction and transmission electron microscopy, J. Appl. Phys. **100**, 083514 (2006).

[132]. M. Kahn, M. Cekada, R. Berhauser, W. Waldhauser, C. Bauer, C. Mitterer, E. Brandstätter, Accurate Raman spectroscopy of diamond-like carbon films deposited by an anode layer source, Diam. Relat. Mater. **17**, 1647 (2008).

[133]. D. J. Lockwood, H. X. Xu, and J. -M. Baribeau, Lattice vibration of Si1-xCx epilayer on Si (100), Phys. Rev. B **68,** 115308 (2003).

[134]. Z. H. Ni, W. Chen, X. F. Fan, J. L. Kuo, T. Yu, A. T. S. Wee, and Z. X. Shen, Raman spectroscopy of epitaxial graphene on a SiC substrate, Phys. Rev. B **77**, 115416 (2008).

[135]. J. Wagner, M. Ramsteiner, Ch. Wild, and P. Koidl, Resonant Raman scattering of amorphous carbon and polycrystalline diamond films, Phys. Rev. B. **40**, 1817 (1989).

[136]. R. J. Nemanich, and S. A. Solin, First- and second-order Raman scattering from finite-size crystals of graphite, Phys. Rev. B. **20**, 392 (1979).

[137]. D. S. Knight, and W. B. White, Characterisation of diamond film by Raman spectroscopy, J. Mater. Res. **4**, 385 (1989).

[138]. B. R. Stoner, G. –H. Ma, S. D. Wolter, and J. T. Glass, Characterization of bias-enhanced nucleation of diamond on silicon by in vacuo surface analysis and transmission electron microscopy, Phys. Rev. B **45**, 11067 (1992).

[139]. C. Wild, P. Koidl, W. Müller-Sebert, H. Walcher, R. Kohl, N. Herres, and R. Locher, Chemical vapour deposition and characterization of smooth {100}-faceted diamond films, Diam. Relat. Mater. **2**, 158 (1993).

[140]. Y. Ando, Y. Yokota, T. Tachibana, A. Watanabe, Y. Nishibayashi, K. Kobashi, T. Hirao, K. Oura, Large area deposition of <100>-textured diamond films by a 60-kW microwave plasma CVD reactor, Diam. Relat. Mater. **11**, 596 (2002).

[141]. K. Kobashi, K. Nishimura, Y. Kawate, and T. Horiuchi, Synthesis of diamonds by use of plasma chemical-vapor deposition: Morphology and growth of diamond films, Phys. Rev. B **38**, 4067 (1988).

[142]. S. D. Wolter, B. R. Stoner, J. T. Glass, P. J. Ellis, D. S. Buhaenko, C. E. Jenkins, and P. Southworth, Textured growth of diamond on silicon via in situ carburization and bias-enhanced nucleation, Appl. Phys. Lett. **62**, 1215 (1993).

[143]. H. Maeda, K. Ohtsubo, M. Irie, N. Ohya, K. Kusakabe, and S. Morooka, Determination of diamond [100] and [111] growth rate and formation of highly oriented diamond film by microwave plasma-assisted chemical vapour deposition, J. Mater. Res. **10**, 3115 (1995).

[144]. X. Jiang, C. P. Klages, M. Rölser, R. Zachai, M. Hartweg, H. J. Füsser, Deposition and Characterisation of Diamond Epitaxial Thin Films on Silicon Substrates, Appl. Phys. A **57**, 483 (1993).

[145]. J. J. Gracio, Q. H. Fan, and J. C. Madaleno, Diamond growth by chemical vapour deposition, J. Phys. D: Appl. Phys. **43**, 374017 (2010).

[146]. A. Denisenko, and E. Kohn, Hypothesis on the conductivity mechanism in hydrogen terminated diamond films, Diam. Relat. Mater. **14**, 491 (2005).

[147]. E. Oesterschulze, A. Malavé, U. F. Keyser, M. Paesler, and R. J. Haug, Diamond tips and cantilevers for the characterization of semiconductor devices, Diam. Relat. Mater. **11**, 667 (2002).

[148]. N. Sepulveda, D. Aslam, J. P. Sullivan, Polycrystalline diamond MEMS resonator technology for sensor applications, Diam. Relat. Mater. **15**, 398 (2006).

[149]. J. Iniesta, P. A. Michaud, M. Panizza, G. Cerisola, A. Aldaz, and Ch. Comninellis, Electrochemical oxidation of phenol at boron-doped diamond electrode, Electrochim. Acta. **46**, 3573 (2001).

[150]. G. C. B. Lee, S. Su, J. Li, K. Sugden, N. Roohpour, H. Yan, and H. Ye, Analysis of femtosecond laser surface patterning on bulk single-crystalline diamond, J. Exp. Nanosci. **7**, 662 (2012).

[151]. A. Datta, Y. R. Wu, and Y. L. Yang, Real time observation of ripple structure formation on a diamond surface under focus ion beam bombardment, Phys. Rev. B **63**, 1 (2001).

[152]. Y. Ando, Y. Nishibayashi, K. Kobashi, T. Hirao, and K. Oura, Smooth and high-rate reactive ion etching of diamond, Diam. Relat. Mater. **11**, 824 (2002).

[153]. T. V. Kononenko, M. S. Komlenok, V. P. Pashinin, S. M. Pimenov, V. I. Konov, M. Neff, V. Romano, W. Lüthy, Femtosecond laser micromachining in the bulk of diamond, Diam. Relat. Mater. **18**, 196 (2009).

[154]. G. D. Valle, R. Osellame, and P. Laporta, Micromachining of photonic devices by femtosecond laser pulse, J. Opt. A: Pure Appl. Opt. **11**, 013001 (2009).

[155]. A. M. Ozkan, A. P. Malshe, T. A. Railkar, W. D. Brown, M. D. Shirk, and P. A. Molian, Femtosecond laser-induced periodic structure writing on a diamond crystals and microclusters, Appl. Phys. Lett. **75**, 3716 (1999).

[156]. M. Shinoda, R. R. Gattass, and E. Mazur, Femtosecond laser-induced formation of nanometer-width grooves on synthetic singlecrystal diamond surface, J. Appl. Phys. **105**, 053102 (2009).

[157]. H. O. Jeschke, M. E. Garcia, and K. H. Bennemann, Theory for the ultrafast ablation of graphite films, Phys. Rev. B **60**, R3701 (1999).

[158]. K. E. Carr, Intercalation and oxidation effects on graphite of a mixture of sulphuric and nitric acids, Carbon **8**, 155 (1970).

[159]. Y. von Kaenel, J. Stiegler, J. Michler, and E. Blank, Stress distribution in heteroepitaxial chemical vapour deposited diamond films, J. Appl. Phys. **81**, 1726 (1997).

[160]. Q. G. Zeng, Z. J. Ding, X. D. Tang, and Z. M. Zhang, Pressure effect on photoluminescence and Raman spectra of PPV, J. Lumin. **115**, 32 (2005).

[161]. A. C. Ferrari, and J. Robertson, Raman spectroscopy of amorphous, nanostructured, diamond-like carbon, and nanodiamond, Phil. Trans. R. Soc. Lond. A **362**, 2477 (2004).

[162]. C. Z. Wang, K. M. Ho, M. D. Shirk, and P. A. Molian, Tight-Binding Molecular Dynamics for Carbon and Applications to Nanostructure Formation, Phys. Rev. Lett. **85**, 4092 (2000).

[163]. B. C. Stuart, M. D. Feit, A. M. Rubenchik, B. W. Shore, and M. D. Perry, Ultrashort-pulse laser machining of dielectric materials, Phys. Rev. Lett. **74**, 2248 (1995).

[164]. M. D. Shirk, P. A. Molian, and A. P. Malshe, Ultrashort pulsed laser ablation of diamond, J. Laser Appl. **10**, 64 (1998).

[165]. M. Shinoda, R. R. Gattass, and E. Mazur, Femtosecond laser-induced formation of nanometer-width grooves on synthetic single-crystal diamond surfaces, J. Appl. Phys. **105**, 053102 (2009).

[166]. V. R. Bhardwaj, E. Simova, P. P. Rajeev, C. Hnatovsky, R. S. Taylor, D. M. Rayner, and P. B. Corkum, Fabrication of microchannels in glass using focused femtosecond laser radiation and selective chemical etching, Phys. Rev. Lett. **96**, 057404 (2006).

[167]. *Optical Properties of condensed Matter and Applications*, edited by J. Singh (Wiley, Chichester, West Sussex, 2006), Vol. 6.

[168]. A. C. Ferrari, and J. Robertson, Origin of the 1150 cm-1 Raman mode in nanocrystalline diamond, Phys. Rev. B. **63**, 121405 (2001).

[169]. J. Wagner, C. Wild, and P. Koidl, Resonance effects in Raman scattering from polycrystalline diamond films, Appl. Phys. Lett. **59**, 779 (1991).

[170]. A. C. Ferrari, and J. Robertson, Interpretation of Raman spectra of disordered and amorphous carbon, Phys. Rev. B **61**, 14095 (2000).

[171]. *An investigation of thin amorphous carbon-based sputtered coatings for MEMS and micro-engineering applications*, PhD thesis, G. Wilson, Aston University, (2008).

[172]. M. Yeganeh, P.R. Coxon, A.C. Brieva, V.R. Dhanak, L. Š iller, and Y.V. Butenko, Atomic hydrogen treatment of nanodiamond powder studied with photoemission spectroscopy, Phys. Rev. B **75**, 8 (2007).

[173]. T. Okuchi, H. Ohfuji, S. Odake, H. Kagi, S. Nagamoto, M. Sugata, and H. Sumiya, Micromachining and surface processing of the super-hard nano-polycrystalline diamond by three types of pulsed lasers, App. Phys. A **96**, 833 (2009).

[174]. M. Dubov, I. Bennion, D. N. Nikogosyan, P. Bolger, and A. V. Zayats, J. Opt. A: Pure Appl. Opt. **10**, 025305 (2008).

[175]. M. Chen, E. D. Pierstorff, R. Lam, S. Y. Li, H. Huang, E. Osawa, and D. Ho, Nanodiamond-Mediated Delivery of Water-Insoluble Therapeutics, ACS Nano **3** (7), 2016 (2009).

[176]. G. P. Bogatyreva, M. A. Marinich, E. V. Ishchenko, V. L. Gvyazdovskaya, G. A. Bazalii, and N. A. Oleinik, Application of modified nanodiamonds as catalysts of heterogeneous and electrochemical catalyses, Phys. Sol. Stat. **46** (4), 738 (2004).

[177]. C. C. Fu, H. Y. Lee, K. Chen, T. S. Lim, H. Y. Wu, P. K. Lin, P. K. Wei, P. H. Tsao, H. C. Chang, and W. Fann, Characterization and application of single fluorescent nanodiamonds as cellular biomarkers, P. Natl. Acad. Sci. USA **104** (3), 727 (2007).

[178]. V. S. Bondar', I. O. Pozdnyakova, and A. P. Puzyr', Design of a luminescent biochip with nanodiamonds and bacterial luciferase, Phys. Sol. Stat. **46** (4), 758 (2004).

[179]. T. S. Huang, Y. Tzeng, Y. K. Liu, Y. K. Chen, K. R. Walker, R. Guntupalli, and C. Liu, Immobilization of antibodies and bacterial binding on nanodiamond and carbon nanotubes for biosensor applications, Diamond. Relat. Mater. **13** (4-8), 1098 (2004).

[180]. S. Su, J. Li, V. Kundrát, A. M. Abbot, and H. Ye, Hydrogen-terminated detonation nanodiamond: Impedance spectroscopy and thermal stability studies, J. Appl. Phys. **113**, 023707 (2013).

[181]. *Ultrananocrystalline diamond: Synthesis, Properties, and Applications*, William Andrew, edited by O. A. Shenderova and D. M. Gruen (2007).

[182]. A. M. Schrand, S. A. Ciftan Hens, O. A. Shenderova, Nanodiamond particles: properties and perspectives for bioapplications, Sol. Stat. Mater. Sci. **34**, 18-74 (2009)

[183]. R. Hoffmann, A. Kriele, H. Obloh, J. Hees, M. Wolfer, W. Smirnov, N. Yang, and C. E. Nebel, Electrochemical hydrogen termination of boron-doped diamond, Appl. Phys. Lett. **97**, 052103 (2010).

[184]. H. Ye, O. A. Williams, R. B. Jackman, R. Rudkin, and A. Atkinson, Electrical conduction in polycrystalline CVD diamond: Temperature dependent impedance measurements, Phys. Stat. Sol. A **193** (3), 462 (2002).

[185]. H. Ye, R. B. Jackman, and P. Hing, Spectroscopic impedance studies of nanocrystalline diamond films, J. Appl. Phys. **94** (12), 7878 (2003).

[186]. H. Ye, C. Q. Sun, H. T. Huang, and P. Hing, Dielectric transition of nanostructured diamond films, Appl. Phys. Lett. **78** (13), 1826 (2001).

[187]. H. Ye, O. Gaudin, R. B. Jackman, P. Muret, and E. Gheeraert, DC current and AC impedance measurement on boron-doped single crystalline diamond films, Phys. Stat. Sol. A **199** (1), 92 (2003).

[188]. T. Jiang and K. Xu, FTIR study of ultradispersed diamond powder synthesized by explosive detonation, Carbon **33** (12), 1663 (1995).

[189]. M. Yeganeh, P. R. Coxon, A. C. Brieva, V. R. Dhanak, L. Siller, and Y. V. Butenko, Atomic hydrogen treatment of nanodiamond powder studied with photoemission spectroscopy, Phys. Rev. B **75**, 15 (2007).

[190]. S. Zeppilli, J. C. Arnault, C. Gesset, P. Bergonzo, and R. Polini, Thermal stability and surface modifications of detonation diamond nanoparticles studied with X-ray photoelectron spectroscopy, Diamond. Relat. Mater. **19** (7-9), 846 (2010).

[191]. F. Y. Xie, W. G. Xie, L. Gong, W. H. Zhang, S. H. Chen, Q. Z. Zhang, and J. Chen, Surface characterization on graphitization of nanodiamond powder annealed in nitrogen ambient, Surf. Interface Anal. **42** (9), 1514 (2010).

[192]. M. Bevilacqua, S. Patel, A. Chaudhary, H. T. Ye, and R. B. Jackman, Electrical properties of aggregated detonation nanodiamonds, Appl. Phys. Lett. **93**, 13 (2008).

[193]. A. Chaudhary, J. O. Welch, and R. B. Jackman, Electrical properties of monodispersed detonation nanodiamonds, Appl. Phys. Lett. **96**, 123115 (2010).

[194]. S. Su, J. L. Li, V. Kundrát, A. M. Abbot, and H. Ye, Hydrogen-passivated detonation nanodiamond: An impedance spectroscopy study, Diamond. Relat. Mater. **24**, 49-53 (2011).

[195]. K. Tankala, T. Debroy, M. Alam, Oxidation of diamond film synthesized by hot-filament-assisted chemical vapour deposition, J. Mater. Res. **5**, 2483 (1990).

[196]. A. C. Ferrari, and J. Robertson, Origin of the 1150 cm^{-1} Raman mode in nanocrystalline diamond, Phys. Rev. B **63**, 121405 (2001).

[197]. R. J. Nemanich, J. T. Glass, G. Lucovsky, and R. E. Shroder, Raman scattering characterization of carbon bonding in diamond and diamondlike films, J. Vac. Sci. Technol. A **6**, 1783 (1988).

[198]. N. Tumilty, J. Welch, H. Ye, R. S. Balmer, C. Wort, R. Lang, and R. B. Jackman, Multiple conduction paths in boron δ-doped diamond structures, Appl. Phys. Lett. **94**, 052107 (2009).

[199]. *Fast Ion Transport in Solids*, ELESVIER, edited by M. Kleitz, J. H. Kennedy, P. Vashishta, J. N. Mundy, and G. K. Shenoy, (1979).

[200]. *Impedance Spectroscopy Theory, Experiment, and Applications*, WIELY-INTERSCIENCE, edited by E. Barsoukov, and J. R. Macdonald, (1992).

[201]. N. Gibson, O. Shenderova, T. J. M. Luo, S. Moseenkov, V. Bondar, A. Puzyr, K. Purtov, Z. Fitzgerald, and D. W. Brenner, Colloidal stability of modified nanodiamond particles, Diamond. Relat. Mater. **18** (4), 620 (2009).

[202]. J. B. Zang, Y. H. Wang, S. Z. Zhao, L. Y. Bian, and J. Liu, Electrochemical properties of nanodiamond powder electrodes, Diamond. Relat. Mater. **16**, 16 (2007).

[203]. V. Pichot, M. Comet, E. Fousson, C. Baras, A. Senger, F. Le Normand, D. Spitzer, An efficient purification method for detonation nanodiamonds, Diamond. Relat. Mater. **17** (1), 13 (2008).

[204]. Q. Zou, Y. G. Li, L. H. Zou, and M. Z. Wang, Characterization of structure and surface states of the nanodiamond synthesized by detonation, Mater. Char. **60**, 1257 (2009).

[205]. S. Osswald, G. Yushin, V. Mochalin, S. O. Kucheyev, Y. Gogotsi, Control of sp^2/sp^3 carbon ratio and surface chemistry of nanodiamond powder by selective oxidation in air, J. Am. Chem. Soc. **128**, 11635 (2006).

[206]. P. -H, Chung, E. Perevedentseva, J. -S, Tu, C. C. Chang, C. -L, Cheng, Spectroscopic study of bio-functionalized nanodiamond, Diamond. Relat. Mater. **15**, 622 (2006).

[207]. Y. Kaibara, K. Sugata, M. Tachiki, H. Umezawa, H. Kawarada, Control wettability of the hydrogen-terminated diamond surface and the oxidized diamond surface using an atomic force microscope, Diamond. Relat. Mater. **12**, 560 (2003).

[208]. A. Dementjev, K. Maslakov, I. Kulakova, V.Korolkov, and V. Dolmatov, State of C-atoms on the modified nanodiamond surface, Diamond. Relat. Mater. **16**, 2083-2086 (2007).

[209]. V. N. Mochalin, O. Shenderova, D. Ho, and Y. Gogotsi, The properties and applications of nanodiamonds, Nature Nanotech. **209**, 1 (2011).

[210]. Y. Hu, O. A. Shenderova, Z. Hu, C. W. Padgett, D. W. Brenner, Carbon nanostructures for advanced composites, Rep. Prog. Phys. **69**, 1847 (2006).

[211]. M. Bevilacqua, A. Chaudhary, and R. B. Jackman, The influence of ammonia on the electrical properties of detonation nanodiamond, J. Appl. Phys. **106**, 123704 (2009).

[212]. C. Portet, G. Yushin, and Y. Gogotsi, Electronichemical performance of carbon onions, nanodiamonds, carbon black and multiwalled nanotubes in electrical double layer capacitors, Carbon **45**, 2511 (2007).

[213]. M. Bevilacqua, N. Tumitty, C. Mitra, H. Ye, T. Feygelson. J. E. Butler and J. B. Jackman, Nnaocrystalline diamond as an electrode material: An impedance spectroscopic and Hall effect measurement study, J. Appl. Phys. **107**, 033716 (2010).

[214]. C. E. Nebel, C. Sauerer, F. Ertl, M. Stutzmann, C. F. O. Graeff, P. Bergonzo, O. A. Williams, and R. B. Jackman, Hydrogen-induced transport properties of holes in diamond surface layers, Appl. Phys. Lett. **79**, 45411 (2001).

[215]. M. I. Landstrass, and K. V. Ravi, Resistivity of chemical vapour deposited diamond films, Appl. Phys. Lett. **55**, 1391 (1989).

[216]. A. A. Botev, L. L. Bouilov, B. V. Spitsyn, G. A. Sokolina, V. I. Polyakov, and O. N. Ermakova, Deep level study in polycrystalline diamond film, 3rd Int. Symp. on Diamond Materials 998-1003 (1993).

[217]. Y. Mori, N. Eimori, A. Hatta, T. Ito, and A. Hiraki, Electron affinity of single-crystalline chemical-vapor-deposited diamond studied by ultraviolet synchrotron radiation, Jpn. J. Appl. Phys. Part 2 **31**, L1718 (1992).

[218]. S. Curat, H. Ye, O. Gaudin, and R. B. Jackman, An impedance spectroscopic study of n-type phosphorous-doped diamond, J. Appl. Phys. **98**, 073701 (2005).

[219]. M. Werner, O. Dorsch, A. Hinze, E. Obermeier, R. E. Harper, C. Johnston, P. R. Chalker, and I. M. Buckley-Golder, Space-charge-limited current flow and trap density in undoped diamond films, Diamond. Relat. Mater. **2**, 825 (1993).

[220]. B. Huang, and D. K. Reinhard, Electric field-dependent conductivity of polycrystalline diamond film, Appl. Phys. Lett. **59**, 1494 (1991).

[221]. Y. Muto, T. Sugino, K. Kobashi, and J. Shirafuji, Frequency-dependent conductivity in polycrystalline chemical vapor deposited diamond films, Jpn. J. Appl. Phys. L4, **31** (1992).

[222]. T. Sugino, Y. Muto, K. Karasutani, J. Shirafuji, and K. Kobashi, Electrical characteristics of chemical vapour deposited diamond films, Diamond Relat. Mater. **2**, 803 (1993).

[223]. J. Mort, M. A. Machonkin, and K. Okumura, Compensation effects in nitrogen-doped diamond films, Appl. Phys. Lett. **59**, 455 (1991).

[224]. C. Sun, H. Xie, W. Zhang, H. Ye, P. Hing, Behind the quantum confinement and surface passivation of nanoclusters, J. Phys. D: Appl. Phys. **33**, 2196 (2000).

[225]. Q. Zou, M. Z. Wang, Y. G. Li, L. H. Zou, H. Yu, Y. C. Zhao, Characterization of structure and surface states of the nanodiamond synthesized by detonation, Micro & Nano Lett. **4**, 133 (2009).

[226]. X. Cui, X. Liu, A. S. Tatton, S. P. Brown, H. Ye and A. Marsh, Nanodiamond promotes surfactant-mediated triglyceride removal from a hydrophobic surface at or below room temperature, Appl. Mater. Interface **4** (6), 3225-3232 (2012).

Appendix

Standard Operation Process (SOP) of MPECVD System in Aston University

Important Tips:

1. Please always check the main release valve, make sure it is closed before the experiment.
2. The main release valve can be open only when the chamber is vacuum (about 0 Torr on MKS 250 pressure controller). It must not be used to release in other situation.
3. Do not start the plasma (microwave) without confirming the gas inside the chamber is appropriate.
4. If there is no experiment for a long time, please leave the chamber vacuum.
5. Use the flow controller system (MKS 250 and flow control valve) and its pipe to pump out dangerous/unknown gas.

1. Preparation (Security Examination)

i. Check the main release valve (**Fig.1**) is closed.

ii. Check the gas control panel (**Fig.2**): main valve and three gas valves are all closed.

iii. Plug the main power (**Fig.3**) into the socket and turn on the power switch (**Fig.4**).

iv. Turn on the four switches (**Fig.5, Fig.6**) on the wall which supply power to the PIRANI 11 barometer(**Fig.7**), main rotary fan pump(**Fig.8**), cyclic water cooling system(**Fig.9**), Bronkhost flow controller and MKS 250 pressure controller(**Fig.10**), respectively.

v. Turn on the MKS 250 pressure controller and check the pressure inside the chamber. If the pressure is higher than 0.000×100 Torr, please follow these steps:

vi. Turn off the main pump valve (**Fig.11**), turn on the MKS 250 pressure controller and turn the mode switch to the close. Turn off the pressure control valve (**Fig.12**) as well as the main release valve, and then turn on the rotary fan pump. Open the pressure controller valve and set to manual (Man. On the panel, now the pressure control is 100% open). Wait several minutes till the pressure in the chamber is lower than 0.010×100 Torr. Shut the pressure controller and the valve, then open the Main valve and pump out the rest gas inside chamber. Wait until the pressure is lower than 0.000 Torr (about 20 mins).

vii. Turn on the main switch (microwave power and cooling fan power) on the control panel of the ASTEX (**Fig.13**). Check that the Local/Remote light is on (for local setting) on the microwave power generator (**Fig.14**).

2. Gas supplement

i. Make sure the main release valve is shut off, and there is no air in the chamber (Avoid mixing the air with the hydrogen).

ii. Double check all the valves on the gas flow control panel are closed, as well as the two main valves on the wall.

iii. Open the hydrogen and methane storage cage and turn them on, record the pressure data.

iv. Make sure that the pressure in the chamber is 0.000 or lower. Open the valves on the wall (×2, H_2 and CH_4) and on the panel (×3, Argon, H_2 and methane), as well as the main valve on the panel.

3. Pre-treatment process

i. Turn on the pressure control valve and set the MKS 250 pressure controller to manual (100% open). Turn off the main pump valve.

ii. Set the hydrogen flow value for pre-treatment (about 200-300 s.c.c.m) and set the MKS 250 pressure controller to auto (usually, we set 20 Torr for next step to generate the palsma).

iii. Leave several minutes till reach the set pressure and barometer maintain stable, now the hydrogen gas is filling inside the chamber.

4. Start plasma

i. Set the power below 3/75 (equals to about 600 W), and press ‘HV on’.

ii. Examine that the light blue plasma inside the chamber (around the bell jar, or below that).

iii. Carefully increase the microwave power, until the bowl shape plasma generates (light blue mixed with a bit grey). Now the power level should be around 800-1000. If the bowl does not generate, please turn off the power and turn the power lower than 3/75, then increase again. Repeat this procedure until the bowl plasma is shown.

iv. Changing the phase shifter (**Fig.15**) to make the reflect microwave power is low enough (often around 0 Watt).

5. Pre-heating

i. Gradually increase the pressure to 50 Torr, change the power level up to 1200 W.

ii. Wait for 10 minutes, the surface becomes pink and a bit red, wait for several minutes till it is stable.

6. Nucleating

i. Increase the methane flow rate (2-6 s.c.c.m). Maintain the pressure and microwave power for a certain time (1 hour).

7. Diamond growth

i. Decrease the methane flow rate to 2 s.c.c.m. Maintain the pressure and microwave power for a certain time (more than 2 hours)

8. Surface H-termination process

i. Turn off the methane gas and maintain the condition for at least 20 minutes.

9. Cooling

i. Turn off the microwave power.

ii. Reduce the H_2 gas to 200 s.c.c.m, maintain the state for at least 20 minutes.

iii. Turn off the H_2 gas flow. Wait for the pressure get lower than 3 Torr. Then, switch off the flow control valve and turn the MKS 250 panel controller for ‘auto’ to ‘off’.

iv. Open the main valve. Vacuum the chamber.

10. Take out sample

i. When the chamber is cooling down, take off the four bolts under the sample holder. Carefully take out the metal holder inside.

ii. Weight the sample with electrical balance, and record the data.

11. New sample installation setup

i. Pre-clean process to clean the Mo holder surface.

ii. Weight the substrate with electrical balance, and record the data.

iii. Put the substrate on to the holder (square area on the top), and then vertically insert the metal holder inside the chamber. Screw the four bolts tightly (**Fig.16**).

12. Chamber Vacuum process

i. Turn off the main release valve.

ii. Keep the pressure control pipe is shut down (MKS 250 controller panel is switching to ‘off’) and the pressure control valve is off.

iii. Open the main vacuum valve, pipe out the air inside the chamber (the pressure on MKS 250 is lower than 0.000, about 20 minute).

iv. Turn off the main vacuum valve.

13. Cut off power supply

i. Turn off the microwave main power switch.

ii. Turn off the gas supply valve (on panel ×3, on wall ×2, main valve on panel).

iii. Turn off the gas storage (outside), record the pressure data.

iv. Turn off the rotary vacuum pump.

v. Turn off the two switches inside the control box of the MWCVD.

Figures:

Fig.1 Main release valve

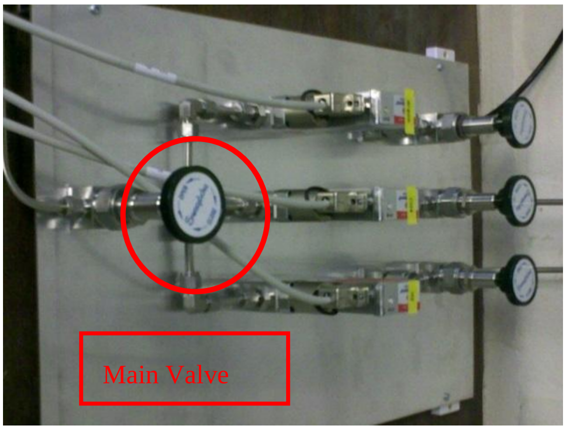

Fig.2 Gas control panel

Fig.3 Main power and socket

Fig.4 Switch for main power supply

Fig.5 Power supply for barometer and pump

Fig. 6 Power supply for MKS 250

Fig.7 PIRANI 11 barometer

Fig.8 main rotary fan pump

Fig.9 cyclic water cooling system

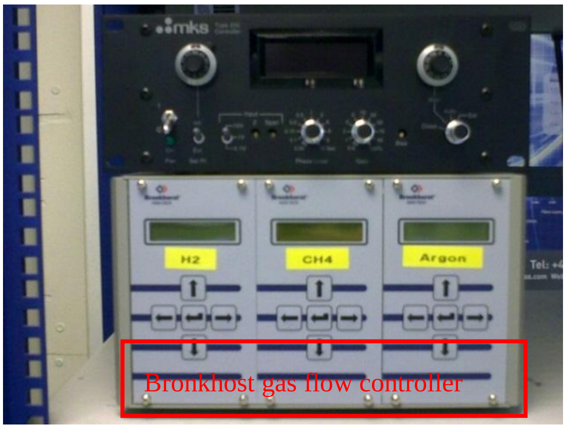

Fig. 10 Bronkhost flow controller and MKS 250 pressure controller

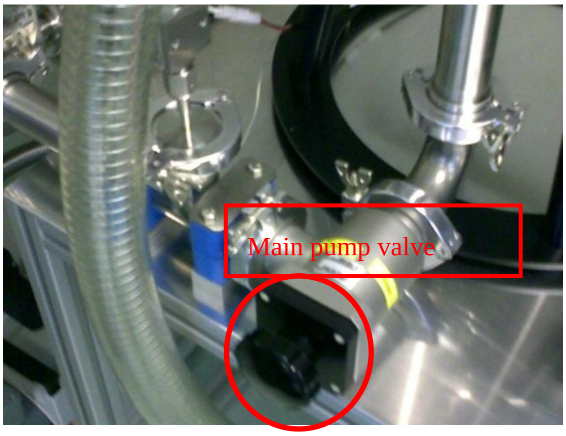

Fig.11 Main pump valve

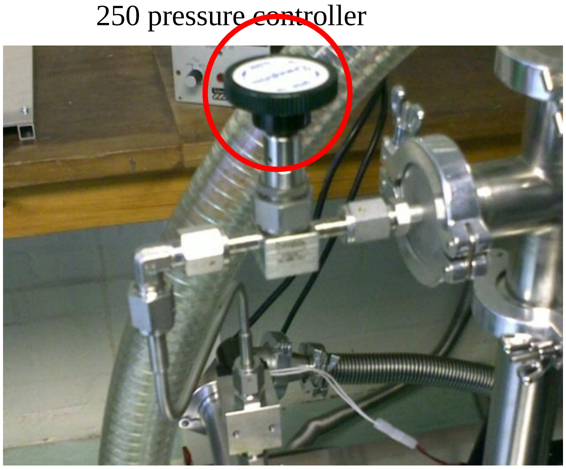

Fig.12 Pressure control valve

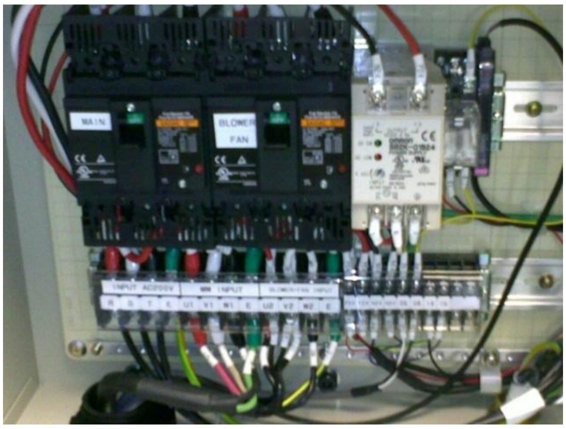

Fig.13 control panel of the ASTeX^{TM}

Fig.14 Microwave power generator

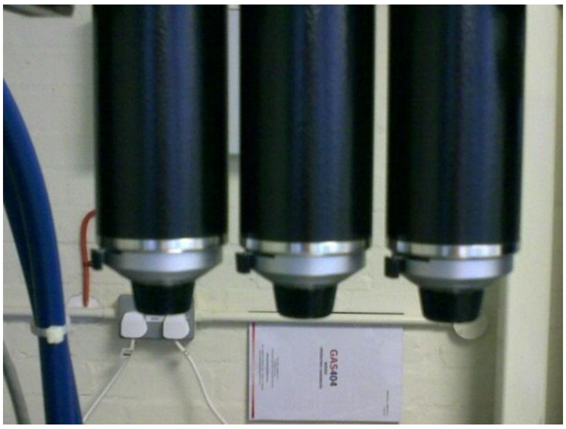

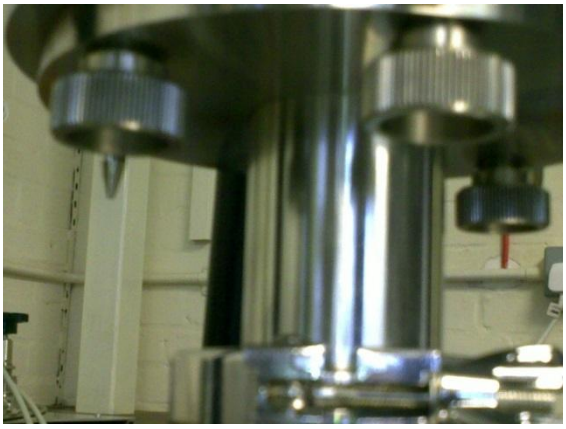

Fig.15 Phase shifter of the microwave power generator

Fig. 16 Screws under the sample holder